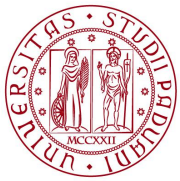

UNIVERSITÀ
DEGLI STUDI
DI PADOVA

Sede Amministrativa: Università degli Studi di Padova

Dipartimento di Scienze Chimiche

SCUOLA DI DOTTORATO DI RICERCA IN: SCIENZE MOLECOLARI
INDIRIZZO: SCIENZE CHIMICHE
CICLO: XXVII

Understanding the Properties of 3D Monolayers on Au_{25} Clusters

Direttore della Scuola: **Prof. Antonino Polimeno**

Supervisore: **Prof. Flavio Maran**

Dottorando: **Tiziano Dainese**

Riassunto

Lo studio delle proprietà di nanoparticelle metalliche con dimensioni inferiori a pochi nanometri, ricoperte e protette da monostrati organici (Monolayer-Protected-Cluster: MPC) è una delle aree di ricerca più attive nel campo delle nanoscienze e delle nanotecnologie. Gli MPC d'oro sono composti da un nucleo metallico circondato da un monostrato organico protettivo, costituito in generale da complessi tiolo-oro. Questa Tesi affronta gli aspetti riguardanti le proprietà dei più importanti MPC tra quelli che manifestano un comportamento molecolare: i cluster $Au_{25}(SR)_{18}$ (SR: alcantiolato). L'attenzione è stata dedicata principalmente alla struttura e al comportamento del monostrato protettivo, in particolare nell'ottica delle possibili applicazioni di questi materiali ibridi, dove l'interazione tra il nucleo d'oro del cluster e il mezzo circostante è determinata dalle proprietà del monostrato stesso.

La Tesi è strutturata come segue.

Capitolo uno. In questa sezione si fornisce una panoramica generale della letteratura scientifica relativa agli MPC d'oro, su come variano le loro dimensioni e su come queste influiscano sul comportamento dei cluster e sulle loro principali proprietà chimico-fisiche. Viene inoltre definito l'obiettivo della Tesi. In questo capitolo sono inclusi anche un numero di riferimenti bibliografici, per ragioni pratiche ognuno dei successivi capitoli contiene le proprie citazioni bibliografiche.

Capitolo due. Viene descritta la procedura generale di sintesi e caratterizzazione dei cluster $Au_{25}(SR)_{18}$, sia nel loro stato nativo in forma di anione, che nella loro configurazione neutra (o ossidata) in cui si comportano come specie paramagnetiche. Sono descritte in dettaglio quattro particolari sintesi. Viene delineato il controllo dello stato di carica degli MPC e il suo effetto sulle proprietà ottiche e magnetiche. Infine è presente una sezione sperimentale generale. Maggiori dettagli comunque sono aggiunti alla fine di ogni capitolo successivo a seconda dell'argomento trattato.

Capitolo tre. Descrive i risultati pubblicati in: Dainese, T.; Antonello, S.; Gascón, J. A.; Pan, F.; Perera, N. V.; Ruzzi, M.; Venzo, A.; Zoleo, A.; Rissanen, K.; Maran, F. $Au_{25}(SEt)_{18}$, a Nearly Naked Thiolate-Protected Au_{25} Cluster: Structural Analysis by Single Crystal X-ray Crystallography and Electron Nuclear Double Resonance. *ACS Nano* **2014**, *8*, 3904-3912. Sono stati sintetizzati e caratterizzati nanocluster d'oro protetti con etantiolo, il legante più corto tra quelli riportati in letteratura. Le forma anioniche e neutre di questo particolare cluster,

$Au_{25}(SEt)_{18}$, sono state completamente caratterizzate tramite spettroscopia ^{1}H e ^{13}C NMR, che confermano le proprietà del monostrato e il paramagnetismo della forma neutra $Au_{25}(SEt)_{18}^{0}$. Le misure di diffrazione a raggi X effettuate su quest'ultima hanno permesso la pubblicazione della prima struttura cristallografica di un cluster d'oro protetto da un semplice alcantiolo lineare. Il nanocluster è stato studiato per mezzo di avanzate tecniche di risonanza paramagnetica elettronica e i risultati sono stati analizzati tramite calcoli quantomeccanici basati sulla teoria del funzionale di densità (DFT), non intaccati da approssimazioni nella struttura od omissioni.

Capitolo quattro. Vengono discussi i risultati pubblicati in Antonello, S.; Arrigoni, G.; Dainese, T.; De Nardi, M.; Parisio, G.; Perotti, L.; René, A.; Venzo, A.; Maran, F. Electron Transfer through 3D Monolayers on Au_{25} Clusters. *ACS Nano* **2014**, *8*, 2788–2795. E' stata sintetizzata una vasta gamma di cluster $Au_{25}(SC_nH_{2n+1})_{18}$ (n = 2, 4, 6, 8, 10, 12, 14, 16, 18) monodispersi, ed è stato studiato il modo in cui gli elettroni attraversano il monostrato organico protettivo. I risultati derivati dalle misure di trasferimento elettronico, adeguatamente supportati tramite spettroscopia ^{1}H NMR, spettroscopia di assorbimento IR e calcoli di dinamica molecolare, mostrano l'esistenza di una lunghezza critica della catena alchilica, che definisce la transizione tra leganti corti, formanti un monostrato con una struttura del tutto fluida, e catene alchiliche più lunghe, che si auto-organizzano in fasci. Il monostrato organico avvolgente le nanoparticelle d'oro con dimensioni inferiori a pochi nanometri, è generalmente rappresentato come l'equivalente 3D dei monostrati auto-assemblati 2D (Self-Assembled Monolayer: SAM) su superfici estese d'oro. I nostri risultati comunque dimostrano che, a differenza del caso dei SAM bi-dimensionali, è possibile un efficiente comunicazione elettronica tra il nucleo del cluster e l'ambiente circostante anche in presenza di leganti aventi lunghe catene alchiliche. Queste conclusioni forniscono un chiaro schema di come un cluster d'oro di dimensioni estremamente ridotte, interagisce con il mezzo circostante attraverso il suo monostrato organico, che protegge ma non isola completamente il nucleo.

Capitolo cinque. Vengono introdotte come naturale continuazione dei capitoli precedenti le proprietà di trasferimento elettronico in stato solido dei nanocluster sintetizzati. Sono stati presi in considerazione i cluster con formula generale $Au_{25}(SC_nH_{2n+1})_{18}$, con n = 3, 4, 5, 6, 8, and 10. Tramite drop casting da soluzione e successiva essicazione degli MPC depositati, sono stati preparati dei film depositati direttamente su elettrodi interdigitati (IDAs). La dipendenza lineare

della conduttività rispetto *n*, indica un meccanismo di trasferimento elettronico che prevede il salto (hopping) fra stati energetici localizzati, nel quale i nuclei dei nanocluster si comportano come accettori o donatori di elettroni, e i leganti alchilici agiscono come spaziatori che determinano l'efficienza del tunneling elettronico attraverso il monostrato organico. I risultati sperimentali sono stati comparati con quelli ottenuti per gli stessi cluster in soluzione (capitolo 4). Gli esiti delle misure di trasferimento elettronico indicano un sostanziale ripiegamento delle catene alchiliche lineari di questi MPC nello stato solido, ma in misura ridotta rispetto a quanto osservato in soluzione, dove è possibile una maggiore fluidità del monostrato organico.

Capitolo sei. Vengono incorporati i risultati più importanti e le metodologie introdotte nei capitoli precedenti. L'inserimento di un metile in sostituzione di un idrogeno (in posizione β rispetto l'atomo di zolfo) in un metilene del butantiolo, origina un alcantiolo ramificato con un centro stereogenico. Nonostante siano stati impiegati tioli commerciali racemi, è stato riscontrato che in realtà possiedono un eccesso enantiomerico (e.e.) dell'isomero (*S*), come verificato attraverso la sintesi dello stesso enantiomero puro. Sono stati preparati diversi cluster $Au_{25}(SMeBu)_{18}^{0}$ (HSMeBu = 2-metil-1-butantiolo) caratterizzati tramite diverse tecniche, tra le quali spettroscopia ^{1}H-NMR e spettroscopia di dicroismo circolare (CD). Entrambe le metodologie forniscono la stessa informazione: come l'e.e. del tiolo impiegato nella sintesi raggiunge un valore di circa il 75 %, il cluster corrispondente risulta contenere solo l'isomero (*S*) del legante. E' stato quindi osservato per la prima volta, il fenomeno della risoluzione spontanea in un MPC. Queste conclusioni fondate sui risultati spettroscopici, sono state perfettamente confermate risolvendo la struttura cristallografica di un cluster che, in principio, avrebbe dovuto possedere un monostrato organico avente il 77 % di e.e. dell'isomero (*S*). Invece la struttura cristallografica sperimentale, esibisce solo l'isomero (*S*) sulla superficie del nucleo del cluster $Au_{25}(SMeBu)_{18}^{0}$.

Abstract

The study of the properties and applications of small gold monolayer-protected clusters (MPCs) is one of the most active research areas in nanosciences and nanotechnologies. MPCs are composed of a gold core surrounded by a capping monolayer usually consisting in thiolates and further Au atoms. This Thesis addresses aspects concerning the properties of the most important MPC displaying molecular behavior: $Au_{25}(SR)_{18}$. The main focus is on the structure and behavior of the capping thiolate monolayer, particularly in view of possible applications of these hybrid materials where the interaction between the gold core and the surrounding medium is dictated by the monolayer's properties themselves. The Thesis is structured as follows.

Chapter one provides a general introduction to MPCs, their size difference and how this factor affects their behavior, the main physicochemical properties of molecular MPCs, and finally the aims of this Thesis. This Chapter also includes a number of references. For practical reasons, however, each of the following Chapters contains its own references.

Chapter two describes the general synthesis and characterization of these clusters, whether in their native anionic state or as neutral, paramagnetic species obtained by controlled oxidation of the former. Four selected syntheses are described in detail. The control of the charge state and its effect on the optical and NMR properties are described. Finally, a general experimental section is provided. More details, however, will be added at the end of each Chapter, depending on the specific topic addressed.

Chapter three describes findings that have been published: Dainese, T.; Antonello, S.; Gascón, J. A.; Pan, F.; Perera, N. V.; Ruzzi, M.; Venzo, A.; Zoleo, A.; Rissanen, K.; Maran, F. $Au_{25}(SEt)_{18}$, a Nearly Naked Thiolate-Protected Au_{25} Cluster: Structural Analysis by Single Crystal X-ray Crystallography and Electron Nuclear Double Resonance. *ACS Nano* **2014**, *8*, 3904-3912. We prepared and characterized a 25-gold atom nanocluster protected by the smallest ligand ever used, ethanethiol. The anionic and the neutral form of $Au_{25}(SEt)_{18}$ were fully characterized by ^{1}H and ^{13}C NMR spectroscopy, which confirmed the monolayer's properties and the paramagnetism of neutral $Au_{25}(SEt)_{18}^{0}$. X-ray crystallography analysis of the latter provided the first structure of a gold cluster protected by a simple, linear alkanethiolate. The cluster was studied by advanced electron paramagnetic techniques and the results analyzed also by DFT calculations, which were not affected by structure's approximations or omissions.

Chapter four also describes findings that have been published: Antonello, S.; Arrigoni, G.; Dainese, T.; De Nardi, M.; Parisio, G.; Perotti, L.; René, A.; Venzo, A.; Maran, F. Electron Transfer through 3D Monolayers on Au_{25} Clusters. *ACS Nano* **2014**, *8*, 2788–2795. We prepared a large series of monodisperse $Au_{25}(SC_nH_{2n+1})_{18}$ clusters (*n* = 2, 4, 6, 8, 10, 12, 14, 16, 18) and studied how electrons tunnel through these monolayers. Electron transfer results, nicely supported by ^1H NMR spectroscopy, IR absorption spectroscopy, and molecular dynamics results, show that there is a critical ligand length marking the transition between short ligands, which form a quite fluid monolayer structure, and longer alkyl chains, which self-organize into bundles. The monolayer protecting small gold nanoparticles is generally represented as the 3D equivalent of 2D SAMs on extended gold surfaces. We found, however, that at variance with the truly protecting 2D SAMs, efficient electronic communication of the Au_{25} core with the outer environment is thus possible even for long alkyl chains. These conclusions provide a different picture of how an ultrasmall gold core talks with the environment through/with its protecting but not-so-shielding monolayer.

Chapter five introduces a natural follow up of the previous Chapters. We used a series of linear-chain thiolate protected clusters having the general formula $Au_{25}(SC_nH_{2n+1})_{18}$, with *n* = 3, 4, 5, 6, 8, and 10, and carried out conductivity measurements on their dry films, which were formed by drop casting these MPCs onto interdigitated electrodes (IDAs). The linear dependence of the conductivity on *n* points to a hopping mechanism where the cores of the nanoclusters behave as a localized electron-donor or acceptor site, and the ligands as spacers dictating the efficiency of electron tunneling. The experimental results were compared with those obtained for the same clusters in solution (Chapter 4). The electron-transfer results point to a substantial folding of the linear chains of these MPCs in the solid state, but to a lesser extent compared to what observed in solution, where more fluidity is possible.

Chapter six basically incorporates the most important results and methodologies described in the previous Chapters. We introduced branching (one methyl group in place of one hydrogen at position β with respect to the sulfur atom) along a butanethiolate chain, which thus introduces a stereogenic center. Although we used commercially available racemic thiols, we discovered that these thiols possess, in fact, an enantiomeric excess (e.e.) of the (*S*)-enantiomer, as verified through synthesis of the pure (*S*)-enantiomer. We prepared several $Au_{25}(SMeBu)_{18}^0$ clusters (HSMeBu = 2-methyl-1-butanethiol)

and characterized them by various techniques. Among them, we used ^{1}H NMR spectroscopy and circular dichroism (CD) spectroscopy. Both techniques provided the same information: as the e.e. of the thiol employed reaches a value of ca. 75%, the resulting Au_{25} clusters only contain the *S*-thiolate. We thus observed, for the first time, the phenomenon of spontaneous resolution for an MPC. These conclusions based on spectral data were perfectly confirmed by solving the single crystal structure of a cluster that, in principle, should have contained thiols possessing 77% e.e. of the (*S*)-enantiomer. Instead, X-ray crystallography showed that only the (*S*)-enantiomer is capping the Au_{25} core.

Ringraziamenti

Desidero innanzitutto ringraziare il mio Supervisore, Prof. Flavio Maran, ed esprimergli la mia sincera gratitudine per i preziosi insegnamenti durante questi anni di dottorato, per le numerose ore dedicate alla mia Tesi, per la sua paziente supervisione e per il suo entusiastico incoraggiamento per questo progetto. Ringrazio sentitamente la Prof. Sabrina Antonello, per il suo sostegno, per la sua gentilezza, sempre disponibile a dirimere i miei dubbi e ad aiutarmi durante la stesura di questo lavoro.

Ringrazio il Dottor Alfonso Venzo, per le numerose ore dedicate alle misure NMR, per la sua pazienza, la sua disponibilità e per i suoi numerosi consigli.

Vorrei ringraziare tutte le persone che mi hanno accompagnato e hanno contribuito in un modo o nell'altro a questa Tesi, in particolare i miei attuali compagni di lavoro, Federico, Ivan, Marco, Anna, Swetha, Andrea con cui ho condiviso opinioni e consigli. Un ringraziamento va anche al Dr. Marco Ruzzi e al Dr. Alfonso Zoleo, ed ai Prof. José A. Gascòn e Kari Rissanen per il loro supporto scientifico in parti di questa Tesi.

Infine desidero ringraziare la mia famiglia ed i miei amici più cari per la loro pazienza ed il loro supporto, non solo in questi tre anni di dottorato, ma nella mia intera vita.

Table of Contents

Chapter 1: Introduction 17
1.1 Monolayer Protected Gold Clusters 17
1.1.1 Size Matters 20
1.1.2 Molecular MPCs 23
1.2 Physicochemical Properties of the Molecular $Au_{25}(SR)_{18}$ Cluster 24
1.2.1 UV-vis Behavior 25
1.2.2 Nuclear Magnetic Resonance 28
1.2.3 Electron Paramagnetic Resonance 30
1.2.4 Electrochemistry 32
1.3 Aims and Summary of the Thesis 35
1.4 References 37

Chapter 2: Synthesis and Characterization of $Au_{25}(SR)_{18}$ 47
2.1 Synthesis 47
2.1.1 $Au_{25}(SC_2H_5)_{18}$ 47
2.1.2 $Au_{25}(SC_3H_7)_{18}$ 48
2.1.3 $Au_{25}(SC_4H_9)_{18}$ 49
2.1.4 $Au_{25}(SC_5H_{11})_{18}$ 51
2.2 Control of Charge and Optical Characterization 51
2.3 Control of Charge and Nuclear Magnetic Resonance 55
2.4 General Experimental Information 57
2.4.1 Chemicals 57
2.4.2 Methods and Instrumentations 58
2.5 References 59
2.6 Acknowledgements 59

Chapter 3: $Au_{25}(SEt)_{18}$, a Nearly Naked Thiolate-Protected Au_{25} Cluster: Structural Analysis by Single Crystal X-ray Crystallography and Electron Nuclear Double Resonance 61
3.1 Abstract 61
3.2 Introduction 61
3.3 Results and Discussion 64
3.3.1 Synthesis and Characterization of $Au_{25}(SEt)_{18}$ 64
3.3.2 Electrochemistry 64

3.3.3 NMR Spectroscopy 66
3.3.4 The X-ray Structure 68
3.3.5 ENDOR Analysis and DFT Calculations 72
3.4 Conclusions 78
3.5 Experimental Section 79
3.5.1 UV-vis Absorption Spectroscopy 79
3.5.2 Mass Spectrometry 79
3.5.3 Electrochemistry 79
3.5.4 NMR Spectroscopy 80
3.5.5 X-ray Single Crystal Diffraction 80
3.5.6 ENDOR Spectroscopy 81
3.5.7 Computational Methods 85
3.6 References 86
3.7 Acknowledgements 90

Chapter 4: Electron Transfer through 3D Monolayers on Au_{25} Clusters 91
4.1 Abstract 91
4.2 Introduction 91
4.3 Results and Discussion 93
4.3.1 Synthesis of $Au_{25}(SC_nH_{2n+1})_{18}$ 93
4.3.2 UV-vis Absorption Spectroscopy 94
4.3.3 MALDI-TOF Mass Spectrometry 95
4.3.4 NMR Spectroscopy 96
4.3.5 IR Absorption Spectroscopy 99
4.3.6 Heterogeneous Electron Transfer 101
4.3.7 Molecular Dynamics Calculations 106
4.4 Conclusions 108
4.5 Experimental Section 108
4.5.1 MALDI-TOF Mass Spectrometry 108
4.5.2 UV-vis Absorption Spectroscopy 109
4.5.3 Infrared Absorption Spectroscopy 109
4.5.5 Electrochemistry 109
4.5.6 Molecular Dynamics Calculations 110
4.6 References 111
4.7 Acknowledgements 115

Chapter 5: Electron Transfer in Au_{25} Films 117
5.1 Abstract 117
5.2 Introduction 117
5.3 Results and Discussion 119
5.3.1 Synthesis of $Au_{25}(SC_nH_{2n+1})_{18}$, n = 3 and 5 119
5.3.2 Heterogeneous Electron Transfer 119
5.3.3 Conductivity of Au_{25} Films 120
5.3.4 Comparison Between Solution and Solid-State ETs 123
5.3.5 Further Insights: The case of $Au_{25}(SMeBu)_{18}$ 128
5.4 Conclusions 130
5.5 Experimental Section 130
5.6 References 131
5.7 Acknowledgements 132

Chapter 6: Chiral $Au_{25}(SR)_{18}$ Clusters 133
6.1 Abstract 133
6.2 Introduction 133
6.3 Results and Discussion 135
6.3.1 Synthesis of the Chiral Thiol 135
6.3.2 Polarimetry and CD Spectroscopy of the Thiol 136
6.3.3 Synthesis of $Au_{25}(SMeBu)_{18}$ 138
6.3.4 Optical and Electrochemical Behaviors 139
6.3.5 The X-ray Structure 142
6.3.6 CD Spectroscopy of $Au_{25}(SMeBu)_{18}$ 143
6.3.7 NMR of $Au_{25}(SMeBu)_{18}$ 145
6.4 Conclusions 157
6.5 Experimental Section 158
6.6 References 159
6.7 Acknowledgements 162

Chapter 1: Introduction

1.1 Monolayer Protected Gold Clusters

In 1981, Schmid and his co-workers showed that particularly small Au clusters, Au_{55}, could be prepared using phosphines as stabilizing agents.[1,2] This paved the way to using these materials in nanotechnologies but also to posing a number of fundamental questions about the properties of these new objects. A crucial step forward was provided by the groundbreaking paper by Brust *et al* who described a sound method to prepare thiolate-capped Au nanoparticles.[3] This successful idea was based on the knowledge meanwhile accumulated as a consequence of the Nuzzo and Allara's observations concerning the formation of self-assembled monolayers (SAMs) of thiols on extended gold surfaces.[4,5] The relationship between the latter 2D SAMs and the corresponding 3D monolayers capping an Au cores is, in fact, still a very important topic of current research, as recently reviewed.[6,7] The capping thiols (as thiolates) have the main function of stabilizing cores composed by a limited amount of gold atoms, as well as to prevent aggregation between particles to form larger entities. These monolayers thus function as protecting shields and this is the reason why these unique nanosystems have been named monolayer protected clusters (MPCs).[8] As described by Murray and his co-workers, alkanethiolate MPCs differ from conventional colloids and nanoparticles prepared by other routes in that they can be repeatedly isolated from and redissolved in common organic solvents without irreversible aggregation or decomposition.[9] It soon became clear that MPCs constitute a entirely class of systems endowed by very special characteristics and properties.

The study of the properties and applications of small gold MPCs is indeed one of the most active research areas in nanosciences and nanotechnologies. Over 20 years have already elapsed since publication of the groundbreaking paper by Brust *et al*.[3] This discovery triggered active research worldwide, and after just a decade the amount of available information was already significant.[10] These and following contributions[11] established solid grounds for future research and thus the number of fundamental questions regarding MPCs, particularly ultrasmall MPCs, kept increasing. Besides fundamental aspects, some of which will be dealt with in detail in the following Sections and Chapters, it is worth stressing that a number of possible applications have been addressed by several

groups worldwide, particularly in the context of catalysis and biomedical applications.[12-16]

Bulk gold has long been considered too inert to be a catalyst until the discovery that supported Au(III) could be very catalytic for acetylene hydrochlorination[17] and supported Au nanoparticles (AuNPs) for CO oxidation.[18] Supported Au and other metal nanoparticles have been successfully shown to catalyze various chemical reactions.[14,19-22] It soon became clear that the catalytic properties of AuNPs strongly depend on the particles' size and stability. In particular, AuNPs with diameters <5 nm are the most effective catalysts for many processes.[23] Generally, performing redox reactions both selectively and efficiently is an inherently challenging task. Problems may arise because of poor selectivity or yield, which is often attributed to the low loading of AuNPs, along with their polydispersity, on solid support materials. Most important, the presence of a protective monolayer may limit accessibility of the reacting molecules to the gold core. The ligands are often removed by calcination at 200-400 ^{o}C, which may cause the AuNPs to sinter/aggregate;[24,25] this procedure is not suitable, *e.g.*, when polymers are used as supports. In this regard, the Maran's and Asefa's groups showed that the catalytic activity and selectivity of supported Au_{25} and Au_{144} clusters toward oxidation reaction can be significantly enhanced by controlled reductive deprotection under mild conditions.[26] Some solution-phase reactions, however, proceed rather well even when relatively bulky ligands are still on the surface. This is the case of very small molecules such as for CO_2 reduction[27] and CO oxidation,[28] but also larger substrates, such as in the oxidation of sulfides to sulfoxides[29] hydrogenation of α,β-unsaturated ketones and aldehydes,[30] or reduction of 4-nitrophenol.[31,32] Besides chemical catalysis, it is worth mentioning the potentialities of electrochemically induced homogeneous redox catalysis, particularly with $Au_{25}(SR)_{18}$, as the Maran Group proved in detail[33,34] and others also showed.[27,35-37] For catalytic reactions in which the monolayer is not removed, it is thus of outmost relevance to understand how reactants may penetrate the monolayer itself in order to then react on the catalytic gold surface. Therefore, gaining information on the monolayer structure in solution is particularly important. This is the main goal of this Thesis.

As we said, AuNPs and MPCs are of significant interest also for their potential technological applications in biomedicine.[13,16] Their interaction with proteins and cells constitute important aspects of this general area. The target of this Thesis is limited to ultrasmall MPCs and thus we will only mention some

relevant aspects. For biomedical applications, the ability to independently tailor the metal core and the nanocluster organic monolayer with required optical and biocompatible attributes has been recently demonstrated by studying protein-Au nanocluster bioconjugates.[38-42] Very few reports have focused on ultrasmall Au clusters: the protein-directed synthesis of highly fluorescent gold nanoclusters, presumably Au_{25}, has been described;[39] Au_{102}(*p*-MBA)$_{44}$ nanoparticles (*p*-MBA = *para*-mercaptobenzoic acid) could be derivatized with proteins and DNA. Exchange could be limited to a single protein;[40] a cryo-microscopy method for estimating the positional displacement of protein bound Au_{144} nanoparticles was presented and discussed;[41] calculations of the interaction of β_2-microglobulin to hydrophobic $Au_{25}(SR)_{18}^-$ indicated that binding yields persistent complexes.[42] In most biomedicine applications, the nanoparticles are required to cross cell membranes and the search for both critical particle size and morphology are of special significance and could be instrumental to devise suitable systems.[13] Compared to larger AuNPs,[43,44] information concerning ultrasmall Au MPCs (core diameters of <2 nm) is very scarce. Relevant papers concern cellular uptake of glutathione-protected Au_{144} clusters, which was assessed by transmission electron microscopy imaging,[45] and theoretical contributions focusing on the effect of charged ligands on Au_{144} penetration into the hydrophobic part of membrane bilayer.[46,47] The Maran group and co-workers have studied the interaction of substituted Au_{144} clusters and supported lipid monolayers and bilayers and found that it is possible to either incorporate the MPC inside the membrane or pierce the latter with peptide ligands while keeping the actual gold core outside it.[43] Overall, very few bio-related studies have been carried out with molecular gold clusters. Although these topics will not be specifically addressed in this Thesis, we wish to stress that most of the methodologies that we tested and refined could be, in principle, applied to the preparation and study of Au_{25} bioconjugates. Once again, the outcome of the aforementioned exemplifying studies show how important is obtaining insights into the properties of both the Au core and the surrounding monolayer, as well as to assess how the former interacts with the environment via the latter.

In these and further applications, the size factor is of paramount importance. Size dictates the separation between energy levels and thus the optical and electrochemical behavior, and thus the electron transfer (ET) properties. For particularly small MPCs, the discrete nature of both core atoms and protecting ligands is such to allow for precise use of further investigation

tools, such as nuclear magnetic resonance (NMR), electron paramagnetic resonance (EPR), mass spectrometry, X-ray crystallographic analysis. In the following Sections, we will briefly describe the most relevant differences between Au NPs and MPCs (Section 1.1.1) and some of their most salient physicochemical properties (Section 1.2), also functional to the scope of this Thesis. The specific Aims of the Thesis will be summarized in Section 1.3.

1.1.1 Size Matters

The number of interacting atoms affects the properties of the resulting systems in a dramatic way. Bulk gold is characterized by a continuum of electronic states resulting in its well-known optical behavior. It can also be used as an efficient electrode material providing, once again, a continuum of states and thus electrochemical driving forces. At the other extreme, we have molecules, such as gold complexes. In this case, the number of electronic states is much more limited and the electrochemical behavior is characterized by very few discrete (voltammetric) peaks. The energy difference between the highest occupied molecular orbital (HOMO) and the lowest unoccupied molecular orbital (LUMO) is very large. Consequently, within the usual potential window allowed by conventional solvent/electrolyte systems, not many are the molecules showing discrete oxidation and reduction peaks for the formation of the corresponding radical cations or anions (if starting from a neutral molecule). In between these two well-defined cases, there is a progressive change of the properties that can be monitored in a particularly efficient way by optical and electrochemical techniques.

One has to start by realizing that although the preparation of gold nanoparticles and clusters has improved dramatically, particularly over the last few years, for most AuNPs the actual composition, as usually determined by a combination of transmission electron microscopy (TEM), which provide the size of the gold core, and thermogravimetric analysis (TGA), which provides the mass ratio between the organic monolayer and the metallic part, is liable to provide only an average composition. The size is, therefore, not truly monodisperse. Let us focus on differences that can easily be detected electrochemically through observation of the give AuNP's voltammetric behavior at an inert working electrode. For AuNPs in which the monolayer does not carry electroactive functions, Murray defines:[11] "Three voltammetric regimes - defined by ranges of core size **-** can be imagined (all experimentally known). I label these bulk-

continuum, quantized double layer charging, and molecule-like." Here we will adopt the same terminology.

The first regime corresponds to comparatively large MPCs, typically of size larger than 3-4 nm. These MPCs have a number of metal core atoms sufficiently large to that make the energy levels appear as basically a continuum of states, also because of the effect of thermal energy. In the electrochemical experiment, one observes just a featureless, gradually rising amperometric currents.[48] On the other hand, use of the Brust-Schiffrin approach allows preparing particularly small MPCs.[3] This method is based on transferring $AuCl_4^-$ from water to toluene by using tetraoctylammonium bromide as the phase-transfer agent, addition of the given thiol in appropriate excess, which causes an initial reduction of Au(III) to Au(I), and finally reaction with sodium borohydride to form Au(0). The reaction can be controlled by balancing the rates of Au core growth and thiolate passivation in order to limit the reaction's outcome to formation of reasonably controlled average sizes. MPCs prepared by this or slightly modified methodologies allowed preparation of small, stable gold MPCs. If sufficiently small, these MPCs display a distinct, discrete voltammetric behavior characterized by a series of quite regularly spaced peaks. This is the regime defined as quantized double layer charging. The most notable example is that of $Au_{144}(SR)_{60}$. For organic thiolates, such as phenylethanethiolate, a typical differential pulse voltammetry trace, obtained in dichloromethane (DCM) containing 0.1 M tetrabutylammonium hexafluorophosphate (TBAH) is as shown in Figure 1. Research by electrochemical groups[49-51] showed that these MPCs display average peak-to-peak separations of 0.22-0.25 V and capacitances of 0.60-0.70 aF, the actual values depending on the specific ligand and solvent/electrolyte system. The very observation of discrete peaks indicates that the spacing between energy levels is now such that temperature cannot cause observation of a continuum behavior.

Finally, for MPCs with gold cores of diameter <1.6 nm, electronic-band energetics leads to particularly evident quantum confinement effects that make these gold clusters display the same general features of "simple" molecules. Notably, this is particularly evident through observation of well-defined electrochemical energy gap. Molecular clusters will be the topic of this Thesis and thus we will have several occasions to recall their very nice electrochemical behavior. Within the framework of this Section, however, it is worth showing a

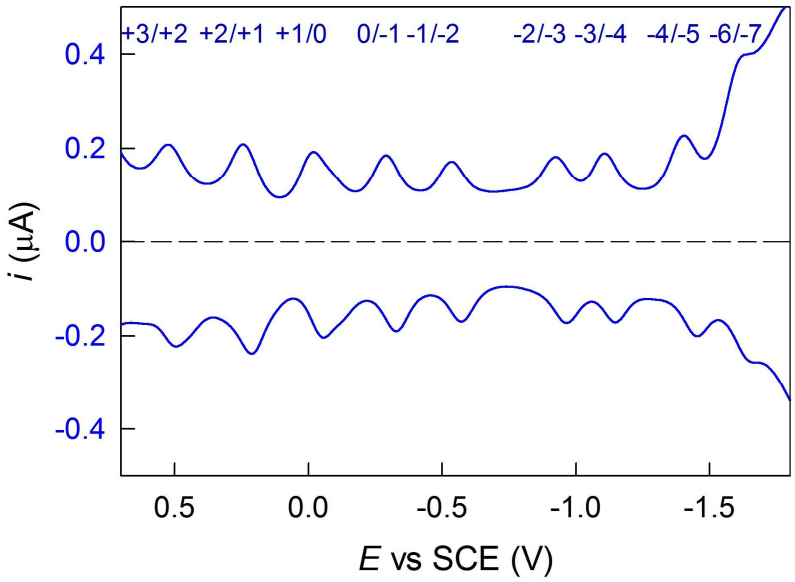

Figure 1. Typical differential pulse voltammetry behavior of 0.13 mM $Au_{144}(SC_2H_4Ph)_{60}$ in DCM/0.1 M TBAH. Glassy carbon electrode, 25 °C.

revised version of a picture that Murray prepared for his 2008 review.[11] We modified this figure by taking into account also later relevant results concerning new cluster stoichiometries. Figure 2 shows the HOMO-LUMO gaps (in red, eV)

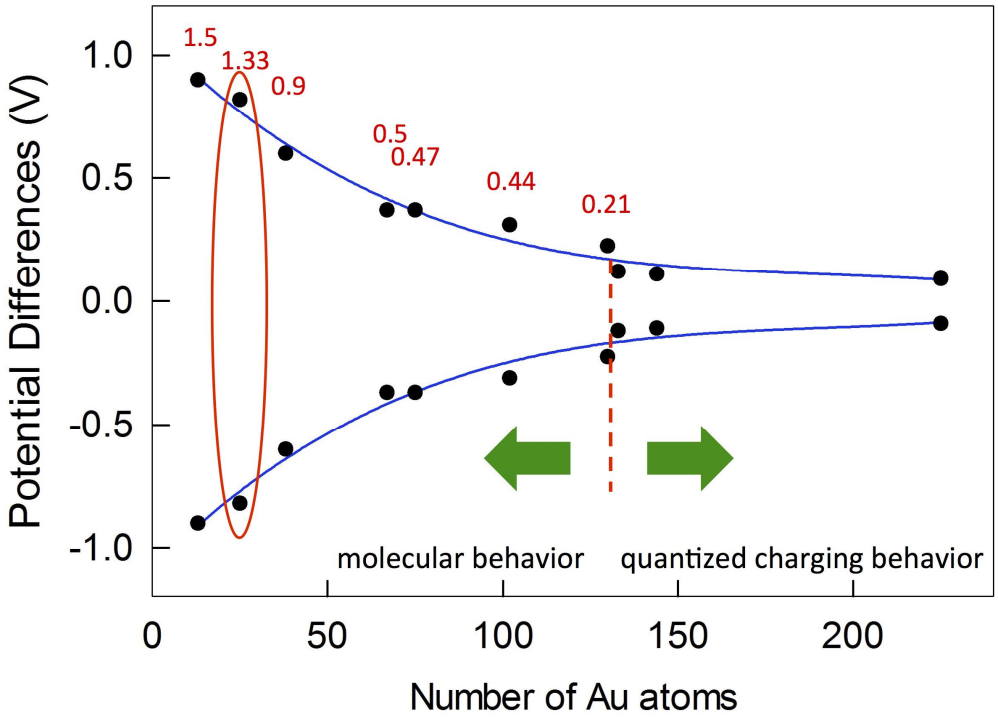

Figure 2. Electrochemical and optical gaps as function of the number of Au atoms. The blue curves have the only meaning of highlighting the trend.

and (Y axis) the corresponding electrochemical gaps (for molecular MPCs) or peak-to-peak separations (quantize double layer charging behavior) as a function of the number of Au atoms composing the cluster (X axis). The red dashed line marks the approximate size at which the transition occurs. The data show the following MPCs, which were characterized by electrochemical means particularly well in organic solvents such as DCM: Au_{225},[52] Au_{144},[49-51] Au_{133},[53] Au_{130},[54] Au_{102},[55] Au_{75},[56] Au_{67},[57] Au_{38},[50,58] Au_{25},[33,59,60] Au_{13}.[61] Au_{25} is evidenced because it will be the topic of this Thesis.

Figure 2 nicely evidences the onset of a distinct HOMO-LUMO gap for clusters smaller than ca. Au_{144}. To date, the cluster that displays the most clear-cut electrochemical features of both molecular and quantized double layer charging behaviors is Au_{130}.[54] That the transition occurs at this cluster size is also supported by a recent investigation that concluded that whereas for Au cores of ≤ 1.6 nm (Au_{144}) the clusters have molecular-like electronic structures and non-fcc geometric structures, larger Au cores have structures resembling those of bulk gold.[62] Other recent theoretical studies also points to clusters in the range of Au_{144} as marking the transition toward the birth of a localized surface plasmon resonance.[63,64]

1.1.2 Molecular MPCs

As we have seen, MPCs with gold cores of diameter <1.6 nm display the same general features of molecules. Their borderline behavior between actual molecules and slightly larger MPCs makes the study of their fundamental properties particularly fascinating and often intriguing. This PhD Thesis explores frontiers of this area of science.

The main reason that has proved to be expedient for observing, characterizing and understanding fine molecular properties of ultrasmall MPCs is practical: as opposed to only slightly larger MPCs, such as $Au_{144}(SR)_{60}$ (1.6 nm, SR = generic thiolate ligand) which we have seen to belong to the class of clusters displaying quantized double-layer charging behavior, only molecule-like MPCs could be so far prepared in a truly monodisperse form, with atomic precision. A breakthrough came in 2007 when the single crystal structure of $Au_{102}(SR)_{44}$ was solved by X-ray crystallography, revealing unexpected structural features (staple-like motifs).[65] Structures of a few smaller gold clusters were then published.[66-74] One of this contributions, concerning $Au_{25}(SEt)_{18}$,[69] will be

described in detail in Chapter 3. The structure of the largest MPC so far crystallized, $Au_{133}(SR)_{52}$, has been successfully described very recently by two research groups.[53,75] Proper synthesis and purification coupled to knowledge of the relevant structures have thus provided the necessary grounds for obtaining a deeper understanding of these systems and developing tools suitable to study the fine structure and electronic distribution of nanoclusters.[6,12,69,76,77] In this framework, $Au_{25}(SR)_{18}$ has been and still is a "gold mine" because it keeps furnishing an effective benchmark for gaining insights into properties and possible applications of molecular MPCs as well as developing and testing new concepts at the nanoscale.[76] For space limitations, here we do not have room enough to cover everything that has been done in this direction, but good recent reviews are available.[6,12,76,77] This Thesis is entirely focused on a series of aspects concerning $Au_{25}(SR)_{18}$ and, therefore, we will now describe some of those fundamental physicochemical properties that we and others have been particularly focused on, also in view of introducing our research objectives.

1.2 Physicochemical Properties of the Molecular $Au_{25}(SR)_{18}$ Cluster

$Au_{25}(SR)_{18}$ is a particularly stable molecular MPC with a metal core diameter of only 1 nm. Figure 3 shows the structure of a particularly small Au_{25} MPC that was prepared and studied during this Thesis work, $Au_{25}(SEt)_{18}^{0}$.[69] More structural details will be described in Chapter 3, whereas here we will use it to stress the general features of all clusters possessing the general formula $Au_{25}(SR)_{18}$. The structure shows a 13-atom icosahedral inner Au core (highlighted in yellow) surrounded by six –(SR)-Au-(SR)-Au-(SR)- staple-like semicrowns (in blue).[66-69] The 18 thiolated ligands forming the monolayer thus split into a group of 12 inner ligands (in red), in which sulfur makes bonds with one Au atom of the gold core and one staple Au atom, and a group of 6 outer ligands (in green) in which the bonds are with two staple Au atoms.

Several properties of $Au_{25}(SR)_{18}$ have been studied in detail. In the following Sections, we will provide the essential background to properly frame the following Chapters. Most of these concepts will be addressed in more depth also later, depending on the specific topic dealt with in each Chapter.

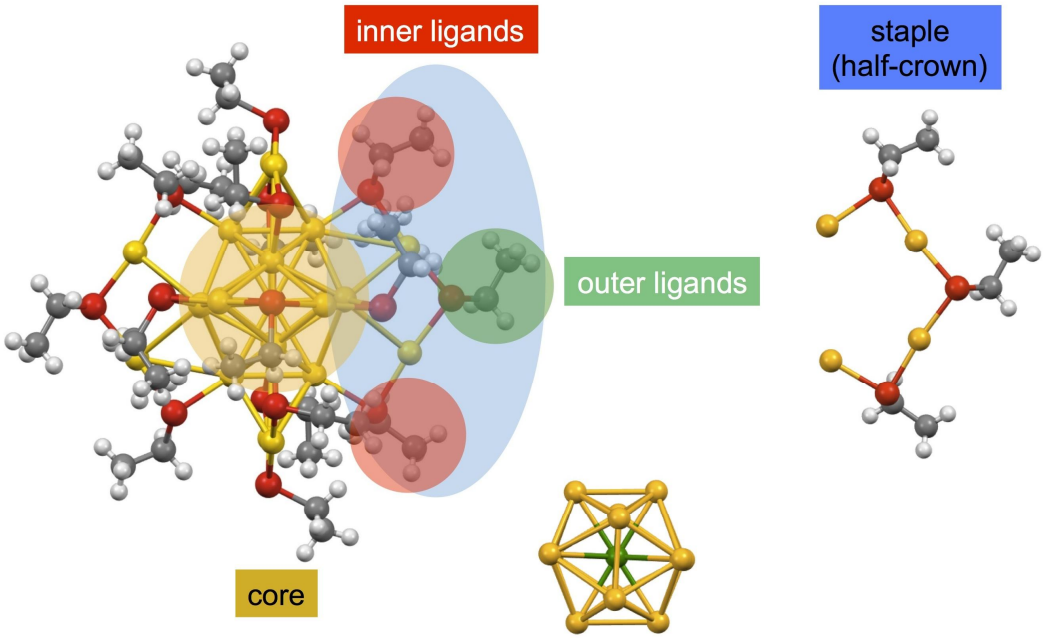

Figure 3. X-ray crystal structure of $Au_{25}(SEt)_{18}^{0}$. Au = yellow, S = red, C = gray, H = white. For the highlighted parts, see text. Close views of the staple (half-crown) and core (central Au atom in green) are shown on the right-hand side and the bottom, respectively.

1.2.1 UV-vis Behavior

Molecular clusters such as $Au_{25}(SR)_{18}$ display UV-vis absorption spectra containing several fine features. In its native form, this cluster is an anion and is usually stabilized by a *n*-tetraoctylammonium countercation ([*n*-Oct_4N^+][$Au_{25}(SR)_{18}^-$]) used as the phase-transfer agent in Brust-type syntheses. Some properties of the corresponding neutral $Au_{25}(SR)_{18}^{0}$ clusters were initially obtained by chemical[68,78] or electrochemical oxidation of $Au_{25}(SR)_{18}^-$.[59] The Maran group introduced a very precise method for the controlled oxidation of $Au_{25}(SR)_{18}^-$ to form $Au_{25}(SR)_{18}^{0}$ and then $Au_{25}(SR)_{18}^+$.[79] This original strategy was then devised to obtain clean optical spectra and uncomplicated ^1H and ^{13}C NMR spectra (see Section 1.2.2). The oxidant was required to (i) be soluble in the same solvents as the cluster, (ii) bear no protons, (iii) generate a diamagnetic species, and (iv) the redox reaction was required to proceed quantitatively, irreversibly and with clearly identifiable products and counter-ions. The selected oxidant was bis(pentafluorobenzoyl) peroxide, a very reactive dibenzoyl peroxide that acts as an efficient electron acceptor according to a concerted dissociative electron-transfer (ET) process,[80,81] a process typical of peroxides.[82-84] The

reaction, which can be carried out also with other ring-substituted dibenzoyl peroxides,[34] is a two-electron process only generating the stable carboxylate anion $C_6F_5CO_2^-$:

(1) $(C_6F_5CO_2)_2 + Au_{25}(SR)_{18}^{0/1-} \longrightarrow C_6F_5CO_2^- + C_6F_5CO_2^{\bullet} + Au_{25}(SR)_{18}^{0/1+}$

(2) $C_6F_5CO_2^{\bullet} + Au_{25}(SR)_{18}^{0/1-} \longrightarrow C_6F_5CO_2^- + Au_{25}(SR)_{18}^{0/1+}$

The irreversible ET reaction of $(C_6F_5CO_2)_2$ with $Au_{25}(SR)_{18}$ was monitored by UV-vis absorption spectroscopy.[34,79] Figure 4 (upper graph) shows the progressive transition from $Au_{25}(SR)_{18}^-$ to $Au_{25}(SR)_{18}^0$, for R = C_2H_4Ph (0.023 mM, DCM, 10 mm cuvette), also in terms of absorption derivative (lower graph). Figure 5 (upper

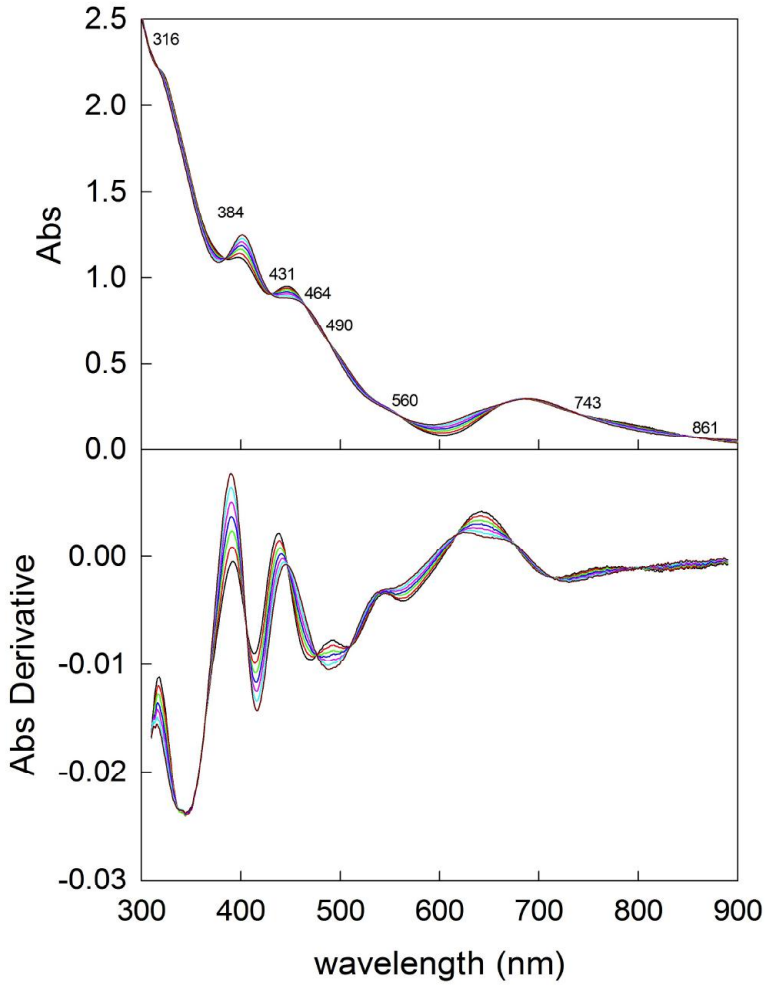

Figure 4. Effect of the progressive addition of bis(pentafluorobenzoyl) peroxide on the UV-vis absorbance spectrum (upper graph) and corresponding derivative (lower graph) of 0.023 mM $Au_{25}(SR)_{18}^-$ in DCM. Addition was calibrated to arrive to full conversion to $Au_{25}(SR)_{18}^0$.

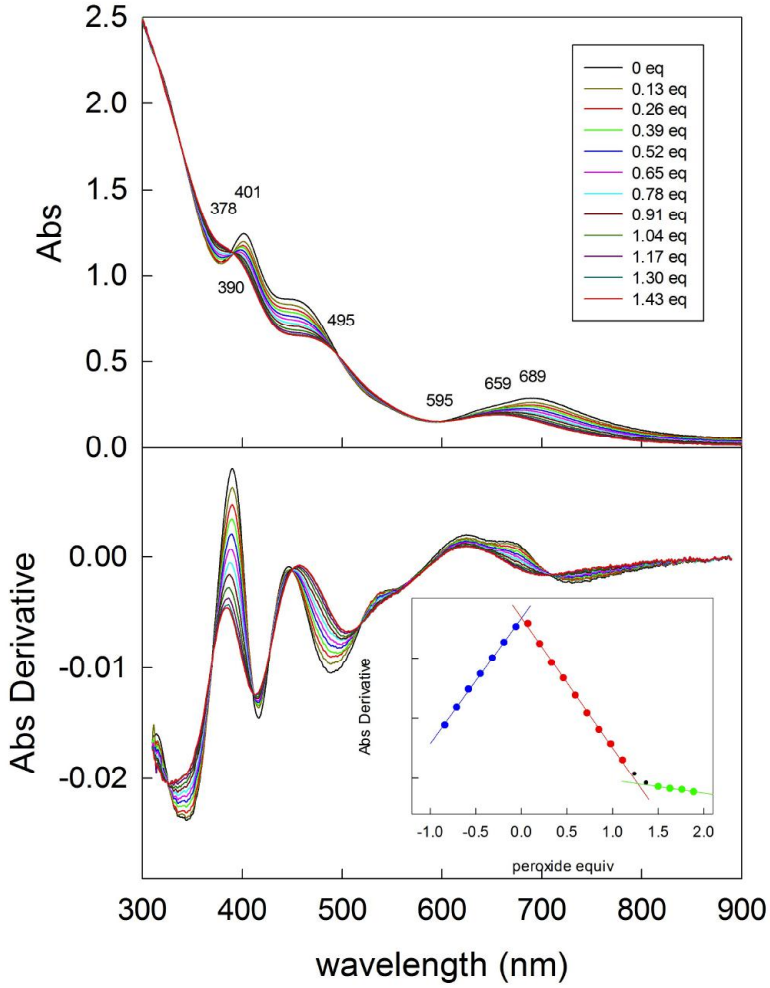

Figure 5. Effect of the addition of bis(pentafluorobenzoyl) peroxide on the UV-vis absorbance spectrum (upper graph) and corresponding derivative (lower graph) of 0.023 mM $Au_{25}(SR)_{18}^{0}$ in DCM. For details, see text. This figure is reproduced from ref. 79.

graph) shows the transition from $Au_{25}(SR)_{18}^{0}$ to $Au_{25}(SR)_{18}^{+}$, also as a derivative plot (lower graph). The number of equivalents in the legend refers to the theoretical amount of peroxide required for full conversion of $Au_{25}(SR)_{18}^{0}$ into $Au_{25}(SR)_{18}^{+}$ (two-electron process: sum of reactions 1 and 2). The numbers on the two optical plots (Figures 4 and 5) show the main wavelengths (in nm) corresponding to the main minima, maxima and isosbestic points. The inset to Figure 5, lower graph, shows the corresponding variation in the absorbance derivative (at 390 nm) as a function of the peroxide equiv (the zero was arbitrarily set at the point corresponding to pure $Au_{25}(SR)_{18}^{0}$). The absorbance derivative at 496 nm or the absorbance at 369 or 401 nm gave virtually identical results. This shows very nicely how the course of the redox reaction can be assessed very

precisely. The molar extinction coefficient of $Au_{25}(SR)_{18}^{0}$ in DCM at 401 nm was determined to be $\varepsilon = 5.38 \times 10^4$ M^{-1} cm^{-1}.[79] Further details can be found in the original papers.[34,79]

From the absorbance onset, the HOMO-LUMO gap of $Au_{25}(SR)_{18}^{-}$ was evaluated to be 1.33 eV,[59] whereas the changes observed on the low energy side of the spectrum show that when $Au_{25}(SR)_{18}^{-}$ is oxidized to radical $Au_{25}(SR)_{18}^{0}$ the gap increases, as already commented upon.[85] The increase is ca. 0.16 eV. According to the spectra of Figure 5a, converted from wavelengths to eV, further oxidation to $Au_{25}(SR)_{18}^{+}$ increases the gap to ca. 1.53 eV, a value lower which suggests that absorption now involves an orbital lower in energy by 0.2 eV compared to $Au_{25}(SR)_{18}^{-}$. This is contrast with earlier density functional theory (DFT) calculations on simple models of these clusters, $Au_{25}(SH)_{18}$ and $Au_{25}(SMe)_{18}$, which pointed to three almost degenerate HOMOs (highest occupied molecular orbitals).[86-89] A DFT study of $Au_{25}(SR)_{18}^{-}$ with *para*-substituted thiophenolate ligands pointed to one of the HOMOs as slightly higher in energy than the other two (0.12–0.13 eV).[90] The problem of this difference in energy was addressed in detail later.[91] As opposed to commonly accepted views, analysis of EPR[90] and NMR results[79] provided definite evidence for a difference in the HOMOs' energy (see, also, Sections 1.2.2 and 1.2.3), in agreement with the aforementioned optical behavior. DFT calculations confirmed that the state of charge affects the relative energy of these HOMOs very significantly.

To conclude, the UV-vis absorption spectra of molecular $Au_{25}(SR)_{18}$ clusters not only display truly molecular features but they also are very sensitive to the actual charge state. The optical spectra thus provide a perfect way to assess the purity, monodispersity, and charge state of the cluster, as well as its concentration through the already mentioned molar extinction coefficient, which not only is virtually independent of the solvent,[79] but also does not vary with the alkyl group (R in SR).[92]

1.2.2 Nuclear Magnetic Resonance

As we saw, in its native form, $Au_{25}(SR)_{18}$ bears a negative charge and its electroneutrality is granted by a *n*-tetraoctylammonium cation used as the phase-transfer agent in Brust-type syntheses. We also showed that these clusters can be oxidized in a very precise manner using a dissociative-type peroxide acceptor. This strategy allowed the Maran Group to characterize the NMR behavior of $Au_{25}(SR)_{18}$ (R = phenylethanethiolate) as a function of its charge state, -1, 0,

+1.[79] This study could confirm (for the -1 and 0 states) some previous results from the Murray Group,[93] correct some of the conclusions, and provide a clear picture of the magnetism of $Au_{25}(SC_2H_4Ph)_{18}$ as a function of the charge state. In this Section, we will introduce the main results and concepts, made possible by the preparation of atomically monodisperse $Au_{25}(SC_2H_4Ph)_{18}$. Further aspects and more insights into the NMR of $Au_{25}(SR)_{18}$ clusters will be provided in the following Chapters. Concerning the preparation of the same neutral cluster, we should note that another chemical oxidation route, making use of an oxoammonium cation, was later described also by the Zhu's and Jin's groups.[94]

$Au_{25}(SC_2H_4Ph)_{18}$ was studied by ^1H and ^{13}C NMR spectroscopy, using one- and two-dimensional techniques, in various solvents, and as a function of temperature.[79] The charge state of the Au_{25} clusters could be precisely controlled by using the smooth oxidant bis(pentafluorobenzoyl) peroxide. Since the peroxide and its reduction product do not introduce hydrogen atoms, this dissociative ET proved to be a particularly convenient approach for NMR purposes. Analysis of the NMR spectra $[n\text{-}Oct_4N^+][Au_{25}(SC_2H_4Ph)_{18}^-]$ led to evidence, quantitatively, the presence of the two families of inner and outer ligands, in agreement with the x-ray crystallography structure. Similar outcome was verified for its oxidized form, $Au_{25}(SC_2H_4Ph)_{18}^0$. In this case, however, a series of remarkable chemical-shift differences, caused by the paramagnetism of this Au_{25} charge state, are observed. As expected because of the singly occupied molecular orbital (SOMO) is mostly localized onto the gold core, the inner ligands are particularly sensitive to the unpaired electron. This is particularly true for the $(\alpha\text{-}CH_2)_{in}$ peak that undergoes a dramatic downfield shift toward ca. 25 ppm. This peak can be evidenced by increasing the temperature, as illustrated in Figure 6. A dramatic effect of paramagnetism is also evident in the ^{13}C NMR spectrum for both $(\alpha\text{-}C)_{in}$ and $(\beta\text{-}C)_{in}$. The presence of two distinct ligand populations could be quantitatively verified. DFT calculations of chemical shifts, provided insights into the extent of spin delocalization and the nature of the ligands.

Further oxidation of the cluster to the corresponding cation $Au_{25}(SC_2H_4Ph)_{18}^+$ basically led to observe a very similar NMR behavior to that of $Au_{25}(SC_2H_4Ph)_{18}^-$, once again with distinct contributions from the two types of ligand. This led to conclude that the positively-charged cluster is a diamagnetic species. Figure 7 illustrates the outcome of this second oxidation. These results provided the first piece of information pointing to the three HOMOs as not being energetically equivalent.

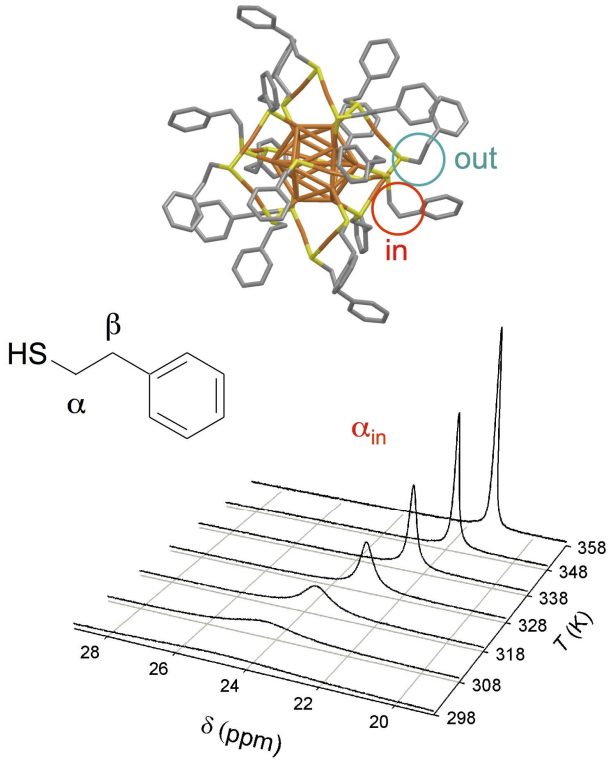

Figure 6. ^{1}H NMR spectrum of monodisperse 3 mM $Au_{25}(SC_2H_4Ph)_{18}^{0}$ in toluene-d_8 as a function of temperature. The spectra (ref. 79) only show the $(\alpha\text{-}CH_2)_{in}$ zone.

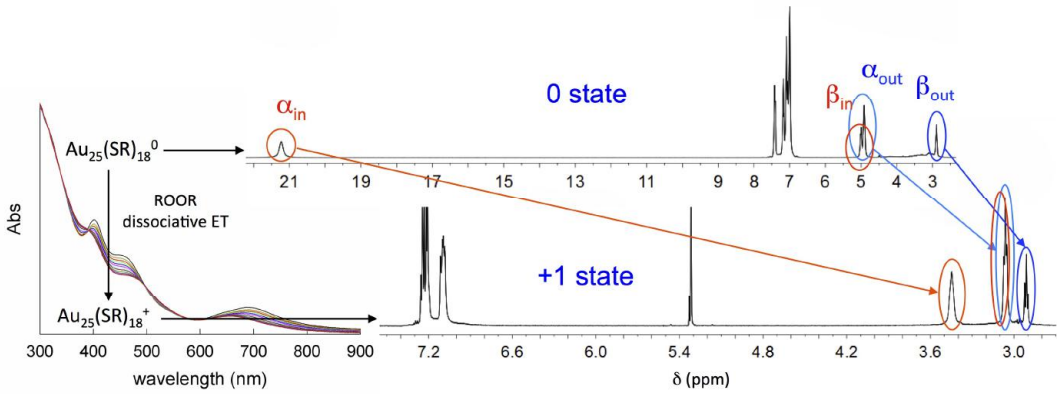

Figure 7. ^{1}H NMR spectrum of 3 mM $Au_{25}(SC_2H_4Ph)_{18}^{0}$ (upper graph, in toluene-d_8, 358 K) and $Au_{25}(SC_2H_4Ph)_{18}^{+}$ (lower graph, dichloromethane-d_2, 298 K) obtained by quantitative oxidation of the former.

1.2.3 Electron Paramagnetic Resonance

Under mild oxidizing conditions, such as in the presence of oxygen, or upon addition of a suitable oxidant, $Au_{25}(SR)_{18}^{-}$ undergoes oxidation to form the very stable $Au_{25}(SR)_{18}^{0}$ species.[68,79] The latter is a paramagnetic species and

thus not only displays a characteristic NMR behavior, as we just saw in Section 1.2.2, but also an interesting EPR behavior. This starts to be evident as the temperature decreases below 100 K, as described in detail by Zhu *et al* for $Au_{25}(SC_2H_4Ph)_{18}^0$.[95] Thus, continuous-wave EPR (cw-EPR) of frozen, glassy solutions of $Au_{25}(SR)_{18}$ shows a broad peak displaying the typical features of a paramagnetic state. Further studies,[69,70,91] also carried out on other $Au_{25}(SR)_{18}^0$, such as $Au_{25}(SEt)_{18}^0$ (Chapter 3)[69] and $Au_{25}(SBu)_{18}^0$,[70] confirmed the same behavior and also that very similar EPR parameters can be used to describe different clusters, which points to the importance of the core rather than the monolayer itself. Electron nuclear double resonance (ENDOR), a very sensitive superhyperfine technique, provided further insights into structural features of $Au_{25}(SEt)_{18}$, the smallest Au_{25} so far prepared (for details, please refer to Chapter 3 and ref. 69).

It is of particular interest to gain further insights into the issue of the three HOMOs. As we said, previous DFT calculations on simple models of these clusters, $Au_{25}(SH)_{18}$ and $Au_{25}(SMe)_{18}$, pointed to three almost degenerate HOMOs,[86-89] although another study concerning $Au_{25}(SR)_{18}^-$ (SR = *para*-substituted thiophenolates) revealed that one of the HOMOs could be slightly higher in energy.[90] Because of the paramagnetism of $Au_{25}(SR)_{18}^0$ and the apparent nearly degeneracy of three HOMOs, further oxidation of the cluster to its +1 charge state could generate another paramagnetic (diradical) species. The NMR evidence, however, clearly showed that the cation is as diamagnetic as the anion, at least at room temperature.[79] A similar conclusion was later reached by using a different oxidant.[94] In a more recent paper,[96] on the other hand, some EPR spectral behavior attributed to paramagnetism of $Au_{25}(SR)_{18}^+$, obtained from $Au_{25}(SR)_{18}^0$ by following the oxidation approach developed by the Maran Group.[79] This inconsistency was addressed in detail but cw-EPR of frozen, glassy solutions of a freshly prepared $Au_{25}(SR)_{18}^+$ sample revealed that the latter is not EPR active in the temperature range 6 – 260 K,[91] in full agreement with NMR results. The DFT-computed optical absorption spectra and density of states of the -1, 0, and +1 charge states could nicely reproduce the experimentally estimated dependence of the HOMO-LUMO energy gap on the actual charge carried by the cluster. DFT calculations could thus provide a clear picture of the evolution of the frontier orbitals, confirming that the +1 charge state must be considered diamagnetic due to a significant splitting of the HOMO energy levels.[91]

Magnetism in gold nanoparticles is indeed becoming a new frontier of MPC research. It is, however, still poorly understood.[96] In this context, the Maran Group and collaborators made very recently a breakthrough discovery:[70] whereas $Au_{25}(SBu)_{18}^{0}$ is a paramagnetic MPC that in solution displays the same molecular behavior of other Au_{25} clusters, in the solid-state single crystal X-ray crystallographic analysis reveals formation of a linear polymer composed by $Au_{25}(SBu)_{18}$ units interconnected by single Au-Au bonds (Figure 8 the structures on top correspond to the area circled in green, and for simplicity are shown without the ligands) and stabilized by interlocking of ligands. The otherwise unpaired electrons of the $Au_{25}(SBu)_{18}^{0}$ clusters pair up, with generation of a nonmagnetic ground state, *i.e.*, an antiferromagnetic state. DFT calculations pointed to a room-temperature behavior of a narrow-gap semiconductor. While in an organic solution, however, the polymer dissolves and the behavior is typical of that displayed by all other $Au_{25}(SR)_{18}^{0}$ clusters.

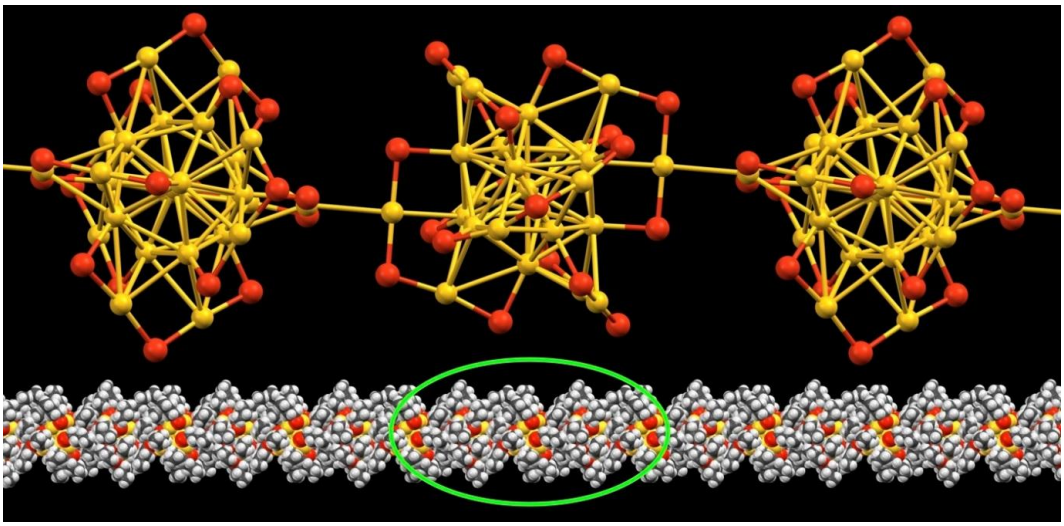

Figure 8. Formation of the antiferromagnetic $[Au_{25}(SBu)_{18}^{0}]_n$ polymer.

1.2.4 Electrochemistry

Electron-transfer characterization of the $Au_{25}(SR)_{18}$ native cluster shows that Au_{25} behaves in all regards as a simple molecular redox species.[33,59,60,91] Figure 9 shows typical cyclic voltammetry (CV) pattern of $Au_{25}(SC_2H_4Ph)_{18}^{-}$ in DCM/0.1 M TBAH studied on a glassy carbon electrode.[33] The CVs shows the first two oxidations (the actual cluster is in its anionic form) and first reduction. At low scan rate (v) values and for the two most positive peaks, the separation between the anodic and the cathodic peak potentials (ΔE_p) is typical of a fully

reversible process. ΔE_p increases only for sufficiently high *v* values. The peak for the reduction to the dianion is irreversible, in agreement with a fast ET followed by chemical reaction/s. Voltammetric analysis and digital simulation showed that initial ET triggers a cascade of chemical and electrochemical steps corresponding to a sequence of stepwise dissociative ETs.

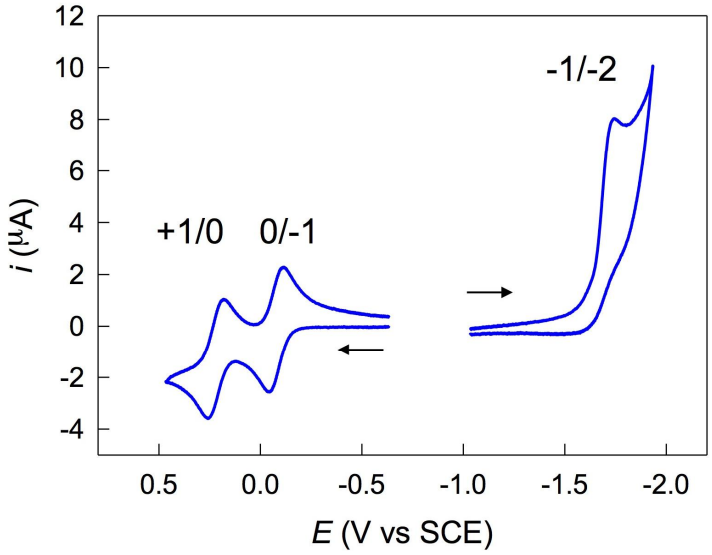

Figure 9. Background-subtracted CVs of 1 mM $Au_{25}(SC_2H_4Ph)_{18}^-$ in DCM/0.1 M TBAH. *v* = 0.2 V s^{-1}, glassy carbon electrode, 25 °C.

The redox formal potential (*E*°) values of Au_{25} clusters can be varied by proper substitution of the capping ligands.[51,97] In is worth noticing that whereas very basic electrochemical information (such as *E*° values and *E*° differences) has been reported for some molecule-like clusters and under different environment conditions (solvents, electrolytes, temperature), studies focusing on their actual ET properties, such as intrinsic barriers, activation parameters, and ET rate constants, are still very scarce. The Maran Group was the first to assess the ET properties of $Au_{25}(SR)_{18}^-$,[33] albeit in this and most of former papers (before 2008) this cluster was believed to be $Au_{38}(SR)_{24}^0$ instead of $Au_{25}(SR)_{18}^-$.[76] Similarly, it was later showed that the cluster believed to be[11] $Au_{140}(SR)_{53}$ had a slightly different stoichiometry, $Au_{144}(SR)_{60}$.[98] ET characterization showed that Au_{25} behaves in all regards as a molecular redox species whose redox potentials can be varied by proper substitution of the capping ligands. Heterogeneous ET kinetics revealed that the intrinsic barrier for the oxidation of $Au_{25}(SR)_{18}^-$ is predominantly in the form of inner reorganization rather then solvent reorganization as usually is verified with common organic donors or acceptors.[81]

This unusually large heterogeneous ET inner reorganization result is in agreement with ET self-exchange measurements (0 and -1 forms) in the solid state[99] and in solution.[93]

Au_{25} clusters have been used to catalyze several redox processes.[14] From the viewpoint of pure ET reactions triggered by the homogeneous redox catalysis appraoch, they have been used as redox catalysis mediators toward peroxide acceptors,[34] for the reduction of diphenyl disulfide and benzyl bromide,[33] and the corresponding ET rate constants were compared with those obtained using conventional one-electron donors. Concerning the latter study, the acceptors were chosen so as to be reduced within the lifetime of the actual reductant, $Au_{25}(SR)_{18}^{2-}$, which has a lifetime of only 4 ms owing to the aforementioned chemical reactions associated to the electrode reduction.[33] In a following contribution, the lifetime of other redox forms derived from $Au_{25}(SR)_{18}^{0}$ were also assessed.[91] Thus, as opposed to the stable -1, 0, and +1 charge states, $Au_{25}(SR)_{18}^{2-}$, $Au_{25}(SR)_{18}^{2+}$, and $Au_{25}(SR)_{18}^{3+}$ were proved to be labile species with lifetimes of 4 ms, 0.33 s, and 20 ms, respectively. These results casted doubts on some interpretations reached in recent publications.[91] Figure 10 summarizes in a

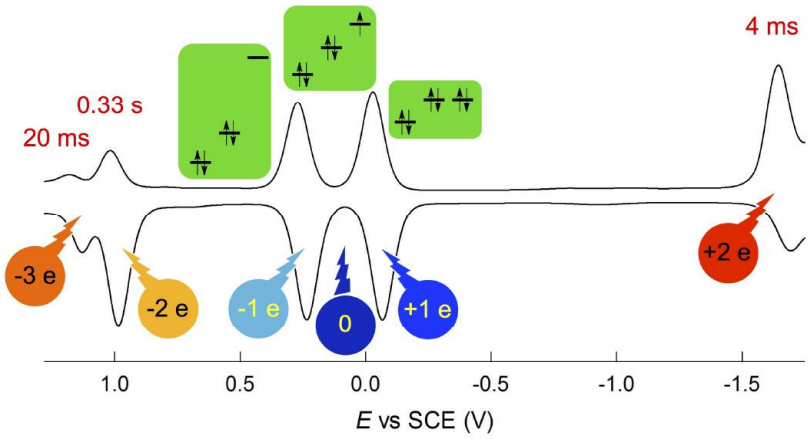

Figure 10. DPV of 1 mM $Au_{25}(SC_2H_4Ph)_{18}^{0}$ in DCM/0.1 M TBAH. Glassy carbon electrode, 25 °C. The color codes stress the stability of the relevant charge states, with blue and red as the most stable and unstable forms, respectively.

pictorial way the lifetimes and electrode electron uptakes or releases for the same cluster of Figure 9, although now starting from the zero charge state.[91] The corresponding changes in the HOMOs energies are also depicted. The electrochemical behavior is here seen in terms of differential pulse voltammetry

(DPV). A comparison with the DPV behavior of $Au_{144}(SC_2H_4Ph)_{60}$ shown in Figure 1 highlights the very different behavior displayed by the two type of MPCs.

Concerning the homogeneous redox catalysis for the reduction of a series of dibenzoyl peroxides,[34] use of a different donor with a comparable *E*° allowed verifying that in these redox processes the monolayer thickness affects the rate rather significantly. Analysis of these results thus pointed to these MPCs as acting in ET reactions as roughly the 3D equivalent of SAMs formed on extended gold surfaces.

1.3 Aims and Summary of the Thesis

This Thesis addresses aspects concerning the properties of the most popular MPC displaying molecular behavior: $Au_{25}(SR)_{18}$. The main objective was to devise experiments suitable to provide information for setting up a sound description of how the gold core and the surrounding medium communicate through the capping monolayer. The Thesis is structured according to six Chapters. For practical reasons each Chapter contains its own references.

As we have seen, Chapter 1 reviews some among the most salient, pertinent to this Thesis, aspects of the physical chemistry of molecular $Au_{25}(SR)_{18}$.

As described in Chapter 2, various methods and techniques were implemented for the preparation of atomically pure $Au_{25}(SR)_{18}$. A lot of effort was also devoted to master the control of the MPC's charge state and assess how the optical and NMR properties change accordingly.

We then focused on preparing and characterized a 25-gold atom nanocluster protected by the smallest ligand ever used, ethanethiol, as described in Chapter 3 (published: *ACS Nano* **2014**, *8*, 3904-3912). Not only we could prepare this cluster but also determine its structure by single crystal X-ray crystallography. This gave us the possibility of carrying out an unprecedented analysis of the gold-core and thiolate ligands properties. We found that the gold core is composed by sufficiently different types of gold atoms to be detected by advanced electron paramagnetic techniques (ENDOR). The results were addressed by DFT calculations that, thanks to the use of a very short thiol as the protecting ligand, allowed us to analyze the data without structure's approximations or omissions.

$Au_{25}(SEt)_{18}$ is a "nearly naked thiolate-protected Au_{25} cluster": the next question was to devise a method to gain information on the dynamic structure of

this and progressively thicker thiolate monolayers. In Chapter 4 (published: *ACS Nano* **2014**, *8*, 2788–2795) we describe the characterization of the largest series of monodisperse $Au_{25}(SC_nH_{2n+1})_{18}$ clusters ever prepared (*n* = 2, 4, 6, 8, 10, 12, 14, 16, 18). The goal was to use electron tunneling as a probe of the monolayer structure in solution. ET results, nicely supported by ^{1}H NMR spectroscopy, IR absorption spectroscopy, and molecular dynamics results, showed that there is a critical ligand length marking the transition between short ligands, which form a quite fluid monolayer structure, and long alkyl chains, which self-organize into two oppositely directed bundles. At variance with the truly protecting 2D SAMs, efficient electronic communication of the Au_{25} core with the outer environment is possible even for long alkyl chains. This research has thus provided a different picture of how an ultrasmall gold core talks with the environment through/with its protecting but not-so-shielding monolayer.

Chapter 5 is a natural follow up of Chapter 4. The idea was to verify how ET proceeds in the solid state, also in view of possible uses of Au_{25} films in practical applications requiring conductive materials in the solid state. We used a series of linear-chain thiolate protected clusters having the general formula $Au_{25}(SC_nH_{2n+1})_{18}$ (*n* = 3, 4, 5, 6, 8, 10) and carried out conductivity measurements on their dry films on interdigitated electrodes. We found a linear dependence of the conductivity on *n*, which points to a hopping mechanism where the Au cores behave as a localized electron-donor or acceptor site, whereas the ligands act as spacers dictating the efficiency of electron tunneling. The ET results clearly point to a substantial folding of the linear chains of these MPCs in the solid state, but to a lesser extent compared to what observed in solution, where more fluidity is possible.

Chapter 6 originates from Chapters 3-5. For the ET studies we needed to introduce branching along the alkyl chain and check how this factor would have affected the effective monolayer thickness. Thus, we introduced one methyl group in place of one hydrogen at position β (with respect to the sulfur atom) along a butanethiolate chain. This type of thiol thus contains a stereogenic center. We found that commercially available racemic thiols are, in fact, nonracemic, but possess an enantiomeric excess (e.e.) of the (*S*)-enantiomer, as verified through synthesis of the pure (*S*)-enantiomer. By varying the e.e. of the thiol, we could prepare several of $Au_{25}(SMeBu)_{18}^0$ clusters. Both ^{1}H NMR spectroscopy and CD spectroscopy showed that as the e.e. of the thiol employed reaches a value of ca. 75%, the resulting Au_{25} clusters only contain the (*S*)-

thiolate. We thus observed, for the first time, the phenomenon of spontaneous resolution for an MPC. These conclusions based on spectral data were perfectly confirmed by solving the single crystal structure of one of these clusters, which in principle should have contained an 77% e.e. of the (*S*)-enantiomer: instead, X-ray crystallography showed that only the (*S*)-enantiomer *is* capping the Au_{25} core.

1.4 References

(1) Schmid, G.; Pfeil, R.; Boese, R.; Bandermann, F.; Meyer, S.; Calis, G. M. H.; Vandervelden, W. A. $[Au_{55}\{P(C_6H_5)_3\}_{12}Cl_6]$ – A Gold Cluster of Unusual Size. *Chem. Ber*. **1981**,*114*, 3634-3642.

(2) Schmid, G. Large Clusters and Colloids. *Chem. Rev.* **1992**, *92*, 1709-1727.

(3) Brust, M.; Walker, M.; Bethell, D.; Schiffrin, D. J.; Whyman, R. Synthesis of Thiol-derivatised Gold Nanoparticles in a Two-Phase Liquid**-**Liquid System. *J. Chem. Soc., Chem. Commun.* **1994**, 801-802.

(4) Nuzzo, R. G.; Allara, D. L. Adsorption of Bifunctional Organic Disulfides on Gold Surfaces. *J. Am. Chem. Soc.*, **1983**, *105*, 4481-4483.

(5) Love, J. C.; Estroff, L. A.; Kriebel, J. K.; Nuzzo, R. G.; Whitesides, G. M. Self-Assembled Monolayers of Thiolates on Metals as a Form of Nanotechnology. *Chem. Rev.* **2005**, *105*, 1103-1169.

(6) Häkkinen, H. The Gold–Sulfur Interface at the Nanoscale. *Nat. Chem.* **2012**, *4*, 443–455.

(7) Pensa, E.; Cortéz, E.; Corthey, G.; Carro, P.; Vericat, C.; Fonticelli, M. H.; Benitez, G.; Rubert, A. A.; Salvarezza, R. C. The Chemistry of the Sufur–Gold Interface: In Search of a Unified Model. *Acc. Chem. Res.* **2012**, *45*, 1183-1192.

(8) Templeton, A. C.; Hostetler, M. J.; Warmoth, E. K.; Chen, S. W.; Hartshorn, C. M.; Krishnamurthy, V. M.; Forbes, M. D. E.; Murray, R. W. Gateway Reactions to Diverse, Polyfunctional Monolayer-Protected Gold Clusters. *J. Am. Chem. Soc.* **1998**, *120*, 4845-4849.

(9) Templeton, A. C.; Wuelfing, W. P.; Murray, R. W. Monolayer-Protected Cluster Molecules. *Acc. Chem. Res.* **2000**, *33*, 27-36.

(10) Daniel, M.-C.; Astruc, D. Gold Nanoparticles: Assembly, Supramolecular Chemistry, Quantum-Size-Related Properties, and Applications toward Biology, Catalysis, and Nanotechnology. *Chem Rev.* **2004**, *104*, 293-346.

(11) Murray, R. W. Nanoelectrochemistry: Metal Nanoparticles, Nanoelectrodes, and Nanopores. *Chem. Rev.* **2008**, *108*, 2688-2720.

(12) Tsukuda, T. Toward an Atomic-Level Understanding of Size-Specific Properties of Protected and Stabilized Gold Clusters. *Bull. Chem. Soc. Jpn*. **2012**, *85*, 151-168.

(13) Saha, K.; Agasti, S. S.; Kim, C.; Li, X.; Rotello, V. M. Gold Nanoparticles in Chemical and Biological Sensing. *Chem. Rev.* **2012**, *112,* 2739-2779.

(14) Li, G.; Jin, R. Atomically Precise Gold Nanoclusters as New Model Catalysts. *Acc. Chem. Res.* **2013**, *46*, 1749-1758.

(15) Negishi, Y.; Kurashige, W.; Niihori, Y.; Nobusada, K. Toward the Creation of Stable, Functionalized Metal Clusters. *Phys. Chem. Chem. Phys.* **2013**, *15*, 18736-18751.

(16) Howes, P. D.; Chandrawati, R.; Sevens, M. M. Colloidal Nanoparticles as Advanced Biological Sensors. *Science* **2014**, *346*, 1247390-1-10.

(17) Hutchings, G. J. Vapor Phase Hydrochlorination of Acetylene: Correlation of Catalytic Activity of Supported Metal Chloride Catalysts. *J. Catal*. **1985**, *96*, 292-295.

(18) Haruta, M.; Kobayashi, T.; Sano, H.; Yamada, N. Novel Gold Catalysis for the Oxidation of Carbon Monoxide. *Chem. Lett*. **1987**, *16*, 405-408.

(19) Stephen, A.; Hashmi, K.; Hutchings, G. J. Gold Catalysis. *Angew. Chem., Int. Ed.* **2006**, *45*, 7896-7936.

(20) Stratakis, M.; Garcia, H. Catalysis by Supported Gold Nanoparticles beyond Aerobic Oxidative Processes. *Chem. Rev.* **2012**, *112*, 4469-4506.

(21) Ma, G.; Binder, A.; Chi, M.; Liu, C. Jin, R.; Jiang, D.; Fan, J.; Dai, S. Stabilizing Gold Clusters by Heterostructured Transition-Metal Oxide–Mesoporous Silica Supports for Enhanced Catalytic Activities for CO Oxidation. *Chem. Commun*. **2012**, *48*, 11413-11415.

(22) Della Pina, C. D.; Falletta, E.; Rossi, M. Update on Selective Oxidation using Gold. *Chem. Soc. Rev.* **2012**, *41*, 350-369.

(23) Valden, M.; Lai, X.; Goodman, D. W. Onset of Catalytic Activity of Gold Clusters on Titania with the Appearance of Nonmetallic Properties. *Science* **1998**, *281*, 1647-1650.

(24) Coutts, M. J.; Cortie, M. B.; Ford, M. J.; McDonagh, A. M. Rapid and Controllable Sintering of Gold Nanoparticle Inks at Room Temperature Using a Chemical Agent. *J. Phys. Chem. C*, **2009**, *113*, 1325-1328.

(25) Ma, Z.; Dai, S. Development of Novel Supported Gold Catalysts: A Materials Perspective. *Nano Res*. **2011**, *4*, 3-32.

(26) Das, S.; Goswami, A.; Hesari, M.; Al-Sharab , J. F.; Mikmeková, E.; Maran, F.; Asefa, T. Reductive Deprotection of Monolayer Protected Nanoclusters: An Efficient Route to Supported Ultrasmall Au Nanocatalysts for Selective Oxidation. *Small* **2014**, *10*, 1473-1478.

(27) Kauffman, D. R.; Alfonso, D.; Matranga, C.; Qian, H.; Jin, R. Experimental and Computational Investigation of Au_{25} Clusters and CO_2: A Unique Interaction and Enhanced Electrocatalytic Activity. *J. Am. Chem. Soc.* **2012**, *134*, 10237-10243.

(28) Nie, X.; Qian, H.; Ge, Q.; Xu, H.; Jin, R. CO Oxidation Catalyzed by Oxide-Supported $Au_{25}(SR)_{18}$ Nanoclusters and Identification of Perimeter Sites as Active Centers. *ACS Nano* **2012**, *6*, 6014-6022.

(29) Li, G.; Qian, H.; Jin, R. Gold Nanocluster-Catalyzed Selective Oxidation of Sulfide to Sulfoxides. *Nanoscale*, **2012**, *4*, 6714-6717.

(30) Zhu, Y.; Qian, H.; Drake, B. A.; Jin, R. Atomically Precise $Au_{25}(SR)_{18}$ Nanoparticles as Catalysts for the Selective Hydrogenation of α,β-Unsaturated Ketones and Aldehydes. *Angew. Chem., Int. Ed.* **2010**, *49*, 1295-1298.

(31) Yamamoto, H.; Yano, H.; Kouchi, H.; Obora, Y.; Arakawa, R.; Kawasaki, H. *N,N*-Dimethylformamide-stabilized Gold Nanoclusters as a Catalyst for the Reduction of 4-Nitrophenol. *Nanoscale* **2012**, *4*, 4148-4154.

(32) Shivhare, A.; Ambrose, S. J.; Zhang, H.; Purves, R. W.; Scott, R. W. J. Stable and Recyclable Au_{25} Clusters for the Reduction of 4-Nitrophenol. *Chem. Commun.* **2013**, *49*, 276-278.

(33) Antonello, S.; Holm, A. H.; Instuli, E.; Maran, F. Molecular Electron-Transfer Properties of Au_{38} Clusters. *J. Am. Chem. Soc.* **2007**, *129*, 9836.

(34) Antonello, S.; Hesari, M.; Polo, F.; Maran, F. Electron Transfer Catalysis with Monolayer Protected Au_{25} Clusters. *Nanoscale* **2012**, *4*, 5333-5342.

(35) Chen, W.; Chen, S. Oxygen Electroreduction Catalyzed by Gold Nanoclusters. *Angew. Chem. Int. Ed*. **2009**, *48*, 4386-4389.

(36) Kumar, S. S.; Kwak, K.; Lee, D. Amperometric Sensing Based on Glutathione Protected Au_{25} Nanoparticles and Their pH Dependent Electrocatalytic Activity. *Electroanalysis* **2011**, *23*, 2116-2124.

(37) Liu, Z.; Xu, Q.; Jin, S.; Wang, S.; Xu, G. Electron Transfer Reaction Between Au_{25} Nanocluster and Phenothiazine-Tetrachloro-*p*-Benzoquinone Complex *Int*. *J. Hydrog. Energy* **2013**, *38*, 16722-16726.

(38) Luo, Z.; Zheng, K.; Xie, J. Engineering Ultrasmall Water-Soluble Gold and Silver Nanoclusters for Biomedical Applications. *Chem. Commun.* **2014**, *50*, 5143-5155.

(39) Xie, J.; Zheng, Y.; Ying, J. Y. Protein-Directed Synthesis of Highly Fluorescent Gold Nanoclusters. *J. Am. Chem. Soc.* **2009**, *131*, 888-889.

(40) Levi-Kalisman, Y.; Jadzinsky, P. D.; Kalisman, N.; Tsunoyama. H.; Tsukuda, T.; Bushnell, D. A.; Kornberg, R. D. Synthesis and Characterization of Au_{102}(*p*-MBA)$_{44}$ Nanoparticles. *J. Am. Chem. Soc.* **2011**, *133*, 2976-2982.

(41) Sexton, J. Z.; Ackerson, C. J. Determination of Rigidity of Protein Bound Au144 Clusters by Electron Cryomicroscopy. *J. Phys. Chem. C* **2010**, *114*, 16037-16042.

(42) Brancolini, G.; Toroz, D.; Corni, S. Can Small Hydrophobic Gold Nanoparticles Inhibit β2-Microglobulin Fibrillation? *Nanoscale* **2014**, *6*, 7903-7911.

(43) Becucci, L.; Guidelli, R.; Polo, F.; Maran, F. Interaction of Mixed-Ligand Monolayer-Protected Au_{144} Clusters with Biomimetic Membranes as a Function of the Transmembrane Potential. *Langmuir* **2014**, *30*, 8141-8151.

(44) Huang, K.; Ma, H.; Liu, J.; Huo, S.; Kumar, A.; Wei, T.; Zhang, X.; Jin, S.; Gan, Y.; Wang, P. C.; He, S.; Zhang, X.; Liang, X.-J. Size-Dependent Localization and Penetration of Ultrasmall Gold Nanoparticles in Cancer Cells, Multicellular Spheroids, and Tumors in Vivo. *ACS Nano* **2012**, *6*, 4483-4493.

(45) Sousa, A. A.; Morgan, J. T.; Brown, P. H.; Adams, A.; Jayasekara, M. P. S.; Zhang, G.; Ackerson, C. J.; Kruhlak, M. J.; Leapman, R. D. Size-Dependent Localization and Penetration of Ultrasmall Gold Nanoparticles in Cancer Cells, Multicellular Spheroids, and Tumors in Vivo. *Small* **2012**, *8*, 2277-2286.

(46) Heikkilä, E.; Martinez-Seara, H.; Gurtovenko, A. A.; Javanainen, M.; Häkkinen, H.; Vattulainen, I.; Akola J. Cationic Au Nanoparticle Binding with Plasma Membrane-like Lipid Bilayers: Potential Mechanism for Spontaneous Permeation to Cells Revealed by Atomistic Simulations. *J. Phys. Chem. C* **2014,** *118*, 11131-11141.

(47) Heikkilä, E.; Martinez-Seara, H.; Gurtovenko, A. A.; Vattulainen, I.; Akola, J. Atomistic Simulations of Anionic $Au_{144}(SR)_{60}$ Nanoparticles Interacting with Asymmetric Model Lipid Membranes. *Biochim. Biophys. Acta* **2014**, *1838*, 2852-2860.

(48) Ung, T.; Giersign, M.; Dunstan, D.; Mulvaney, P. Spectroelectrochemistry of Colloidal Silver. *Langmuir* **1997**, *13*, 1773-1782.

(49) Hicks, J. F.; Miles, D. T.; Murray, R. W. Electrochemical and NMR Characterization of Octanethiol-Protected Au Nanoparticles. *J. Electroanal. Chem.* **2003**, *554*, 127-132.

(50) Quinn, B. M.; Liljeroth, P.; Ruiz, V.; Laaksonen, T.; Kontturi, K. Electrochemical Resolution of 15 Oxidation States for Monolayer Protected Gold Nanoparticles. *J. Am. Chem. Soc.* **2003**, *125*, 6644-6645.

(51) Holm, A. H.; Ceccato, M.; Donkers, R. L.; Fabris, L.; Pace, G.; Maran, F. Effect of Peptide Ligand Dipole Moments on the Redox Potentials of Au_{38} and Au_{140} Nanoparticles. *Langmuir* **2006**, *22*, 10584**-**10589.

(52) Wolfe, R. L.; Murray, R. W. Analytical Evidence for the Monolayer-Protected Cluster $Au_{225}[(S(CH_2)_5CH_3)]_{75}$. *Anal. Chem*. **2006**, *78*, 1167-1173.

(53) Dass, A.; Theivendran, S.; Nimmala, P. R.; Kumara, C.; Jupally, V. R.; Fortunelli, A.; Sementa, L.; Barcaro, G.; Zuo, X.; Noll, B. C. $Au_{133}(SPh\text{-}t Bu)_{52}$ Nanomolecules: X-ray Crystallography, Optical, Electrochemical, and Theoretical Analysis. *J. Am. Chem. Soc.* **2015**, *137*, 4601-4613

(54) Jupally, V. R.; Thrasher, J. G.; Dass, A. Quantized Double Layer Charging of $Au_{130}(SR)_{50}$ Nanomolecules. *Analyst* **2014**,*139*, 1826-1829.

(55) Dass, A. Personal communication.

(56) Balasubramanian, R.; Guo, R.; Mills, A. J.; Murray, R. W. *J.* Reaction of $Au_{55}(PPh_3)_{12}Cl_6$ with Thiols Yields Thiolate Monolayer Protected Au_{75} Clusters. *Am. Chem. Soc.* **2005**, *127*, 8126-8132.

(57) Nimmala, P. R.; Yoon, B.; Whetten, R. L.; Landman, U.; Dass, A. $Au_{67}(SR)_{35}$ Nanomolecules: Characteristic Size-Specific Optical, Electrochemical, Structural Properties and First-Principles Theoretical Analysis. *J. Phys. Chem. A* **2013**, *117*, 504-517.

(58) Toikkanen, O.; Ruiz, V.; R**ö**nnholm, G.; Kalkkinen, N.; Liljeroth, P.; Quinn, B. M. Synthesis and Stability of Monolayer-Protected Au_{38} Clusters. *J. Am. Chem. Soc.* **2008**, *130*, 11049-11055.

(59) Lee, D.; Donkers, R. L.; Wang, G.-L.; Harper, A. S.; Murray, R. W. Electrochemistry and Optical Absorbance and Luminescence of Molecule-like Au_{38} Nanoparticles. *J. Am. Chem. Soc.* **2004**, *126*, 6193-6199.

(60) Jimenez, V. L.; Georganopoulou, D. G.; White, R. J.; Harper, A. S; Mills, A. J; Lee, D.; Murray, R. W. Hexanethiolate Monolayer Protected 38 Gold Atom Cluster. *Langmuir* **2004**, *20*, 6864-6870.

(61) Menard, L. D.; Gao, S.; Xu, H.; Twesten, R. D.; Harper, A. S.; Song, Y.; Wang, G.; Douglas, A. D.; Yang, J. C.; Frenkel, A. I.; Nuzzo, R. G.; Murray, R. W.

Sub-Nanometer Au Monolayer-Protected Clusters Exhibiting Molecule-like Electronic Behavior: Quantitative High-Angle Annular Dark-Field Scanning Transmission Electron Microscopy and Electrochemical Characterization of Clusters with Precise Atomic Stoichiometry. *J. Phys. Chem. B* **2006**, *110*, 12874-12883.

(62) Negishi, Y.; Nakazaki, T.; Malola, S.; Takano, S.; Niihori, Y.; Kurashige, W.; Yamazoe, S.; Tsukuda, T.; Häkkinen, H. A Critical Size for Emergence of Nonbulk Electronic and Geometric Structures in Dodecanethiolate-Protected Au Clusters. *J. Am. Chem. Soc*. **2015**, *137*, 1206**-**1212.

(63) Malola, S.; Lehtovaara, L.; Enkovaara, J.; Häkkinen, H. Birth of the Localized Surface Plasmon Resonance in Monolayer-Protected Gold Nanoclusters. *ACS Nano* **2013**, *7*, 10263**-**10270.

(64) Weissker, H.-C.; Lopez-Acevedo, O.; Whetten, R. L.; López-Lozano, X. Optical Spectra of the Special Au_{144} Gold-Cluster Compounds: Sensitivity to Structure and Symmetry. *J. Phys. Chem. C* **2015**, *119*, 11250-11259.

(65) Jadzinsky, P. D.; Calero, G.; Ackerson, C. J.; Bushnell, D. A.; Kornberg, R. D. Structure of a Thiol Monolayer-Protected Gold Nanoparticle at 1.1 Å Resolution. *Science* **2007**, *318*, 430-433.

(66) Heaven, M. W.; Dass, A.; White, P. S.; Holt, K. M.; Murray, R. W. Crystal Structure of the Gold Nanoparticle $[N(C_8H_{17})_4][Au_{25}(SCH_2CH_2Ph)_{18}]$. *J. Am. Chem. Soc.* **2008**, *130*, 3754-3755.

(67) Zhu, M.; Aikens, C. M.; Hollander, F. J.; Schatz, G. C.; Jin, R. Correlating the Crystal Structure of a Thiol-Protected Au_{25} Cluster and Optical Properties. *J. Am. Chem. Soc.* **2008**, *130*, 5883-5885.

(68) Zhu, M.; Eckenhoff, W. T.; Pintauer, T.; Jin, R. Conversion of Anionic $[Au_{25}(SCH_2CH_2Ph)_{18}]^{-}$ Cluster to Charge Neutral Cluster *via* Air Oxidation. *J. Phys. Chem. C* **2008**, *112*, 14221-14224.

(69) Dainese, T.; Antonello, S.; Gascón, J. A.; Pan, F.; Perera, N. V.; Ruzzi, M.; Venzo, A.; Zoleo, A.; Rissanen, K.; Maran, F. $Au_{25}(SEt)_{18}$, a Nearly Naked Thiolate-Protected Au_{25} Cluster: Structural Analysis by Single Crystal X-ray Crystallography and Electron Nuclear Double Resonance. *ACS Nano* **2014**, *8*, 3904-3912.

(70) De Nardi, M.; Antonello, S.; Jiang, D.; Pan, F.; Rissanen, K.; Ruzzi, M.; Venzo, A.; Zoleo, A.; Maran, F. Gold Nanowired: A Linear $(Au_{25})_n$ Polymer from Au_{25} Molecular Clusters. *ACS Nano* **2014**, *8*, 8505-8512.

(71) Qian, H.; Eckenhoff, W. T.; Zhu, Y.; Pintauer, T.; Jin, R. Total Structure Determination of Thiolate-Protected Au_{38} Nanoparticles. *J. Am. Chem. Soc.* **2010**, *132*, 8280-8281.

(72) Zeng, C.; Qian, H.; Li, T.; Li, G.; Rosi, N. L.; Yoon, B.; Barnett, R. N.; Whetten, R. L.; Landman, U.; Jin, R. Total Structure and Electronic Properties of the Gold Nanocrystal $Au_{36}(SR)_{24}$. *Angew. Chem., Int. Ed.* **2012**, *51*, 13114-13118.

(73) Zeng, C.; Liu, C.; Chen, Y.; Rosi, N. L.; Jin, R. Gold−Thiolate Ring as a Protecting Motif in the $Au_{20}(SR)_{16}$ Nanocluster and Implications. *J. Am. Chem. Soc.* **2014**, *136*, 11922-.....

(74) Crasto, D.; Malola, S. A.; Brosofsky, G.; Dass, A.; Häkkinen, H. Single Crystal XRD Structure and Theoretical Analysis of the Chiral $Au_{30}S(S\text{-}t\text{-}Bu)_{18}$ Cluster. *J. Am. Chem. Soc.* **2014**, *136*, 5000-5005.

(75) Zeng, C.; Chen, Y.; Kirschbaum, K.; Appavoo, K.; Sfeir, M. Y.; Jin, R. Structural Patterns at All Scales in a Nonmetallic Chiral $Au_{133}(SR)_{52}$ Nanoparticle. *Sci. Adv.* **2015**, *1*, e1500045.

(76) Parker, J. F.; Fields-Zinna, C. A.; Murray, R. W. The Story of a Monodisperse Gold Nanoparticle: $Au_{25}L_{18}$. *Acc. Chem. Res.* **2010**, *43*, 1289-1296.

(77) Qian, H.; Zhu, M.; Wu, Z.; Jin, R. Quantum Sized Gold Nanoclusters with Atomic Precision. *Acc. Chem. Res.* **2012**, *45*, 1470-1479.

(78) Song, Y.; Harper, A. S.; Murray, R. W. Ligand Heterogeneity on Monolayer-Protected Gold Clusters. *Langmuir* **2005**, *21*, 5492–5500.

(79) Venzo, A.; Antonello, S.; Gascón, J. A.; Guryanov, I.; Leapman, R. D.; Perera, N. V.; Sousa, A.; Zamuner, M.; Zanella, A.; Maran, F. Effect of the Charge State (z = –1, 0, +1) on the Nuclear Magnetic Resonance of Monodisperse $Au_{25}[S(CH_2)_2Ph]_{18}^{z}$ Clusters. *Anal. Chem.* **2011**, *83*, 6355–6362.

(80) Savéant. J.-M. A Simple Model for the Kinetics of Dissociative Electron Transfer in Polar Solvents. Application to the Homogeneous and Heterogeneous Reduction of Alkyl Halides. *J. Am. Chem. Soc.* **1987**, *109*, 6788-6795.

(81) Antonello, S.; Maran, F. Intramolecular Dissociative Electron Transfer. *Chem. Soc. Rev.* **2005**, *34*, 418-428.

(82) Antonello, S.; Musumeci, M.; Wayner, D. D. M.; Maran, F. Activation-Driving Force Relationships and Bond Dissociation Free Energies. *J. Am. Chem. Soc.* **1997**, *119*, 9541-9549.

(83) Antonello, S.; Maran, F. The Role and Relevance of the Transfer Coefficient α in the Study of Dissociative Electron Transfers: Concepts and Examples from the Electroreduction of Perbenzoates. *J. Am. Chem. Soc.* **1999**, *121*, 9668-9676.

(84) Maran, F.; Wayner, D. D. M.; Workentin, M. S. Kinetics and Mechanisms of the Dissociative Reduction of C-X and X-X Bonds (X = O, S). *Adv. Phys. Org. Chem.* **2001**, *36*, p. 85-166.

(85) Parker, J. P.; Weaver, J. E. F.; McCallum, F.; Fields-Zinna, C. A.; Murray, R. W. On the Synthesis of Monodisperse $[Oct_4N_+][Au_{25}(SR)_{18}^-]$ Nanoparticles, with Some Mechanistic Observations. *Langmuir* **2010**, *26*, 13650-13654.

(86) Akola, J.; Walter, M.; Whetten, R. L.; Häkkinen, H.; Grönbeck, H. On the Structure of Thiolate-Protected Au_{25}. *J. Am. Chem. Soc.* **2008**, *130*, 3756-3757.

(87) Aikens, C. M. Origin of Discrete Optical Absorption Spectra of $M_{25}(SH)_{18}^-$ Nanoparticles (M = Au, Ag). *J. Phys. Chem. C* **2008**, *112*, 19797-19800.

(88) Aikens, C. M. Effects of Core Distances, Solvent, Ligand, and Level of Theory on the TDDFT Optical Absorption Spectrum of the Thiolate-Protected Au_{25} Nanoparticle. *J. Phys. Chem. A* **2009**, *113*, 10811-10817.

(89) Aikens, C. M. Electronic Structure of Ligand-Passivated Gold and Silver Nanoclusters. *J. Phys. Chem. Lett.* **2011**, *2*, 99**-**104.

(90) Aikens, C. M. Geometric and Electronic Structure of $Au_{25}(SPhX)_{18}^-$ (X = H, F, Cl, Br, CH_3, and OCH_3). *J. Phys. Chem. Lett.* **2010**, *1*, 2594-2599.

(91) Antonello, S.; Perera, N. V.; Ruzzi, M.; Gascón, J. A.; Maran, F. Interplay of Charge State, Lability, and Magnetism in the Molecule-like $Au_{25}(SR)_{18}$ Cluster. *J. Am. Chem. Soc.* **2013**, *135*, 15585-15594.

(92) Antonello, S.; Arrigoni, G.; Dainese, T.; De Nardi, M.; Parisio, G.; Perotti, L.; René, A.; Venzo, A.; Maran, F. Electron Transfer through 3D Monolayers on Au_{25} Clusters. *ACS Nano* **2014**, *8*, 2788–2795.

(93) Parker, J. F.; Choi, J.-P.; Wang, W.; Murray, R. W. Electron Self-exchange Dynamics of the Nanoparticle Couple $[Au_{25}(SC_2Ph)_{18}]^{0/1-}$ by Nuclear Magnetic Resonance Line-Broadening. *J. Phys. Chem. C* **2008**, *112*, 13976**–**13981.

(94) Liu, Z.; Zhu, M.; Meng, X.; Xu, G.; Jin, R. Electron Transfer between $[Au_{25}(SC_2H_4Ph)_{18}]^-$ TOA+ and Oxoammonium Cations. *J. Phys. Chem. Lett.* **2011**, *2*, 2104**-**2109.

(95) Zhu, M.; Aikens, C. M.; Hendrich, M. P.; Gupta, R.; Qian, H.; Schatz, G. C.; Jin, R. Reversible Switching of Magnetism in Thiolate-Protected Au_{25} Superatoms. *J. Am. Chem. Soc.* **2009**, *131*, 2490-2492.

(96) Nealon, G. L.; Donnio, B.; Greget, R.; Kappler, J.-P.; Terazzi, T.; Gallani, J.-L. Magnetism in gold nanoparticles. *Nanoscale* **2012**, *4*, 5244-5258.

(97) Guo, R.; Murray, R. W. Substituent Effects on Redox Potentials and Optical Gap Energies of Molecule-like $Au_{38}(SPhX)_{24}$ Nanoparticles. *J. Am. Chem. Soc.* **2005**, *127*, 12140-12143.

(98) Qian, H.; Jin, R. Controlling Nanoparticles with Atomic Precision: The Case of $Au_{144}(SCH_2CH_2Ph)_{60}$. *Nano letters* **2009**, *9*, 4083-4087.

(99) Choi, J.-P.; Murray, R. W. Electron Self-Exchange between $Au_{140}^{+/0}$ Nanoparticles is Faster Than That between $Au_{38}^{+/0}$ in Solid-State, Mixed-Valent Films. *J. Am. Chem. Soc.* **2006**, *128*, 10496-10502.

Chapter 2: Synthesis and Characterization of $Au_{25}(SR)_{18}$

2.1 Synthesis

2.1.1 $Au_{25}(SC_2H_5)_{18}$

A typical synthesis of $[n\text{-}Oct_4N^+][Au_{25}(SEt)_{18}^-]$ was carried out as follows.[1] 0.50 g (1.27 mmol) of $HAuCl_4 \cdot 3H_2O$ was dissolved in 40 ml THF and then 0.833 g of tetra-*n*-octylammonium bromide (1.52 mmol, 1.2 equiv) were added. The resulting red solution was stirred for 15 min at 20 °C. Stirring speed was set to 100 rpm and 0.367 ml (5.08 mmol, 4 equiv) of ethanethiol (attempts were made with different amounts of ethanethiol, 7 and 20 equiv but in both cases a lower clusters yield was obtained), dissolved in 10 ml of ice-cooled THF (to limit evaporation of the low-boiling ethanethiol, boiling point = 35 °C), was added dropwise over a period of ca. 3 min. The solution quickly became yellow and then, after ca. 45 min became colorless. The stirring speed was raised to 600 rpm and a freshly prepared icy-cold aqueous solution (10 ml) of $NaBH_4$ (0.48 g, 12.7 mmol, 10 equiv) was quickly added to the mixture, which was kept at 20°C. The solution immediately became black, the typical color observed during MPC formation, and plenty of gas evolved. After addition of $NaBH_4$, the necks of the reaction flask were loosely capped to allow gases escape upon a slight positive pressure. The reaction progress was monitored by UV-vis absorption spectroscopy. After two days, the reaction mixture was filtered on paper to remove black/dark grey residues insoluble in THF. The filtered solution had a dark-brown color with orange hues. THF was removed with a rotary evaporator to leave a reddish-brown oily solid covered by a colorless liquid (residual H_2O from aq. $NaBH_4$). The water phase was removed, and the solid was dissolved in toluene and washed with water (4 x 40 ml) in a separatory funnel. Toluene was evaporated and the product was extracted with acetonitrile, leaving a black residue. Acetonitrile was evaporated and the resulting orange-reddish oily solid was dissolved in diethyl ether to yield a clear orange solution. This caused precipitation of a white crystalline-like powder, constituted by excess tetra-*n*-octylammonium bromide (this white crystalline-like powder was collected, dissolved in THF and a drop of $HAuCl_4 \cdot 3H_2O$ in THF was added to it, obtaining the typical red-orange solution), which has very low solubility in this solvent. To eliminate the last excess of tetra-*n*-octylammonium bromide, the product dissolved in diethyl ether was treated by silica-gel chromatography, using diethyl

ether as the eluent and argon as the pushing gas. The so-purified [*n*-Oct_4N^+][$Au_{25}(SEt)_{18}^-$] clusters were obtained as a dark-brown orange powder, which was stored at 4 °C in the dark. The oxidized cluster $Au_{25}(SEt)_{18}^0$ was obtained by means of the methods described in Section 2.2.

2.1.2 $Au_{25}(SC_3H_7)_{18}$

0.50 g (1.27 mmol) of $HAuCl_4 \cdot 3H_2O$ was dissolved in 40 ml THF and then 0.833 g of tetra-*n*-octylammonium bromide (1.52 mmol, 1.2 equiv) were added to form a red solution. After stirring for 15 min at room temperature at moderate speed, magnetic stirring was increased to 100 rpm and then 0.460 ml (5.08 mmol, 4 equiv) of 1-propanethiol in 10 ml of THF was added dropwise over a period of some minutes. The solution quickly became yellow and then, after ca. 30 min, became colorless. Magnetic stirring was increased to 600 rpm and a freshly prepared icy-cold aqueous solution (10 ml) of $NaBH_4$ (0.48 g, 12.7 mmol, 10 equiv) was quickly added to the mixture at room temperature. This caused the solution to become black, indicative of the formation of gold nanoparticles, and gas generation was observed. After two days, the reaction mixture was filtered on paper to remove the white-grey residues insoluble in THF. THF was removed from the filtered solution, which had a dark-brown color with orange hues, to leave a reddish-brown oily solid covered by residual H_2O from aq. $NaBH_4$. The water phase was removed, and the solid was dissolved in toluene and washed with water (4 x 40 ml) in a separatory funnel. Toluene was evaporated, the solid was dissolved in 50 ml of DCM, and the resulting solution was left to rest overnight in the dark at 4°C. The white residue precipitated during this treatment was discarded and DCM was then evaporated. The resulting oily solid was further purified by dissolving it in a mixture of diethyl ether and pentane to precipitate most of the residual tetraoctylammonium salt. The last traces of salt were eliminated by washing the product a few times with icy-cold methanol. The final product, [*n*-Oct_4N^+][$Au_{25}(SPr)_{18}^-$], is a dark-orange brown powder. To eliminate possible traces of the oxidized cluster (easily detectable by NMR) that could form by air oxidation during the methanol washes, the product was rinsed a few times with pentane. This cluster was could be deliberately oxidized as described in Section 2.2. The resulting neutral cluster $Au_{25}(SPr)_{18}^0$ had the expected molecular mass as observed with matrix-assisted laser desorption ionization time-of-flight (MALDI-TOF) mass spectrometry (Figure 1).

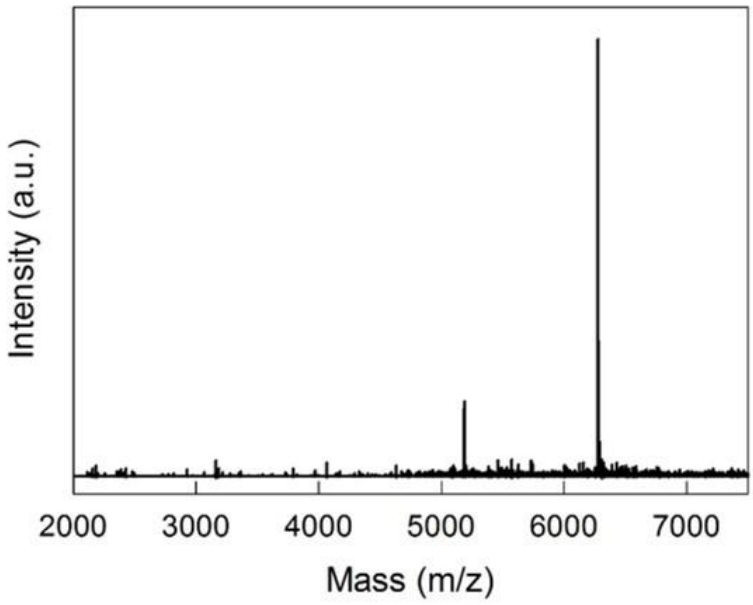

Figure 1. Positive-mode MALDI-TOF spectrum of $Au_{25}(SPr)_{18}^{0}$.

The neutral cluster was recrystallized by adding a drop of acetonitrile to a concentrated solution of the cluster in 1:2 toluene-pentane and leaving the solvents to evaporate for some days in the dark at room temperature. Its structure was resolved by X-ray diffraction and is illustrated in Figure 2.

2.1.3 $Au_{25}(SC_4H_9)_{18}$

The synthesis of [*n*-Oct_4N^+][$Au_{25}(SBu)_{18}^-$] was carried out as follows.[2] 6 equiv of 1-butanethiol (816 μl, 7.62 mmol) were added dropwise, under stirring and at room temperature, to a tetrahydrofuran (THF) solution (50 ml) of $HAuCl_4 \cdot 3H_2O$ (500 mg, 1.27 mmol) and tetra-*n*-octylammonium bromide (779 mg, 1.425 mmol). After 1 h, a freshly-prepared ice-cold solution of $NaBH_4$ (480 mg, 12.7 mmol) in water (10 ml) was rapidly added under vigorous stirring. The resulting black mixture was stirred for ca. 3 days and then filtered on paper. THF was removed by rotary evaporation to leave a red-brownish oil covered by an aqueous phase. The latter was removed by dissolving the product in 50 ml of toluene followed by washing the solution with water (4 x 25 ml). The toluene solution was concentrated to ca. 10 ml and left to age overnight at 4 °C. The solution was filtered to remove residual white polymer-like material, and the solvent evaporated. By this procedure, the cluster is obtained as [*n*-Oct_4N^+][$Au_{25}(SBu)_{18}^-$]. The product was then further purified or oxidized. In the first case, the solid was washed with pentane (2 x 10 ml), to remove possible thiol

and disulfide, and then dried. The solid was dissolved in diethyl ether, which leaves undissolved most of residual tetraoctylammonium salt. The solvent was evaporated and the solid washed thrice with icy cold methanol, to remove the remaining salt. The red-brownish solid was finally dried and then dissolved in benzene-d_6 for the NMR experiments.

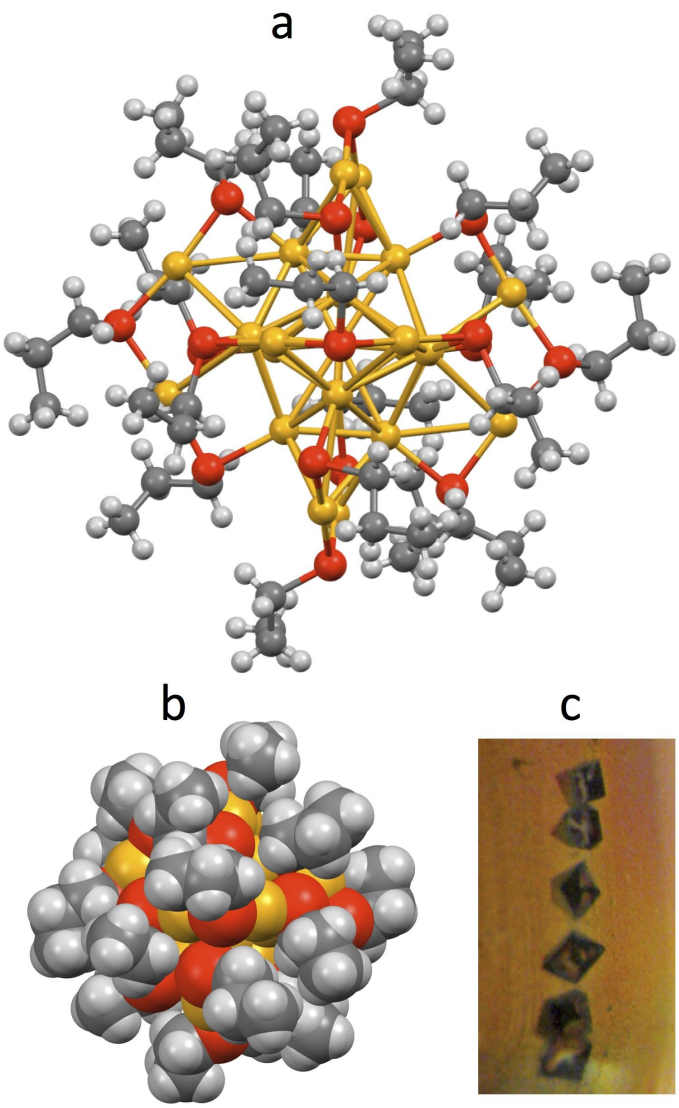

Figure 2. (a) Ball-and-stick projection showing the X-ray crystal structure of $Au_{25}(SPr)_{18}^{0}$. Au = yellow, S = red, C = gray, H = white. (b) The same structure as seen by spacefill rendering. (c) Photography of the actual crystals (inside the glass tube used for crystallization) used for the X-ray crystallographic analysis. The size of the bricks is about one millimeter.

2.1.4 $Au_{25}(SC_5H_{11})_{18}$

A typical synthesis of $Au_{25}(SC_5H_{11})_{18}^-$ was performed with minimum changes compared to the syntheses described above. 0.50 g (1.27 mmol) of $HAuCl_4 \cdot 3H_2O$ was dissolved in 40 ml THF, followed by addition of 0.833 g of tetra-*n*-octylammonium bromide (1.52 mmol, 1.2 equiv) to form a red solution that was stirred for 15 min at 20 °C. The stirring speed was set to 100 rpm and 0.840 ml (7.62 mmol, 6 equiv) of 1-pentanethiol in 10 ml of THF was added dropwise over a period of ca. 3 min. The solution quickly became yellow and after ca. 30 min colorless. The stirring speed was increased to 600 rpm and a freshly prepared icy-cold aqueous solution (10 ml) of $NaBH_4$ (0.48 g, 12.7 mmol, 10 equiv) was quickly added to the reaction flask, which was kept at room temperature. The solution immediately became black. The reaction progress was monitored by UV-vis absorption spectroscopy and after a little more than 24 h the reaction mixture could be filtered on paper to remove the white residues insoluble in common solvents. The filtered solution had a dark-brown color with orange hues. THF was removed with a rotary evaporator to leave a reddish-brown oily solid covered by a colorless liquid (residual H_2O from aq. $NaBH_4$). After removal of the water phase, the crude product was dissolved in toluene and washed with water (4 x 40 ml) in a separatory funnel. Toluene was evaporated, the solid was dissolved in DCM (50 ml), and the resulting solution left to rest for about 12 h in the dark at 4°C. By this procedure, the cluster is obtained as [*n*-Oct_4N^+][$Au_{25}(SC_5H_{11})_{18}^-$]. The product was then further purified or oxidized. In the first case, the solid was dissolved in diethyl ether, which leaves undissolved most of the residual tetraoctylammonium salt. The solvent was evaporated and the solid washed thrice with icy-cold methanol to remove the remaining salt. The red-brownish solid was finally dried. Concerning the oxidized cluster, prepared according to the methodology described in Section 2.2, it had the expected MALDI-TOF pattern (Figure 3).

2.2 Control of Charge and Optical Characterization

As mentioned in the Introduction, controlling the charge state is of paramount importance. This can be done chemically according to the strategy developed in the Maran Group and relying on the use of a very powerful peroxide oxidant.[3,4] For more routine applications, we developed an alternative method that was consistently applied to convert all clusters to their zero charge state.

This method will be described in this Section for two of the above Au_{25} clusters, together with a description of the ensuing changes in the optical behavior.

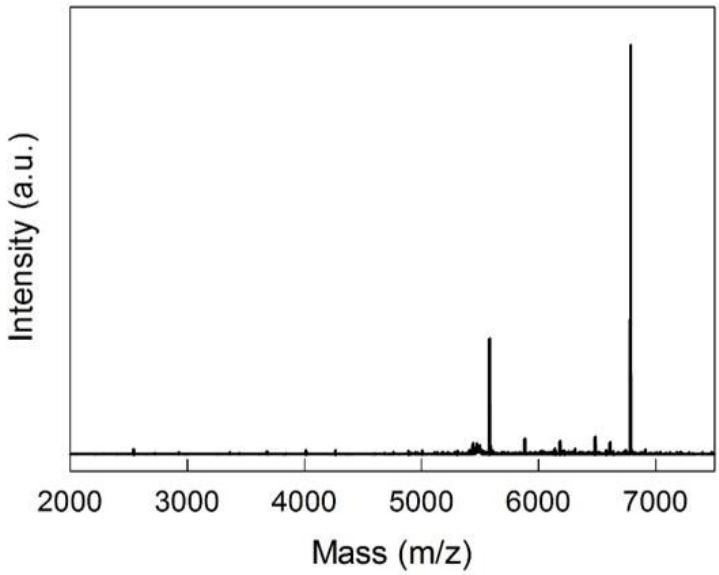

Figure 3. Positive-mode MALDI-TOF spectrum of $Au_{25}(SC_5H_{11})_{18}^0$.

Oxidation of the as prepared cluster $[n\text{-}Oct_4N^+][Au_{25}(SEt)_{18}^-]$ to obtain the paramagnetic species $Au_{25}(SEt)_{18}^0$ was performed by a passage through a silica-gel chromatography column, using DCM as eluent and compressed air as the pushing gas. The orange solution of the anionic cluster in DCM was injected into the column and soon turned green while passing through the column (Figure 4, inset A). After evaporation of the so-treated DCM solution, the oxidized clusters appeared as a black-brownish powder. The clusters were further purified by washing them thrice with acetonitrile and thrice with hexane; in both solvents $Au_{25}(SEt)_{18}^0$ is insoluble.

The UV-vis spectra of the anionic and neutral forms of $Au_{25}(SEt)_{18}$ are compared in Figure 4, together with pictures of (A) the silica-gel column just before and during passage of the MPC solution, and (B) the two cuvettes used to take the optical spectra. The so-obtained neutral cluster had the same spectral features described in Section 1.2.1.

Oxidation of $[n\text{-}Oct_4N^+][Au_{25}(SBu)_{18}^-]$ to its neutral form was accomplished by dissolution in DCM (5 ml) followed by passage through a silica-gel column under aerobic conditions. The DCM solution was concentrated to ca. 3 ml and then left to age for 2-5 days at 4 °C to remove possible residual cream-white material. The DCM solution was concentrated to ca. 1 ml and a droplet of

acetonitrile was added. Very slow evaporation of the solution (over some days) at room or low temperature caused precipitation of the final product, as a black powder. $Au_{25}(SBu)_{18}^{0}$ was dried and stored at 4 °C in the dark.

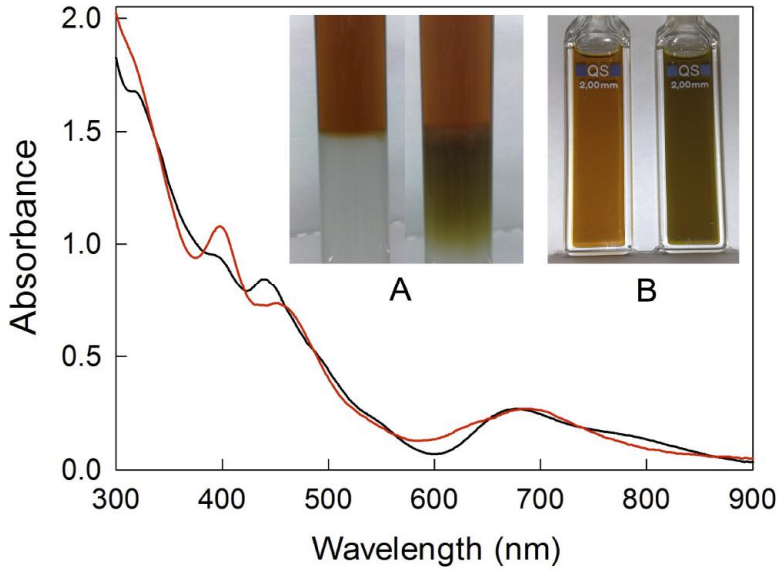

Figure 4. Comparison of the UV-vis absorption spectra of $Au_{25}(SEt)_{18}^{0}$ in DCM (red curve) and $Au_{25}(SEt)_{18}^{-}$ in acetonitrile (black curve). Both spectra were obtained using a quartz cuvette with a 2 mm optical-path length, at room temperature, and at 0.10 mM concentration. The insets show: (A) the chromatography column containing a solution of $Au_{25}(SEt)_{18}^{-}$ in DCM before (left) and during passage through the column (right); (B) cuvettes containing 0.2 mM solutions of $Au_{25}(SEt)_{18}^{-}$ (left) and $Au_{25}(SEt)_{18}^{0}$ (right) in DCM.

Figure 5a shows the resulting optical behavior and Figure 5b the corresponding differential pulse voltammetry curve. Absorbance plot is shown as a function of the photon energy in order to evidence how the optical HOMO-LUMO gap can be estimated from the optical absorption onset. Figure 3b shows how a very similar gap can be estimated from the electrochemical standard potentials corrected for the charging contribution.[5] Figure 6 shows the optical behavior as function of wavelength for both the anionic and neutral clusters.

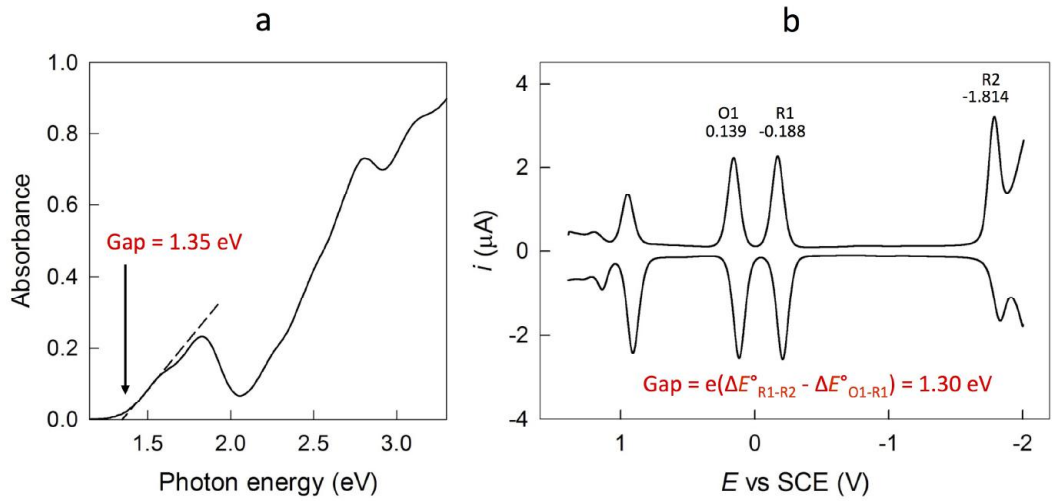

Figure 5. Comparison between the (a) optically and (b) electrochemically determined HOMO-LUMO gaps. The UV-vis absorption spectrum pertains to 0.10 mM [*n*-Oct_4N^+][$Au_{25}(SBu)_{18}^-$] in DCM (quartz cuvette with a 2 mm optical-path length; 22 °C), and the gap is estimated from the onset of optical absorption. The differential pulse voltammetry curve is for 0.42 mM $Au_{25}(SBu)_{18}^0$ in DCM/0.1 M TBAH, as obtained at 25 °C using a glassy carbon microelectrode. The peaks are labeled according to progressive electron uptake or release by the neutral cluster; the *E*° values (in Volt) refer to the corresponding formal potentials, as determined by cyclic voltammetry analysis.

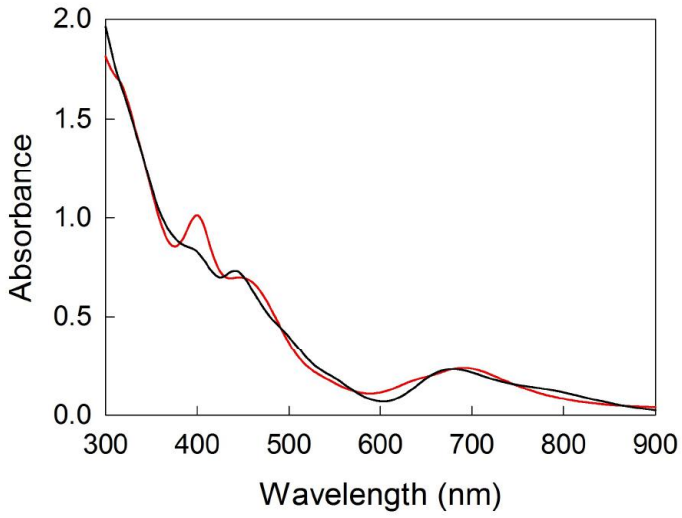

Figure 6. Comparison of the UV-vis absorption spectra of $Au_{25}(SBu)_{18}^0$ (red curve) and [*n*-Oct_4N^+][$Au_{25}(SBu)_{18}^-$]in DCM (black curve). Both spectra were obtained using a quartz cuvette with a 2 mm optical-path length, at room temperature, and at 0.10 mM concentration.

2.3 Control of Charge and Nuclear Magnetic Resonance

As described in detail in Section 1.2.2, the NMR behavior of the molecular Au_{25} clusters is extremely dependent on the cluster's charge state. We studied both the anionic and neutral forms for a number of clusters and here we will show some selected examples. The first case is a comparison between [*n*-Oct_4N^+][$Au_{25}(SPr)_{18}^-$] and $Au_{25}(SPr)_{18}^0$ (Figure 7). Symbols α and β refer to the positions of inner and outer methylene groups from sulfur, as indicated in the structure (for clarity, only one staple is displayed). Symbol γ relates to the methyl group of the inner and outer ligands. The arrows indicate the most significant shifts observed upon oxidation of $Au_{25}(SPr)_{18}^-$ to $Au_{25}(SPr)_{18}^0$. For the latter, the $(\alpha\text{-}CH_2)_{in}$ resonance is at 25 ppm.

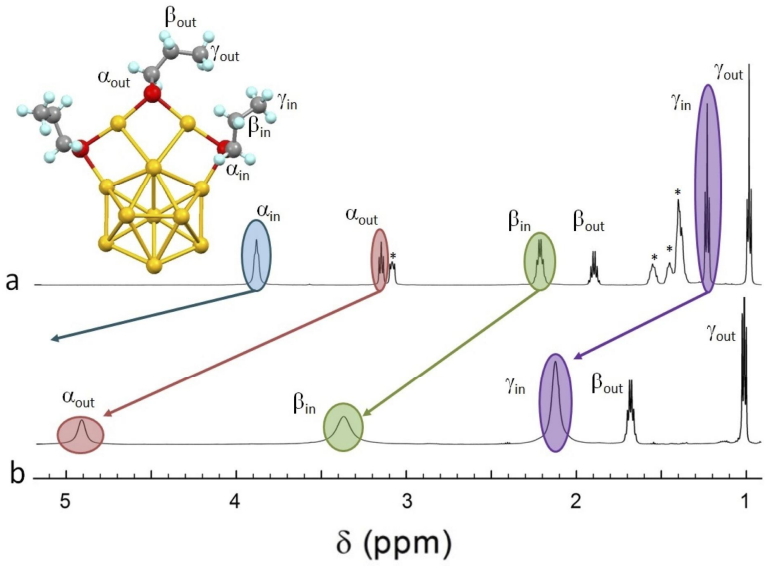

Figure 7. (a) ^{1}H NMR spectrum of [*n*-Oct_4N^+][$Au_{25}(SPr)_{18}^-$]. The peaks marked with an asterisk (*) pertain to [n-Oct_4N]$^+$. (b) ^{1}H NMR spectrum of $Au_{25}(SPr)_{18}^0$. Both spectra were obtained in benzene-d_6 at 25 °C, using samples at 3 mM concentration.

Figure 7 shows that the unpaired electron mostly concerns the methylene groups in positions α, β and the methyl γ of the inner ligands and the α methylene of the outer ligands. This is a situation that we could verify also with other clusters. This NMR behavior is caused by the contact interaction of the nuclear magnetic moments with the unpaired electron, and can be taken as a probe of whether the singly occupied MO (SOMO), and thus the spin density, spreads

onto those specific nuclei. Distance from the gold core is thus a crucial parameter. In this connection it is particularly instructive to see Figure 8, which shows the spectra of [*n*-Oct_4N^+][$Au_{25}(SBu)_{18}^-$] and $Au_{25}(SBu)_{18}^0$.[2] Symbols α, β and γ refer to the positions of inner and outer methylene groups from sulfur, as indicated in the structure (for clarity, only one staple is displayed). The letter δ relates to the methyl group of the inner and outer ligands.

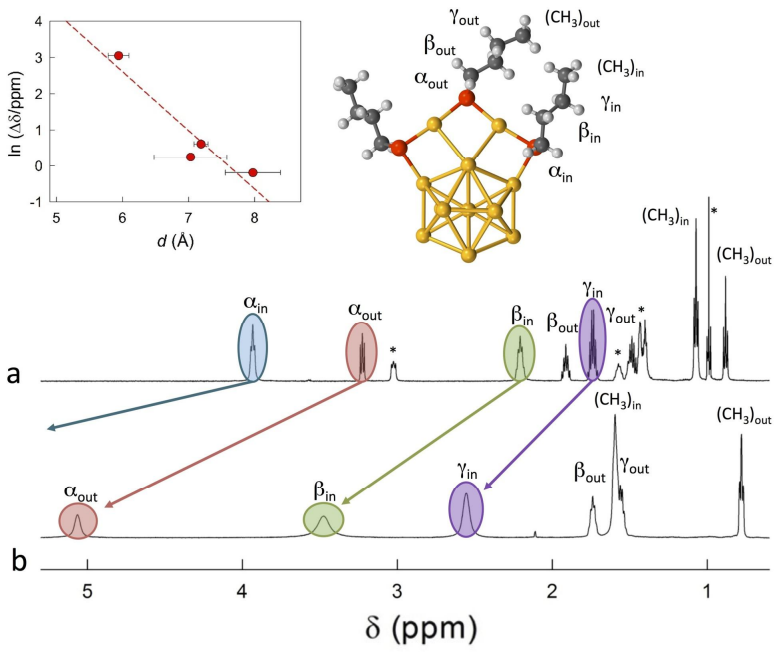

Figure 8. (a) ^{1}H NMR spectrum of [*n*-Oct_4N^+][$Au_{25}(SBu)_{18}^-$]. The peaks marked with a star pertain to [n-$Oct_4N]^+$. (b) ^{1}H NMR spectrum of $Au_{25}(SBu)_{18}^0$. Both samples were in benzene-d_6 at 25 °C, at 2.3 mM concentration. The Figure is reproduced from ref. 2.

As for Figure 7, the arrows mark the most significant shifts observed upon oxidation of $Au_{25}(SBu)_{18}^-$ to $Au_{25}(SBu)_{18}^0$. For the latter, the $(\alpha\text{-}CH_2)_{in}$ resonance is at 25 ppm, as observed for the $Au_{25}(SPr)_{18}^0$ cluster. The inset shows the resonance difference against the average distance of the corresponding CH_2 groups (of all staples of the two MPC types, with standard-deviation error bars) from the icosahedron central Au atom. These distances were calculated from the single-crystal X-ray structures. The effect of the unpaired electron is felt at distances no longer than 8 Å from the central Au atom.

Finally, Figure 9 shows the ^{1}H NMR spectrum of $Au_{25}(SC_5H_{11})_{18}^{0}$. The spectrum shows that despite the paramagnetism of $Au_{25}(SC_5H_{11})_{18}^{0}$, all inner and outer resonances could be successfully assigned.

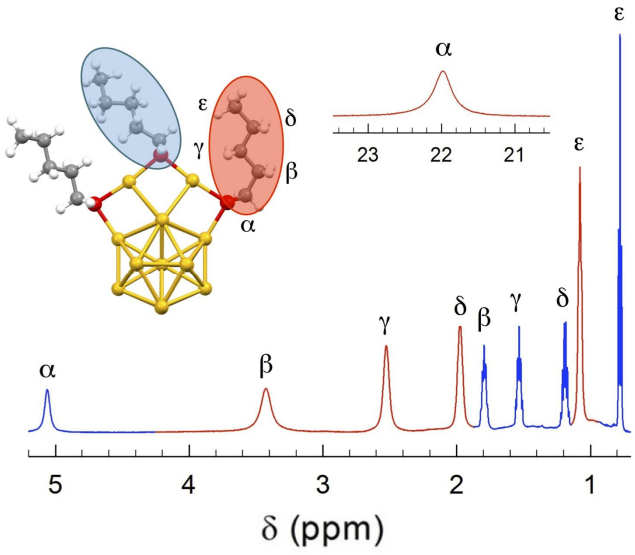

Figure 9. ^{1}H NMR spectrum of $Au_{25}(SC_5H_{11})_{18}^{0}$ in benzene-d_6 at 25 °C. Symbols α, β, γ and δ refer to the positions of inner and outer methylene groups from sulfur, as indicated in the structure (for clarity, only one staple is displayed). The symbol ε specifies the methyl group of the inner and outer ligands. The inner thiolate is highlighted in red, whereas the outer thiolate is in blue. The inset on the right-hand side showed the $(\alpha\text{-}CH_2)_{in}$ resonance, 21.98 ppm, as observed at 75 °C.

2.4 General Experimental Information

2.4.1. Chemicals

Hydrogen tetrachloroaurate trihydrate (99.9%), tetra-*n*-octylammonium bromide (98%), sodium borohydride (99%), ethanethiol (97%), 1-propanethiol (99%), 1-buthanethiol (99%), 1-pentanethiol (98%), 1-hexanethiol (95%), 1-octanethiol (98.5+%), 1-decanethiol (96%), 1-dodecanethiol (98+%), 1-tetradecanethiol (≥98.0%), 1-octadecanethiol (98%), (*S*)-(-)-2-methyl-1-butanol (99%), methane sufonyl chloride (>99.7%), potassium thioacetate (98%), trimethylamine (≥99%), ammonia solution (7 M) in methanol, tetrahydrofuran (THF, 99.9%), toluene (99.7%), diethyl ether (99.8%), acetonitrile (≥99.9%), ethanol (≥99.8%), pentane (≥99%), cyclohexane (≥ 99.7%), methanol (≥99.8%),

N,N-dimethylformamide (99.8%), acetonitrile-d_3 (99.8%, d_3), benzene-d_6 (99.6%, d_6), and *trans*-2-[3-(4-*tert*-butylphenyl)-2-methyl-2-propenylidene] malononitrile (DCTB, ≥98%) were purchase by Sigma-Aldrich and used as received. 2-Methyl-1-butanethiol were purchased both by Sigma-Aldrich (≥ 95%) and Alfa Aesar (99%), 1-hexadecanethiol by TCI Europe N.V (> 97%) and used as received. For electrochemistry, dichloromethane (DCM, VWR, 99.8%) was freshly distilled over CaH_2 and stored under an argon atmosphere. Tetra-*n*-butylammonium hexafluorophosphate (Fluka, 99%) was recrystallized from ethanol. Low conductivity water was milliQ Water pro analysis (Merck). Column chromatography was carried out using silica gel from Macherey-Nagel (MN-Kieselgel 60 M, 230-400 mesh).

2.4.2. Methods and Instrumentations

The UV-vis spectra were obtained at 0.1 mM concentration in DCM, with 2 mm cuvettes. We used a Thermo Scientific Evolution 60S spectrophotometer or, during syntheses, an Ocean Optics QE65000 spectrophotometer equipped with a DH-2000-BAL light source. The spectra resolution was 1 or 0.8 nm, respectively.

MALDI-TOF mass spectra were obtained with an Applied Biosystems 4800 MALDI-TOF/TOF spectrometer equipped with a Nd:YAG laser operating at 355 nm. The laser firing rate was 200 Hz and the accelerating voltage was 25 kV. The laser pulse intensity was kept at threshold values and then progressively increased. $Au_{25}(SEt)_{18}^0$ was dissolved in benzene containing the matrix, DCTB, to obtain 0.1 mM solutions with a 1:400 MPC/matrix ratio. 2 μl of solution were dropcasted onto the sample plate and air-dried before loading into MALDI-TOF. The spectra were recorded using the reflectron positive- or negative-ion mode. As a standard, we used $Au_{25}(SC_2H_4Ph)_{18}$, which has a MW of 7394.

The electrochemical experiments were carried out in DCM containing 0.1 M TBAH, under an Ar atmosphere in a glass cell thermostatted at 25 °C. The working electrode was a 0.55 mm radius glassy carbon disk, the counter electrode was a Pt wire, and an Ag wire served as the quasi-reference electrode. The latter was then referenced against the KCl saturated calomel electrode, SCE. For routine electrochemical measurements we used a CHI 660c electrochemical workstation. To minimize the ohmic drop between the working and the reference electrodes, we used the positive feedback correction.

^{1}H NMR spectra were obtained in C_6D_6 with a Bruker Avance DMX-600 MHz spectrometer equipped with a 5 mm TX-1 x,y,z-gradient powered, triple-resonance inverse probe operating at 599.90 MHz. The temperature was controlled at 25 ± 0.1 °C, unless otherwise indicated, with a Bruker BVT-300 automatic temperature controller. Chemical shifts are in ppm (δ□ units with reference to tetramethylsilane used as an internal standard. The proton assignments were performed by standard chemical shift correlations as well as by 2D correlation spectroscopy (COSY), total correlation spectroscopy (TOCSY), and nuclear Overhauser enhancement spectroscopy (NOESY) experiments, as previously done for $Au_{25}(SC_2H_4Ph)_{18}$.[3]

2.5 References

(1) Dainese, T.; Antonello, S.; Gascón, J. A.; Pan, F.; Perera, N. V.; Ruzzi, M.; Venzo, A.; Zoleo, A.; Rissanen, K.; Maran, F. $Au_{25}(SEt)_{18}$, a Nearly Naked Thiolate-Protected Au_{25} Cluster: Structural Analysis by Single Crystal X-ray Crystallography and Electron Nuclear Double Resonance. *ACS Nano* **2014**, *8*, 3904-3912.

(2) De Nardi, M.; Antonello, S.; Jiang, D.; Pan, F.; Rissanen, K.; Ruzzi, M.; Venzo, A.; Zoleo, A.; Maran, F. Gold Nanowired: A Linear $(Au_{25})_n$ Polymer from Au_{25} Molecular Clusters. *ACS Nano* **2014**, *8*, 8505-8512.

(3) Venzo, A.; Antonello, S.; Gascón, J. A.; Guryanov, I.; Leapman, R. D.; Perera, N. V.; Sousa, A.; Zamuner, M.; Zanella, A.; Maran, F. Effect of the Charge State (z = –1, 0, +1) on the Nuclear Magnetic Resonance of Monodisperse $Au_{25}[S(CH_2)_2Ph]_{18}^z$ Clusters. *Anal. Chem.* **2011**, *83*, 6355–6362.

(4) Antonello, S.; Hesari, M.; Polo, F.; Maran, F. Electron Transfer Catalysis with Monolayer Protected Au_{25} Clusters. *Nanoscale* **2012**, *4*, 5333-5342.

(5) Lee, D.; Donkers, R. L.; Wang, G.-L.; Harper, A. S.; Murray, R. W. Electrochemistry and Optical Absorbance and Luminescence of Molecule-like Au_{38} Nanoparticles. *J. Am. Chem. Soc.* **2004**, *126*, 6193-6199.

2.6 Acknowledgements

TD is particularly thankful to Alfonso Venzo for his contribution to the NMR measurements, and Rissanen and Fangfang Pan (University of Jyväskylä) for the X-ray crystallographic studies.

Chapter 3: $Au_{25}(SEt)_{18}$, a Nearly Naked Thiolate-Protected Au_{25} Cluster: Structural Analysis by Single Crystal X-ray Crystallography and Electron Nuclear Double Resonance

3.1 Abstract

This Chapter describes findings that have been published: Dainese, T.; Antonello, S.; Gascón, J. A.; Pan, F.; Perera, N. V.; Ruzzi, M.; Venzo, A.; Zoleo, A.; Rissanen, K.; Maran, F. $Au_{25}(SEt)_{18}$, a Nearly Naked Thiolate-Protected Au_{25} Cluster: Structural Analysis by Single Crystal X-ray Crystallography and Electron Nuclear Double Resonance. *ACS Nano* **2014**, *8*, 3904-3912.

X-ray crystallography has been fundamental in discovering fine structural features of ultrasmall gold clusters capped by thiolated ligands. For still unknown structures, however, new tools capable of providing relevant structural information are sought. We prepared a 25-gold atom nanocluster protected by the smallest ligand ever used, ethanethiol. This cluster displays the electrochemistry, mass spectrometry, and UV-vis absorption spectroscopy features of similar Au_{25} clusters protected by 18 thiolated ligands. The anionic and the neutral form of $Au_{25}(SEt)_{18}$ were fully characterized by ^{1}H and ^{13}C NMR spectroscopy, which confirmed the monolayer's properties and the paramagnetism of neutral $Au_{25}(SEt)_{18}^{0}$. X-ray crystallography analysis of the latter provided the first known structure of a gold cluster protected by a simple, linear alkanethiolate. Here, we also report the direct observation by electron nuclear double resonance (ENDOR) of hyperfine interactions between a surface-delocalized unpaired electron and the gold atoms of a nanocluster. The advantages of knowing the exact molecular structure and having used such a small ligand allowed us to compare the experimental values of hyperfine couplings with DFT calculations unaffected by structure's approximations or omissions.

3.2 Introduction

Formation of different thiolate-protected gold clusters is a delicate balance of thiol selection, relative concentrations, experimental conditions, and modus operandi.[1-4] As for the analogous SAMs of thiols on flat gold surfaces,[5] interaction of the thiolated heads with the surface gold atoms yields interesting structural

features.[6-8] For MPCs, single crystal X-ray crystallography has provided evidence and details of both the inner gold-core structures and the staple-like, half-crown motifs by which the outermost gold atoms interact with sulfur atoms. For homogeneous series of thiolate ligands (SR), the structures so far identified crystallographically are $Au_{102}(SR)_{44}$,[9] $Au_{38}(SR)_{24}$,[10] $Au_{36}(SR)_{24}$,[11] $Au_{28}(SR)_{20}$,[12] $Au_{25}(SR)_{18}$,[13-15] and $Au_{23}(SR)_{16}$.[16] Noteworthy, in none of these structures the ligands were simple linear alkanethiols but rather were aryl and arene-type thiols (phenylethanethiol, 4-*tert*-butylbenzenethiol, 4-mercaptobenzoic acid) or a hindered alkanethiol (cyclohexanethiol). Indeed, due to the intrinsic complexity of MPCs, particularly because of the conformational mobility that ligands may experience, successful preparation of crystals suitable for X-ray diffraction analysis and atomic structure determination is a very challenging task. Devising alternative approaches suitable for obtaining relevant structural information is thus of outmost importance.

Independently of the approach employed, the necessary starting point is identification of the chemical formula. Mass spectrometry techniques proved to be very effective, particularly MALDI-TOF mass spectrometry[17] and electrospray ionization (ESI) mass spectrometry.[18,19] Mass spectra were indeed instrumental to establish the correct cluster formula in advance of the actual structural determination for $Au_{25}(SR)_{18}$,[18,19] formerly believed to be $Au_{38}(SR)_{24}$.[20] Very recently, structural characteristics of clusters whose single crystal X-ray diffraction structure is still unknown were inferred by different approaches. Rapid electron diffraction in scanning transmission electron microscopy (STEM) was employed to gain insights into the structure of $Au_{130}(SR)_{50}$,[21] a gold MPC very recently reported,[22,23] and $Au_{144}(SR)_{60}$.[24] In both cases, structural analysis was supported by the good agreement with DFT calculations.[21,24] Structural information about $Au_{144}(SR)_{60}$ was also obtained by a combination of infrared spectroscopy, ^{13}C NMR spectroscopy, and X-ray diffraction of a single crystal.[25]

$Au_{25}(SR)_{18}$ is the most well-known and characterized MPC displaying a distinct molecule-like behavior.[20] The latter is evident from its characteristic UV-vis absorption spectrum that provides the energy gap between the HOMO and the LUMO.[26] The spectrum depends on the charge state and so does the HOMO-LUMO gap.[27] Sensitive electrochemical methods such as cyclic voltammetry and differential pulse voltammetry show series of peaks marking the stepwise charging of the gold core, and allow estimating the electrochemical HOMO-LUMO gap that upon correction for charging energy furnishes essentially the

same gap energy.[26,28] These charge states display quite different stability.[27] One-electron oxidation of the as-prepared cluster, a diamagnetic anionic species, generates a paramagnetic species. The latter displays a distinct EPR behavior,[27,29] best detected at liquid helium temperatures, and very particular ^{1}H and ^{13}C NMR spectroscopy patterns.[30,31] The above discussion shows that a crucial feature to obtain reliable insights into the properties of molecule-like MPCs is to prepare them in a truly monodisperse form, with atomic precision. Overall, $Au_{25}(SR)_{18}$ is thus the ideal candidate for testing new concepts, techniques, and methodologies to investigate structural properties of molecule-like and possibly larger clusters.

Here, we describe a new strategy to address these issues. We prepared a monodisperse Au_{25} cluster protected by the smallest ligand ever used, ethanethiol. $Au_{25}(SEt)_{18}$ was fully characterized by MALDI-TOF, UV-vis, electrochemistry, and ^{1}H and ^{13}C NMR spectroscopy of both the anion and the neutral forms. Successful preparation of high-purity samples and single crystals allowed us to obtain the first X-ray structure of a gold cluster protected by a very short alkanethiolate. For this purpose, we used the neutral cluster, $Au_{25}(SEt)_{18}^{0}$, and found that the gold and sulfur atoms are structurally arranged as previously described for $Au_{25}(SC_2H_4Ph)_{18}^{0}$ and $Au_{25}(SC_2H_4Ph)_{18}^{-}$,[13-15] but also with some differences around the Au_{13} icosahedral core. We focused on using a very short thiol ligand also because of the possibility of carrying out particularly accurate DFT calculations, that is, with fewer approximations than required for describing more complex ligand systems.

We then used frozen glassy solutions (at 5.5 K) of paramagnetic $Au_{25}(SEt)_{18}^{0}$ to obtain the first ENDOR results for an MPC. ENDOR is a superhyperfine technique able to determine hyperfine coupling constants that are unresolved in the cw-EPR spectra.[32] Pulse ENDOR is a particularly sensitive method of performing ENDOR.[33] ENDOR is especially suited to elucidate hyperfine interactions between an unpaired electron and surrounding nuclei. Each group of equivalent magnetic nuclei with nuclear spin I = 1/2 gives rise to a doublet of lines in the ENDOR spectrum, independently of the number of equivalent nuclei coupled to the electron spin. If the hyperfine coupling A is smaller than twice the nucleus Larmor frequency ν the doublet is centered at ν and the two lines are separated by A. If $A > 2\nu$ the doublet is centered at A/2 and the two lines are separated by 2ν. For a nuclear spin larger than 1/2, the quadrupolar interaction affects the ENDOR spectra by further splitting the

ENDOR lines. This is indeed the case of ^{197}Au (I = 3/2), which exhibits both quadrupolar and hyperfine interaction.[34] $Au_{25}(SEt)_{18}^{0}$ showed a very nice ENDOR pattern that enabled us to determine the hyperfine interaction between the unpaired electron and the gold atoms. Through knowledge of the exact 3D structure of $Au_{25}(SEt)_{18}^{0}$, we carried out a specific DFT study aimed to determine the relevant isotropic and anisotropic hyperfine coupling constants. A good match of the outcome of DFT calculations and ENDOR results was observed, which allowed assigning each ENDOR signal to specific types of Au atoms forming the cluster. Our results show that ENDOR is a valuable technique that can be successfully employed for obtaining relevant information about the fine structure and the electronic distribution of nanoclusters.

3.3 Results and Discussion

3.3.1 Synthesis and Characterization of $Au_{25}(SEt)_{18}$

The synthesis of $Au_{25}(SEt)_{18}$ was carried out as detailed in Section 2.1.1. Briefly, addition of ethanethiol to a red tetrahydrofuran solution of tetrachloroauric acid (molar ratio 4:1) and tetra-*n*-octylammonium bromide (1.2 equiv) eventually yielded a colorless solution of reactive Au(I)-thiolate species. Reduction to Au(0) was carried out by addition of aqueous sodium borohydride. After 2 days under stirring, the clusters were separated from the reaction mixture and purified. $Au_{25}(SEt)_{18}$, initially obtained as $[n\text{-}Oct_4N^+][Au_{25}(SEt)_{18}^-]$, was eventually oxidized to $Au_{25}(SEt)_{18}^{0}$ by silica-gel column chromatography under aerobic conditions. The anionic and neutral forms show the UV-vis spectra expected for $Au_{25}(SR)_{18}$ clusters (Figure 1 in Section 2.2).[15,26,30] The chemical composition, purity, and monodispersity of $Au_{25}(SEt)_{18}^{0}$ were assessed by MALDI-TOF mass spectrometry.[31] In particular, the spectrum of the purified sample shows a peak centered at 6024 that corresponds to the unfragmented cluster. The main fragmentation pattern, which increases as the laser intensity increases, reveals stepwise loss of four AuSEt units (mass = 258.1) to form $Au_{21}(SEt)_{14}$ (mass = 4992) (Figure 1).

3.3.2 Electrochemistry

The electrochemical behavior of $Au_{25}(SEt)_{18}$ was studied in DCM/0.1 M TBAH. The electrochemical pattern is quite similar to that of $Au_{25}(SC_2H_4Ph)_{18}$, *i.e.*, two main reversible peaks O1 and R1 associated with the +1/0 and 0/-1 redox couples, and further oxidation or reduction peaks corresponding to

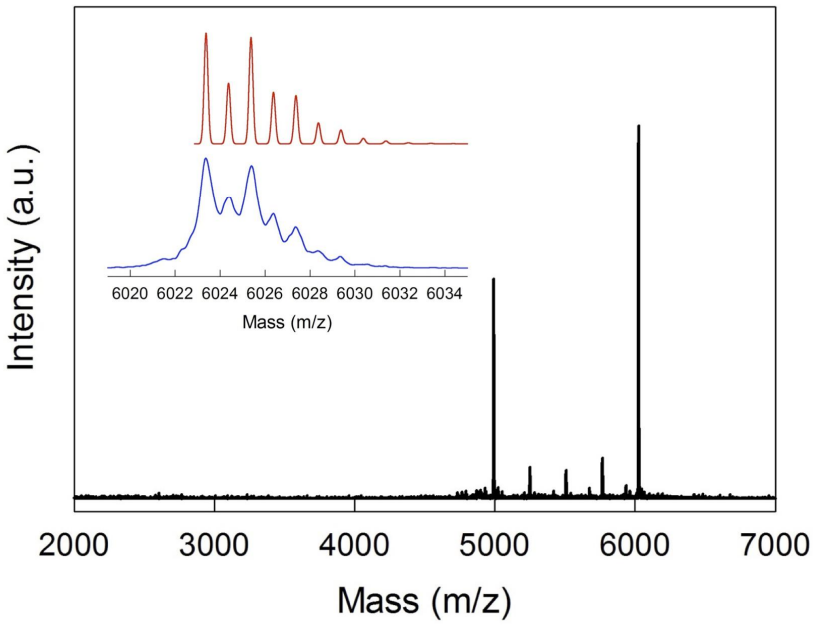

Figure 1. MALDI-TOF mass spectrum of $Au_{25}(SEt)_{18}$. To evidence the main fragmentation pattern, the laser pulse intensity was kept a bit above threshold values. Inset shows the theoretical (red) and experimental (blue) isotopic pattern.

formation of higher positive or negative charge states.[26] In CV, the latter are chemically irreversible. For example, Figure 2A, obtained starting from $Au_{25}(SEt)_{18}^{0}$, shows that the peak current of the irreversible peak R2 is much larger than that of R1; as a matter of fact, its peak current corresponds to ca. 5 electron/molecule at 0.1 V s^{-1}, a value larger than that of *ca*. 3.5 electron/molecule observed for $Au_{25}(SC_2H_4Ph)_{18}$.[28] Peaks R2 and O2 can be made reversible by increasing the CV scan rate and/or lowering the temperature. Figure 2B, obtained starting from $Au_{25}(SEt)_{18}^{-}$, shows the situation observed for O2 (and O3) at -49 °C, in which O2 is partially reversible. By carrying out CV analysis of the peaks, according to previously described methodologies,[27,28] the lifetimes of the corresponding electrogenerated species (at 25 °C) were estimated to be 0.11 s and 3 ms for O2 and R2, respectively. Comparison with the values of 0.33 s (O2) and 4 ms (R2) measured for $Au_{25}(SC_2H_4Ph)_{18}$ under similar experimental conditions shows that the ethanetiolate ligands make the higher charge states less chemically stable. The lability of the species generated at O2 and R2, conceivably a radical dication and a radical dianion,[27] respectively, is thus incompatible with their use in NMR and, particularly, ENDOR experiments. In the following, we will thus focus on the only stable radical state, $Au_{25}(SEt)_{18}^{0}$.

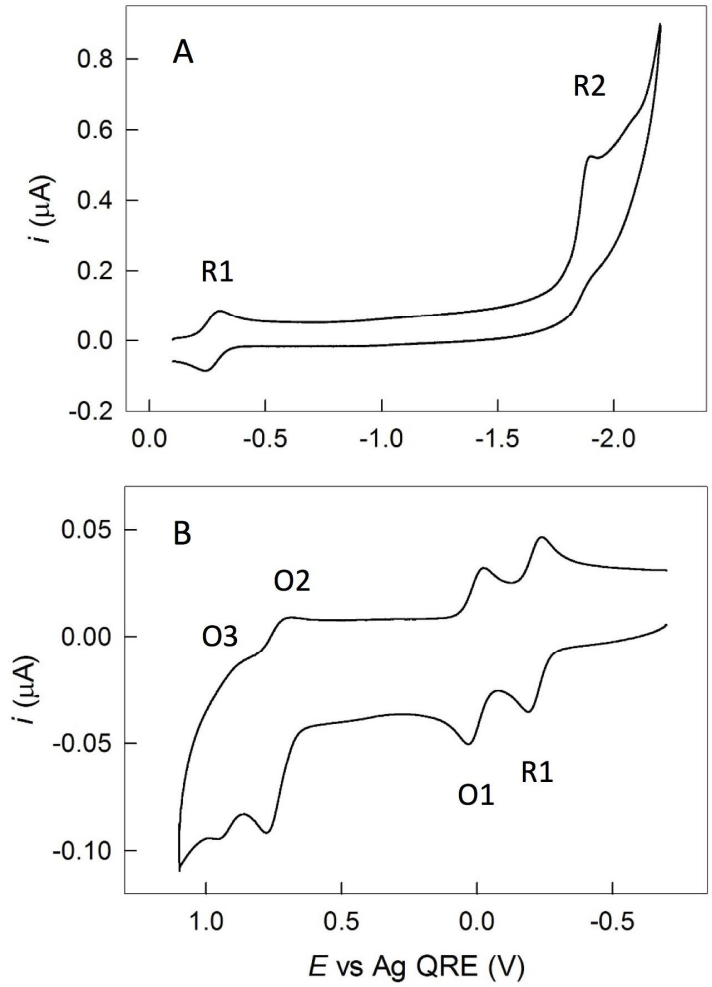

Figure 2. CV pattern for (A) the reduction of 0.32 mM $Au_{25}(SEt)_{18}^{0}$ at 25 °C and (B) the oxidation of 0.30 mM $Au_{25}(SEt)_{18}^{-}$ at -49 °C in DCM/0.1 M TBAH, on a glassy carbon electrode at 0.2 V s^{-1}. The peaks are labeled according to electron uptake or release by the neutral cluster.

3.3.3 NMR Spectroscopy

The ^{1}H-NMR spectrum of an acetonitrile-d_3 solution of [*n*-Oct_4N^{+}][$Au_{25}(SEt)_{18}^{-}$] shows two sharp CH_3-CH_2 typical patterns (triplet and quartet), together with signals associated with the tetra-*n*-octylammonium countercation (Figure 3A). When taking the area of the ammonium N-CH_2 resonance (3.05 ppm) as a standard for integration, the resonances at 1.30 and 2.94 ppm pertain to CH_3 and CH_2 of the 6 ethyl groups of the outer ligands, whereas the corresponding resonances of the 12 ethyl groups of the inner ligands are found at 1.43 and 3.36 ppm. It is worth noting that a larger shielding is experienced by the groups belonging to the outer ligands, and that the integrals confirm the inner-to-outer ligand 2:1 ratio. The corresponding ^{13}C

resonances are observed at 33.21 $(CH_2)_{in}$ and 21.88 ppm $(CH_3)_{in}$, and 29.27 $(CH_2)_{out}$ and 19.88 ppm $(CH_3)_{out}$.

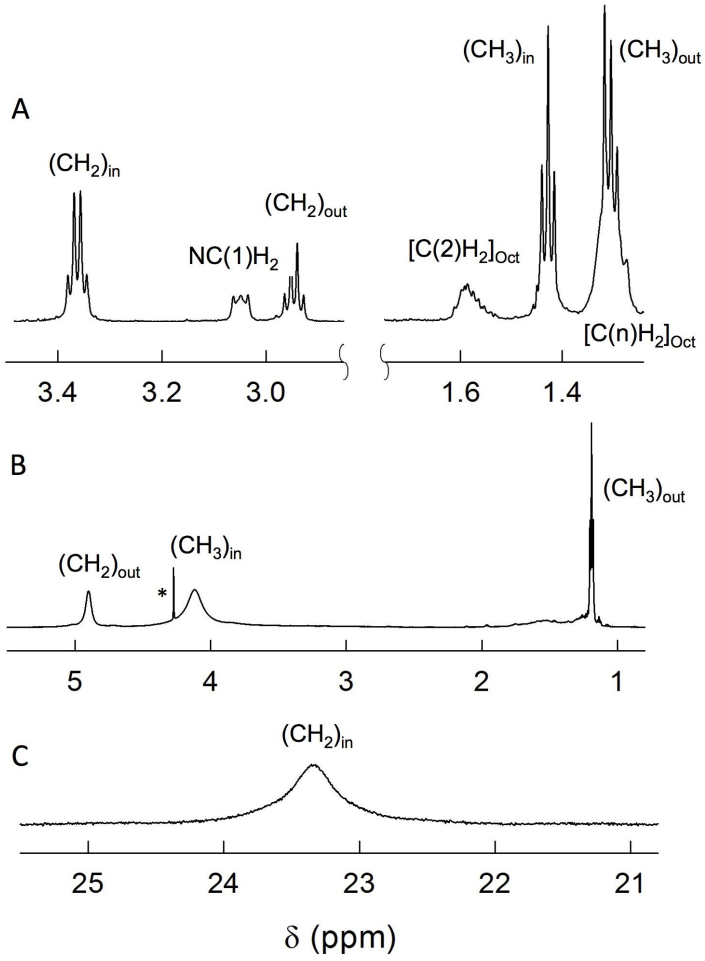

Figure 3. ^{1}H NMR spectra of (A) [*n*-$(Oct)_4N^+$] [$Au_{25}(SEt)_{18}^-$] in acetonitrile-d_3 at 25 °C, and $Au_{25}(SEt)_{18}^0$ in benzene-d_6 (B) at 25 and (C) 65 °C. The spectra show the relevant zones and resonances, including some peaks of *n*-$(Oct)_4N^+$, as indicated. The asterisk (*) marks an impurity (DCM).

For solubility reasons, the spectra of $Au_{25}(SEt)_{18}^0$ were obtained in benzene-d_6 (Figure 3B). This neutral cluster is expected to be a radical and, as a matter of fact, the resonances of both its outer and inner ligands are broadened due to proximity with the paramagnetic metal center. The COSY-correlated CH_3-CH_2 resonances of the outer ligands are at 1.19 and 4.83 ppm, respectively, whereas those of the corresponding inner groups are 4.12 (CH_3) and 23.4 ppm (CH_2, measured at 65 °C). The highly deshielded $(CH_2)_{in}$ resonance is very broad at 25 °C (ca. 3000 Hz) but becomes sharper as the temperature is increased to

65 °C, at which a COSY correlation with the CH_3 signal at 4.12 ppm is detected. Under these conditions, the corresponding integrals are in very good agreement with the expected inner-to-outer ligand 2:1 ratio. The ^{13}C resonances of the outer ligands are detected at 28.0 (CH_3) and 35.5 ppm (CH_2). On the other hand, the very long instrumental time (at least 48 h at 65 °C) required for observing the very broad ^{13}C resonances of the inner ligands induces extensive sample decomposition. The general NMR behavior of $Au_{25}(SEt)_{18}^0$ is thus in keeping with that of other paramagnetic $Au_{25}(SR)_{18}^0$ clusters.[30,31]

3.3.4 The X-ray Structure

The X-ray single-crystal diffraction experiment confirmed the compositional and structural deduction from the mass spectrometry, the electrochemical, and the spectral analyses. The crystals used for X-ray crystallographic study were obtained by diffusing diisopropyl ether vapor into the toluene solution containing $Au_{25}(SEt)_{18}^0$. The compound crystallizes in a centrosymmetric triclinic space group *P*-1, with the central Au atom at the inversion center, as observed for $Au_{25}(SC_2H_4Ph)_{18}^0$.[15] The central Au atom is surrounded by 12 Au atoms. These 13 atoms form the inner (body-centered) icosahedral core (Figure 4A). The Au-Au bond distances between the central Au atom to the 12 inner layer Au atoms vary very little and are between 2.785 and 2.801 Å. In addition to being bound to the central Au atom, each of the 12 inner shell Au atoms is coordinated to five icosahedron Au atoms and one S atom. Interestingly, whereas six of them are also bound to three stellated Au atoms, the remaining six atoms show interactions only with two stellated Au atoms. In other words, the staples are distorted so that whereas one of the two Au(stellated)-Au(icosahedron) distances is, on average, 3.315 Å, the second one is 3.241 Å (the latter is evidenced as a bond in Figure 4). This kind of dissymmetry is not observed in the $Au_{25}(SC_2H_4Ph)_{18}$, where the average distance is 3.23 and 3.22 Å for the neutral[15] and anionic cluster,[13] respectively. The outer shell of the Au_{25} cluster consists of 12 stellated Au atoms included in six half-crowns, -(SEt)-Au-(SEt)-Au-(SEt)-, where the Au atom of each -(SEt)-Au-(SEt)- structure is bound to three inner shell Au atoms and two S atoms, with the S-Au-S angle ranging from 170 to 173.5 degrees. These Au-Au bonds, however, are longer than the icosahedral Au-Au bonds (Table 1) and could be considered to be aurophilic in nature. This feature is also present in the previously reported Au_{25} clusters,[13-15] but is missing in the Au_{13} cluster without further aurophilic bonds.[35,36] Whereas

the gold cluster is not disordered (see below), the ethyl-chain carbon atoms exhibit larger thermal movement. In the solid state, weak intermolecular C-H¨¨S hydrogen bonds (S…C distance of 3.65 Å, with C-H…S angle of 137°) joins the clusters to a loose one-dimensional (1-D) chain along crystallographic (110) vector (Figure 5). A packing coefficient of 65.8% illustrates the close packing of the Au_{25} clusters.

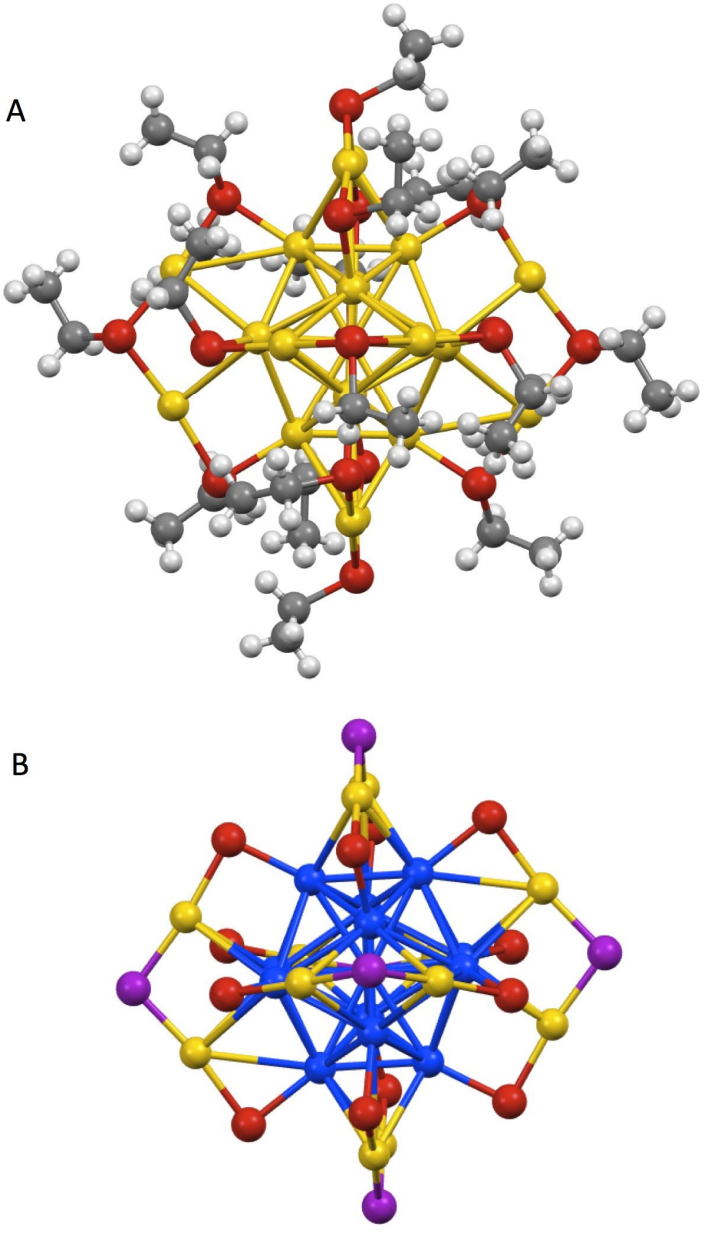

Figure 4. (A) Projection showing the X-ray crystal structure of $Au_{25}(SEt)_{18}^{0}$. Au = yellow, S = red, C = gray, H = white. (B) View of the twisted staple (H and C atoms removed for clarity). Au_{ico} = blue, Au_{staple} = yellow, inner-ligand S = red, outer-ligand S = purple.

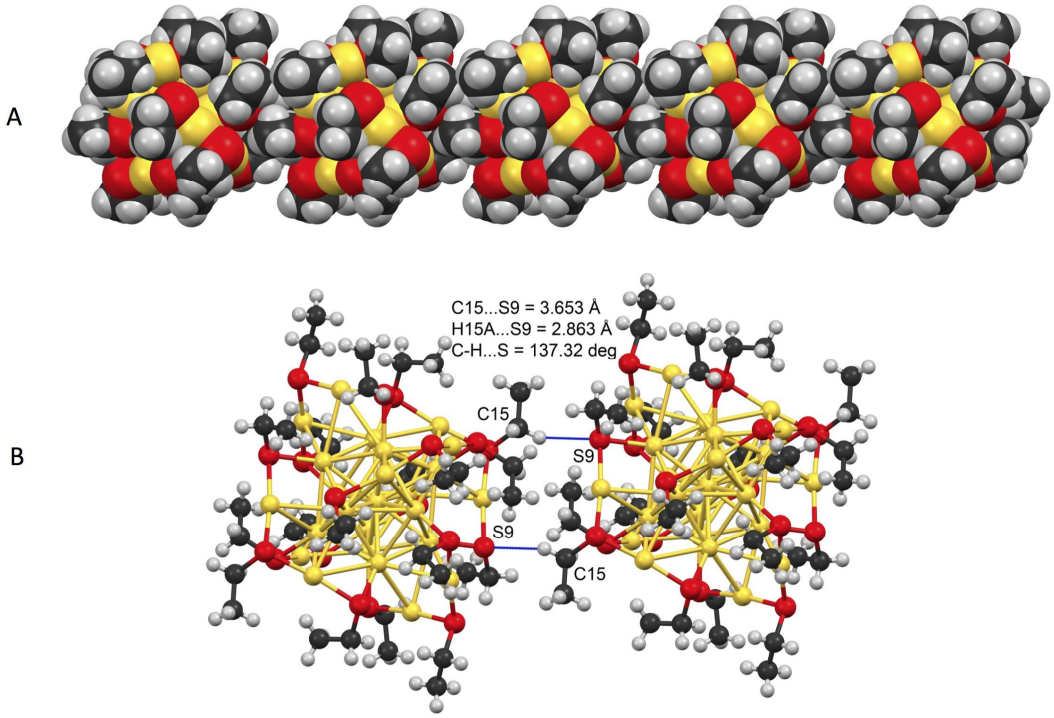

Figure 5. (A) Projection showing the loose 1-D chain. (B) View of the corresponding weak intermolecular C-H...S hydrogen bonds. Au = yellow, S = red, C = gray, H = white.

The structure of $Au_{25}(SEt)_{18}^{0}$ is the first known example of single crystal X-ray crystallography structure of an Au_{25} cluster entirely protected by a short alkanethiol. It is, therefore, instructive to make a comparison with relevant parameters obtained from the structures of the corresponding phenylethanethiolate stabilized clusters. Table 1 shows some selected average bond distances.

Concerning the icosahedron, its size does not depend on ligands and charge state. Similarly, in all three structures, the bond distance between the pairs of gold atoms directly under the central sulfur atom of the six staples is also virtually constant and detectably smaller (by ca. 0.2 Å) than that of all other icosahedral Au-Au bonds. The distance between the stellated and the nearest icosahedron Au atoms is larger by ca. 0.4 Å than that between most icosahedral Au-Au bonds. No significant S-Au bond-length differences are evident among the three clusters, at least within experimental error: this observation could be relevant in gaining insights into the hypothesis of a possible Au-S bond length variation upon changing the charge state of the cluster, as detected by Raman

Table 1. Relevant Average Bond Distances[a] in $Au_{25}(SR)_{18}$ Clusters as Obtained from Single Crystal X-ray Crystallography Structures.

Bond	R = Et charge = 0	R = C_2H_4Ph charge = 0 (ref. 15)	R = C_2H_4Ph charge = -1 (ref. 13)
$Au_{central} – Au_{ico}$ [b]	2.79	2.79	2.78
$Au_{ico} – Au_{ico}$ [c]	2.98	2.97	2.95
$Au_{ico} – Au_{ico}$ [d]	2.79	2.78	2.80
$Au_{staple} – Au_{ico}$ [e]	3.18	3.15	3.16
$S – Au_{ico}$ [f]	2.37	2.38	2.37
$S – Au_{staple}$ [g]	2.30	2.30	2.31

[a] All bond lengths are in angstroms; the $Au_{25}(SC_2H_4Ph)_{18}$ data were taken from the known structures,[13,15] as obtained from Cambridge Structural Database (v. 5.34 2013), The Cambridge Crystallographic Data Centre, Cambridge, U.K. (2013). [b] From the central Au atom to the 12 Au atoms of the icosahedron surface. [c] Bonds between icosahedral Au atoms not under staples. [d] Bonds between the six Au-Au pairs below the six staples. [e] Distance between stellated Au atoms and the three icosahedron Au atoms directly below. [f] S-Au bonds involving icosahedral Au atoms. [g] Bond between stellated gold and sulfur atoms.

spectroscopy.[37] A comparison between the geometry of the staples also is quite interesting. It has been observed that albeit similar, the structures of the anionic and the neutral state of $Au_{25}(SC_2H_4Ph)_{18}$ display two main differences.[15] Whereas the anionic cluster shows that all staples are distorted in the sense that the S-Au-S-Au-S motif is twisted with respect to the plane formed by the σ_h mirror in the D_{2h} subgroup of the icosahedron, none of the staples of the neutral cluster display any significant distortion. This was attributed to a possible effect of the charge state or a solid-state effect induced by the presence of the bulky counterion for the anionic state. Interestingly, however, in the neutral cluster $Au_{25}(SEt)_{18}^0$ we find two couples of linear staples (as shown in Figure 4A) and one couple (Figure 4B) displaying the same distortion mentioned above for $Au_{25}(SC_2H_4Ph)_{18}^-$: therefore, neither charge nor the presence of the counterion can be the primary cause of such a structural feature.

From the viewpoint of the orientation of the ligands in the monolayer, another interesting feature makes all three structures different. In each staple of $Au_{25}(SC_2H_4Ph)_{18}^0$, the three ligands are oriented in a, say, down-up-down

direction with respect to the plane containing the S(R)-Au-S(R)-Au-S(R) motif.[15] In $Au_{25}(SC_2H_4Ph)_{18}^-$, on the other hand, the orientation is always of the down-up-up type.[13] In $Au_{25}(SEt)_{18}^0$ we find an even different situation: whereas the ligands of two couples of staples display the same down-up-up orientation (Figure 6A) of anion $Au_{25}(SC_2H_4Ph)_{18}^-$, the third couple of staples shows the novel feature that all three ligands are oriented on the same side of the S(R)-Au-S(R)-Au-S(R) plane (Figure 6B). These comparisons clearly show that, at least in the solid state, not only charge somehow affects the structure but also the ligand type does.

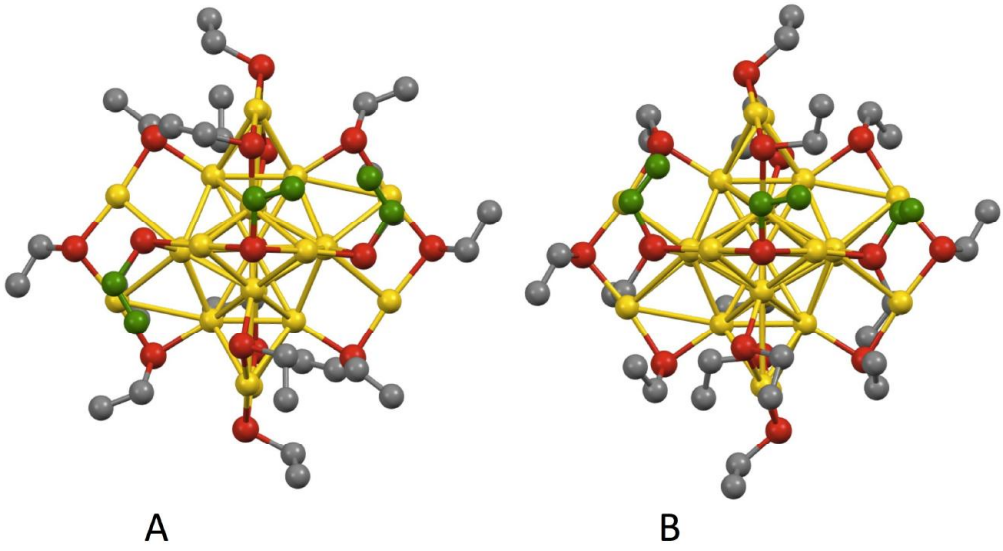

Figure 6. (A) View of the down-up-up ligand orientation in the front staple. (B) View of the up-up-up orientation. In both cases, the carbon atoms are shown in green. Hydrogen atoms removed for clarity.

3.3.5 ENDOR Analysis and DFT Calculations

The Davies ENDOR[33] spectrum was obtained in frozen matrix at 5.5 K for a 0.5 mM solution of $Au_{25}(SEt)_{18}^0$ in toluene. The spectrum was acquired at the field of 291.1 mT, corresponding to the maximum of the EPR signal. The spectrum shows five broad lines in the range from 0 to 90 MHz, with maxima located at 9.8, 24.7, 42.1, 60.9, and 77.9 MHz (Figure 7, red trace). The fact that the spectrum shows peaks at frequency larger than 40 MHz is only consistent with hyperfine and quadrupolar couplings with ^{197}Au. Other possible ENDOR lines could come from the ligands' protons for which, however, the spin-density is low and lines around the proton-free Larmor frequency (12 MHz, at the magnetic

field used for the ENDOR experiment) are expected. Because the number of ENDOR lines is related to the groups of equivalent Au atoms, the intriguing issue now is to explain the spectral pattern while considering that, apparently, Au_{25} clusters are composed by three such groups: central Au, 12 icosahedron Au atoms, and 12 staple Au atoms.

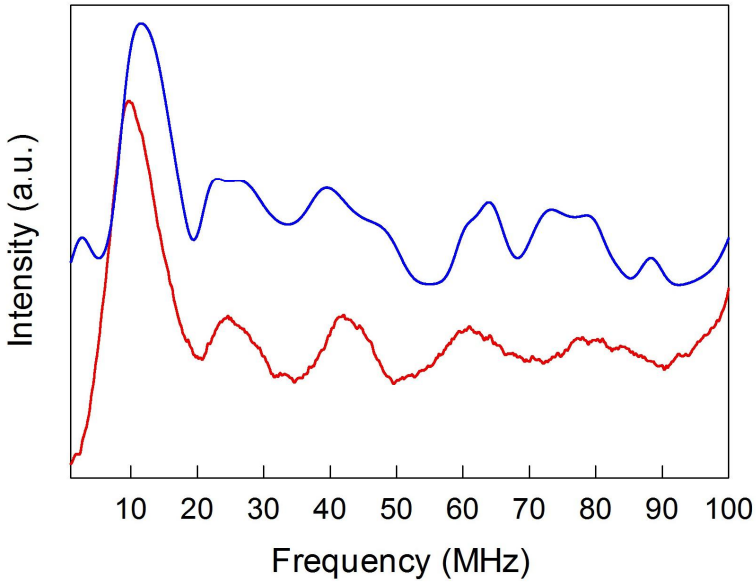

Figure 7. Davies ENDOR spectrum of a frozen 0.5 mM solution of $Au_{25}(SEt)_{18}^{0}$ in toluene at 5.5 K (red line). The blue line shows the corresponding simulation (vertically shifted for clarity) based on the hyperfine and quadrupole components obtained by DFT (see text). The ENDOR spectrum was recorded at a field of 291.1 mT.

To gain insights into this aspect, we carried out specific DFT calculations aimed to obtain the hyperfine and the quadrupolar tensors. We used the single crystal X-ray diffraction structure as the starting point, and the calculations were performed on two models, that is, the actual $Au_{25}(SEt)_{18}^{0}$ MPCs and the corresponding structure where SMe replaces SEt. The rationale was to test whether and to what extent a small ligand change could affect the quality of calculations, in comparison with an actual experimental system. This is an important aspect because, so far, accurate MPC calculations have been performed mostly on SH or SMe ligands, more or less implicitly assuming that an increase of the ligand length or change of its nature does not affect the outcome of electronic structure calculations.

The hyperfine and the quadrupole DFT-calculated tensors of $Au_{25}(SEt)_{18}^{0}$ were used to simulate the experimental ENDOR spectrum. The former are

gathered in Table 2, while the latter and other relevant data are provided for both SEt and SMe in Section 3.5.6.

Table 2. DFT-Computed Values of the Anisotropic Hyperfine Tensors for $Au_{25}(SEt)_{18}^{0}$.

Atom label[a]	Ax (MHz)	Ay (MHz)	Az (MHz)	Ave[b] (MHz)
Au1(central)	20.7	14.2	11.6	15.5
Au4(ico)	40.3	44.5	36.7	40.5
Au3(ico)	52.8	45.1	48.5	48.8
Au7(ico)	9.1	22.7	12.6	14.8
Au2(ico)	39.5	40.8	47.6	42.6
Au5(ico)	50.8	61.6	52.7	55.0
Au6(ico)	11.4	14.3	23.9	16.5
Au8(staple)	1.9	1.9	3.1	2.3
Au11(staple)	20.0	18.6	18.9	19.2
Au9(staple)	4.0	2.9	2.8	3.2
Au10(staple)	3.7	5.0	4.3	4.3
Au12(staple)	21.0	18.3	19.4	19.6
Au13(staple)	10.3	11.1	9.8	10.4

[a] Except for the central atom, Au1, for symmetry reasons all other labels pertain to couples of equivalent Au atoms (labeling refers to the deposited structure). [b] Average of Ax, Ay, and Az.

Inspection of Table 2 shows a most evident fact that the 12 Au atoms on the icosahedron surface can be divided into two groups: whereas a first group of 8 atoms (labeled as 2, 3, 4, and 5: for symmetry and with the obvious exception of the central atom, each label corresponds to two equivalent Au atoms) is characterized by strong and similar hyperfine couplings (x, y, and z averages of 41-55 MHz), a second group of 4 Au atoms (labeled as 6 and 7) have much smaller hyperfine couplings (averages of 15-17 MHz). We should also note that whereas the DFT-calculated tensors pertain to a single configuration, on the ENDOR time scale we expect the hyperfine and quadrupolar tensors of these atoms to be dynamically averaged by vibrational motion. To simulate the ENDOR response, for each group of similar core nuclei we thus used the average of each Cartesian component of the hyperfine and quadrupolar tensors, and their Euler

angles. Staple nuclei have low hyperfine couplings and, if we assume a dynamical averaging also for this group of nuclei, their main contribution is in the range 0-5 MHz of the spectrum; due to the pulse sequence used, this region is not detectable in the experimental ENDOR and, therefore, we neglected the contribution of the staple Au atoms in the simulation. The simulation for SEt (blue line in Figure 7) shows that the main features of the experimental spectrum can be reproduced quite satisfactory. It is also worth noting that the use of average values indeed improved the quality of the simulation of the ENDOR spectrum quite significantly (Figure 7, blue line, to be compared with the results shown in Figure 8, where tensors were not averaged).

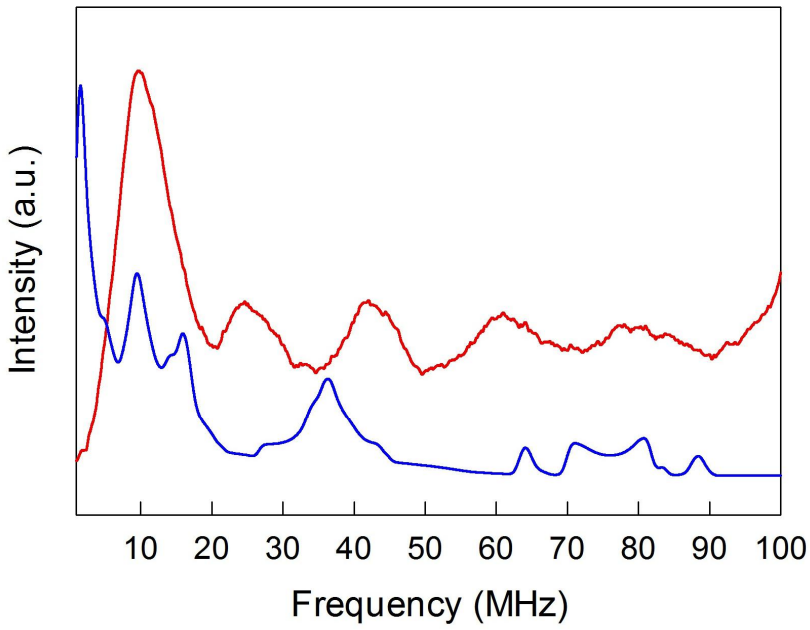

Figure 8. Davies ENDOR spectrum of a frozen 0.5 mM solution of $Au_{25}(SEt)_{18}^{0}$ in toluene at 5.5 K (red line). The blue line shows the corresponding simulation based on using, for each group of atoms, the specific x, y, and z hyperfine and quadrupolar components.

Figure 9 provides insights into the simulations for the groups of Au atoms. The results can be summarized as follows: (i) the peaks at 24.7 and 42.1 MHz are mainly due to the first group of 8 Au core atoms, whereas (ii) the second group of 4 core atoms contributes to the strong peak at 9.8 MHz; (iii) the 77.9 MHz peak matches the simulated high-frequency structured quadrupolar peak of the central Au atom; (iv) the 60.9 MHz peak receives contributions from both the

first group of core atoms and the high-frequency quadrupolar peak of the central Au atom; (v) the group of staple Au atoms only contributes to the peak at 9.8 MHz, although use of the dynamically averaged values makes its effect to the simulated peak as marginal.

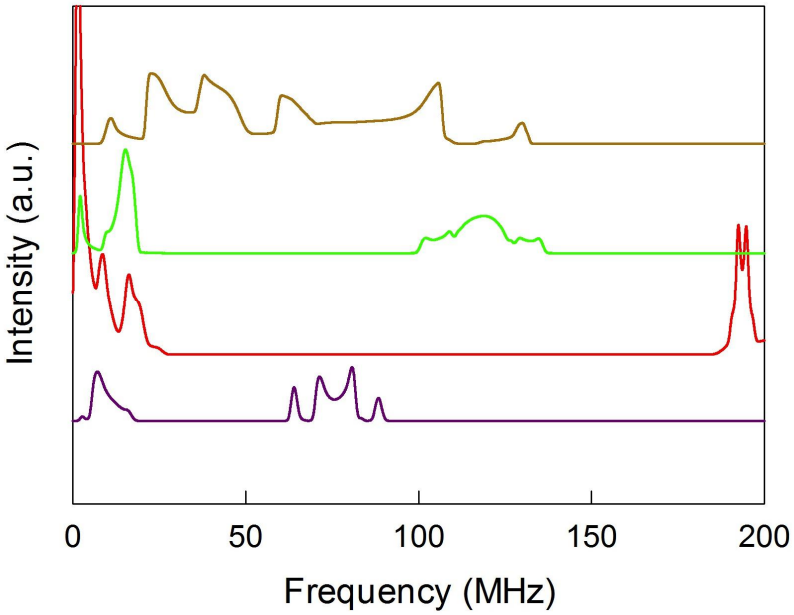

Figure 9. Simulation of the Davies ENDOR spectrum: from top to bottom, simulations pertain to the first (gold curve) and second groups of icosahedral atoms (green curve), staple Au atoms (red curve), and central atom (purple curve). The first two traces correspond to the average values. The simulations show a larger frequency range than that experimentally accessible.

In the context of ENDOR simulations, the agreement between the experimental and the predicted spectra of Figure 7 is indeed very good. In fact, it is also worth noting that the simulations carried out by using the DFT parameters obtained for the SMe ligands did not lead to the same satisfactory match with the experimental ENDOR spectrum, as illustrated in Figure 10. This is actually a quite unexpected finding because there is a general consensus about considering the effect of ligands on the MPC electronic structure as very small, at least as long as the nature of the ligand does not change significantly.[38]

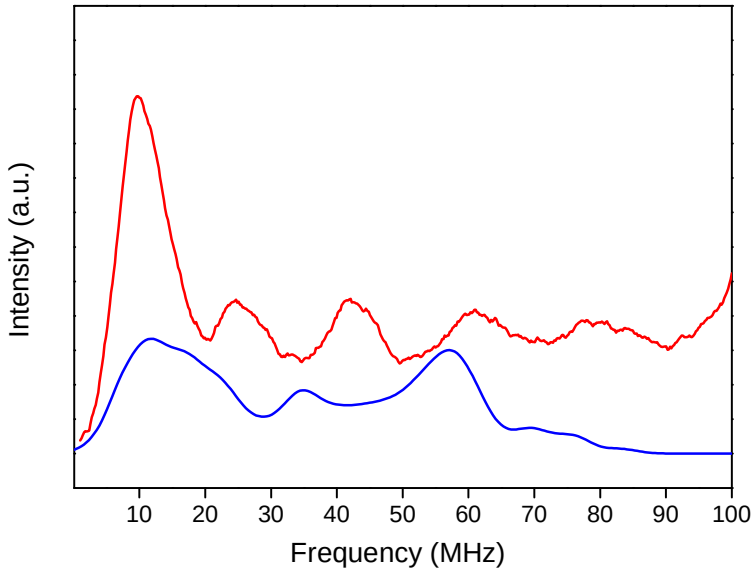

Figure 10. Davies ENDOR spectrum of a frozen 0.5 mM solution of $Au_{25}(SEt)_{18}^{0}$ in toluene at 5.5 K (red line). The blue line shows the corresponding simulation for $Au_{25}(SMe)_{18}^{0}$, carried out as described for Figure 7.

The question now is as to why the 12 atoms of the icosahedral surface split into two groups. We note that the two couples of Au atoms forming the second group, and labeled as 6 and 7, correspond to those atoms for which the distance from the stellated Au atom of the same staple (see above) is the largest observed in the X-ray structure (3.31 – 3.35 Å). This suggests that a small disorder can cause interferences in the wave function leading to nonequivalent electron densities at the icosahedral nuclei. We also note that in the DFT-optimized structure, which is representative of the structure in a low-dielectric solvent (as the one analyzed by ENDOR), also shows disorder. In particular, the unique atoms Au6 and Au7, form a rectangle (Figure 11) with dimensions different from those of the other two rectangles (those involving atoms Au3 with Au4 and Au2 with Au5).

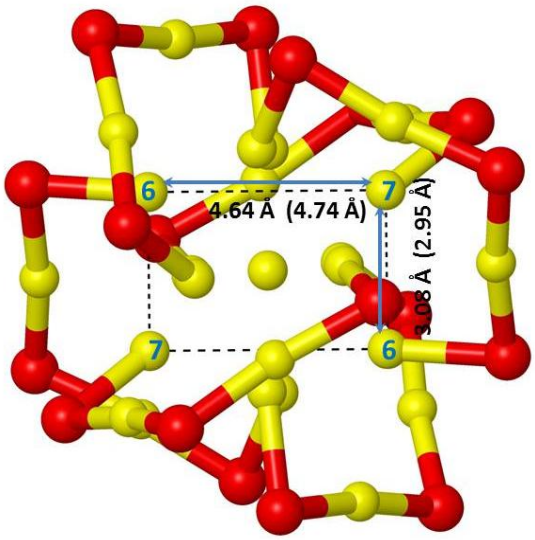

Figure 11. DFT structure of $Au_{25}(SEt)_{18}^{0}$ showing non-equivalent distances in the rectangle containing atoms Au6 and Au7, compared to the same distances on the rectangles containing the other icosahedral atoms (average values in parenthesis). A similar effect, albeit less pronounced, is seen in the X-ray structure. H and C atoms and most bonds removed for clarity.

3.4 Conclusions

Devising methods for obtaining relevant information about the structure of MPCs is of paramount importance for both fundamental and applied (*e.g.*, in catalysis) viewpoints. We prepared a 25-gold atom nanocluster protected by the smallest ligand ever used, ethanethiol. Its composition, charge state, and magnetic properties were assessed by a combination of MALDI-TOF, UV-vis spectroscopy, electrochemistry, and NMR spectroscopy results. The structure of $Au_{25}(SEt)_{18}^{0}$ could be determined precisely by X-ray crystallography analysis of high-quality single crystals. Knowledge of the exact 3D structure of $Au_{25}(SEt)_{18}^{0}$ allowed us to determine the relevant isotropic and anisotropic hyperfine coupling constants by DFT calculations void of those approximations associated with the use of simplified ligand models. The Davies ENDOR spectrum showed a distinct pattern that, in comparison with the DFT results, allowed us to understand that the Au atoms of the cluster can be divided into four groups: besides the central atom and the 12 staple Au atoms, the 12 icosahedron Au atoms split into a group of 8 and a group of 4 atoms. Such nonequivalence among icosahedron atoms comes from the small dissymmetries associated with dissimilar staple motifs. Such small distortions propagate into the core atoms giving rise to nonequivalent

electron densities at the icosahedral nuclei and, therefore, hyperfine couplings. Pulse ENDOR thus proves to be a powerful method to study the structure and the electronic distribution of nanoclusters. The technique requires the presence of an unpaired electron and this is, in principle, always possible as long as a stable paramagnetic charge state can be attained *via* calibrated oxidation (or reduction) of an otherwise diamagnetic MPC, as others and we showed previously.[27,29-31,39]

3.5 Experimental Section

3.5.1 UV-vis Absorption Spectroscopy

The UV-vis spectra were obtained at 0.1 mM concentration in DCM, with 2 mm cuvettes. We used a Thermo Scientific Evolution 60S spectrophotometer or, during syntheses, an Ocean Optics QE65000 spectrophotometer equipped with a DH-2000-BAL light source. The spectra resolution was 1 or 0.8 nm, respectively.

3.5.2 Mass Spectrometry

MALDI-TOF mass spectra were obtained with an Applied Biosystems 4800 MALDI-TOF/TOF spectrometer equipped with a Nd:YAG laser operating at 355 nm. The laser firing rate was 200 Hz and the accelerating voltage was 25 kV. The laser pulse intensity was kept at threshold values and then progressively increased. $Au_{25}(SEt)_{18}^{0}$ was dissolved in benzene containing the matrix, DCTB, to obtain 0.1 mM solutions with a 1:400 MPC/matrix ratio. Two μl of solution were dropcasted onto the sample plate and air-dried before loading into MALDI-TOF. The spectra were recorded using the reflectron positive-ion mode. As a standard, we used $Au_{25}(SC_2H_4Ph)_{18}$, which has a MW of 7394.

3.5.3 Electrochemistry

The experiments were carried out in DCM containing 0.1 M TBAH, under an Ar atmosphere in a glass cell thermostatted at 25 °C, unless otherwise specified. The working electrode was a glassy carbon disk (9.4×10^{-4} cm^2), prepared and activated as already described.[27] A Pt wire was the counter electrode and an Ag wire served as the quasi-reference electrode. At 25 °C, the latter has a potential of -0.187 V against the KCl saturated calomel electrode (SCE). Calibration was performed by addition of ferrocene at the end of the experiments; in the above solvent/electrolyte, the ferricenium/ferrocene redox couple has E^o = 0.460 V vs SCE. We used a CHI 760d electrochemical

workstation, and the feedback correction was applied to minimize the ohmic drop between the working and the reference electrodes.

3.5.4 NMR Spectroscopy

^{1}H and ^{13}C NMR spectra were obtained at 1 mM MPC concentration in acetonitrile-d_3 or benzene-d_6 for [*n*-Oct_4N^+][$Au_{25}(SEt)_{18}^-$] or $Au_{25}(SEt)_{18}^0$, respectively, with a Bruker Avance DMX-600 MHz spectrometer equipped with a 5 mm TX-1 x,y,z-gradient powered, triple resonance inverse probe operating at 599.90 and 150.07 MHz, respectively. The temperature was controlled with a Bruker BVT-300 automatic temperature controller. Unless otherwise indicated, the probe temperature was maintained at 25.0 ± 0.1 °C. Chemical shifts are in parts per million (δ) units with reference to Me_4Si used as an internal standard for both ^{1}H and ^{13}C NMR. To ensure a complete relaxation for all the resonances, integral values for the proton spectra were obtained by a prescan delay of 10 s. As previously done for $Au_{25}(SC_2H_4Ph)_{18}$,[30] the proton assignments were performed by standard chemical shift correlations as well as by 2D correlation spectroscopy (COSY), total correlation spectroscopy (TOCSY), and nuclear Overhauser enhancement spectroscopy (NOESY) experiments; the ^{13}C chemical shift values were obtained and assigned through 2D-heteronuclear correlation experiments (heteronuclear multiple quantum coherence, HMQC).

3.5.5 X-ray Single Crystal Diffraction

Black crystals of the title compound $Au_{25}(SEt)_{18}$ were obtained by vapor diffusion of diisopropyl ether into a toluene solution of $Au_{25}(SEt)_{18}$. Crystal data for compound $Au_{25}(SEt)_{18}$: black bricks, 0.04 × 0.04 × 0.07 mm, *FW* = 6024.32, $C_{36}H_{90}Au_{25}S_{18}$, triclinic, space group *P*-1, *a* = 13.7727(6) Å, *b* = 13.8864(6) Å, *c* = 14.1519(5) Å, α = 104.383(3), β = 101.406(3)°, γ = 119.292(4), *V* = 2116.91(16) Å^3, *Z* = 1, D_c = 4.726 g/cm^3, *F*(000) = 2569, μ= 83.388 mm^{-1} , *T* = 123(2) K, $2\theta_{max}$ = 153.294°, 8455 reflections, 6681 with $I_o > 2\sigma(I_o)$, R_{int} = 0.1503, 365 parameters, 66 restraints, GoF = 1.038, R_1 = 0.061 [$I_o > 2\sigma(I_o)$], wR_2= 0.180 (all reflections), -2.557 < Δρ < 2.671 e/Å^3. Crystallographic data of $Au_{25}(SEt)_{18}$ were collected at 123 K with Cu Kα radiation (λ = 1.54184 Å) on an Agilent SuperNova dual wavelength diffractometer equipped with Atlas CCD area detector. CrysAlisPro[40] software was employed for the data measurements and processing. The structure was solved by direct methods integrated in the program of Olex2,[41] and full-matrix least-squares refinements on F^2 were performed using SHELXL.[42]

Analytical numeric absorption correction[43] was applied to treat the reflections. Due to slight disorder, distances restraints were applied for all the ethyl groups. For H atoms, except for those attached to C2, C6, and C8, all the others were calculated to their idealized positions with constraint isotropic thermal factors [1.2 or 1.5 times of U_{eq}(C)] and refined as riding atoms. The H atoms bonded to C2, C6, and C8 were fixed at calculated positions, as the riding mode refinement could not reach convergence. The crystal structure has been deposited to the Cambridge Crystallographic Data Centre with CCDC number of 984217.

3.5.6 ENDOR Spectroscopy

The ^{197}Au ENDOR spectrum was recorded with a Bruker Elexsys E580 spectrometer equipped with a pulse ENDOR dielectric probe head and an Oxford CF935 cryostat. The 0.5 mM solutions of $Au_{25}(SEt)_{18}^{0}$ in toluene were introduced into 3 (o.d.) x 2 mm (i.d.) quartz tubes, degassed by several freeze-pump thaw cycles and sealed off under vacuum (5×10^{-5} Torr). The samples were then rapidly cooled down to 80 K, and the actual measurements were finally carried out at 5.5 K. We used the Davies ENDOR pulse sequence, with 32 ns of microwave inversion pulse and 16 – 32 ns pulse sequence for echo detection. The radiofrequency pulse was 4 μs long and was amplified by a 500 W Bruker RF amplifier. The frequency range was limited to below 100 MHz to avoid frequency artifacts. With the use of the DFT values as input for the nucleus-electron interaction Hamiltonian, ENDOR simulations were performed with the EasySpin software program[44] working on the MatLab 7.12 calculation environment.

Figure 12 shows the cw-EPR spectrum of $Au_{25}(SEt)_{18}^{0}$. The spectrum resembles that already seen for $Au_{25}(SC_2H_4Ph)_{18}^{0}$.[27,29] The Pulse ENDOR spectrum was recorded at the field corresponding to the maximum of the cw-EPR spectrum (291 mT). Simulation of the ENDOR spectrum was performed with the routine ‘salt’ of the EasySpin program, running on the MatLab 7 platform. A 65 MHz excitation window was selected, which approximately corresponds to the inversion microwave pulse bandwidth. The average values of the tensors of the hyperfine (Table 2) and the quadrupole components (Table 3) were used, together with the corresponding Euler angles, for the icosahedral nuclei. The simulated spectra, which are the same as those of Figure 6 but also contain further information, are shown in Figure 13 up to 200 MHz in order to discuss the appearance of the different features.

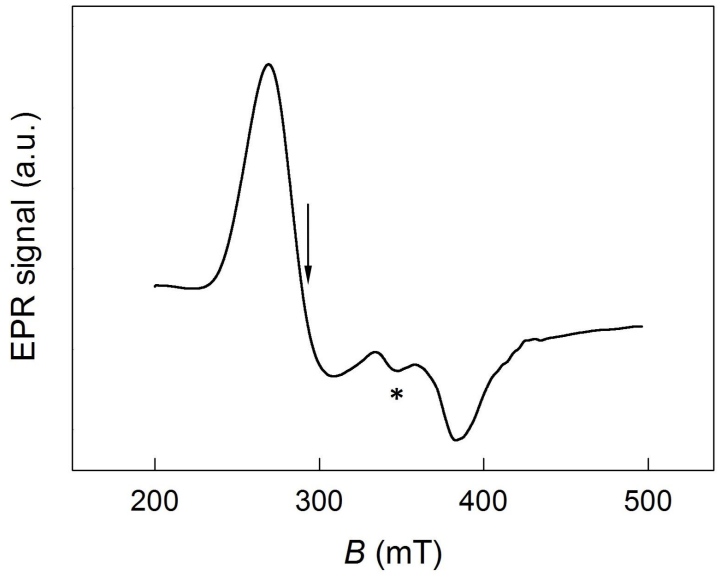

Figure 12. cw-EPR spectrum of $Au_{25}(SEt)_{18}^{0}$ at 20 K. The star symbol marks a background signal due to the probe head. The arrow marks the magnetic field at which the ENDOR spectrum was acquired (291.1 mT). Parameters: modulation field, 0.3 mT; microwave frequency, 9.765 GHz; 20 scans.

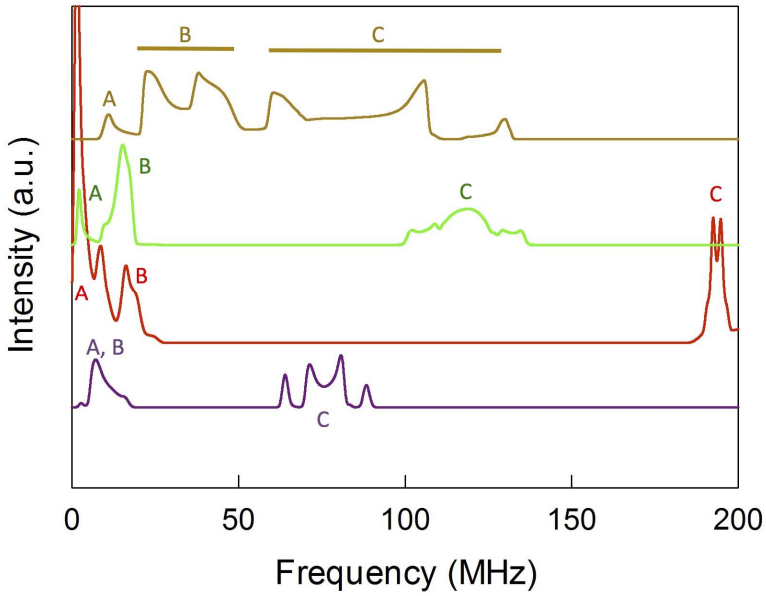

Figure 13. Simulation of the Davies ENDOR spectrum: from top to bottom, simulations pertain to the first (gold curve) and second groups of icosahedral atoms (green curve), staple Au atoms (red curve), and central atom (purple curve). The first two traces correspond to the average values.

Table 3. DFT-Computed Quadrupole Values and Euler Angle Values for the Hyperfine and the Quadrupolar Components for $Au_{25}(SEt)_{18}^{0}$.

	Hyperfine Euler Angles[b]			Quadrupolar Values			Quadrupolar Euler Angles[b]		
Atom label[a]	α (°)	β (°)	γ (°)	Qx (MHz)	Qy (MHz)	Qz (MHz)	α (°)	β (°)	γ (°)
Au1(central)	-8.6	85.4	5.7	-17.3	-7.4	24.7	88.9	90.0	-88.9
Au4(ico)	-2.0	22.8	-24.2	43.9	32.7	-76.5	83.5	89.3	-3.0
Au3(ico)	-24.3	57.6	21.9	46.0	13.3	-59.3	-29.9	156.8	-24.6
Au7(ico)	-4.7	70.2	42.7	31.0	15.8	-46.9	70.1	103.1	-22.4
Au2(ico)	4.8	40.3	-48.7	30.7	19.3	-50.1	-34.7	19.1	-82.6
Au5(ico)	-39.9	63.5	-36.6	48.8	12.3	-61.1	35.7	114.0	-22.2
Au6(ico)	35.1	37.0	55.0	47.1	16.6	-63.7	-25.2	55.6	7.7
Au8(staple)	-1.6	16.1	89.3	100.1	12.1	-112.2	-78.0	54.0	22.5
Au11(staple)	-7.1	86.0	-5.8	42.6	24.5	-67.1	-35.9	149.9	-85.1
Au9(staple)	22.5	43.9	49.7	46.9	15.0	-61.9	45.5	105.8	-25.8
Au10(staple)	3.4	31.3	-0.4	78.6	4.5	-83.1	83.9	81.0	28.7
Au12(staple)	27.7	58.2	15.9	100.9	1.9	-102.8	36.2	38.6	-47.4
Au13(staple)	-13.7	52.2	1.9	76.9	9.4	-86.3	42.0	93.8	-81.3

[a] Except for the central atom, Au1, for symmetry reasons all other labels pertain to couples of equivalent Au atoms. [b] The values of α, β, and γ correspond to components x, y, and z, respectively.

The first group of 8 core atoms with similar hyperfine values is characterized by strong quadrupolar and hyperfine interactions: by averaging the tensors (gold trace), this results in three main bands related to the quadrupolar interaction below 20 MHz (A), between 20 and 50 MHz (B), and between 50 and 140 MHz (C). Band B is characterized by two main peaks corresponding to the experimental ones, while band C is characterized by a peak at ca. 60 MHz, corresponding to the experimental one, and a couple of peaks just beyond 100 MHz, one of which is probably associated with the ENDOR signal increase observed just before 100 MHz. The second group of 4 core atoms is characterized by lower hyperfine interaction but still strong quadrupolar interaction: by averaging the tensors (green trace), band A is at very low frequency and is thus in a region not experimentally accessible with the strong microwave pulse sequence used for acquiring the ENDOR spectrum. Band B is below 20 MHz, while band C is beyond 100 MHz.

Staples Au atom (red trace) are characterized by strong to very strong quadrupolar interaction and weak hyperfine interaction: band A is at very low frequency, band B is around 20 MHz, and bands C are near and beyond 200 MHz. The central atom (purple trace) is characterized by weak quadrupolar and hyperfine interactions and, therefore, band A and band B are below 20 MHz; band C is around 80 MHz and approximately corresponds to the experimental band at 80 MHz.

As explained in Section 3.3.5, the best simulation is based on a group of 8 dynamically equivalent core nuclei, with average hyperfine couplings of 40-55 MHz, and a group of 4 dynamically equivalent core nuclei, with smaller average hyperfine couplings (15-17 MHz). If instead of average icosahedron nuclei parameters one uses all actual x, y, and z components of Tables 2 and 3, the simulation is as shown in Figure 8. Simulating the experimental spectrum with the average values obtained from the DFT calculations carried out for $Au_{25}(SMe)_{18}^{0}$ (data in Table 4) also does not reproduce the experimental spectrum satisfactorily, as shown in Figure 10. Inspection of Table 4 shows that also for $Au_{25}(SMe)_{18}^{0}$ the icosahedron atoms split into two groups but now the group with

Table 4. DFT-Computed Hyperfine, Quadrupolar, and Corresponding Euler Angle Values for $Au_{25}(SMe)_{18}^{0}$.

	Hyperfine Values[b]			Hyperfine Euler Angles[c]			Quadrupolar Values[b]			Quadrupolar Euler Angles[c]		
Atom[a]	Ax	Ay	Az	α	β	γ	Qx	Qy	Qz	α	β	γ
Au1(central)	11.6	8.9	18.6	-43.3	8.2	-65.7	-13.5	-11.0	24.5	58.2	80.3	-12.2
Au4(ico)	41.3	44.0	50.4	-16.3	38.8	-40.8	40.5	31.5	-71.8	2.0	29.6	-79.2
Au3(ico)	26.0	23.0	20.4	-39.1	27.5	-77.3	48.2	11.7	-59.9	39.2	84.8	86.7
Au7(ico)	17.7	30.9	20.6	-33.7	67.2	-36.0	35.2	10.5	-45.7	62.7	88.7	33.9
Au2(ico)	67.9	62.1	61.6	13.6	59.1	-33.9	34.3	16.8	-51.0	-6.4	139.5	-58.3
Au5(ico)	17.0	19.8	27.4	33.8	30.3	49.5	52.7	11.0	-63.6	-26.5	51.5	25.4
Au6(ico)	21.5	31.5	23.6	-8.2	72.9	43.3	39.6	25.2	-64.5	84.0	80.2	20.2
Au8(staple)	3.7	5.0	4.3	39.3	32.2	-29.5	96.5	17.7	-114.2	35.9	90.1	27.0
Au11(staple)	24.0	24.9	23.8	-17.0	54.0	-64.3	58.7	13.5	-72.2	38.4	77.7	81.6
Au9(staple)	8.8	7.6	7.6	-5.7	85.1	-8.7	45.9	14.4	-60.3	-13.3	52.4	15.1
Au10(staple)	-0.7	0.0	-0.7	-40.1	75.2	-15.2	85.0	7.5	-92.5	-22.3	124.5	12.7
Au12(staple)	9.8	10.1	12.2	26.7	12.6	33.1	98.1	5.8	-103.9	-55.6	134.8	-23.2
Au13(staple)	13.7	13.1	14.9	-42.6	11.0	-76.7	69.4	13.7	-83.2	35.1	144.7	78.0

[a] Labels as in Table 3; except for the central atom, Au1, for symmetry reasons all other labels pertain to couples of equivalent Au atoms. [b] Values in MHz. [c] The values of α, β, and γ (degrees) correspond to components x, y, and z, respectively.

larger hyperfine tensor values is composed by 4 Au atoms and that with smaller values by 8 Au atoms. Interestingly enough, the relative population of the two groups is thus reversed.

Although the intensity of the ENDOR lines is not directly related to the number of ^{197}Au nuclei, we note that a different choice of equivalent core nuclei would imply pretty different average hyperfine and quadrupolar tensors, which leads to a simulation that does not match sufficiently well the experimental spectrum. This includes the simulation in which all 12 icosahedron nuclei are considered equivalent (Figure 14).

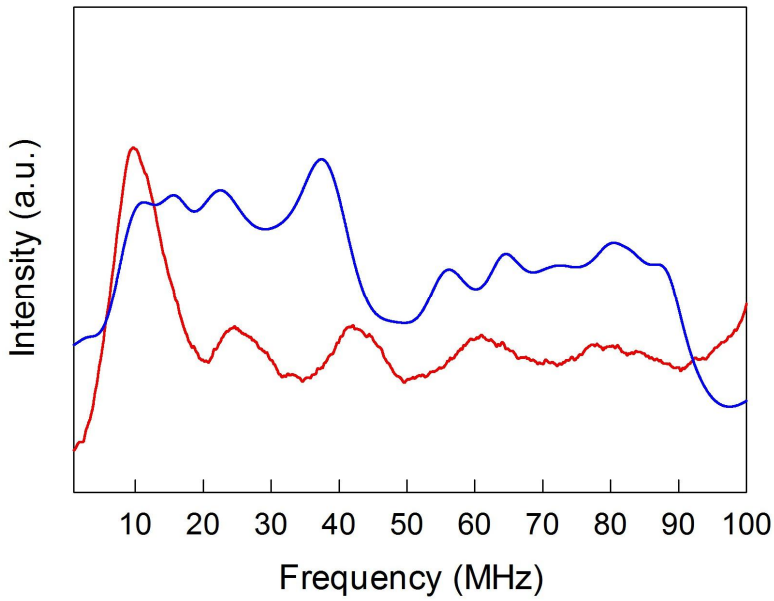

Figure 14. Davies ENDOR spectrum of a frozen 0.5 mM solution of $Au_{25}(SEt)_{18}^{0}$ in toluene at 5.5 K (red line). The blue line shows the corresponding simulation based on using the average hyperfine and quadrupolar components of the icosahedral Au atoms.

3.5.7 Computational Methods

Starting from the X-ray structure, the $Au_{25}(SEt)_{18}$ cluster was optimized using DFT as implemented in Turbomole V6.3.1.[45] For the energy minimization step, we employed the s-vwn functional and def2-TZVP basis set for all atoms with a def2-ecp effective core potential for all Au atoms. At the optimized geometry, hyperfine constants and quadrupole tensors were calculated using Orca 2.9.1.[46]

These calculations were carried out using unrestricted DFT with the GGA functional (BP86), the TZVP basis set for Au, and the DZP basis set for all other atoms. Scalar relativistic effects were introduced using Zeroth-Order Regular Approximation (ZORA).[47] All core electrons were included explicitly in the calculation of hyperfine and quadrupolar tensors, using the segmented all-electron relativistically constructed (SARC) basis set.[48] The Orca-euler utility program was used to calculate the Euler rotation of the hyperfine tensor and the electric field gradient tensor with respect to the g-tensor.

3.6 References

(1) Murray, R. W. Nanoelectrochemistry: Metal Nanoparticles, Nanoelectrodes, and Nanopores. *Chem. Rev.* **2008**, *108*, 2688–2720.

(2) Tsukuda, T. Toward an Atomic-Level Understanding of Size-Specific Properties of Protected and Stabilized Gold Clusters. *Bull. Chem. Soc. Jpn*. **2012**, *85*, 151–168.

(3) Qian, H.; Zhu, M.; Wu, Z.; Jin, R. Quantum Sized Gold Nanoclusters with Atomic Precision. *Acc. Chem. Res.* **2012**, *45*, 1470–1479.

(4) Negishi, Y.; Kurashige, W.; Niihori, Y.; Nobusada, K. Toward the Creation of Stable, Functionalized Metal Clusters. *Phys. Chem. Chem. Phys.* **2013**, *15*, 18736–18751.

(5) Cossaro, A.; Mazzarello, R.; Rousseau, R.; Casalis, L.; Verdini, A.; Kohlmeyer, A.; Floreano, L.; Scandolo, S.; Morgante, A.; Klein, M. L. *et al.* X-ray Diffraction and Computation Yield the Structure of Alkanethiols on Gold(111). *Science* **2008**, *321*, 943–946

(6) Jiang, D. The Expanding Universe of Thiolated Gold Nanoclusters and Beyond. *Nanoscale* **2013**, *5*, 7149–7160.

(7) Häkkinen, H. The Gold–Sulfur Interface at the Nanoscale. *Nat. Chem.* **2012**, *4*, 443–455.

(8) Pensa, E.; Cortéz, E.; Corthey, G.; Carro, P.; Vericat, C.; Fonticelli, M. H.; Benitez, G.; Rubert, A. A.; Salvarezza, R. C. The Chemistry of the Sufur–Gold Interface: In Search of a Unified Model. *Acc. Chem. Res.* **2012**, *45*, 1183–1192.

(9) Jadzinsky, P. D.; Calero, G.; Ackerson, C. J.; Bushnell, D. A.; Kornberg, R. D. Structure of a Thiol Monolayer-Protected Gold Nanoparticle at 1.1 Å Resolution. *Science* **2007**, *318*, 430–433.

(10) Qian, H.; Eckenhoff, W. T.; Zhu, Y.; Pintauer, T.; Jin, R. Total Structure Determination of Thiolate-Protected Au_{38} Nanoparticles. *J. Am. Chem. Soc.* **2010**, *132*, 8280–8281.

(11) Zeng, C.; Qian, H.; Li, T.; Li, G.; Rosi, N. L.; Yoon, B.; Barnett, R. N.; Whetten, R. L.; Landman, U.; Jin, R. Total Structure and Electronic Properties of the Gold Nanocrystal $Au_{36}(SR)_{24}$. *Angew. Chem., Int. Ed.* **2012**, *51*, 13114–13118.

(12) Zeng, C.; Li, T.; Das, A.; Rosi, N. L.; Jin, R. Chiral Structure of Thiolate-Protected 28-Gold-Atom Nanocluster Determined by X–ray Crystallography. *J. Am. Chem. Soc.* **2013**, *135*, 10011–10013.

(13) Heaven, M. W.; Dass, A.; White, P. S.; Holt, K. M.; Murray, R. W. Crystal Structure of the Gold Nanoparticle $[N(C_8H_{17})_4][Au_{25}(SCH_2CH_2Ph)_{18}]$. *J. Am. Chem. Soc.* **2008**, *130*, 3754–3755.

(14) Zhu, M.; Aikens, C. M.; Hollander, F. J.; Schatz, G. C.; Jin, R. Correlating the Crystal Structure of a Thiol-Protected Au_{25} Cluster and Optical Properties. *J. Am. Chem. Soc.* **2008**, *130*, 5883–5885.

(15) Zhu, M.; Eckenhoff, W. T.; Pintauer, T.; Jin, R. Conversion of Anionic $[Au_{25}(SCH_2CH_2Ph)_{18}]^-$ Cluster to Charge Neutral Cluster *via* Air Oxidation. *J. Phys. Chem. C* **2008**, *112*, 14221–14224.

(16) Das, A.; Li, T.; Nobusada, K.; Zeng, C.; Rosi, N. L.; Jin, R. Nonsuperatomic $[Au_{23}(SC_6H_{11})_{16}]^-$ Nanocluster Featuring Bipyramidal Au_{15} Kernel and Trimeric $Au_3(SR)_4$ Motif. *J. Am. Chem. Soc.* **2013**, *135*, 18264–18267.

(17) Dass, A.; Stevenson, A.; Dubay, G. R.; Tracy, J. B.; Murray, R. W. Nanoparticle MALDI-TOF Mass Spectrometry without Fragmentation: $Au_{25}(SCH_2CH_2Ph)_{18}$ and Mixed Monolayer $Au_{25}(SCH_2CH_2Ph)_{18-x}(L)_x$. *J. Am. Chem. Soc.* **2008**, *130*, 5940–5946.

(18) Negishi, Y.; Nobusada, K.; Tsukuda, T. Glutathione-Protected Gold Clusters Revisited: Bridging the Gap between Gold(I)– Thiolate Complexes and Thiolate-Protected Gold Nanocrystals. *J. Am. Chem. Soc.* **2005**, *127*, 5261–5270.

(19) Tracy, J. B.; Kalyuzhny, G.; Crowe, M. C.; Balasubramanian, R.; Choi, J.-P.; Murray, R. W. Poly(ethylene glycol) Ligands for High-Resolution Nanoparticle Mass Spectrometry. *J. Am. Chem. Soc.* **2007**, *129*, 6706–6707.

(20) Parker, J. F.; Fields-Zinna, C. A.; Murray, R. W. The Story of a Monodisperse Gold Nanoparticle: $Au_{25}L_{18}$. *Acc. Chem. Res.* **2010**, *43*, 1289–1296.

(21) Tlahuice-Flores, A.; Santiago, U.; Bahena, D.; Vinogradova, E.; Conroy, C. V.; Ahuja, T.; Bach, S. B. H.; Ponce, A.; Wang, G.; José-Yacamán, M.; Whetten, R. L. Structure of the Thiolated Au_{130} Cluster. *J. Phys. Chem. A* **2013**, *117*, 10470–10476.

(22) Tang, Z.; Robinson, D. A.; Bokossa, N.; Xu, B.; Wang, S.; Wang, G. Mixed Dithiolate Durene-DT and Monothiolate Phenylethanethiolate Protected Au_{130} Nanoparticles with Discrete Core and Core-Ligand Energy States. *J. Am. Chem. Soc.* **2011**, *133*, 16037–16044.

(23) Negishi, Y.; Sakamoto, C.; Tatsuya, O.; Tsukuda, T. Synthesis and the Origin of the Stability of Thiolate–Protected Au_{130} and Au_{187} Clusters. *J. Phys. Chem. Lett.* **2012**, *3*, 1624–1628.

(24) Bahena, D.; Bhattarai, N.; Santiago, U.; Tlahuice, A.; Ponce, A.; Bach, S. B. H.; Yoon, B.; Whetten, R. L.; Landman, U.; José-Yacamán, M. STEM Electron Diffraction and High-Resolution Images Used in the Determination of the Crystal Structure of the $Au_{144}(SR)_{60}$ Cluster. *J. Phys. Chem. Lett*. **2013**, *4*, 975–981.

(25) Koivisto, J.; Salorinne, K.; Mustalahti, S.; Lahtinen, T.; Malola, S.; Häkkinen, H.; Pettersson, M. Vibrational Perturbations and Ligand–Layer Coupling in a Single Crystal of $Au_{144}(SC_2H_4Ph)_{60}$ Nanocluster *J. Phys. Chem. Lett.* **2014**, *5*, 387–392.

(26) Lee, D.; Donkers, R. L.; Wang, G.; Harper, A. S.; Murray, R. W. Electrochemistry and Optical Absorbance and Luminescence of Molecule-like Au_{38} Nanoparticles. *J. Am. Chem. Soc.* **2004**, *126*, 6193–6199.

(27) Antonello, S.; Perera, N. V.; Ruzzi, M.; Gascón, J. A.; Maran, F. Interplay of Charge State, Lability, and Magnetism in the Molecule-like $Au_{25}(SR)_{18}$ Cluster. *J. Am. Chem. Soc.* **2013**, *135*, 15585–15594.

(28) Antonello, S.; Holm, A. H.; Instuli, E.; Maran, F. Molecular Electron-Transfer Properties of Au_{38} Clusters. *J. Am. Chem. Soc.* **2007**, *129*, 9836–9837.

(29) Zhu, M.; Aikens, C. M.; Hendrich, M. P.; Gupta, R.; Qian, H.; Schatz, G. C.; Jin, R. Reversible Switching of Magnetism in Thiolate-Protected Au_{25} Superatoms. *J. Am. Chem. Soc.* **2009**, *131*, 2490–2492.

(30) Venzo, A.; Antonello, S.; Gascón, J. A.; Guryanov, I.; Leapman, R. D.; Perera, N. V.; Sousa, A.; Zamuner, M.; Zanella, A.; Maran, F. Effect of the Charge State (z = –1, 0, **+**1) on the Nuclear Magnetic Resonance of Monodisperse $Au_{25}[S(CH_2)_2Ph]_{18}^{z}$ Clusters. *Anal. Chem.* **2011**, *83*, 6355–6362.

(31) Antonello, S.; Arrigoni, G.; Dainese, T.; De Nardi, M.; Parisio, G.; Perotti, L.; René, A.; Venzo, A.; Maran, F. Electron Transfer through 3D Monolayers on Au_{25} Clusters. *ACS Nano* **2014**, *8*, 2788–2795.

(32) Weil, J. A.; Bolton, R. J. Double-Resonance Techniques. *Electron Paramagnetic Resonance: Elementary Theory and Practical Applications,* 2nd Edition; Wiley-Interscience: Hoboken, New Jersey, 2007; pp 385-413.

(33) Davies, E. R. A New Pulse ENDOR Technique. *Phys. Lett.* **1974**, *47A*, 1–2.

(34) Van Willigen, H.; Van Rens, J.G.M. Quadrupole Effects on the Hyperfine Structure of a Gold(II) Complex. *Chem. Phys. Lett.* **1968**, *2*, 283-285.

(35) Briant, C. E.; Theobald, B. R. C.; White, J. W.; Bell, L. K.; Mingos, D. M. P.; Welch, A. J. Synthesis and X-ray Structural Characterization of the Centred Icosahedral Gold Cluster Compound $[Au_{13}(PMe_2Ph)_{10}Cl_2](PF_6)_3$; the Realization of a Theoretical Prediction. *Chem. Soc., Chem. Commun.* **1981**, 201–202.

(36) Shichibu, Y.; Konishi, K. HCl-Induced Nuclearity Convergence in Diphosphine-Protected Ultrasmall Gold Clusters: A Novel Synthetic Route to "Magic-Number" Au_{13} Clusters. *Small* **2010**, *10*, 1216–1220.

(37) Parker, J. F.; Choi, J.-P.; Wang, W.; Murray, R. W. Electron Self-Exchange Dynamics of the Nanoparticle Couple $[Au_{25}(SC_2Ph)18]^{0/1-}$ by Nuclear Magnetic Resonance Line-Broadening. *J. Phys. Chem. C* **2008**, *112*, 13976–13981.

(38) Tlahuice-Flores, A.; Whetten, R. L.; Jose-Yacaman, M. Ligand Effects on the Structure and the Electronic Optical Properties of Anionic $Au_{25}(SR)_{18}$ Clusters. *J Phys. Chem. C* **2013**, *117*, 20867–20875.

(39) McCoy, R. S.; Choi, S.; Collins, G.; Ackerson, B. J., Ackerson, C. J. Superatom Paramagnetism Enables Gold Nanocluster Heating in Applied Radiofrequency Fields. *ACS Nano* **2013**, *7*, 2610–2616.

(40) CrysAlisPro, version 1.171.36.28; Agilent Technologies Ltd: Yarnton, England, 2013.

(41) Dolomanov, O. V.; Bourhis, L. J.; Gildea, R. J.; Howard, J. A. K.; Puschmann, H. OLEX2: a Complete Structure Solution, Refinement and Analysis Program. *J. Appl. Cryst.* **2009**, *42*, 339–341.

(42) Sheldrick, G. M. A Short History of SHELX. *Acta Crystallogr.* **2008**, *A64*, 112–122.

(43) Clark, R. C.; Reid, J. S. The Analytical Calculation of Absorption in Multifaceted Crystals. *Acta Crystallogr*. **1995**, *A51*, 887–897.

(44) Stoll, S.; Schweiger, A. EasySpin, a Comprehensive Software Package for Spectral Simulation and Analysis in EPR. *J. Magn. Reson.* **2006**, *178*, 42–55.

(45) Ahlrichs, R.; Bär, M.; Häser, M.; Horn, H.; Kölmel, C. Electronic Structure Calculations on Workstation Computers: The Program System Turbomole. *Chem. Phys. Lett.* **1989**, *162*, 165–169.
(46) Neese, F. The ORCA Program System. *Wiley Interdiscip. Rev. Comput. Mol. Sci.* **2012**, *2*, 73–78.
(47) van Wüllen, C. Molecular Density Functional Calculations in the Regular Relativistic Approximation: Method, Application to Coinage Metal Diatomics, Hydrides, Fluorides and Chlorides, and Comparison with First-Order Relativistic Calculations. *J. Chem. Phys.* **1998**, *109*, 392–399.
(48) Pantazis, D. A.; Chen, X.-Y.; Landis, C. R.; Neese, F. All-Electron Scalar Relativistic Basis Sets for Third-Row Transition Metal Atoms. *J. Chem. Theory Comput.* **2008**, *4*, 908–919.

3.7 Acknowledgements

Besides acknowledging the contribution from other group members, TD is thankful to José A. Gascón and Neranjan V. Perera (University of Connecticut) for the DFT calculations, Kari Rissanen and Fangfang Pan (University of Jyväskylä) for the X-ray crystallographic study, and Marco Ruzzi and Alfonso Zoleo for the ENDOR analysis.

Chapter 4: Electron Transfer through 3D Monolayers on Au_{25} Clusters

4.1 Abstract

This Chapter describes findings that have been published: Antonello, S.; Arrigoni, G.; Dainese, T.; De Nardi, M.; Parisio, G.; Perotti, L.; René, A.; Venzo, A.; Maran, F. Electron Transfer through 3D Monolayers on Au_{25} Clusters. *ACS Nano* **2014**, *8*, 2788–2795.

The monolayer protecting small gold nanoparticles is generally represented as the 3D equivalent of 2D SAMs on extended gold surfaces. However, despite the growing relevance of MPCs in important applied areas, such as catalysis and nanomedicine, our knowledge of the structure of 3D SAMs in solution is still extremely limited. We prepared a large series of monodisperse $Au_{25}(SC_nH_{2n+1})_{18}$ clusters (*n* = 2, 4, 6, 8, 10, 12, 14, 16, 18) and studied how electrons tunnel through these monolayers. Electron transfer results, nicely supported by ^1H NMR spectroscopy, IR absorption spectroscopy, and molecular dynamics results, show that there is a critical ligand length marking the transition between short ligands, which form a quite fluid monolayer structure, and longer alkyl chains, which self-organize into bundles. At variance with the truly protecting 2D SAMs, efficient electronic communication of the Au_{25} core with the outer environment is thus possible even for long alkyl chains. These conclusions provide a different picture of how an ultrasmall gold core talks with the environment through/with its protecting but not-so-shielding monolayer.

4.2 Introduction

By far, $Au_{25}(SR)_{18}$ is the most representative case of a stable MPC possessing a metal core sufficiently small (1 nm) to cause the system display a distinct molecule-like behavior.[1] MPC monolayers are generally depicted as capping shields protecting the core from aggregation and a way to display functional groups for possible applications.[2-5] These monolayers are, in fact, complex 3D nanosystems. The structure of $Au_{25}(SC_2H_4Ph)_{18}$ shows a 13-atom icosahedral inner Au core surrounded by 6 $Au_2(SC_2H_4Ph)_3$ staple-like semirings.[6-8] Staple-like bonding motifs are also present in larger clusters.[9-12] Interestingly, similar thiolate-Au features are also found in SAMs on extended gold surfaces

(2D SAMs).[13] That the same Au-S binding motifs can be found in both 2D and 3D SAMs points to very similar interactions and mutual stabilization of surface Au atoms and thiolated species.[14,15] However, whereas in 2D SAMs molecular adsorbates primarily interact *via* interchain van der Waals forces allowing formation of regular domains of parallel molecules,[16] it is not clear if similar interactions are equally important or even present at all in the monolayers of molecule-like MPCs. For example, whereas 2D SAMs are sufficiently compact to hamper penetration of molecular probes (so-called blocking effect: reduction or oxidation of molecular probes present in solution is hampered),[17] electrochemistry provided evidence that MPC monolayers allow some solvent/electrolyte penetration.[18,19] The possible structure of 3D SAMs has been discussed on the basis of earlier seminal IR-absorption, solid-state NMR, and molecular dynamics (MD) studies of larger MPCs.[20-24] Concerning molecule-like MPCs, however, and despite their interest as catalytic systems in redox processes, the monolayer structure in solution is still undefined. Because of its well-defined composition[25,26] and unique electrochemical, optical and magnetic features,[27-29] the atomically monodisperse $Au_{25}(SR)_{18}$ cluster provides an ideal benchmark for addressing this issue through the study of reactions occurring at, in, or through a 3D SAM or, to better say, the complex interfacial region between the gold core and the surrounding medium.

A reaction particularly appealing to assess the structure of MPCs' monolayers is electron transfer. ET is an extremely important reaction ubiquitous to a variety of biochemical and chemical areas,[30,31] including redox catalysis with ultrasmall Au nanoparticles.[3,5,19,32] Our understanding of the rate and mechanisms of long-range ETs through molecular bridges strongly relies on the outcome of studies carried out with 2D SAMs.[17] These and related studies allowed establishing distance-dependence descriptors for a number of molecular bridges.[30,33,34] According to the superexchange mechanism,[31,34] the ET rate constant (k_{ET}) depends exponentially on the donor-acceptor distance (r_{DA}) *via* eq 1,

(1) $$k_{ET} = k_{ET}^{0} \exp(-\beta r_{DA})$$

where the parameter β describes the falloff of the electron tunneling rate through the specific bridge and k_{ET}^{0} is the ET rate constant at contact distance. For an alkyl chain in its all-*trans* conformation, which is the most efficient conformation for mediating ETs,[34] the distance "ruler" is β = 0.8-1.0 $Å^{-1}$.[30,33,34] This important

insight comes from studies of well-organized 2D SAMs,[17] metal-bridge-metal junctions,[33] and rigid donor-bridge-acceptor systems.[34] Can we now reverse the concept and use ET rulers as probes of the solution-phase structure of the otherwise elusive 3D monolayers of molecule-like MPCs such as $Au_{25}(SR)_{18}$? To which extent can the general picture valid for 2D SAMs be extended to the monolayer of 3D SAMs such as those formed on Au_{25} clusters?

Here we address these issues by studying the kinetics of electron tunneling through the monolayer of $Au_{25}(SR)_{18}$ clusters. By using a large series of alkanethiols, ranging from the shortest (C2) to the longest (C18) ligand ever used for such clusters, we prepared a large, homogeneous family of monodisperse $Au_{25}(SC_nH_{2n+1})_{18}$ clusters, with n = 2, 4, 6, 8, 10, 12, 14, 16, 18. Our study provides the first analysis of the distance effect on the ET rate through 3D monolayers assembled on a gold cluster. Unexpected heterogeneous ET rates, together with converging results obtained by solution-phase ^{1}H NMR spectroscopy, IR absorption spectroscopy and MD calculations, provide compelling evidence that while for the shorter ligands the monolayer can be described by a fluid structure of folded chains, longer alkyl chains self-organize into bundles. At variance with 2D SAMs, which provide efficient shields of the underlying gold surface, efficient electronic communication of the Au_{25} core with the outer environment is thus possible even for long alkyl chains.

4.3 Results and Discussion

4.3.1 Synthesis of $Au_{25}(SC_nH_{2n+1})_{18}$

We prepared a series of $Au_{25}(SC_nH_{2n+1})_{18}$ clusters in which n = 2, 4, 6, 8, 10, 12, 14, 16, 18. The syntheses of the nice clusters were carried out in tetrahydrofuran according to similar protocols to that described for $Au_{25}(SC_2H_4Ph)_{18}$.[28] Briefly, a solution of tetrachloroauric acid in the presence of 1.1 equiv of tetraoctylammonium bromide is allowed to react with the appropriate alkanethiol until the initially red solution becomes colorless, which is indicative of quantitative reduction of Au(III) to form reactive Au(I)-thiolate species. Addition of an aqueous solution of sodium borohydride causes rapid reduction to Au(0), with formation of a black solution. After typically 3 days under stirring, the clusters are separated from the reaction solution. As a final step, the Au_{25} clusters, which originally form in the anionic state,[25,26] are quantitatively oxidized to their stable neutral form; we found that silica-gel column chromatography performs particularly well to obtain $Au_{25}(SC_nH_{2n+1})_{18}^0$ in a very pure form. We will now

denote the clusters simply as $Au_{25}(SC\mathit{n})_{18}$, where *n* is the number of carbon atoms.

A typical synthesis is here exemplified for the specific case of $Au_{25}(SC\mathit{10})_{18}$. To a red THF solution (50 ml) of $HAuCl_4 \cdot 3H_2O$ (500 mg, 1.27 mmol) and tetra-*n*-octylammonium bromide (779 mg, 1.425 mmol), 6 equiv of 1-decanethiol (1.61 ml, 7.61 mmol) were added dropwise, under stirring, at room temperature. After 60 min stirring, the solution becomes colorless. Under fast stirring conditions, an ice-cold, freshly prepared solution of $NaBH_4$ (480 g, 12.7 mmol) in 10 ml of water was rapidly added, and the resulting black mixture, indicative of MPC formation, was left to age. The outcome of the reaction was periodically monitored by UV-vis absorption spectroscopy. After ca. 3 days the reaction mixture was filtered on paper and THF was removed, leaving a red-brownish oil covered by an aqueous phase. The crude product was dissolved in toluene and the solution washed with water (4 x 25 ml). The toluene solution was concentrated, left to age for one night at low temperature, filtered to remove residual white polymer-like material, and the solvent evaporated. The resulting solid, $\mathit{n}\text{-}Oct_4N^+$ $Au_{25}(SC\mathit{10})_{18}^-$, was dissolved in DCM and purified by silica-gel column chromatography under aerobic conditions. The so-collected solid was tetra-*n*-octylammonium-free $Au_{25}(SC\mathit{10})_{18}^0$, which was then stored at 4 °C in the dark.

4.3.2 UV-vis Absorption Spectroscopy

The UV-vis spectra of $Au_{25}(SC\mathit{n})_{18}^0$ (Figure 1) show the expected features of monolayer protected Au_{25} clusters in their 0 charge state,[8,28] such as the presence of a peak at 400 nm, a shoulder at ca. 445 nm, and a broad peak at 690 nm. We note that the features corresponding to the -1 or the +1 charge state, the latter possibly obtained by further oxidation of $Au_{25}(SC\mathit{n})_{18}^0$, are distinctly different.[28] For $n = 2 – 14$, the average molar extinction coefficient at 400 nm is 5.5×10^4 M^{-1} cm^{-1}, that is, virtually the same as that of $Au_{25}(SC_2H_4Ph)_{18}$, 5.38×10^4 M^{-1} cm^{-1}, which nicely points to the optical behavior of $Au_{25}(SR)_{18}$ clusters (SR = generic thiolated ligand) as virtually only determined by the structure of the gold core. We found that for the longer ligands ($n = 14 – 18$), the peak at 400 nm increases while the band at 690 nm becomes less pronounced. This behavior is attributed to aggregation phenomena in solution and, as a matter of fact, when these solutions are sonicated (ultrasounds), the spectra become much more similar to those of the other clusters: the spectra of Figure 1 ($n = 14 – 18$) were

obtained after sonication. Benzene solubilizes the C14, C16 and C18 MPCs in an amount of time (~3, 10, and 15 min, respectively) shorter than any other solvent tested.

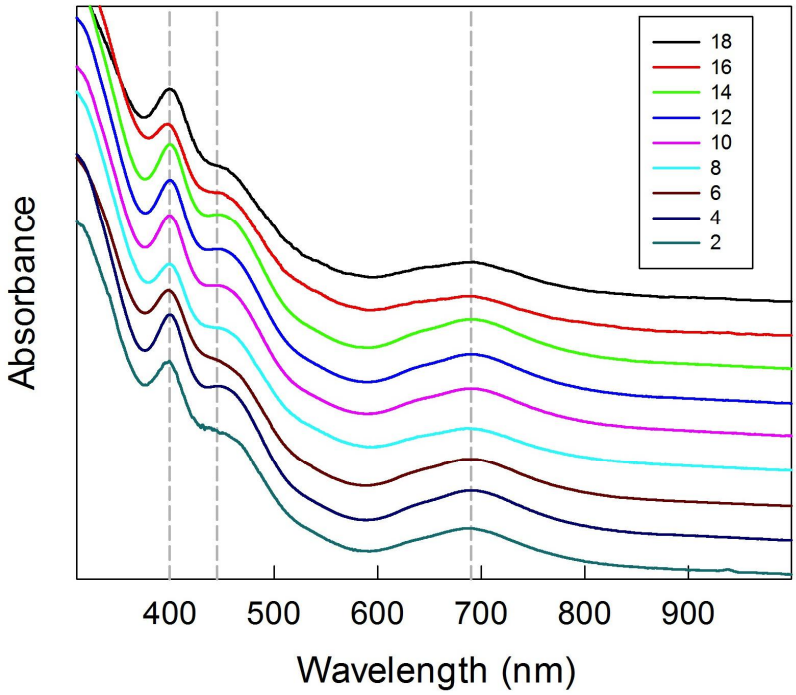

Figure 1. Comparison of the UV-vis absorption spectra of $Au_{25}(SCn)_{18}^{0}$. The measurements were carried out in dichloromethane (C2 – C14) or benzene (C16, C18) at 25 °C. For clarity, the spectra have been vertically shifted. Dashed lines mark the main spectral features.

4.3.3 MALDI-TOF Mass Spectrometry

The composition and monodispersity of each $Au_{25}(SCn)_{18}$ cluster were assessed by matrix-assisted laser desorption ionization time-of-flight (MALDI-TOF) mass spectrometry, a particularly effective technique for this class of clusters.[35] Figure 2 shows that each spectrum displays the peak corresponding to the parent cluster, and some evidence of the main fragmentation pattern. Although fragmentation can be minimized to virtually nothing by decreasing the intensity of the laser power as much as possible, it is nonetheless useful because close inspection of the spectra obtained with a slightly larger laser energy reveals that the clusters undergo the same fragmentation pattern already noted for $Au_{25}(SC_2H_4Ph)_{18}$, that is, stepwise loss of AuSR fragments to form $Au_{21}(SR)_{14}$. The parent peaks have masses perfectly matching the calculated molecular weights. Noteworthy, this is also true for the C14, C16 and C18 MPCs, despite

their pronounced sonication-dependent UV-vis behavior. Overall, MALDI-TOF thus provides compelling evidence that all $Au_{25}(SCn)_{18}$ investigated share the same formula and features.

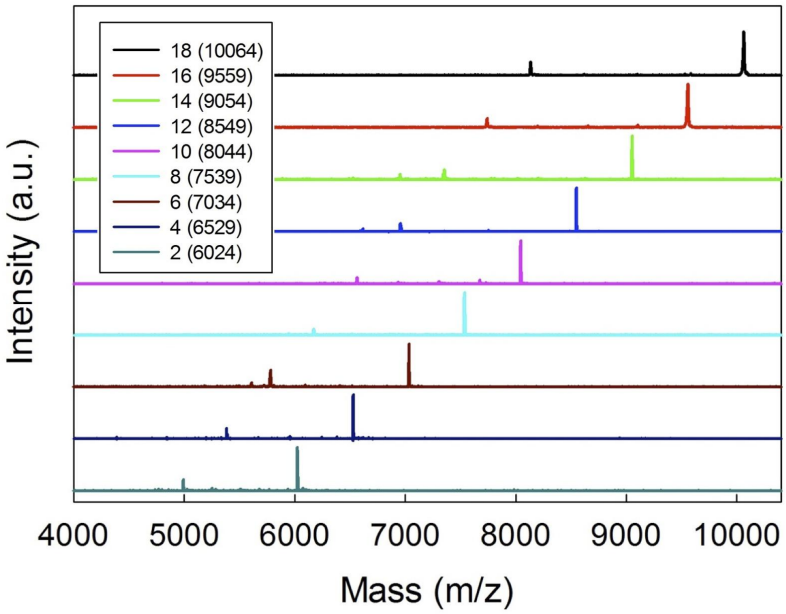

Figure 2 MALDI-TOF mass spectra of $Au_{25}(SCn)_{18}^{0}$. For clarity, the spectra have been vertically shifted. The legend shows the MPCs' molecular weights.

4.3.4 NMR Spectroscopy

The ^{1}H NMR behavior of the ligands capping Au_{25} clusters is very sensitive to the specific ligand type.[1,28] The 18 ligands split into a group of 6 outer and 12 inner ligands: we here define as outer the ligands in which S is bound to two stellated Au atoms and as inner those in which one of the two S-Au bonds involves the 13-atom icosahedral Au core (Figure 3A). The ^{1}H NMR measurements were carried out in benzene-d_6. The spectra revealed the same general features of $Au_{25}(SC_2H_4Ph)_{18}$, for which we could solve the details of each resonance of the two ligand groups as a function of the core charge state.[28] $Au_{25}(SCn)_{18}^{0}$ is paramagnetic: for the 12 inner ligands, the resonance of the methylene group closer to the sulfur atom, $(\alpha\text{-}CH_2)_{in}$, is particularly sensitive to the paramagnetic character of the cluster, and is found at very large chemical shift (δ) values. This resonance is barely observable at 25 °C but develops into a nicely detectable peak at higher temperatures (for example, see Figure 4): for n = 4 – 18, $\delta = 22.5 \pm 0.2$ at 65 °C. The other features of the ^{1}H NMR spectra are also very similar. All resonances, which were assigned by analysis of homo- and

heteronuclear 2D correlation spectra, occur at δ values that reflect the specific type of ligand (with integrals in a 2:1 ratio, in agreement with 12 inner *vs* 6 outer ligands) and the position of methylene with respect to sulfur (α, β, γ, and so on).

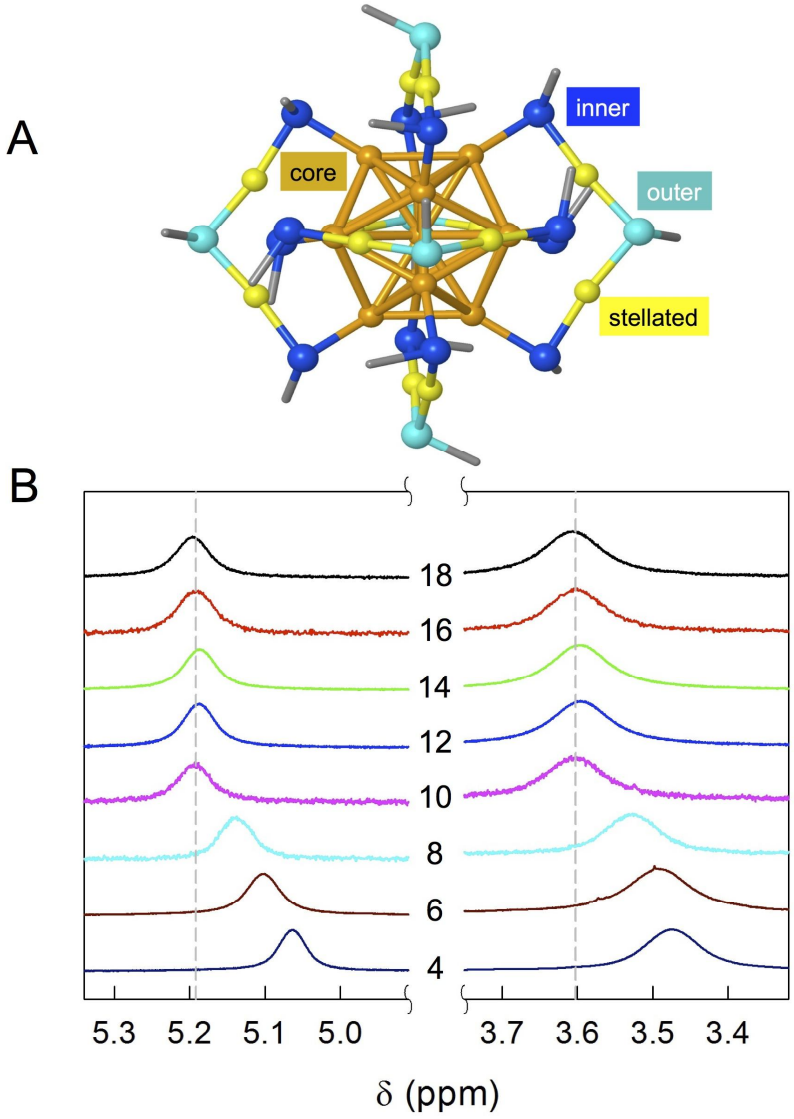

Figure 3. (A) Main structural features of $Au_{25}(SR)_{18}^{0}$ (coordinates from ref. 8): core Au atoms (dark yellow), stellated Au atoms (light yellow), inner-ligand S atoms (blue), and outer-ligand S atoms (light blue). (B) ^{1}H NMR spectra of monodisperse $Au_{25}(SC\mathit{n})_{18}^{0}$ in benzene-d_6 at 25 °C: the spectral zones show the $(\alpha\text{-}CH_2)_{out}$ (left) and $(\beta\text{-}CH_2)_{in}$ (right) resonances. Dashed lines mark the average chemical shifts calculated for C10 – C18.

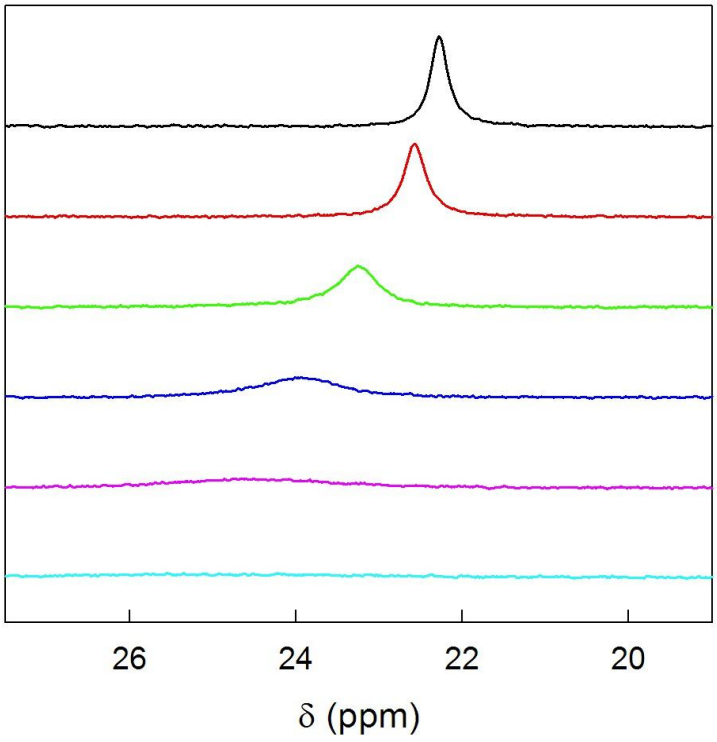

Figure 4. ^{1}H NMR spectra of monodisperse $Au_{25}(SC\mathit{18})_{18}$ in benzene-d_6 as a function of temperature. The spectra show the $(\alpha\text{-}CH_2)_{in}$ zone. Bottom to top: 298, 308, 318, 328, 338, and 343 K.

The peaks of the methylene groups closer to the Au core occur at: $(\alpha\text{-}CH_2)_{out}$, 5.06 – 5.20 ppm; $(\beta\text{-}CH_2)_{in}$, 3.48 – 3.61 ppm; $(\gamma\text{-}CH_2)_{in}$, 2.56 – 2.67 ppm; $(\delta\text{-}CH_2)_{in}$, 1.96 – 2.10 ppm; $(\beta\text{-}CH_2)_{out}$, 1.74 – 1.92 ppm; $(\gamma\text{-}CH_2)_{out}$, 1.57 – 1.71 ppm. Figure 3B shows the spectral regions pertaining to $(\alpha\text{-}CH_2)_{out}$ and $(\beta\text{-}CH_2)_{in}$ (for the full spectra, see Figure 5). Comparison of the spectra shows the interesting pattern that the $(\alpha\text{-}CH_2)_{out}$ and $(\beta\text{-}CH_2)_{in}$ resonances do not appreciably change as one goes from n = 18 to n = 10, but when the chain becomes shorter, δ distinctly decreases (upfield shift). The other methylene resonances display a very similar trend, once again with C10 as the turning point at which δ starts shifting to lower values. These results indicate that for C10 and longer chains there is no significant difference in terms of the chemical environment experienced by the above methylene groups. A plausible hypothesis is thus that the longer ligands interact with each other in a way that is virtually unaffected by further elongation of the chain. Shorter chains, on the other hand, have more conformational freedom and are thus more extensively surrounded by

benzene molecules, a solvent known to cause resonances to undergo an upfield shift.[36]

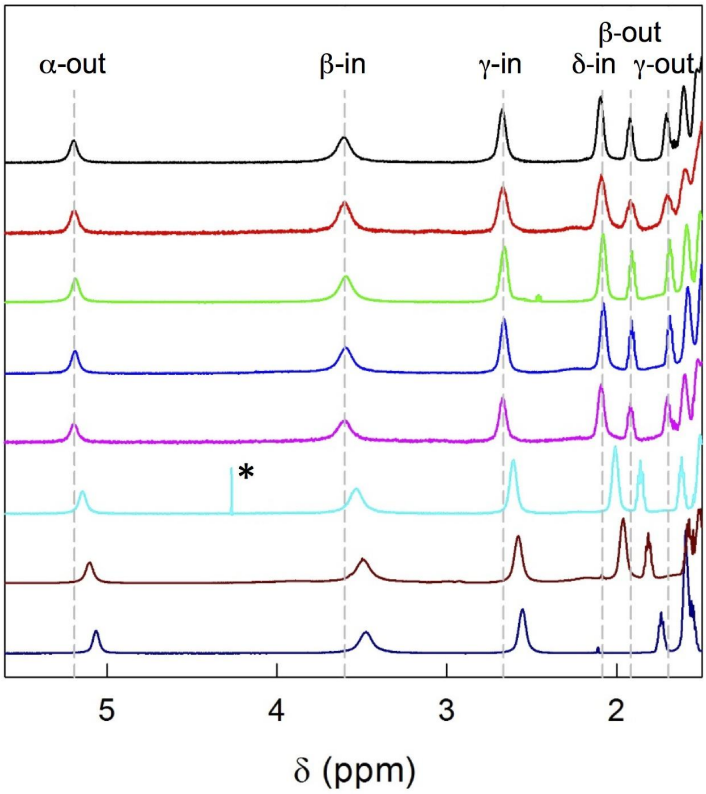

Figure 5. ^{1}H NMR spectra of monodisperse $Au_{25}(SC\mathit{n})_{18}$ in benzene-d_6 at 298 K. Bottom to top, n = 4, 6, 8, 10, 12, 14, 16, and 18. Dashed lines mark the average chemical shifts calculated for the pertinent resonances from the spectra of C10 – C18. The star symbol marks a peak due to a solvent impurity (DCM).

4.3.5 IR Absorption Spectroscopy

IR absorption spectroscopy has proved to be a valuable tool for studying the structure of alkanethiolate SAMs on flat gold.[16] Studies with alkanethiolate-protected Au nanoparticles larger than Au_{25} MPCs[20-22] showed that compared to conventional 2D SAMs the average surface curvature of MPCs is such to make the monolayer periphery relatively mobile. In this framework, the $Au_{25}(SC\mathit{n})_{18}$ family provides a new situation for both the smaller (and totally controlled) core dimension and the presence of different binding sites (not facets, as for larger clusters) for the thiolates. For both symmetric (d+) and antisymmetric (d-) CH_2 stretching modes, which are particularly diagnostic for obtaining information about the conformation of alkyl chains, we found that as n increases up to 10 the frequencies undergo a progressive red shift (Figures 6-8) similar to that observed

for the free alkanethiols. For longer ligands, however, the frequency initially increases and then drops to values similar to those measured for 2D SAMs[37] and larger MPCs,[38] which are typical of extended all *trans* conformation. Overall, the IR results thus concur with the NMR evidence in indicating a structural transition as one goes from shorter to longer ligands.

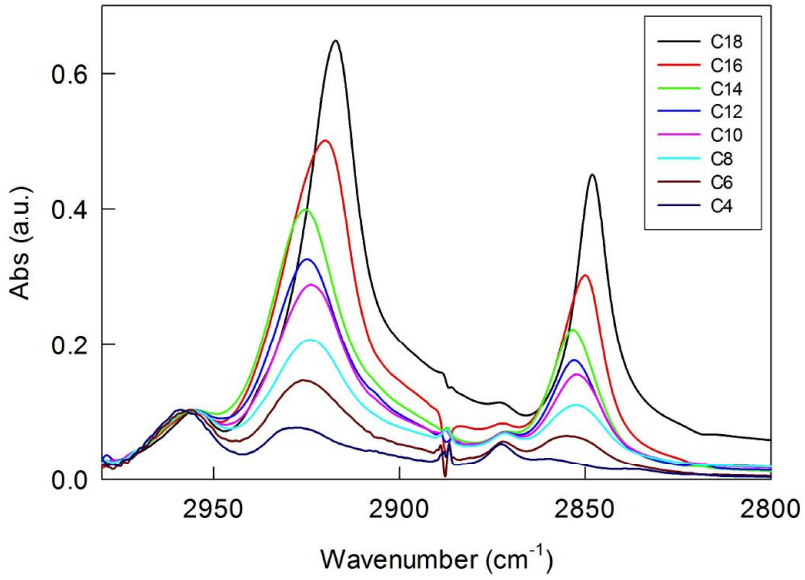

Figure 6. IR absorption spectroscopy spectra of $Au_{25}(SC\mathit{n})_{18}$ in benzene. The spectra have been normalized relative to the methyl CH stretching modes.

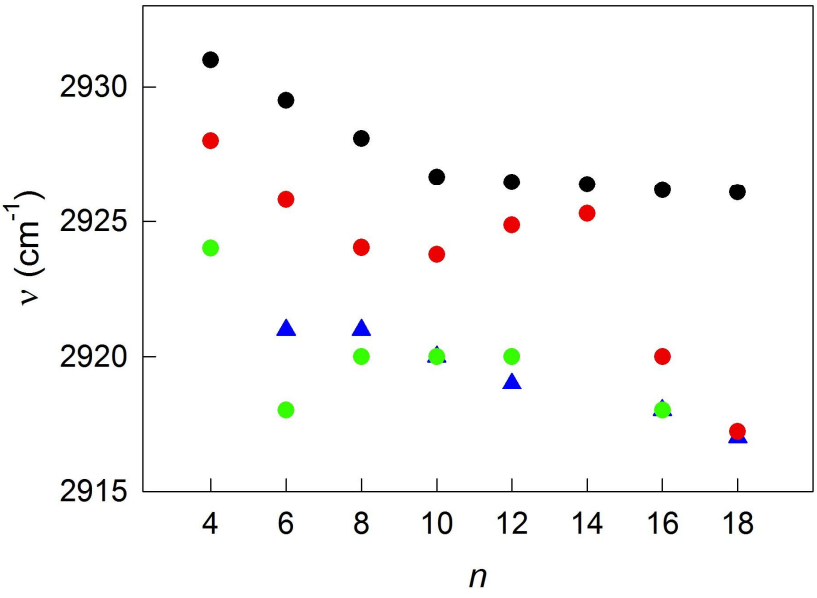

Figure 7. Dependence of the IR antisymmetric methylene stretching (*d*-) on *n* for $Au_{25}(SC\mathit{n})_{18}$ in benzene (λ). The trends of HSC_nH_{2n+1} (λ; benzene, this work), 2D SAMs (σ),[39] and 2.4-2.8 nm MPCs (λ; KBr)[40] are also shown.

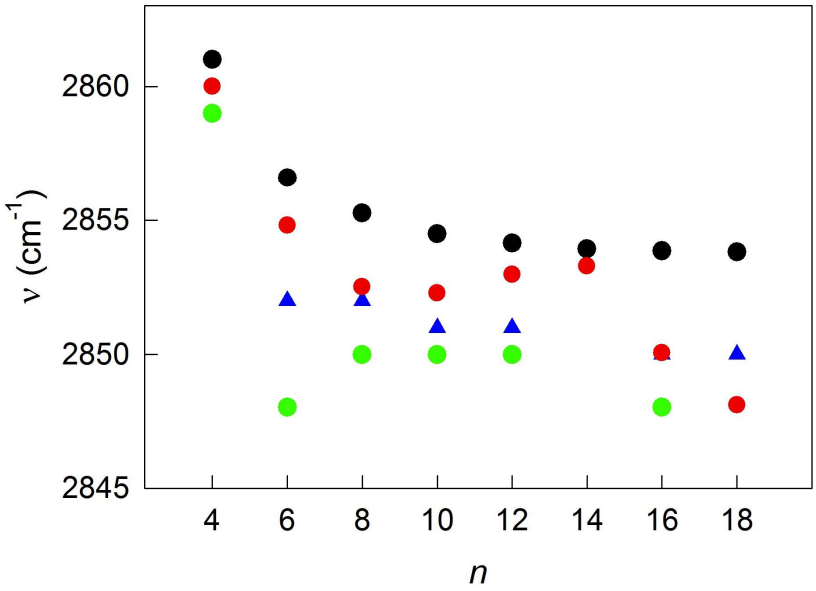

Figure 8. Dependence of the IR symmetric methylene stretching (*d*+) on *n* for $Au_{25}(SCn)_{18}$ in benzene (λ). The trends of HSC_nH_{2n+1} (λ; benzene, this work), 2D SAMs (σ),[39] and 2.4-2.8 nm MPCs (λ; KBr)[40] are also shown.

4.3.6 Heterogeneous Electron Transfer

The electrochemical behavior of $Au_{25}(SCn)_{18}^{0}$ was studied by CV and DPV in DCM/0.1 M TBAH, at 25 °C. Figure 9 illustrates the CV pattern observed with one of the clusters. The general electrochemical pattern is common to all Au_{25} clusters and shows two main reversible peaks associated with the either the oxidation (peak O1) or reduction (peak R1) of $Au_{25}(SCn)_{18}^{0}$. Because the latter is a radical, the two processes correspond to formation of a cation and an anion, respectively. All three species are stable: $Au_{25}(SCn)_{18}^{0}$ is indefinitely stable, $Au_{25}(SCn)_{18}^{-}$ is stable under anaerobic conditions, and $Au_{25}(SCn)_{18}^{+}$ is stable at least for some hours.

Further oxidation and reduction processes corresponding to formation of higher positive or negative charge states are also observed, as illustrated for the most important peaks by the series of DPVs shown in Figure 10. Peak O2, which is related to formation of the dication, is partially reversible at slow scan rate (*v*) values. The third peak (O3) is irreversible. In the negative-going scan, the irreversible peak R2 corresponds to initial formation of the dianion, followed by a sequence of dissociative ET steps, as already discussed for $Au_{25}(SC_2H_4Ph)_{18}$.[19,29] R2 is quite negative and, for the longest alkyl chains (n > 12), not easily detectable because of merging with further redox processes (Figure 10).

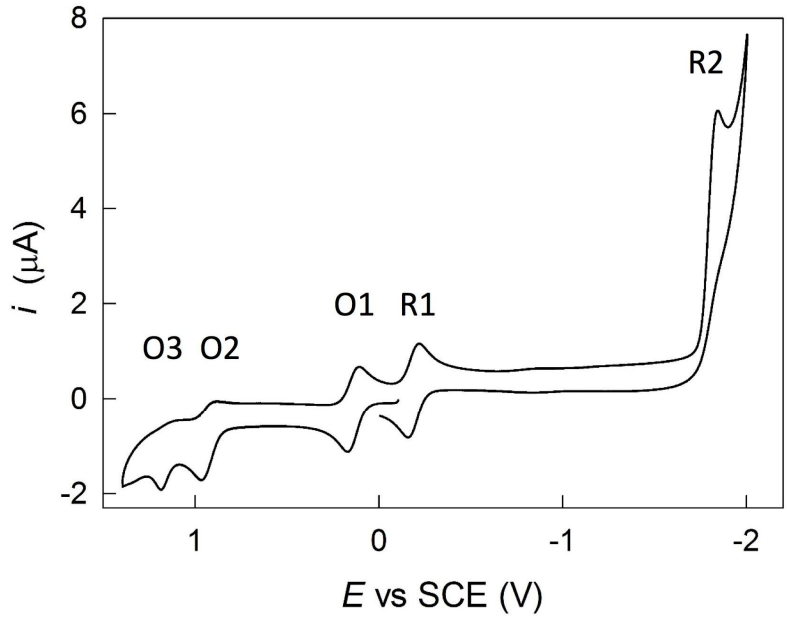

Figure 9. CV of 0.51 mM $Au_{25}(C4)_{18}$ in DCM/ 0.1 M TBAH at v = 0.1 V s^{-1}. Glassy carbon electrode, 25 °C.

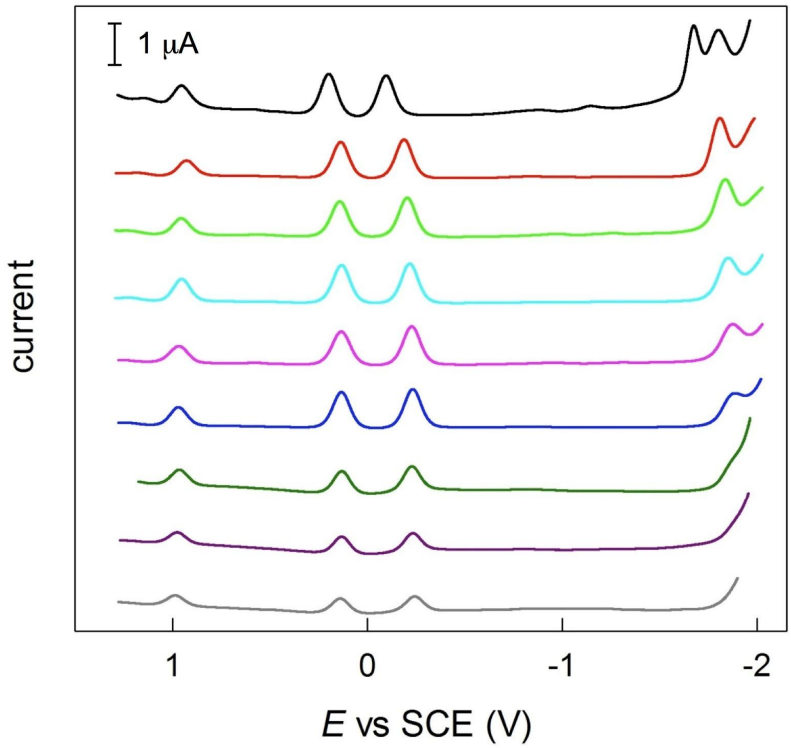

Figure 10. DPV (negative-going scan) of $Au_{25}(Cn)_{18}$ in DCM/ 0.1 M TBAH. n (top to bottom) = 2, 4, 6, 8, 10, 12, 14, 16, 18. For $n \leq 12$, the concentration was ca. 0.5 mM; for $n > 12$ it was ca. 0.2 mM. Glassy carbon electrode, 25 °C.

Over the last 25 years, the rate of electron tunneling through a variety of molecular bridges has been established.[17,30,33,34] Here the concept will be reversed in the sense that ET will be used as an indicator of apparent deviations from the distance dependence expected for alkyl chains. Because ET is sensitive to the distance separating the exchanging centers and the nature of the molecular bridge, to gain further insights into the structure of $Au_{25}(SC\mathit{n})_{18}$ monolayers we studied the effect of the ligand length on electrode kinetics. Au_{25} clusters can be conveniently charged by stepwise electrochemical reduction or oxidation.[18] However, whereas the 0/-1 and 0/+1 redox couples display a chemically reversible voltammetric behavior at all potential scan rates (v), further reduction or oxidation generates species with limited lifetimes.[19,29] We thus focused on the 0/-1 and 0/+1 redox couples. The kinetics of the first reduction (R1) and oxidation steps (O1) of $Au_{25}(SC\mathit{n})_{18}^{0}$ was studied by CV in DCM containing 0.1 M TBAH. Based on the above evidence, the experiments concerning the C14, C16 and C18 MPCs were carried out after sonication of the corresponding solutions for the appropriate time (as assessed by UV-vis control experiments).

At low v values, both R1 and O1 peaks display the typical peak-to-peak separation (ΔE_p) of ~59 mV expected for a reversible one-electron process at 25 °C.[41] On the other hand, when the time scale of the voltammetric experiment is made small, ΔE_p increases, which indicates that the heterogeneous ET becomes quasi-reversible. This is illustrated in the typical plots of Figure 11 for both peaks R1 and O1. The ΔE_p dependence on v can be quantitatively analyzed[41] to obtain the standard heterogeneous ET rate constant $k°$, which is the ET rate constant measured at the formal potential ($E°$). Because we started from the neutral cluster, the R1 and O1 processes could be studied independently by running the CV scan toward negative or positive potentials, respectively, starting from the equilibrium potential of $Au_{25}(SC\mathit{n})_{18}^{0}$. The $k°$ results were confirmed by digital simulation of the CV curves.

Figure 12 illustrates the outcome of these measurements and calculations. The $k°$ values are plotted as a function of the distance d between the surface gold atoms and the solution-side end of the ligands, assuming a fully extended conformation. For both R1 and O1, the plots reveal three important aspects: (i) for ligands with short to moderately long chains (n = 2 to 12), the falloff of the ET rate with distance is linear; (ii) the corresponding β values (eq. 1) are 0.23 and 0.21 $Å^{-1}$, in sharp contrast even to the minimum value of β, 0.8 $Å^{-1}$,

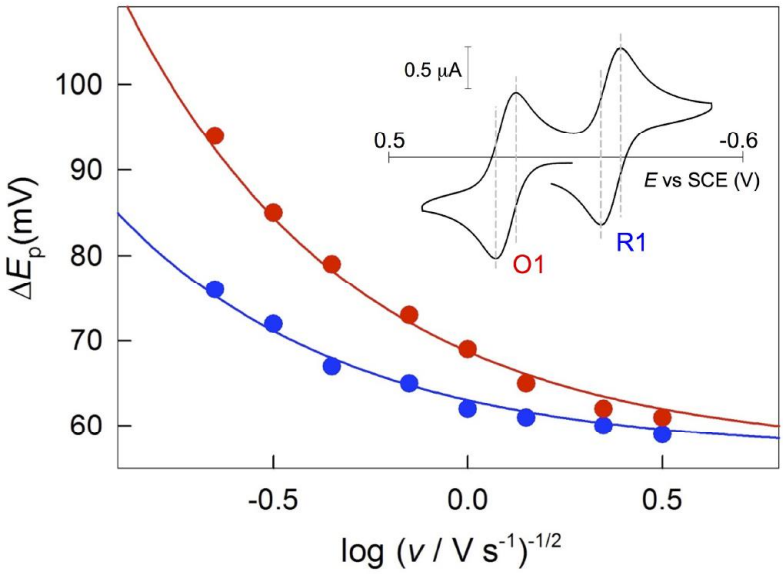

Figure 11. Scan rate dependence of ΔE_p for R1 (λ) and O1 (λ): 0.51 mM $Au_{25}(SC4)_{18}^{0}$ in DCM/0.1 M TBAH on the glassy carbon electrode at 25 °C. The lines are the best fit of the Nicholson curve[41] to the data. The inset shows a typical CV (positive initial scan direction) with vertical lines evidencing ΔE_p.

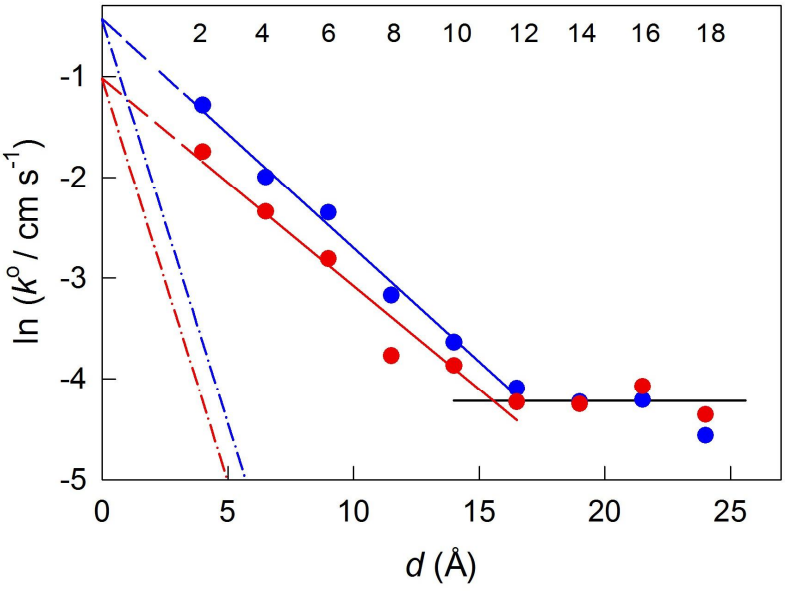

Figure 12. Distance effect of the heterogeneous ET rate constants for R1 (λ) and O1 (λ). The distance *d* corresponds to fully extended conformations. Uncertainty in ln*k*° values is 0.05-0.1. Linear regressions correspond to β = 0.23 (R1) and 0.21 $Å^{-1}$ (O1). The two dash-dot lines and the horizontal line correspond to β = 0.8 and 0 $Å^{-1}$, respectively.

determined for saturated sp^3 carbon chains in solution or 2D SAMs; (iii) for longer ligands (C12 - C18), a sizable change in slope is observed and in fact, the ET rate becomes virtually independent of the ligand length.

Former ET evidence showed that through-bond coupling is maximized (smaller β value) when alkyl chains adopt an all-*trans* conformation, whereas introduction of *cis* kinks decrease the ET rate.[34] Concerning C2 – C12, the observed very low β values cannot thus indicate that a somehow more efficient conformation is attained. Instead, these apparent β factors point to electron tunneling as occurring at an average distance equivalent to approximately one fourth of the fully extended lengths of the ligands. This implies that the monolayer chains are substantially bent with respect to the electrode – gold core separation. The ET rates and mild distance dependencies thus provide smoking-gun evidence that 3D monolayers of molecule-like Au clusters cannot be depicted as a more or less regular arrangement of ligands pointing outward, as often assumed and illustrated. In this context, it is worth mentioning that heterogeneous ET rates measured for larger MPCs (displaying quantized charging behavior)[2] yielded a β value of 0.41 $Å^{-1}$:[42] with all due cautions associated with the polydisperse MPCs employed, comparison with our results would point, not quite unexpectedly, to a core-size dependent ET β factor.

What happens for the longer chains is also very interesting. For the same reasons already described, the virtual independence of the ET rate on the ligand length is only apparent. In fact, the ET can be taken as a sensitive probe of the new situation occurring to the monolayers composed by long ligands. Generally speaking, ET rate constants are the time average of electron tunneling events occurring in a range of rate-significant donor-acceptor distances and, for intramolecular ETs, orientations. Because of this, even subtle differences between intermolecular and intramolecular ET rates can be detected.[43] In principle, heterogeneous ETs to/from symmetrically protected MPCs should provide the very special case of bimolecular ETs occurring through a molecular spacer, like in intramolecular ETs, but with rates independent of orientation. In fact, our results point to an orientation dependent process and, specifically, that the average monolayer thickness is not constant around the MPC. For chains with a length equal or longer than C12 there are MPC's orientations for which ET occurs at a distance that virtually does not change with ligand length. These orientations correspond to the MPC with its thinner sides closer to the electrode surface, and are those providing the dominant contributions to the observed ET

rate constant. The anomalous dependence of the heterogeneous ET rate on distance illustrated in Figure 5 thus detects and amplifies those chain-length dependent monolayer features inferred from the NMR and IR results. We can thus conclude that while on the small surface of Au_{25} clusters the shorter thiolated ligands are quite mobile and the interaction among chains is not significant, longer ligands self-arrange in bundles because of cooperative van der Waals interactions. Since the Au core is small, once the chains start interacting they can only do it along preferred orientations. This implies that the ligands leave the Au core much less shielded than expected on the basis of a fully extended conformation.

4.3.7 Molecular Dynamics Calculations

To shed further light onto this intriguing and fascinating issue, we performed MD calculations of the clusters' monolayers in benzene. The components of the inertia tensor **I** are a measure of the size of $Au_{25}(SC\mathit{n})_{18}$ along its three main axes. Whereas spherical particles are characterized by isotropic tensors, for anisotropic particles asymmetry and relative magnitude of the principal components determine the particle's shape. The components of the tensor **I** monotonically increase with the length of chains but with different dependencies (Figure 13).

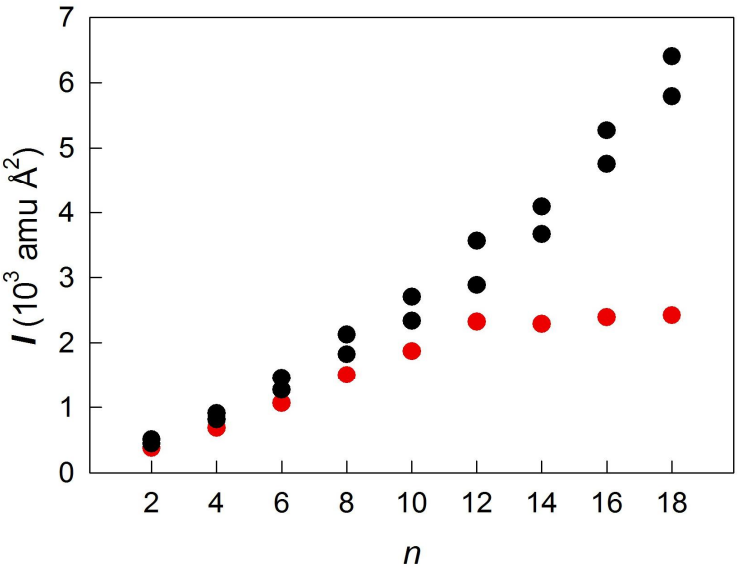

Figure 13. Principal components of the inertia tensor **I**, parallel (λ) or perpendicular (λ) to the MPC's longest axis. Benzene, 300 K.

Figure 14A illustrates that MPCs capped by not-too-long alkanethiolates are indeed nearly spherical, which corresponds to similar components of **I**.

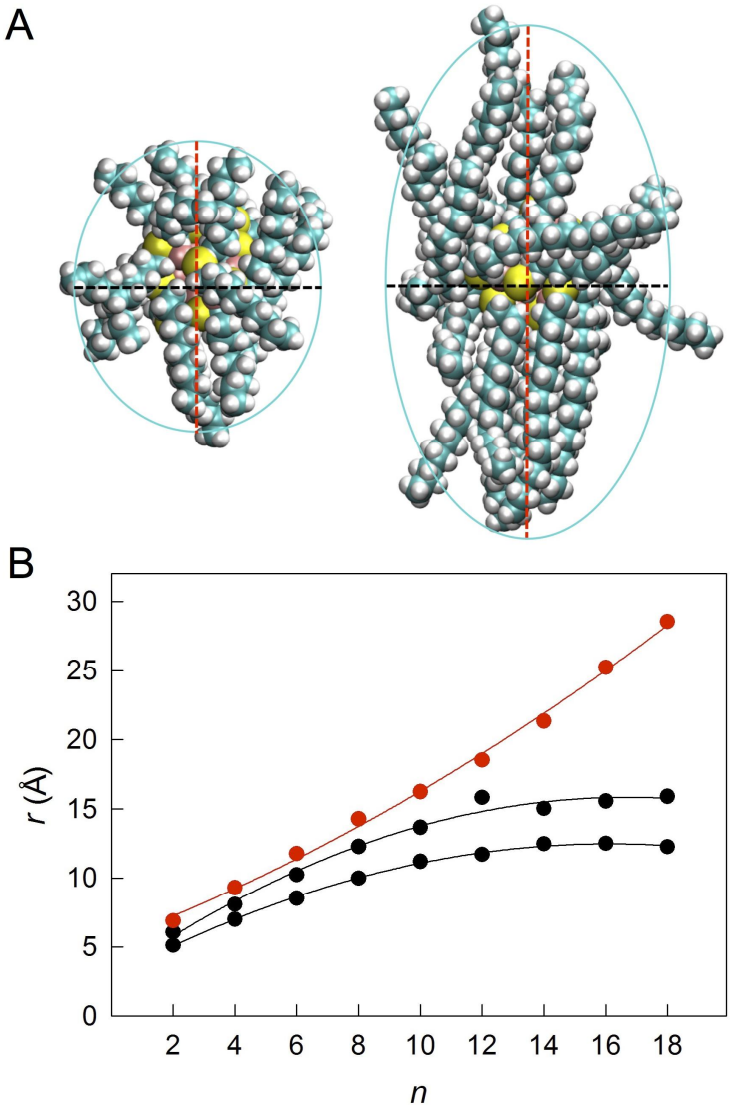

Figure 14. (A) Representative snapshots from the MD trajectories of approximately spherical C10 (left) and elongated C18 MPCs (right), in benzene at 300 K. Dashed lines indicate the long (red) and one of the perpendicular (black) axes. (B) Dependence of the semiaxis lengths *a* (λ), *b* and *c* (λ) on the number of carbon atoms in the chain.

In particular, the MD trajectories show that these chains independently fluctuate in the solvent, without displaying any orientation preference. For longer chains, on the other hand, one of the components of **I** is significantly smaller (corresponding to the longest axis), which imparts the MPCs an elongated shape: this is because the chains tend to attain an extended conformation and assemble

by forming two bundles on opposite sides of the gold core. These snapshots suggest that the MPCs' shape can be satisfactorily described with ellipsoids. In Figure 14B, the lengths *a*, *b*, and *c* of the three semiaxis, obtained from the components of the diagonalized inertia tensor, are plotted as a function of *n.* While *b* and *c* increase and then level off for *n* ~ 12, semiaxis *a* monotonically increases and displays an even slightly steeper dependence on *n* beyond the C12 critical length. Addition of further methylene units to the C12 chain thus induces elongation only in the direction *a*, with chains progressively assuming a more extended conformation.

4.4 Conclusions

By using a large series of alkanethiols, we prepared a homogeneous family of monodisperse Au_{25} clusters. Unexpected ET rates, nicely supported by ^{1}H NMR, IR and MD results, show that there is a critical length marking the transition between short ligands, which form a fluid monolayer structure of folded chains, and longer alkyl chains, which self-organize into bundles. These results thus provide a different scenario for how an ultrasmall gold core talks with the surroundings through/with its monolayer. They also highlight the importance of ET rulers to shed light onto the solution structure of such elusive SAMs. We expect the outcome of this study to be useful for understanding, for example, the ET behavior of MPC layers in devices, the performances of MPCs in redox catalysis, and the interaction of these monolayers with complex environments such as cell membranes.

4.5 Experimental Section

4.5.1 MALDI-TOF Mass Spectrometry

MALDI-TOF experiments were carried out with an Applied Biosystems 4800 MALDI-TOF/TOF spectrometer equipped with a Nd:YAG laser operating at 355 nm. The laser-firing rate was 200 Hz and the accelerating voltage was 25 kV. Trans-2-[3-(4-*tert*-butylphenyl)-2-methyl-2-propenylidene] malononitrile (DCTB) was used as the matrix. The MPCs were dissolved in benzene containing DCTB to obtain 0.1 mM solutions with a 1:400 MPC/matrix ratio. Two microliters of solution was dropcasted onto the sample plate and air-dried. The spectra were recorded in the reflectron negative mode. As the standard, we used $Au_{25}(SC_2H_4Ph)_{18}$, which has a MW of 7394.

4.5.2 UV-Vis Absorption Spectroscopy.

The UV-vis spectra of the MPCs were obtained at 0.1 mM concentration in DCM, with 2 mm cuvettes. The spectra resolution was 1 nm.

4.5.3 Infrared Absorption Spectroscopy

FT-IR absorption spectra were recorded in benzene solution using 1 mm optical path cells, CaF_2 windows, 1-2 mg ml^{-1} MPC concentrations and an argon flushed ThermoFisher Scientific Nicolet 6700 FT-IR spectrometer. The nominal resolution was 1 cm^{-1} and 16 scans were averaged.

4.5.4 NMR Spectroscopy

^1H NMR spectra were obtained at ~1 mM MPC concentration in C_6D_6 with a Bruker Avance DMX-600 MHz spectrometer equipped with a 5 mm TX-1 x,y,z-gradient powered, triple-resonance inverse probe operating at 599.90 MHz. The temperature was controlled (25 $\pm$ 0.1 °C, unless otherwise indicated) with a Bruker BVT-300 automatic temperature controller. Chemical shifts are in part per millions (δ) units with reference to tetramethylsilane used as an internal standard. To ensure a complete relaxation for all the resonances, integral values for the proton spectra were obtained by a prescan delay of 10 s. The proton assignments were performed by standard chemical shift correlations as well as by 2D correlation spectroscopy (COSY), total correlation spectroscopy (TOCSY), and nuclear Overhauser enhancement spectroscopy (NOESY) experiments, as previously done for $Au_{25}(SC_2H_4Ph)_{18}$.[28]

4.5.5 Electrochemistry

The working electrode was a 0.55 mm radius glassy carbon disk prepared, stored, and activated *in situ* according to a procedure ensuring formation of a reproducible surface suitable for ET studies.[44] A Pt wire was the counter electrode and a Ag wire served as the quasi-reference electrode. At the end of each experiment, the potential of the latter was calibrated against the ferricenium/ferrocene redox couple (in DCM/0.1 M TBAH, $E°$ = 0.460 V against the KCl saturated calomel electrode, SCE). The experiments were conducted in DCM/0.1 M TBAH under an Ar atmosphere in a glass cell thermostatted at 25 °C. For the electrode kinetics experiments we used an EG&G-PARC 173/179 potentiostat-digital coulometer, an EG&G-PARC 175 universal programmer, and a Nicolet 3091 12-bit resolution digital oscilloscope. To optimize the kinetic

analysis, we used all experimental precautions and checks described in detail elsewhere.[19,29] To minimize the ohmic drop between the working and the reference electrodes, careful feedback correction was applied. The electrode-kinetics experiments were also checked with a CHI 660c electrochemical workstation, which employs a different approach to perform feedback correction. The CV analysis was carried out on digital CV curves. For digital simulation, we used the DigiSim 3.03 package, using stepsize = 1 mV and exponential expansion factor = 0.5.

4.5.6 Molecular Dynamics Calculations

MD simulations were performed using the LAMMPS software.[45] Energy minimization was performed by using the steepest descent and then the conjugated gradient algorithm. This was followed by 1 ns in the micro-canonical ensemble (NVE: fixed numbers of atoms N, volume V, and energy E), during which the temperature was taken to 300 K, and 1 ns in the isobaric-isothermal ensemble (NPT), with T = 300 K and P = 1 atm. Two nanoseconds was then run in the canonical ensemble (NVT) and the analysis was performed. 3D periodic boundary conditions were adopted. The Nosé-Hoover approach was used for the temperature and pressure control, with a dumping parameter of 100 and 1000 fs, respectively. The equations of motion were integrated using the velocity Verlet algorithm with a time step of 1 fs for the NVE and NPT simulations, and of 2 fs for the NVT runs. Snapshots were taken every 1000 time steps. The cutoff for Lennard-Jones (LJ) interactions and the real-space part of the electrostatic potential was set to 12 Å. Electrostatic interactions were calculated using the particle-particle particle-mesh solver technique, with a root mean square accuracy of 10^{-4}. The bond lengths involving H atoms were constrained using the SHAKE algorithm. The all-atom CHARMM27 force field[46] was used for thiol chains and benzene. The gold atoms were allowed to interact with the chains and solvent *via* LJ potentials parametrized for the metal according to the universal force field (UFF).[47] LJ cross-term interaction parameters were calculated according to the Lorentz-Berthelot combination rule. Au-Au, Au-S and S-S interactions were set to zero. For Au and S atoms, we used the atomic coordinates of the X-ray structure of $Au_{25}(SC_2H_4Ph)_{18,}$[8] which were kept constant.

For the inertia tensor **I**, we used the following expression:

$$\mathbf{I} = \left\langle \sum_{i=1}^{\substack{number\\ of\ ligands}} \begin{pmatrix} m_C\left(y_i^2 + z_i^2\right) & -m_C x_i y_i & -m_C x_i z_i \\ -m_C x_i y_i & m_C\left(x_i^2 + z_i^2\right) & -m_C y_i z_i \\ -m_C x_i z_i & -m_C y_i z_i & m_C\left(x_i^2 + y_i^2\right) \end{pmatrix} \right\rangle$$

where only the atomic coordinates *x*, *y* and *z* of the *n*-th carbon atoms, of mass m_C, along the thiol chains of $Au_{25}(SCn)_{18}$ were considered. Angular brackets indicate average over the simulation time. The dependence of the three components on *n* is illustrated in Figure 13. The semi-axes *a*, *b*, and *c* were obtained from the diagonalized tensor $\tilde{\mathbf{I}}$, in which *M* is the total mass:

$$\tilde{\mathbf{I}} = \begin{pmatrix} \tilde{I}^a & 0 & 0 \\ 0 & \tilde{I}^b & 0 \\ 0 & 0 & \tilde{I}^c \end{pmatrix} = \begin{pmatrix} M\left(b^2 + c^2\right)/3 & 0 & 0 \\ 0 & M\left(a^2 + c^2\right)/3 & 0 \\ 0 & 0 & M\left(a^2 + b^2\right)/3 \end{pmatrix}$$

4.6 References

(1) Parker, J. F.; Fields-Zinna, C. A.; Murray, R. W. The Story of a Monodisperse Gold Nanoparticle: $Au_{25}L_{18}$. *Acc. Chem. Res.* **2010**, *43*, 1289-1296.

(2) Murray, R. W. Nanoelectrochemistry: Metal Nanoparticles, Nanoelectrodes, and Nanopores. *Chem. Rev.* **2008**, *108*, 2688–2720.

(3) Tsukuda, T. Toward an Atomic-Level Understanding of Size-Specific Properties of Protected and Stabilized Gold Clusters. *Bull. Chem. Soc. Jpn*. **2012**, *85*, 151-168.

(4) Saha, K.; Agasti, S. S.; Kim, C.; Li, X.; Rotello, V. M. Gold Nanoparticles in Chemical and Biological Sensing. *Chem. Rev.* **2012**, *112,* 2739-2779.

(5) Li, G.; Jin, R. Atomically Precise Gold Nanoclusters as New Model Catalysts. *Acc. Chem. Res.* **2013**, *46*, 1749-1758.

(6) Heaven, M. W.; Dass, A.; White, P. S.; Holt, K. M.; Murray, R. W. Crystal Structure of the Gold Nanoparticle $[N(C_8H_{17})_4][Au_{25}(SCH_2CH_2Ph)_{18}]$. *J. Am. Chem. Soc.* **2008**, *130*, 3754–3755.

(7) Zhu, M.; Aikens, C. M.; Hollander, F. J.; Schatz, G. C.; Jin, R. Correlating the Crystal Structure of A Thiol-Protected Au_{25} Cluster and Optical Properties. *J. Am. Chem. Soc.* **2008**, *130*, 5883–5885.

(8) Zhu, M.; Eckenhoff, W. T.; Pintauer, T.; Jin, R. Conversion of Anionic $[Au_{25}(SCH_2CH_2Ph)_{18}]^-$ Cluster to Charge Neutral Cluster *via* Air Oxidation. *J. Phys. Chem. C* **2008**, *112*, 14221–14224.

(9) Jadzinsky, P. D., Calero, G., Ackerson, C. J., Bushnell, D. A.; Kornberg, R. D. Structure of a Thiol Monolayer-Protected Gold Nanoparticle at 1.1 Å Resolution. *Science* **2007**, *318*, 430-433.

(10) Qian, H.; Eckenhoff, W. T.; Zhu, Y.; Pintauer, T.; Jin, R. Total Structure Determination of Thiolate-Protected Au_{38} Nanoparticles. *J. Am. Chem. Soc.* **2010**, *132*, 8280-8281.

(11) Zeng, C.; Qian, H.; Li, T.; Li, G.; Rosi, N. L.; Yoon, B.; Barnett, R. N.; Whetten, R. L.; Landman, U.; Jin, R. Total Structure and Electronic Properties of the Gold Nanocrystal $Au_{36}(SR)_{24}$. *Angew. Chem. Int. Ed.* **2012**, *51*, 13114-13118.

(12) Zeng, C.; Li, T.; Das, A.; Rosi, N. L.; Jin, R. Chiral Structure of Thiolate-Protected 28-Gold-Atom Nanocluster Determined by X-ray Crystallography. *J. Am. Chem. Soc.* **2013**, *135*, 10011-10013.

(13) Cossaro, A.; Mazzarello, R.; Rousseau, R.; Casalis, L.; Verdini, A.; Kohlmeyer, A.; Floreano, L.; Scandolo, S.; Morgante, A.; Klein, M. L. *et al.* X-ray Diffraction and Computation Yield the Structure of Alkanethiols on Gold(111). *Science* **2008**, *321*, 943-946.

(14) Pensa, E.; Cortéz, E.; Corthey, G.; Carro, P.; Vericat, C.; Fonticelli, M. H.; Benitez, G.; Rubert, A. A.; Salvarezza, R. C. The Chemistry of the Sufur-Gold Interface: in Search of a Unified Model. *Acc. Chem. Res.* **2012**, *45*, 1183-1192.

(15) Häkkinen, H. The Gold-Sulfur Interface at the Nanoscale. *Nature Chem.* **2012**, *4*, 443-455.

(16) Love, J. C.; Estroff, L. A.; Kriebel, J. K.; Nuzzo, R. G.; Whitesides, G. M. Self-Assembled Monolayers of Thiolates on Metals as a Form of Nanotechnology. *Chem. Rev.* **2005**, *105*, 1103-1169.

(17) Adams, D. M.; Brus, L.; Chidsey, C. E. D.; Creager, S.; Creutz, C.; Kagan, C. R.; Kamat, P. V.; Lieberman, M.; Lindsay, S.; Marcus, R. A. *et al.* Charge Transfer on the Nanoscale: Current Status. *J. Phys. Chem. B* **2003**, *107*, 6668-6697.

(18) Lee, D.; Donkers, R. L.; Wang, G.; Harper, A. S.; Murray, R. W. Electrochemistry and Optical Absorbance and Luminescence of Molecule-like Au_{38} Nanoparticles. *J. Am. Chem. Soc.* **2004**, *126*, 6193-6199.

(19) Antonello, S.; Holm, A. H.; Instuli, E.; Maran, F. Molecular Electron-Transfer Properties of Au_{38} Clusters. *J. Am. Chem. Soc.* **2007**, *129*, 9836–9837.

(20) Badia, A.; Lennox, R. B.; Reven, L. A Dynamic View of Self-Assembled Monolayers. *Acc. Chem. Res.* **2000**, *33*, 475-481.

(21) Templeton, A. C.; Wuelfing, W. P.; Murray, R. W. Monolayer-Protected Cluster Molecules. *Acc. Chem. Res.* **2000**, *33*, 127-136.

(22) Schaaff, T. G.; Shafigullin, M. N.; Khoury, J. T.; Vezmar, I.; Whetten, R. L. Properties of a Ubiquitous 29 kDa Au:SR Cluster Compound. *J. Phys. Chem. B* **2001**, *105*, 8785-8796.

(23) Landman, U.; Luedtke, W. D. Structure, Dynamics, and Thermodynamics of Passivated Gold Nanocrystallites and their Assemblies. *J. Phys. Chem.* **1996**, *100*, 13323-13329.

(24) Landman, U.; Luedtke, W. D. Structure and Thermodynamics of Self-Assembled Monolayers on Gold Nanocrystallites. *J. Phys. Chem. B* **1998**, *102*, 6566-6572.

(25) Negishi, Y.; Nobusada, K.; Tsukuda, T. Glutathione-Protected Gold Clusters Revisited: Bridging the Gap between Gold(I)-Thiolate Complexes and Thiolate-Protected Gold Nanocrystals. *J. Am. Chem. Soc.* **2005**, *127*, 5261–5270.

(26) Tracy, J. B.; Kalyuzhny, G.; Crowe, M. C.; Balasubramanian, R.; Choi, J.-P.; Murray, R. W. Poly(ethylene glycol) Ligands for High-Resolution Nanoparticle Mass Spectrometry. *J. Am. Chem. Soc.* **2007**, *129*, 6706–6707.

(27) Zhu, M.; Aikens, C. M.; Hendrich, M. P.; Gupta, R.; Qian, H.; Schatz, G. C.; Jin, R. Reversible Switching of Magnetism in Thiolate-Protected Au_{25} Superatoms. *J. Am. Chem. Soc.* **2009**, *131*, 2490– 2492.

(28) Venzo, A.; Antonello, S.; Gascón, J. A.; Guryanov, I.; Leapman, R. D.; Perera, N. V.; Sousa, A.; Zamuner, M.; Zanella, A.; Maran, F. Effect of the Charge State (z = **-**1, 0, **+**1) on the Nuclear Magnetic Resonance of Monodisperse $Au_{25}[S(CH_2)_2Ph]_{18}^{z}$ Clusters *Anal. Chem.* **2011**, *83*, 6355-6362.

(29) Antonello, S.; Perera, N. V.; Ruzzi, M.; Gascón, J. A.; Maran, F. Interplay of Charge State, Lability, and Magnetism in the Molecule-like $Au_{25}(SR)_{18}$ Cluster. *J. Am. Chem. Soc.* **2013**, *135*, 15585-15594.

(30) Gray, H. B.; Winkler, J. R. Long-Range Electron Transfer. *PNAS* **2005**, *102*, 3534-3539.

(31) Berlin, Y. A.; Grozema, F. C.; Siebbeles, L. D. A.; Ratner, M. A. Charge Transfer in Donor-Bridge-Acceptor Systems: Static Disorder, Dynamic Fluctuations, and Complex Kinetics. *J. Phys. Chem. C* **2008**, *112*, 10988–11000.

(32) Antonello, S.; Hesari, M.; Polo, F.; Maran, F. Electron Transfer Catalysis with Monolayer Protected Au_{25} Clusters. *Nanoscale* **2012**, *4*, 5333-5342.

(33) Holmlin R. E.; Ismagilov, R. F.; Haag, R.; Mujica, V.; Ratner, M. A.; Rampi, M. A.; Whitesides, G. M. Correlating Electron Transport and Molecular Structure in Organic Thin Films. *Angew. Chem. Int. Ed.* **2001**, *40*, 2316-2320.

(34) Paddon-Row, M. N. Superexchange-Mediated Charge Separation and Charge Recombination in Covalently-Linked Donor-Bridge-Acceptor Systems. *Aus. J. Chem.* **2003**, *56*, 729-748.

(35) Dass, A.; Stevenson, A.; Dubay, G. R.; Tracy, J. B.; Murray, R. W. Nanoparticle MALDI-TOF Mass Spectrometry without Fragmentation: $Au_{25}(SCH_2CH_2Ph)_{18}$ and Mixed Monolayer $Au_{25}(SCH_2CH_2Ph)_{18-x}(L)_x$. *J. Am. Chem. Soc.* **2008**, *130*, 5940-5946.

(36) Gottlieb, H. E.; Kotlyar, V.; Nudelman, A. NMR Chemical Shifts of Common Laboratory Solvents as Trace Impurities. *J. Org. Chem.* **1997**, *62*, 7512-7515.

(37) Porter, M. D.; Bright, T. B.; Allara, D. L.; Chidsey, C. E. D. Spontaneously Organized Molecular Assemblies. 4. Structural Characterization of *n*-Alkyl Thiol Monolayers on Gold by Optical Ellipsometry, Infrared Spectroscopy, and Electrochemistry. *J. Am. Chem. Soc.* **1987**, *109*, 3559-3568.

(38) Hostetler, M. J.; Stokes, J. J.; Murray, R. W. Infrared Spectroscopy of Three-Dimensional Self-Assembled Monolayers: *N*-Alkanethiolate Monolayers on Gold Cluster Compounds. *Langmuir* **1996**, *12*, 3604-3612.

(39) Porter, M. D.; Bright, T. B.; Allara, D. L.; Chidsey, C. E. D. Spontaneously Organized Molecular Assemblies. 4. Structural Characterization of *n*-Alkyl Thiol Monolayers on Gold by Optical Ellipsometry, Infrared Spectroscopy, and Electrochemistry. *J. Am. Chem. Soc.* **1987**, *109*, 3559-3568.

(40) Hostetler, M. J.; Stokes, J. J.; Murray, R. W. Infrared Spectroscopy of Three-Dimensional Self-Assembled Monolayers: *N*-Alkanethiolate Monolayers on Gold Cluster Compounds. *Langmuir* **1996**, *12*, 3604-3612.

(41) Nicholson, R. S. Theory and Application of Cyclic Voltammetry for Measurement of Electrode Reaction Kinetics. *Anal. Chem*. **1965**, *37*, 1351-1355.

(42) Peterson, R. R.; Cliffel, D. E. Scanning Electrochemical Microscopy Determination of Organic Soluble MPC Electron-Transfer Rates. *Langmuir* **2006**, *22*, 10307-10314.

(43) Antonello, S.; Crisma, M.; Formaggio, F.; Moretto, A.; Taddei, F.; Toniolo, C.; Maran, F. Insights into the Free Energy Dependence of Intramolecular Dissociative Electron Transfers. *J. Am. Chem. Soc.* **2002**, *124*, 11503-11513.

(44) Meneses, A. B.; Antonello, S.; Arévalo, M.-C; Maran, F. Double-Layer Correction for Electron-Transfer Kinetics at Glassy Carbon and Mercury Electrodes in *N,N*-Dimethylformamide. *Electroanalysis* **2006**, *18*, 363-370.
(45) Plimpton, S. Fast Parallel Algorithms for Short-Range Molecular Dynamics. *J. Comput. Phys*. **1995**, *117*, 1-19.
(46) MacKerell Jr., A. D.; Banavali, N.; Foloppe, N. Development and Current Status of the CHARMM Force Field for Nucleic Acids. *Biopolymers* **2000**, *56*, 257-265.
(47) Rappé, A. K.; Casewit, C. J.; Colwell, K. S.; Goddard III, W. A.; Skiff, W. M. UFF, a Full Periodic Table Force Field for Molecular Mechanics and Molecular Dynamics Simulations. *J. Am. Chem. Soc.* **1992**, *114*, 10024-10035.

4.7 Acknowledgements

Besides acknowledging the contribution from other group members, TD is thankful to Giulia Parisio, for the MD calculations, and Giorgio Arrigoni (Department of Biomedical Sciences, University of Padova), for his assistance in some of the MALDI-TOF experiments.

Chapter 5: Electron Transfer in Au_{25} Films

5.1 Abstract

We carried out conductivity measurements on dry films formed by drop casting monodisperse $Au_{25}(SR)_{18}$ nanoclusters. The effects of changing the length and branching of the alkyl thiolate ligands protecting the Au core were analyzed by studying a series of linear-chain thiolate protected clusters having the general formula $Au_{25}(SC_nH_{2n+1})_{18}$, with n = 3, 4, 5, 6, 8, and 10, in comparison with the behavior of a cluster characterized by a branched alkyl (2-methyl-1-butane) thiolate monolayer. The linear dependence of the conductivity on n points to a hopping mechanism where the cores of the nanoclusters behave as a localized electron-donor or acceptor site, and the ligands as spacers dictating the efficiency of the electron tunneling. The experimental results were analyzed to obtain the value of the exponential electron-tunneling coefficient β ($Å^{-1}$). This β value was then compared with that obtained for the same clusters under direct electrochemistry conditions in solution phase. The β value points to a substantial folding of the linear chains in the monolayer in the solid state, but to a lesser extent compared to what found in the solution ET studies.

5.2 Introduction

Solid-state studies of structure-properties relationship in MPC are still limited, although nanoparticles assemblies already showed to provide a good platform to study charge transport phenomena.[1,2] The drop casting and drying of an MPC solution forms a disordered assembly of nanoparticles but yet this approach represents a simply applicable method to create a film with tailored conductive properties that could be transferred to device fabrication. Therefore, understanding how ultrasmall nanoclusters behaves when in films and, in particular, the analysis of how their electronic conduction properties depend on the nanoclusters' features could bring new tools for fine tuning charge transport in electronic devices.

Conductivity in nanoparticles' dry films has been shown to depend on core dimension, charge state or the relative amount of the different oxidation states, and, particularly, on the distance between the metallic cores, which is in turn dictated by the length of the protecting ligands as well as their chemical structure.[3-8] The choice of the protecting layer is then fundamental in controlling

the resistivity properties of the film. In studies on mixed-valent $Au_{144}(SC6)_{60}$ nanoclusters, the Murray Group showed that the conductivity in films formed by drop casting onto interdigitated array (IDA) gold electrodes, followed by drying of the MPC solution, depends on the charge state of the MPC and reaches a maximum for a 1:1 ratio between the 0 and the +1 charge states[4] The same trend was observed for $Au_{25}(SC_2H_4Ph)_{18}$ assemblies.[6] A bimolecular rate law was proposed to describe the conductivities of such mixed-valent films,[4,6]

(1) $$MPC^{z} + MPC^{z+1} \rightleftharpoons MPC^{z+1} + MPC^{z}$$

The ET rate constant k_{ET} for the exchange reaction ($M^{-1}s^{-1}$) was expressed as:

(2) $$k_{ET} = \frac{6(10^3)RT\sigma}{F^2\delta^2[MPC^{z+1}][MPC^{z}]}$$

where R is the gas constant, T is the temperature, F is the Faraday constant, σ is the conductivity (Ω^{-1} cm^{-1}), δ is the core center-to-center distance (cm). The k_{ET} values calculated for Au_{144} and Au_{25} MPC were ca. 3×10^9 and 2×10^6 $M^{-1}s^{-1}$, respectively, and the corresponding activation energies were ca. 70 and 210 meV. The ET rate showed a strong dependence on the core dimension, with a difference as large as 3 orders of magnitude, that was attributed mostly to a difference in the activation energies. In a more recent paper,[7] however, improved monodispersity in the synthesis of the clusters and more accurate IDA cleaning methods led to refined data for the k_{ET} value calculated for $Au_{144}(SC6)_{60}$, which was determined to be 1×10^8 $M^{-1}s^{-1}$. Carducci and Murray also reported that the ET rate through a film composed by a mixture of +1 and 0 charged $Au_{25}(SC_2H_4Ph)_{18}$ clusters is slower by about one order of magnitude with respect to a 0/-1 mixture. [7] This result was tentatively ascribed to a larger degree of reorganization involved in the formation of the positively charged nanocluster. It also is in agreement with our results about heterogeneous ET in solution (Chapter 4) showing that the standard heterogeneous rate constant for the 0/-1 redox couple (R1 process) is larger than that observed for the corresponding +1/0 redox couple (O1 process).

Systematic studies on the effect of the variation in monolayer thickness and structure were carried out for a series of alkanethiolate-protected nanoparticles with average stoichiometry $Au_{309}(SCn)_{92}$, with n ranging from 4 to 16.[4] The results pointed to an exponential decrease of the ET rate with an

increase in the ligand length. A decay exponential factor β of 0.8 $Å^{-1}$ was calculated by assuming an extensive intercalation of the chains of neighboring MPCs. Indeed, density measurements carried out on such kind of films point to a separation between MPC cores quite close to the length of a single ligand chain. In a subsequent work, the effect of a more "conductive" monolayer was also analyzed by studying MPC capped by an arenethiolate.[5] The larger ET rate found for this system than for the MPCs capped by saturated-chain ligands further pointed to an active role of the monolayer in dictating the film conductivity.

Our ET studies carried out in solution on $Au_{25}(SC\mathit{n})_{18}$ clusters,[9] described in Chapter 4, revealed that the protecting monolayer is not as "thick" as previously assumed. It is, therefore, interesting to investigate the main features of the electronic conduction within molecular nanoclusters films, analyze how conductivity depends on the monolayer thickness and rigidity, and finally compare the results with those obtained for the same clusters in solution.

5.3 Results and Discussion

5.3.1 Synthesis of $Au_{25}(SC_nH_{2n+1})_{18}$, n = 3 and 5

The series of nanoclusters for which the solution heterogeneous ET was initially studied, as described in Chapter 4, was increased in order to obtain a more detailed picture of what happens in the range of *n* varying from 2 to 10, *i.e.*, where the ET rate was found to decrease linearly with *n*. We thus synthetized two new Au_{25} clusters protected by propanethiolate (SC*3*) and pentanethiolate (SC*5*), respectively. These two clusters allowed us to tune more finely the monolayer thickness, as well as to analyze possible odd-even effect sometimes observed for alkane chains.[4] These clusters were synthetized and characterized as detailed in Sections 2.1.2 and 2.1.4. The composition and the monodispersity of the new clusters were assessed by MALDI-TOF mass spectrometry, NMR spectroscopy, and electrochemistry.

5.3.2 Heterogeneous Electron Transfer

The heterogeneous ET to/from $Au_{25}(SC\mathit{3})_{18}$ and $Au_{25}(SC\mathit{5})_{18}$, both in their neutral state, was studied on a glassy-carbon disk electrode in DCM/0.1 M TBAH, along the same lines described for the other $Au_{25}(SC_nH_{2n+1})_{18}$ clusters in Section 4.3.6. The standard ET rate constant $k°$ was thus obtained by studying the v dependence of ΔE_p, according to the Nicholson method.[10] For both O1 and R1 processes, the plot of ΔE_p vs $\log v^{1/2}$ shows an excellent fit to the Nicholson

theoretical curve in the whole scan rate range investigated, 0.1-50 V s^{-1}. Figure 1 shows the ln*k*° values determined (R1 process) for $Au_{25}(SC3)_{18}$ and $Au_{25}(SC5)_{18}$ together with the previous results obtained for the C2-C12 series. The plot shows that these two new data are in line with the overall trend exhibiting a linear decrease with an increase in the ligand length. The slope is 0.23 $Å^{-1}$, when the fully-extended length (d_{fec}) of the alkyl chain is arbitrarily assumed as the actual tunneling distance.

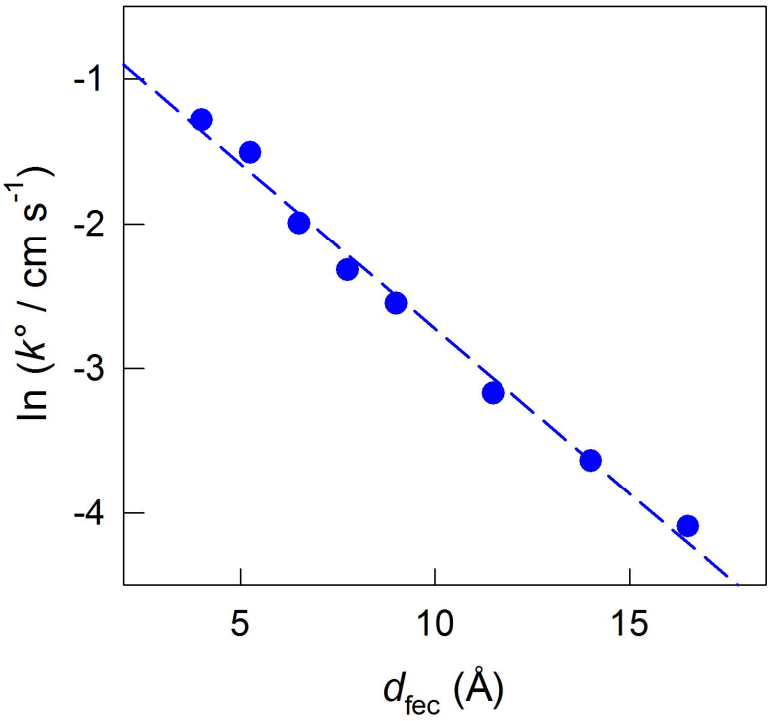

Figure 1. Distance effect on the heterogeneous ET rate constants for R1 (left to right, *n* = 2, 3, 4, 5, 6, 8, 10, 12). The distance d_{fec} corresponds to fully extended conformations. Uncertainty in ln*k*° values is 0.05-0.1. Linear regressions correspond to β = 0.23 $Å^{-1}$.

5.3.3 Conductivity of Au_{25} Films

We performed electronic conductivity measurements on films obtained by drop casting a concentrated solution of the MPC onto IDA gold electrodes, as schematized in the cartoon of Figure 2. This is an approach extensively employed to test the conductivity of similar MPC films.[3-8] Our analysis included a series of $Au_{25}(SC_nH_{2n+1})_{18}$ with *n* = 3, 4, 5, 6, 8, and 10. The samples were dried very carefully in vacuum for 30 min. Conductivity measurements were carried out by scanning the bias potential (*E*) from +1 to -1 V across the IDA fingers. For all

samples and at the potential scan rates used, the current *i* is linear in *E* (Figure 3), *i.e*., the films display ohmic behavior. No hysteresis effects, usually due to ion mobility within the film,[4] were observed. Furthermore, the current response did not show any dependence on the scan rate, which was varied from 0.1 to 10 Vs^{-1}.

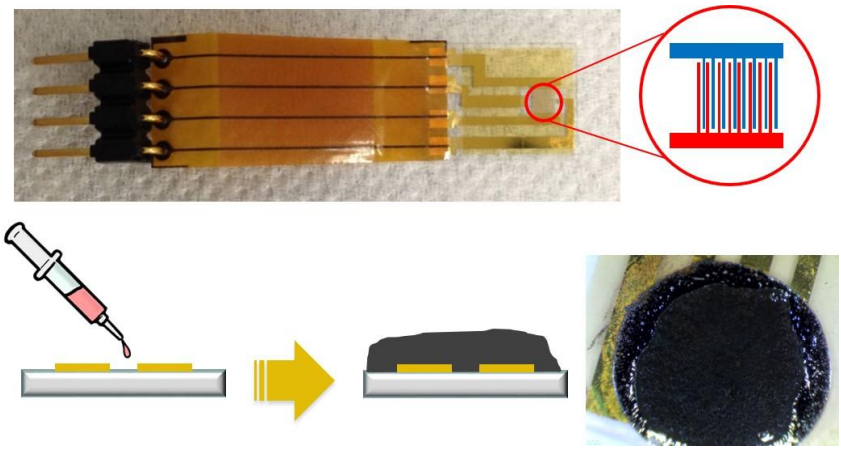

Figure 2. IDA electrode system and cartoon of its side view (not in scale: finger width 10 μm, finger height 96 nm, interfinger distance 5 μm, film thickness ca. 5 μm) after drop casting and drying an MPC solution. A photograph of the resulting film is shown at the right-bottom corner of the figure.

As already described, in their study on $Au_{25}(SC_2H_4Ph)_{18}$ Murray and co-workers found that a mixture of Au_{25}^{0} and Au_{25}^{-} produces a more conductive film with respect to a monovalent assembly.[6,7] In our work, we decided to rely our (comparative) analysis on a single oxidation state in order to guarantee a better reproducibility of the experimental conditions for the different $Au_{25}(SC\mathit{n})_{18}$ samples as well as to prevent contamination associated with chemical or electrochemical oxidation. We employed the $Au_{25}(SC\mathit{n})_{18}^{0}$ radical because it is the most stable and does not introduce further species (counterions). We also found it to be more conductive than $Au_{25}(SC\mathit{n})_{18}^{-}$. For example we found a σ value of 2.3×10^{-7} and 3.9×10^{-8} $\Omega^{-1}cm^{-1}$ for $Au_{25}(SC_2H_4Ph)_{18}$ in its neutral and anionic form, respectively; similarly, we obtained 1.9×10^{-7} and 6.8×10^{-5} for $Au_{25}(SC\mathit{4})_{18}$.

Figure 3 shows that *n* affects the observed current very significantly, with

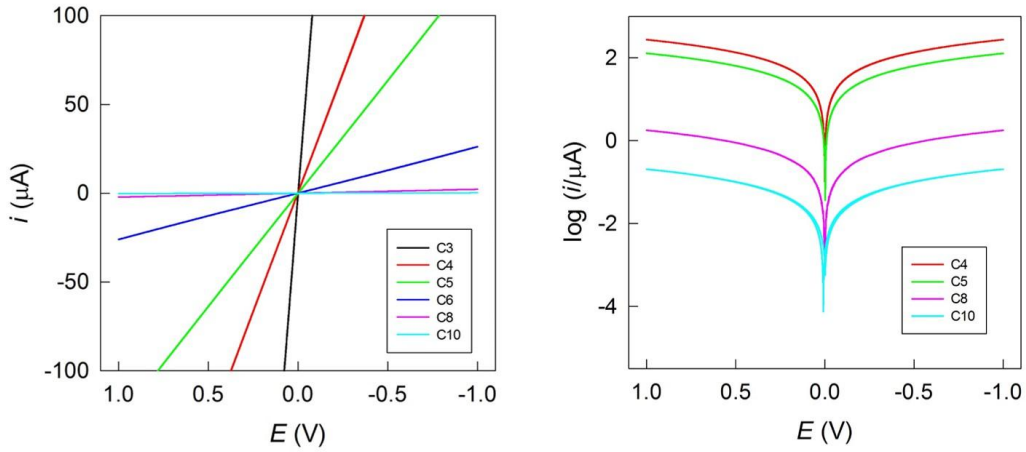

Figure 3. Plots of the current *i* obtained for the $Au_{25}(SCn)_{18}^{0}$ samples (n = 3, 4, 5, 6, 8, 10) as a function of the potential bias between the two comb gold electrodes (left). The corresponding logarithmic plot (selected curves) is shown on the right-hand side.

a substantial decrease of the film electronic conductivity σ as *n* increases. σ was calculated with eq. 3:

(3) $$\sigma = \frac{l}{A_{tot}} \frac{i}{E} = C_{cell} \frac{i}{E}$$

where *l* is the IDA finger gap and A_{tot} is the total area of the electrode/film interface. The cell constant $C_{cell} = l/A_{total}$ was calculated as described by Choi and Murray,[4] as detailed in Section 5.5. The σ values are gathered in Table 1.

Table 1. Electronic conductivity data, MPC concentration in the films and ET rate constants for $Au_{25}(SR)_{18}$ MPCs (see text).

	σ (Ω^{-1} cm^{-1})	C_{film} (M)	k_{ET} (s^{-1})
C3	2.5×10^{-4}	0.61	2.8×10^{7}
C4	6.8×10^{-5}	0.37	8.9×10^{6}
C5	1.9×10^{-5}	0.28	2.8×10^{6}
C6	5.8×10^{-6}	0.20	9.7×10^{5}
C8	5.8×10^{-7}	0.16	1.0×10^{5}
C10	5.9×10^{-8}	0.11	1.1×10^{4}
MeBu	2.3×10^{-5}	0.26	2.2×10^{6}

5.3.4 Comparison between Solution and Solid-State ETs

Figure 4 shows lnσ as a function of an edge-to-edge intercore distance, arbitrarily assumed to correspond to the thickness of two monolayers ($2d_{fec}$) formed by fully extended alkyl chains. The graph shows that the plot is very linear (r^2 = 0.999), in excellent agreement with an ET hopping mechanism where lnσ depends on $2d_{fec}$ according to eq. 4:[4]

(4) $$\ln\sigma = \ln\sigma_0 - E_a/RT - \beta(2d)$$

where β is the exponential factor, E_A is the activation energy, and σ_0 is the hypothetical conductivity for clusters at contact distance.

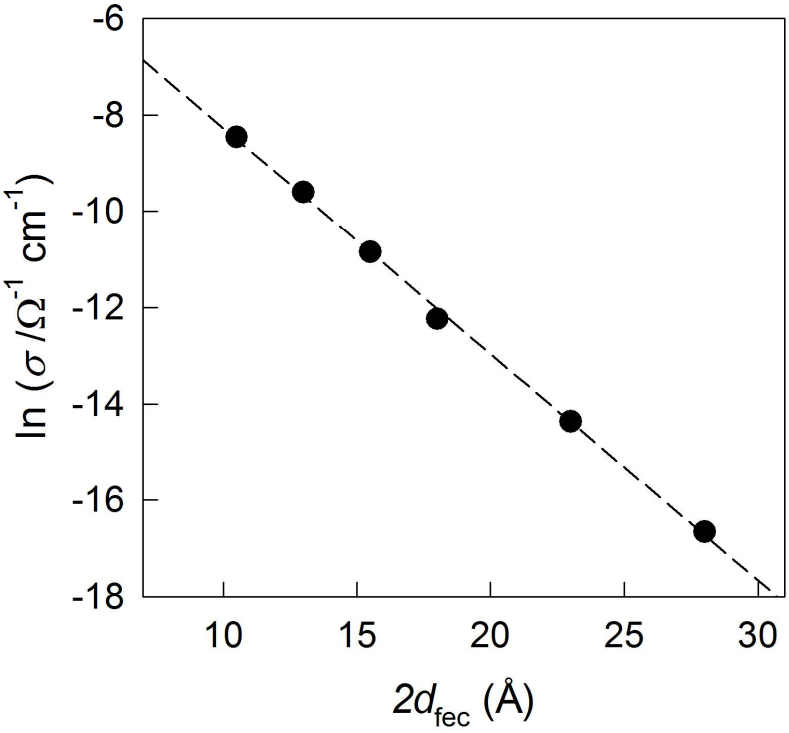

Figure 4. Logarithmic dependence of film conductivity σ (left to right, *n* = 3, 4, 5, 6, 8, 10) as a function of twice the length *d* of the capping thiolates obtained by assuming a fully extended conformation for the alkyl groups. Linear regressions correspond to β = 0.47 $Å^{-1}$.

From the slope of the plot in Figure 4, we calculate an exponential factor of β = 0.47 $Å^{-1}$. This value is much smaller than the values of β = 0.8-1.0 $Å^{-1}$ determined for alkyl chains in the all-*trans* conformation.[11,12] We should also recall that for the same *n* values the β value for freely diffusing $Au_{25}(SC_nH_{2n+1})_{18}$

clusters is even smaller, being only 0.23 $Å^{-1}$. The ET data and other experimental evidence (Chapter 4)[9] indicate that these are, in fact, apparent β values in the sense that they point to monolayers composed by rather fluid structures of folded chains, thereby making the effective monolayer thickness significantly smaller (by a factor of ca. 4) than expected for fully extended chains. The results obtained with the films can be interpreted in a similar way. A slightly larger β, on the other hand, suggests that the ligands of neighboring monolayers might also be partially interdigitated, as already suggested:[3-5] this would make alkyl chains less prone to folding and thus the intercore distance be slightly larger than seen for the MPC-electrode effective distance in solution. This view is supported by the fact that the β values obtained for the larger Au_{144} MPCs (core radius of 1.6 nm, as opposed to 1.0 nm in Au_{25} MPCs) in solution[13] and in the solid state[8] show a similar increase, from 0.41 to 0.5 $Å^{-1}$.

Estimation of the MPCs' radii, and consequently the value of the corresponding monolayer thickness, can be carried out experimentally from the diffusion coefficient (*D*) values, as calculated from the CV peak currents at low scan rates with the Stokes-Einsten equation ($D = k_B T/6\pi\eta r$, where k_B is the Boltzmann constant, η is the solvent viscosity, and *r* is the MPC radius). The results, are shown in Table 2.

Table 2. Diffusion coefficients, radius calculated from Stoke-Einstein equation and monolayer thickness for $Au_{25}(SR)_{18}$ MPCs.

	$D \times 10^{-6}$ ($cm^2\ s^{-1}$)	*r* (Å)	*d* (Å)
C3	6.9	7.7	2.7
C4	5.8	9.1	4.1
C5	5.3	10.0	5.0
C6	4.7	11.2	6.2
C8	4.4	12.1	7.1
C10	3.9	13.5	8.5
MeBu	5.2	10.2	5.2

The so-determined *r* values are in good agreement with the theoretical predictions obtained *via* MD simulations of the MPCs dimensions, as described in Section 4.3.7. MD and all other experimental evidence pointed to a progressive change in the shape of the MPC from a sphere, for lower *n*, to an ellipsoid for

longer chains. This peculiar behavior is due to the degrees of freedom that the ligands holds when bound to these very small nanoclusters. This allows the shorter chains to bend and fold and indeed the *r* values experimentally calculated are smaller than those expected for a fully extended all-*trans* conformation of the alkyl backbone. Although the radius calculated as the average of the three ellipsoid axes is a poor descriptor of the shape of elongated MPCs, its value is in remarkably good agreement with the electrochemically determined hydrodynamic *r* (Figure 5).

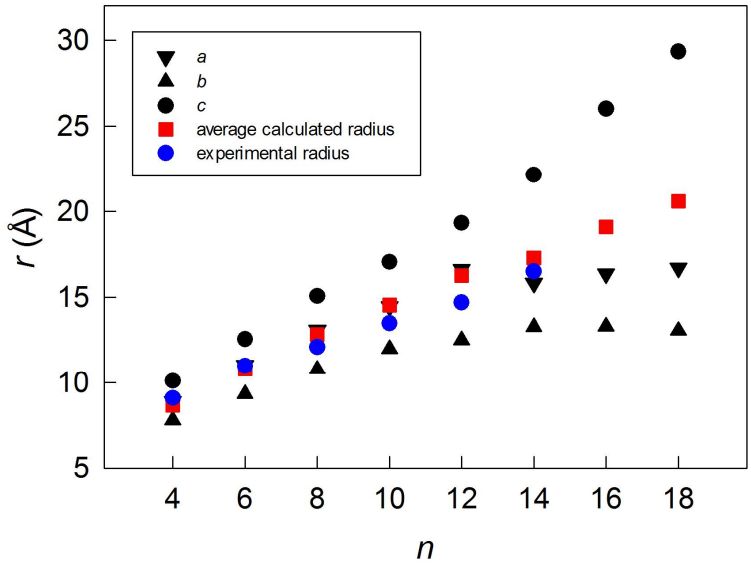

Figure 5. Comparison between calculated and experimentally determined radii as a function of the number of the chain carbon atoms. *a*, *b* and *c* represents the calculated semiaxes as described in Section 4.3.7.

The monolayer thickness value, *d*, is then estimated by subtracting the core radius (5.0 nm) from the experimentally determined MPC radius. The *d* values are also collected in Table 2. Noteworthy, when the lnσ values are plotted against the so-calculated 2*d* values, a linear plot with a slope of 0.74 $Å^{-1}$ is observed (Figure 6).

For proper comparison of the solid-state attenuation factor β due to the distance increase between the clusters Au cores and the corresponding factor β pertaining to the solution results, one should normalize the electronic conductivity results for the nanocluster concentration (*C*) in the film. To carry out this calculation, we used eq. 5 that assumes a hexagonally close packed film (0.7 represents the fill factor for this packing organization), as already done before:[5]

(5) $$C = \frac{0.7(10^3)}{\frac{4}{3}\pi(r+d)^3 N_A}$$

where N_A is the Avogadro's number. For the monolayer thickness d, which defines the Au cores' edge-to-edge distance, we used the values obtained from the D values. The concentration values calculated in this way are gathered in Table 1. It is worth stressing that although these figures were obtained by assuming that while in the solid-state the nanoclusters' ligands have the same average length as in solution, the values are in actually good agreement with the available density data obtained from single-crystal X-ray crystallography. For example, for C3 the concentration calculated for the crystal state is 0.69 M, whereas the value calculated from eq. 5 is 0.61 M.

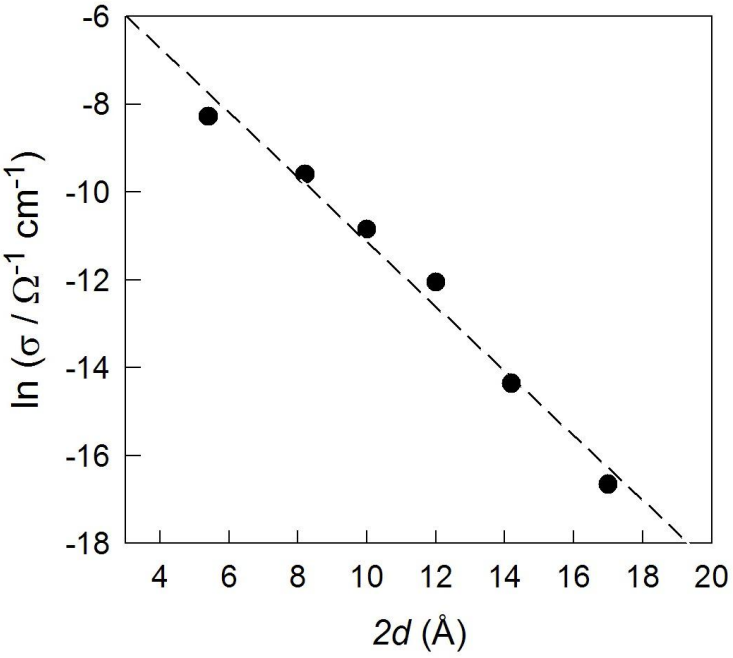

Figure 6. Logarithmic dependence of film conductivity σ (left to right, n = 3, 4, 5, 6, 8, 10) as a function of twice the effective d values of Table 2. Linear regressions correspond to β = 0.74 Å^{-1}.

The electronic conductivity σ can now be converted into the corresponding first-order electron-hopping rate constants k_{ET} (s^{-1}), as done previously for redox polymers and alkanethiolate-protected nanoparticles[4,14,15] with eq. 6:

(6) $$k_{ET} = \frac{6RT\sigma}{10^{-3}F^2\delta^2 C}$$

In eq. 6, it is assumed that the carrier concentration equals the MPC core concentration and this allows normalizing the film conductivity for the nanoparticle's concentration and associated core edge-to-edge distances.

By plotting the so-calculated lnk_{ET} values against the distance, assumed to be the sum of two monolayers thicknesses calculated from the *D* values, we obtain a β value of 0.69 Å^{-1} (Figure 7), *i.e.*, a value that is now not too far from the expected value of 0.79 Å^{-1}. If we use the same abscissa to plot the solution ln*k*°

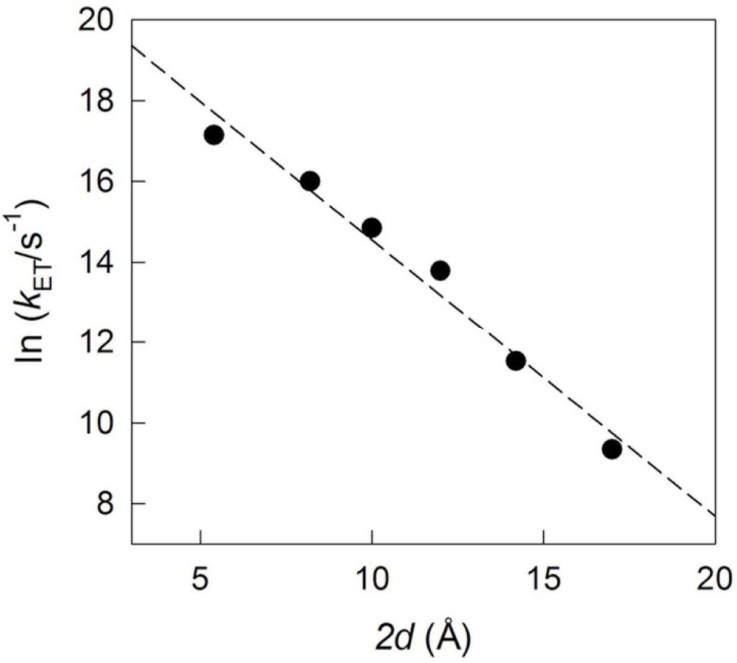

Figure 7. Logarithmic dependence of ET rate constant between MPCs inside the film (left to right, *n* = 3, 4, 5, 6, 8, 10) as a function of twice the length *d* of the capping thiolates obtained from the Stokes-Einstein equation. Linear regressions correspond to β = 0.69 Å^{-1}.

values, the β for the R1 process becomes 0.37 Å^{-1}, that is, a value about ½ of that calculated for the films. This result leads us to conclude that even for the solution state the Stokes radius is not a good descriptor of the effective distance at which the ET takes place. In other words, it is evident that the alkyl chains are rather fluid and this allows for the electrons to tunnel from the electrode to the Au core at a distance substantially shorter than that measured through the average *d*

values calculated from the Stokes radii. The results obtained in the solid state, on the other hand, prove very nicely that while in this physical state the MPCs are in close contact inside the film and that the monolayer thickness now resembles that observed in solution. Nonetheless, the monolayer thickness is still much smaller than that calculated for the fully extended conformation.

5.3.5 Further Insights: The case of $Au_{25}(SMeBu)_{18}$

To further support our conclusion about the dynamic nature of the alkanethiolate chains also in the solid state, we decided to study the behavior, both in solution and in solid state, of a new Au_{25} cluster bringing a more rigid monolayer. We choose to use 2-methyl-1-butanethiol as the ligand, a thiol characterized by the presence of a four-carbon-long chain with a methyl group in the β position to the sulfur. Such branching was expected to induce steric hindrance and thus hamper possible folding effects inside the monolayer. The synthesis and characterization of this nanocluster is fully described in Chapter 6. For this new cluster, $Au_{25}(SMeBu)_{18}$, we measured both the solid state σ (and thus k_{ET}) and the solution ET $k°$. Please note that for this specific thiolate we use the term SMeBu just to stress that the fully-extended length is as that of SBu. The results are shown in Tables 1 and 2.

Figures 8 and 9 show the two plots pertaining to the solid-state and solution phase ET results, respectively. In both cases, *d* is as taken from Table 2. From Figures 8 and 9, it is possible to infer some very interesting conclusions:

(i) When in the monolayer, the 2-methyl-1-butanethiolate ligand is more elongated than the butanethiolate, as revealed by a larger *d* value;

(ii) The ET behavior of $Au_{25}(SMeBu)_{18}$ in the solid state is on the correlation line; however, a slower ET rate and a larger 2*d* value make it display an approximately analogous behavior to that of $Au_{25}(SC\mathit{5})_{18}$, as marked by the red dashed lines;

(iii) In solution, $Au_{25}(SMeBu)_{18}$ behaves quite differently from the other clusters characterized by linear-chain ligands, as its rate constant now falls quite below the correlation line; this is due to a less freely folding monolayer, an effect not seen in the solid state;

(iv) The $Au_{25}(SMeBu)_{18}$ monolayer thickness in solution is comparable to that of a hypothetical $Au_{25}(SC\mathit{7})_{18}$ cluster, as marked by the red dashed lines.

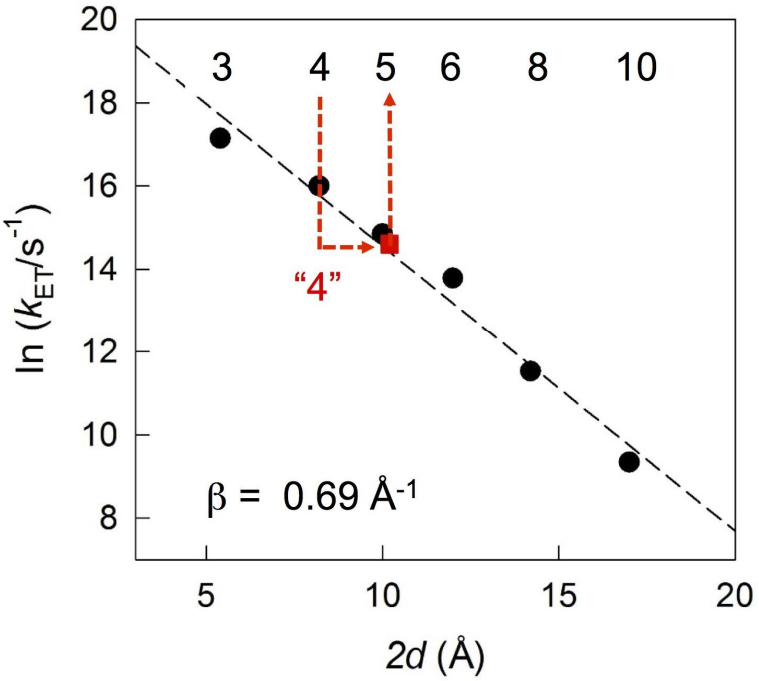

Figure 8. Logarithmic dependence of ET rate constant between the Au_{25} MPCs inside the film (as in Figure 7) with the new data point for $Au_{25}(SMeBu)_{18}$ (red square). The *n* values are also displayed: see text.

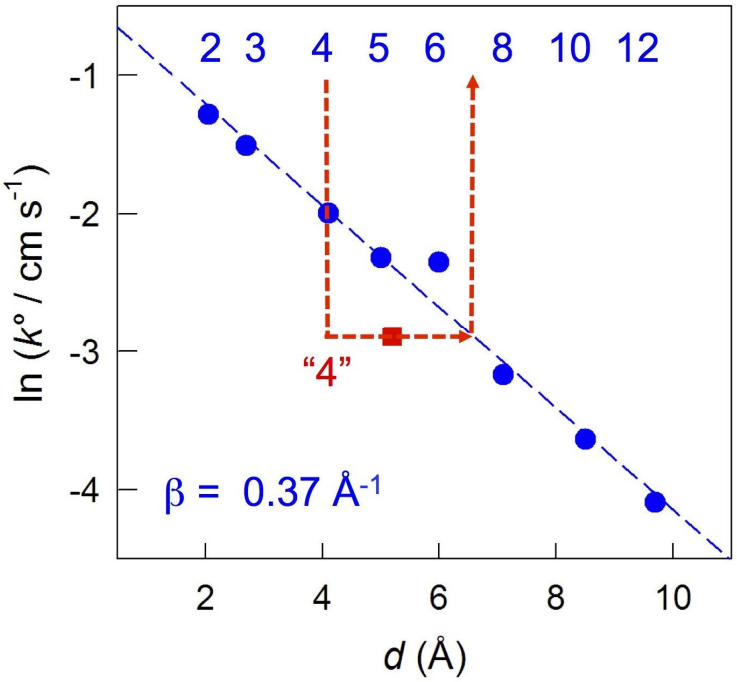

Figure 9. Logarithmic dependence of ET rate constant between the Au_{25} MPCs in solution (as in Figure 1 but for the different *d* value, here taken from Table 2) with the new data point related for $Au_{25}(SMeBu)_{18}$ (red square). The *n* values are also displayed: see text.

5.4 Conclusions

This is the first systematic study on the effect of the monolayer length on the ET between molecular Au_{25} MPC in the solid state. We show that the conductivity of MPC films can be finely tuned by the proper choice of the length and structure of the ligand protecting the Au core. Changing the alkyl chain from C3 to C10 induces a decrease in the film conductivity, σ, of almost 4 orders of magnitude. Our results also reveal that when in film the alkyl chains of the MPCs' monolayer still hold a detectable degree of fluidity, similarly to what observed in solution. The experimental β values allow stating that the average Au core-to-core distance in the film is comparable or even smaller than the average MPC hydrodynamic radius evaluated in solution, which already points to a quite folded monolayer. Compared to the solution ET results, however, the solid sate ET rates point to much less fluid alkyl chains. These conclusions are perfectly confirmed by the results obtained for $Au_{25}(SMeBu)_{18,}$ a cluster characterized by the presence of some steric hindrance in the ligands forming the monolayer.

5.5 Experimental Section

For the conductivity measurements, we used Au interdigitated array (IDA) electrodes manufactured by ALS and consisting of 65 interdigitated Au fingers (length = 2 mm, width = 10 μm, interfinger width = 5 μm, thickness = 0.96 nm). 5 μl of a concentrated DCM solution of the MPC (10 mg/0.1 mL) was drop cast and left to evaporate onto the IDA. The use of a highly concentrated solutions guarantees formation of a film much thicker than the height of the Au fingers and this allows to work under reproducible conditions, as already discussed in detail. The cell constant $C_{cell} = l/A_{total}$ was calculated as described by Choi and Murray,[4] that is, by using for l the IDA gap and for A_{total} the product of the maximum useful conductive MPC film thickness (1 μm) and the finger length (2 mm) times $N - 1$, where N is the total number of fingers (130). Thus, C_{cell} = 0.194 cm^{-1}. The IDA MPC films were dried in vacuum for 30 min: increasing the drying time up to several hours did not affect the measured conductivity values. The bias potential across the IDA fingers was controlled with a CHI 660c electrochemical workstation. The measurements were carried out at 22 °C by scanning the potential between +1 and -1 V, with an initial and final potential of 0 V. The current output was recorded for different potential scan rates in the range from 0.1 to 10 V s^{-1}. No differences were observed by running the experiments in ambient or controlled conditions (vacuum or under an argon atmosphere).

5.6 References

(1) Zabet-Khosousi, A.; Dhirani, A. A. Charge Transport in Nanoparticle Assemblies. *Chem. Rev.* **2008**, *108,* 4072–4124.

(2) Murray, R. W. Nanoelectrochemistry: Metal Nanoparticles, Nanoelectrodes, and Nanopores. *Chem. Rev.* **2008**, *108,* 2688–2720.

(3) Terrill, R. H.; Postlethwaite, T. A.; Chen, C. H.; Poon, C. D.; Terzis, A.; Chen, A.; Hutchison, J. E.; Clark, M. R.; Wignall, G. Monolayers in Three Dimensions: NMR, SAXS, Thermal, and Electron Hopping Studies of Alkanethiol Stabilized Gold Clusters*. J. Am. Chem. Soc.* **1995**, *117*, 12537-12548.

(4) Wuelfing, W. P.; Green, S. J.; Pietron, J. J. ; Cliffel, D. E.; Murray, R. W. Electronic Conductivity of Solid-State, Mixed-Valent, Monolayer-Protected Au Clusters. *J. Am. Chem. Soc.* **2000**, *122*, 11465-11472.

(5) Wuelfing, W. P.; Murray, R. W. Electron Hopping Through Films of Arenethiolate Monolayer-Protected Gold Clusters. *J. Phys. Chem. B* **2002**, *106*, 3139-3145.

(6) Choi, J. P.; Murray, R. W. Electron Self-Exchange between $Au_{140}^{+/0}$ Nanoparticles is Faster than that between $Au_{38}^{+/0}$ in Solid-State, Mixed-Valent Films. *J. Am. Chem. Soc.* **2006**, *128*, 10496-10502.

(7) Carducci, T. M.; Murray, R. W. Kinetics and Low Temperature Studies of Electron Transfers in Films of Small (<2 nm) Au Monolayer Protected Clusters. *J. Am. Chem. Soc.* **2013**, *135*, 11351-11356.

(8) Zamborini, P.; Leopold, M. C.; Hicks, J. F.; Kulesza, P. J.; Malik, M. A.; Murray, R. W. Electron Hopping Conductivity and Vapor Sensing Properties of Flexible Network Polymer Films of Metal Nanoparticles. *J. Am. Chem. Soc.* **2002**, *124*, 8958-8964.

(9) Antonello, S.; Arrigoni, G.; Dainese, T.; De Nardi, M.; Parisio, G.; Perotti, L.; René, A.; Venzo, A.; Maran, F. Electron Transfer through 3D Monolayers on Au_{25} Clusters. *ACS Nano* **2014**, *8*, 2788–2795.

(10) Nicholson, R. S. Theory and Application of Cyclic Voltammetry for Measurement of Electrode Reaction Kinetics. *Anal. Chem*. **1965**, *37*, 1351-1355.

(11) Holmlin, R. E.; Ismagilov, R. F.; Haag, R.; Mujica, V.; Ratner, M. A.; Rampi, M. A.; Whitesides, G. M. Correlating Electron Transport and Molecular Structure in Organic Thin Films. *Angew. Chem. Int. Ed.* **2001**, *40*, 2316-2320.

(12) Paddon-Row, M. N. Superexchange-Mediated Charge Separation and Charge Recombination in Covalently-Linked Donor-Bridge-Acceptor Systems. *Aus. J. Chem.* **2003**, *56*, 729-748.

(13) Peterson, R. R.; Cliffel, D. E. Scanning Electrochemical Microscopy Determination of Organic Soluble MPC Electron-Transfer Rates. *Langmuir* **2006**, *22*, 10307-10314.

(14) Terrill, R. H.; Hutchinson, J. E.; Murray, R. W. Solid State Electron-Hopping Transport and Frozen Concentration Gradients in a Mixed Valent Viologen-Tetraethylene Oxide Copolymer. *J. Phys. Chem. B* **1997**, *101*, 1535.

(15) Hicks, J. F.; Zamborini, F. P.; Osisek, A. J.; Murray, R. W. The Dynamics of Electron Self-Exchange between Nanoparticles *J. Am. Chem. Soc*. **2001**, *123*, 7048-7053.

5.7 Acknowledgements

A special thank is due to Sabrina Antonello for her invaluable assistance in the ET studies.

Chapter 6: Chiral $Au_{25}(SR)_{18}$ Clusters

6.1 Abstract

We prepared a series of monodisperse $Au_{25}[SCH_2CH(CH_3)(C_2H_5)]_{18}$ clusters (hereafter referred to as $Au_{25}(SMeBu)_{18}$) in which the optical purity (enantiomeric excess, e.e.) of the selected ligand (2-methyl-1-butanethiol, HSMeBu) was progressively changed. By using this thiol, we introduced branching, one methyl group in place of one hydrogen at position β with respect to the sulfur atom, along a butanethiolate chain, which thus generates a stereogenic center. Although we used commercially available racemic thiols, we found out that these thiols possess, in fact, an e.e. of the (*S*)-enantiomer, as verified through the synthesis of the pure (*S*)-enantiomer. We prepared several $Au_{25}(SMeBu)_{18}^{0}$ clusters and characterized them extensively. For characterization, we particularly used ^{1}H NMR spectroscopy and circular dichroism (CD) spectroscopy. Both techniques provided the same information: when the e.e. of the thiol employed increases to a value of ca. 75%, the resulting Au_{25} clusters appears to contain only the (*S*)-2-methyl-1-butanethiolate. The results are thus in keeping with the first observation of the phenomenon of spontaneous resolution for an MPC. This conclusion, based on purely spectral data, was perfectly confirmed by solving the single crystal structure of a cluster that, in principle, should have contained thiols possessing 77% e.e. of the (*S*)-enantiomer. Instead, X-ray crystallography showed that only the (*S*)-enantiomer is capping the Au_{25} core.

6.2 Introduction

Chirality is one of the most studied and fascinating phenomena in nature. Its presence in biological systems, such as DNA, RNA, and proteins, fully justifies the demand for the development of drugs, sensors, and catalysts possessing chiral features. Besides chirality in single molecules, the issue of chirality is of paramount interest also for the more complex nanosystems. Chiral nanoparticles can be considered as emerging materials with interesting potentialities, such as photonics[1] and catalysis.[2,3] An excellent review has been published very recently of the chirality in thiolate-protected gold clusters.[4] Chiral metal nanoparticles are particularly interesting because bulk Au and Ag are of face-centered cubic (fcc) structure and, hence, are achiral. An interesting question concerns the origin of

chirality in chiral metal nanoparticles. As a matter of fact, chirality has been found in a variety of nanoparticles.[5-20] Chirality in gold clusters is studied mostly by CD spectroscopy[17,21-25] and single-crystal X-ray diffraction.[14,15] On the other hand, growing high-quality single crystals suitable for X-ray diffraction is inherently very challenging and thus CD turns out to be the most popular method of investigation.

Concerning gold MPCs, an initial report focused on the study of MPCs in which L-glutathione (L-SG) was the protecting ligand.[21] These clusters displayed the CD behavior of the ligand itself (215 nm) but also signal in the metal-based electronic transitions in the visible region. This implied some electronic coupling effect.[6] Preparation of (L-SG)-protected clusters of different size showed that the CD optical behavior depends on size in terms of both the shape and intensity the chiroptical effect.[21] Generally, the use of chiral protective ligands provides the easiest way to impart chirality to MPCs,[2,5,17,18,19,26,27] and the resulting systems display an optical activity that shows the effect of the ligands themselves.[7] Chirality, however, may be intrinsic also of the MPC structure. As a matter of fact, the first structure of a thiolate-protected gold cluster, Au_{102}(p-MBA)$_{44}$ (p-MBA = *para*-mercaptobenzoic acid),[14] revealed that chirality may arise independently of the ligands. In Au_{102}(p-MBA)$_{44}$, as well as in other thiolate-protected gold nanoclusters,[15] the sulfur and the surface gold atoms form shapes (staple motif) in which the protecting ligands are arranged in a chiral fashion. On the other hand, p-MBA is achiral and thus racemic mixtures are obtained: the crystal unit cell is racemic and there is no CD optical behavior in solution. Separation of the enantiomers of $Au_{38}(SC_2H_4Ph)_{24}$ by HPLC enabled the successful measurement of their individual CD spectra.[26] Thermally induced inversion demonstrated that the gold−thiolate interface is quite flexible. $Au_{38}(SC_2H_4Ph)_{24}$ is intrinsically chiral due to the specific binding motif between gold and sulfur: two sulfur atoms stabilize a gold atom, forming -SR-(Au-SR)- or –SR-(Au-SR)$_2$- patterns.[27,28,29] The sulfur atoms become stereogenic centers because they have four different substituents, *i.e.*, two nonequivalent gold atoms, the organic chain, and a lone electron pair.

$Au_{25}(SR)_{18}$ is, instead, achiral. The only way to introduce chirality and study the CD behavior is thus through use of chiral ligands. This has been previously done using the (*R*)- and the (*S*)-isomers of HS-CH_2-$CH(CH_3)$Ph.[23] The two clusters showed specular CD behavior. Main conclusion was that "the mixing of electronic states of ligands with those of surface gold atoms constitutes the

fundamental origin of chirality in such nanoparticles". Knoppe and Bürgi noted[4] that the CD spectra of L-glutathionate,[5] camphorthiolate,[30] and captopril[31] (Au_{25} clusters otherwise displaying the same absorption spectrum of all other $Au_{25}(SR)_{18}$ clusters, including that protected by chiral 1-methyl-2-phenylethylthiolate[23]) are very similar but show differences with respect to the 1-methyl-2-phenylethylthiolate-protectd Au_{25} clusters.[23] This could be related to steric hindrance differences, the latter being less bulky than the aforementioned ligands.[31]

6.3 Results and Discussion

6.3.1 Synthesis of the Chiral Thiol

The synthesis of the enantiopure (S)-(-)-2-methyl-1-butanethiol was performed starting from the enantiopure (S)-(-)-2-methyl-1-butanol according to a known procedure.[32] The synthesis is a summarized in Figure 1.

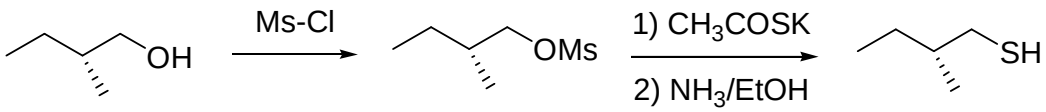

Figure 1. Reaction scheme of the conversion of the (*S*)-(-)-2-methyl-1-butanol into the enantiopure (*S*)-(-)-2-methyl-1-butanethiol.

A solution of the (*S*)-(-)-2-methyl-1-butanol (5.0 g, 6.1 ml, 56.7 mmol), triethylamine (16 ml, 113.4 mmol, 2 equiv), and tetrahydrofuran (100 ml) was stirred together at 0 °C, and then methylsufonyl chloride (5.5 ml, 70.9 mmol, 1.25 equiv) was added dropwise. After stirring for 2 h, the solution was extracted with DCM (3 x 50 ml) and washed by water. The organic phase was dried by Na_2SO_4 then evaporated to give (*S*)-2-methylbutyl methanesulfonate. A solution of (*S*)-2-methylbutyl methanesulfonate (9.42 g, 56.7 mmol) and potassium thioacetate (7.77 g, 68 mmol) dissolved in 200 ml of *N,N*-dimethylformamide was stirred at room temperature over 3 days. Then, 300 ml cold water was added and the mixture was extracted with DCM several times (3 x 100 ml). The organic phases were combined, dried with Na_2SO_4, and the solvent evaporated to give (*S*)-2-methylbutyl thioacetate. The product was purified by flash chromatography, using as eluent cyclohexane and then mixtures cyclohexane-DCM (10:1, 9:3 and 9:4), and finally distilled at normal pressure. ^{1}H NMR (200 MHz, $CDCl_3$): δ 0.8-0.9 (6H, m), 1.1-1.3 (1H, m), 1.3-1.6 (2H, m), 2.3 (3H, s), 2.7-3.0 (2H, m).

(S)-2-Methylbutyl thioacetate (1.5 g) was dissolved in methanol (1.5 ml) and then 0.5 ml of anhydrous ammonia solution (7 M) in methanol was added. The solution was stirred at room temperature until TLC showed no presence of the starting material. The solution was evaporated almost to dryness and extracted a few times with pentane. (*S*)-(-)-2-methyl-1-butanethiol was obtained by silica-gel chromatographic purification with cyclohexane.

6.3.2 Polarimetry and CD Spectroscopy of the Thiols

(*S*)-(-)-2-Methyl-1-butanethiol and the corresponding formally racemic 2-methyl-1-butanethiol samples purchased from Sigma-Aldrich and Alfa Aesar (hereafter referred to as SA-HSMeBu and AA-HSMeBu, respectively) were characterized by polarimetry and CD spectroscopy. As a reference, we employed the same enantiomeric pure (*S*)-(-)-2-methyl-1-butanol used in the synthesis of the enantiopure (*S*)-(-)-2-methyl-1-butanethiol. The measured specific rotation of the (*S*)-(-)-2-methylbutanol sample (neat) was found to be $[\alpha]_D^{24} = -(5.5 \pm 0.1)$ deg dm^{-1} cm^{-3} g^{-1}; the producer, Sigma Aldrich, provides a value of $[\alpha]_D^{23} = -5.8$ deg dm^{-1} cm^{-3} g^{-1} (neat).[33]

The optical rotations of the three thiols were measured both in acetonitrile and dimethyl sulfoxide, at various concentrations. Acetonitrile was chosen due to its high transparency at short wavelengths, at which the CD measurements were performed. Dimethyl sulfoxide, on the other hand, was the solvent employed in the only report concerning the specific rotation of (*S*)-(-)-2-methylbutanethiol.[34] Whereas such literature value is +3.1 deg dm^{-1} cm^{-3} g^{-1}, under the same experimental conditions we obtained the larger value of +6.1 ± 0.8 deg dm^{-1} cm^{-3} g^{-1}. Overall, these measurements thus ensure that (*S*)-(-)-2-methylbutanethiol had the same enantiopurity of the enantiopure (*S*)-(-)-2-methylbutanol used in its synthesis. Table 1 gathers these polarimetric results.

On these grounds, the specific rotations of the two commercial thiols were estimated using the weighted average of the measurements performed in acetonitrile, using 3 different concentrations. The results obtained in acetonitrile were, in fact, considered more reliable than those obtained in dimethyl sulfoxides. The e.e. of the commercial thiols was determined from the ratio between the experimental specific rotations and that of the enantiopure (*S*)-(−)-2-methyl-1-butanethiol that we synthesized. This led us to the discovery that the Alfa-Aesar and Sigma-Aldrich thiols were not racemic as declared, but rather had an (*S*)-e.e. of 77 ± 2 and 35 ± 2 %, respectively.

Table 1. Specific rotation values and experimental conditions employed for the studied compounds.

Sample	Solvent	Concentration (M)	Specific Rotation $[\alpha]_D^{24}$ (deg dm^{-1} cm^{-3} g^{-1})
(*S*)-(-)-2-HOMeBu[a]	-	Neat	-5.8
(*S*)-(-)-2-HOMeBu	-	Neat	- 5.5 ± 0.1
(*S*)-(-)-2-HSMeBu	MeCN	0.2	+ 5.1 ± 0.4
(*S*)-(-)-2-HSMeBu	MeCN	0.1	+ 4.6 ± 0.6
(*S*)-(-)-2-HSMeBu	MeCN	0.05	+ 4.2 ± 0.7
(*S*)-(-)-2-HSMeBu	DMSO	0.2	+ 6.6 ± 0.5
(*S*)-(-)-2-HSMeBu	DMSO	0.1	+ 6.1 ± 0.8
(*S*)-(-)-2-HSMeBu[b]	DMSO	0.096	+ 3.1
AA-HSMeBu	MeCN	0.2	+ 4.0 ± 0.3
AA-HSMeBu	MeCN	0.1	+ 3.6 ± 0.5
AA-HSMeBu	MeCN	0.05	+ 3.0 ± 0.5
AA-HSMeBu	DMSO	0.2	+ 4.5 ± 0.7
AA-HSMeBu	DMSO	0.1	+ 3.6 ± 0.8
SA-HSMeBu	MeCN	0.2	+ 1.8 ± 0.1
SA-HSMeBu	MeCN	0.1	+ 1.7 ± 0.1
SA-HSMeBu	MeCN	0.05	+ 1.4 ± 0.1

[a] Reference 33. [b] Reference 34.

To confirm this unexpected e.e. determination outcome, we carried out CD spectroscopy measurements. The solvent employed in the CD measurements was acetonitrile (cutoff wavelength at 200 nm). Figure 2 shows the CD spectra of the 3 thiols. The CD spectra show that the AA-HSMeBu sample gives a slightly less intense signal than (*S*)-(-)-2-methyl-1-butanethiol. The SA-HSMeBu sample gives a much less intense signal but still significantly higher than zero. The CD results thus confirm the relative e.e. order of the three thiols. The e.e. values (areas and intensities provide very similar values) measured with reference to the enantiopure (*S*)-(-)-2-methyl-1-butanethiol, however, are slightly larger than those estimated from the polarimetry measurements, the (*S*)-e.e. values being 88 and 46% for AA-HSMeBu and SA-HSMeBu, respectively. Particularly because of the experimental noise, these results are considered comparatively less reliable than those obtained from the

polarimetric measurements. In the following, we will thus refer to the e.e. values obtained with the latter approach.

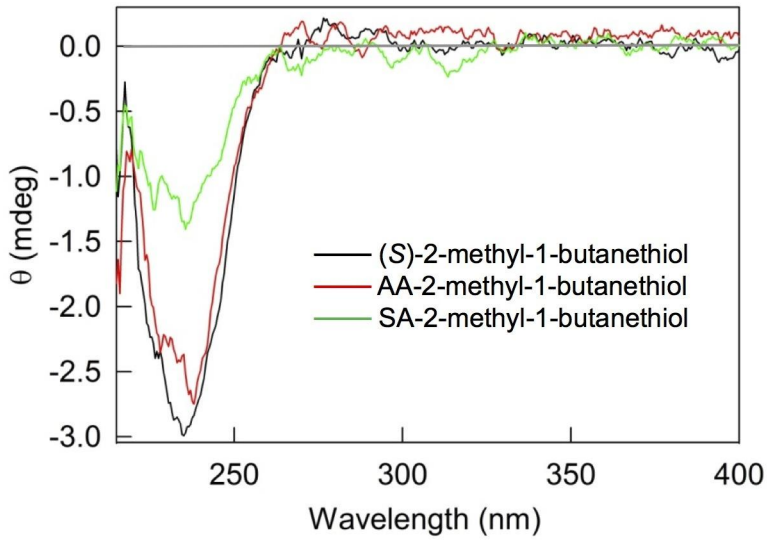

Figure 2. CD spectra of (*S*)-(-)-2-methyl-1-butanethiol, AA-HSMeBu, and SA-HSMeBu.

6.3.3 Synthesis of $Au_{25}(SMeBu)_{18}$

The clusters $[n\text{-}Oct_4N^+][Au_{25}(SMeBu)_{18}^-]$ were synthesized using each of the above three thiols but also selected mixtures of the AA and SA samples. By this strategy, we aimed to modulate the e.e. of the ligands employed for the synthesis. Thus, we prepared the following set of clusters (the optical purity is defined on the basis of the polarimetric results):

Sample A :	SA 100%	35% (*S*)-e.e.
Sample B :	SA-AA 40-60%	60% (*S*)-e.e.
Sample C :	SA-AA 20-80%	69% (*S*)-e.e.
Sample D :	SA-AA 13-87%	72% (*S*)-e.e.
Sample E :	SA-AA 7-93%	74% (*S*)-e.e.
Sample F :	AA 100%	77% (*S*)-e.e.
Sample G :	(*S*)-HSMeBu	100% (*S*)-e.e.

No appreciable differences were observed during the preparation of the different clusters. A typical synthesis of $[n\text{-}Oct_4N^+][Au_{25}(SMeBu)_{18}^-]$ was carried out as follows. 0.50 g (1.27 mmol) of $HAuCl_4 \cdot 3H_2O$ was dissolved in 40 ml THF, and then 0.833 g of tetra-*n*-octylammonium bromide (1.52 mmol, 1.2 equiv) was added. The resulting red solution was stirred for 15 min at 20 °C. The stirring

speed was set to 100 rpm and 0.940 ml (7.62 mmol, 6 equiv) of 2-methyl-1-butanethiol, dissolved in 10 ml of THF, was added dropwise over a period of ca. 3 min. The solution became yellow and then, after ca. 30 min, colorless. The stirring speed was increased to 600 rpm and a freshly prepared icy-cold solution (10 ml) of $NaBH_4$ (0.48 g, 12.7 mmol, 10 equiv) in water was quickly added to the mixture, which was kept at room temperature. The solution immediately became black, as expected. The reaction progress was monitored by UV-vis absorption spectroscopy, which allowed us to understand that in less than 24 h the reaction mixture could be halted by filtering on paper to remove insoluble white residues. The filtered solution had a dark-brown color with orange hues. THF was removed with a rotary evaporator to leave a reddish-brown oily solid covered by residual H_2O from aq. $NaBH_4$. The water phase was removed, and the solid was dissolved in toluene and washed with water (4 x 40 ml) in a separatory funnel. Toluene was evaporated and the product was dissolved in 50 ml of DCM and left to rest for about 12 h in the dark, at 4°C. By this procedure, the cluster is obtained as [*n*-Oct_4N^+][$Au_{25}(SMeBu)_{18}^-$]. The product was further purified or oxidized. In the first case, the solid was dissolved in diethyl ether, which leaves undissolved most of residual tetraoctylammonium salt. The solvent was evaporated and the solid quickly washed thrice with icy-cold methanol to remove the remaining salt. The red-brownish solid was finally dried. [*n*-Oct_4N^+][$Au_{25}(SMeBu)_{18}^-$] is slightly soluble in alkanes (unlike other $Au_{25}(SR)_{18}^-$ nanoparticles protected with alkanethiols of comparable length) and, more generally, in all those solvents that can dissolve the neutral form of the cluster. This prevents a complete separation of the anionic nanoparticle from its oxidized counterpart. Oxidation of [*n*-Oct_4N^+][$Au_{25}(SMeBu)_{18}^-$] to its neutral form was accomplished by dissolution in DCM followed by passage through a silica gel column under aerobic conditions, as described in Section 2.2. DCM was rotary evaporated to leave a greenish-black oily solid. This latter was washed a few times with acetonitrile to obtain a black powder corresponding to pure $Au_{25}(SMeBu)_{18}^0$.

6.3.4 Optical and Electrochemical Behaviors

Figure 3 compares the UV-vis spectrum of $Au_{25}(SMeBu)_{18}^0$ (sample G, enantiopure thiol) and of $Au_{25}(SBu)_{18}^0$, both dissolved in pentane. The spectra of the two clusters show minor differences in optical behavior. This is the case of the relative minimum at 375 nm (for $Au_{25}(SMeBu)_{18}^0$, the dip is less pronounced) and in the derivative spectrum at 660 nm. We note that these minor differences

are not due to impurities (ruled out by the NMR analysis) and they are also present in all other $Au_{25}(SMeBu)_{18}^{0}$ prepared starting from the various thiol mixtures. Hence, these features can be attributed to the presence of a secondary carbon in the β position and to the effect of steric hindrance on the monolayer properties.

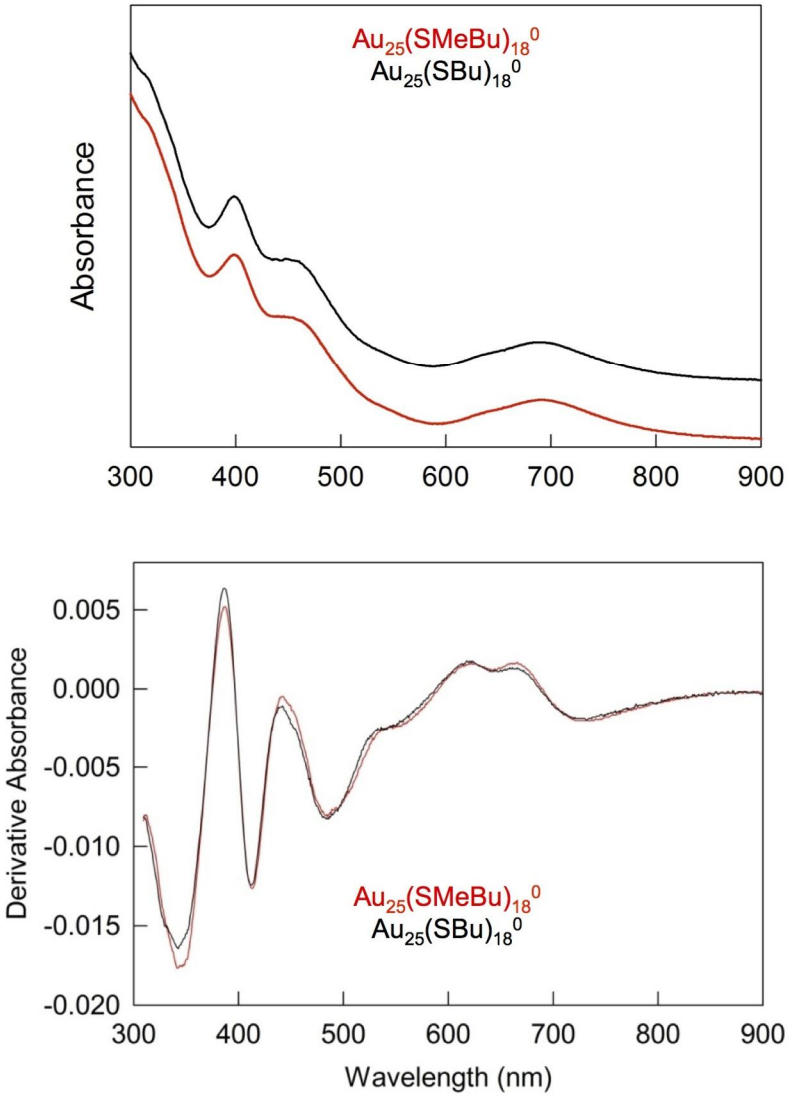

Figure 3. Comparison of the UV-vis absorption spectra (upper graph: for the sake of better comparison, the curves have been shifted vertically) and their derivatives (bottom graph) for $Au_{25}(SMeBu)_{18}^{0}$ (sample G, enantiopure thiol, red curve) and of $Au_{25}(SBu)_{18}$ (black curve). Both spectra were obtained using a quartz cuvette with a 2 mm optical-path length, at room temperature.

That the synthesis truly yields the "usual" Au_{25} cluster is also supported by the DPV analysis. Figure 4 shows a comparison between the two patterns obtained for $Au_{25}(SMeBu)_{18}^0$ (sample F, AA-HSMeBu) and the corresponding $Au_{25}(SBu)_{18}^0$. Because of the same fully-extended length, the latter is considered to be the perfect reference cluster for evaluating the DPV behavior of the $Au_{25}(SMeBu)_{18}^0$ clusters. The DPVs are quite similar and this clearly shows that $Au_{25}(SMeBu)_{18}^0$ has the same stoichiometry and properties as $Au_{25}(SBu)_{18}^0$, as also inferred from the optical behavior. Still, however, some differences are evident. The two reversible peaks near 0 V are less positive than those observed for the reference cluster, a fact that can be attributed to the inductive effect of the methyl group at the β position and thus to stabilization of a positive charge (easier oxidation) and destabilization of a negative charge (more difficult reduction). For the new cluster, the peak for the formation of the dianion (just below -2 V) is less irreversible, probably because of a stiffer monolayer, as also inferred from the solid-state and solution phase ET measurements (Section 5.3.5). The relative potential values for the two most positive peaks are also appreciably different. We have not investigated these differences further because for the sake of this specific research the important aspect was to prepare clusters having the usual structure (see, also, Section 6.3.5).

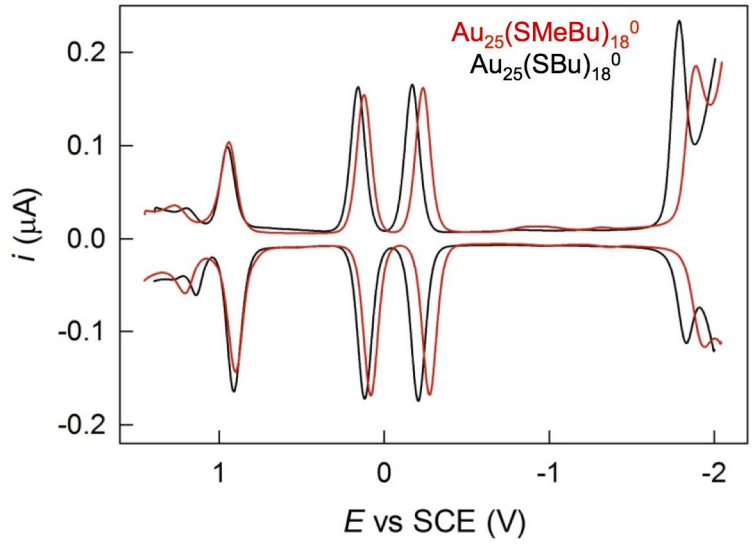

Figure 4. DPV of 1 mM $Au_{25}(SMeBu)_{18}^0$ and $Au_{25}(SBu)_{18}^0$ in DCM/0.1 M TBAH. Glassy-carbon electrode, 25 °C.

6.3.5 The X-ray Structure

Careful recrystallization of $Au_{25}(SMeBu)_{18}^{0}$ (sample F, AA-HSMeBu) toluene-acetonitrile led to nice crystals that were analyzed by X-ray crystallographic analysis. We note that the AA-HSMeBu sample possesses a 77% e.e. of the (*S*)-enantiomer. Instead, the structure of the corresponding $Au_{25}(SMeBu)_{18}^{0}$ clusters reveals the astonishing surprise that only the (*S*)-(-)-2-methyl-1-butanethiolate ligands protect the Au cluster. This is shown in Figure 5. Although we are currently trying to collect the X-ray crystallographic data also for other samples, we do not expect this to be possible for clusters stabilized by less (*S*)-rich thiols and thus clusters capped by different stereochemical scenarios. This result is thus in keeping with the first observation of the phenomenon of spontaneous resolution for an MPC.

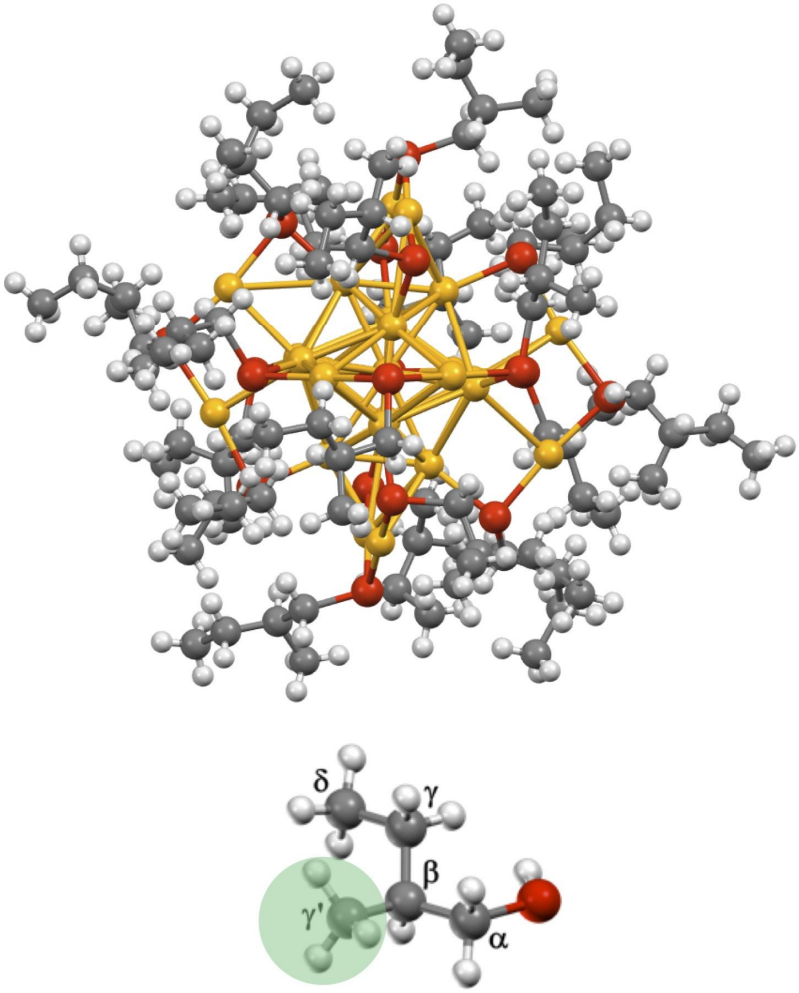

Figure 5. Ball-and-stick projection showing the X-ray crystal structure of $Au_{25}(SMeBu)_{18}^{0}$. Au = yellow, S = red, C = gray, H = white. The structure of the thiol is also shown.

6.3.6 CD Spectroscopy of $Au_{25}(SMeBu)_{18}$

The CD measurements were performed in hexane solutions, accurately checking the concentrations of the various samples. Hexane was chosen as the solvent because of its transparency up to 200 nm and its chemical inertness. Figure 6 shows a qualitative comparison between the CD spectrum of the $Au_{25}(SMeBu)_{18}$ (sample G, enantiopure (S)-2-methyl-1-butanethiol) and that of $Au_{25}[(R)\text{-}SCH_2CH(CH_3)Ph)]_{18}$,[23] which is the $Au_{25}(SR)_{18}$ cluster protected by the chiral ligand closer to those employed in our current study. The CD spectra show similar general features. Not shown is the band corresponding to the chiral thiols themselves. This comparison shows that the main features are thus to be related to some mixing of electronic states of ligands with those of surface gold atoms, as already inferred.[4,23]

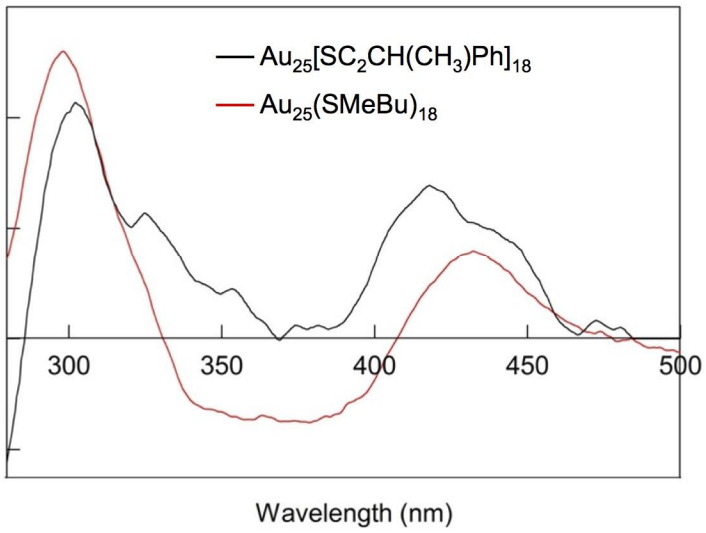

Figure 6. Qualitative comparison of the CD spectra of $Au_{25}(SMeBu)_{18}{}^{0}$ (sample G, enantiopure thiol, red curve) and of $Au_{25}[(R)\text{-}SCH_2CH(CH_3)Ph)]_{18}$ (black curve).[23]

The clusters synthesized starting from thiols characterized by different e.e. values were analyzed by CD spectroscopy. Unfortunately, owing to problems happened during the CD measurements, we cannot provide the analogous spectrum (*i.e.*, under the same experimental conditions) for sample G (100% (*S*)-(−)-2-methyl-1-butanethiol). The results, obtained under exactly the same experimental conditions, are compared in Figure 7. Experimental issues do not allow recording the CD spectra of the clusters in the spectral range corresponding to particularly small wavelengths, as it was possible for the three thiols (*cf*. Figure 2). We could still detect, however, the maximum for the first

band at 215 nm. Figure 7 suggests that the band peaking at ca. 240 nm is particularly suitable to attempt a quantitative evaluation of the intensity and area as a function of the e.e. in the (*S*)-enantiomer. Figures 8a and 8b show the resulting plots. The other bands do not allow performing a similar comparison. Figures 8a and 8b illustrate that no matter how the CD spectra are processed, the signal generally increases as the e.e. also increases. However, some saturation effect starts emerging at 70-75%, as if the amount of the (*S*)-enantiomer in the monolayer is reaching its maximum value. Qualitatively, within the limits of the aforementioned reasons, the cluster prepared from (S)-2-methyl-1-butanethiol is in agreement with this pattern. More important, this pattern is in line with the outcome of the X-ray crystallographic analysis of the cluster sample prepared from the 77% e.e.-(*S*) thiol (Section 6.3.5).

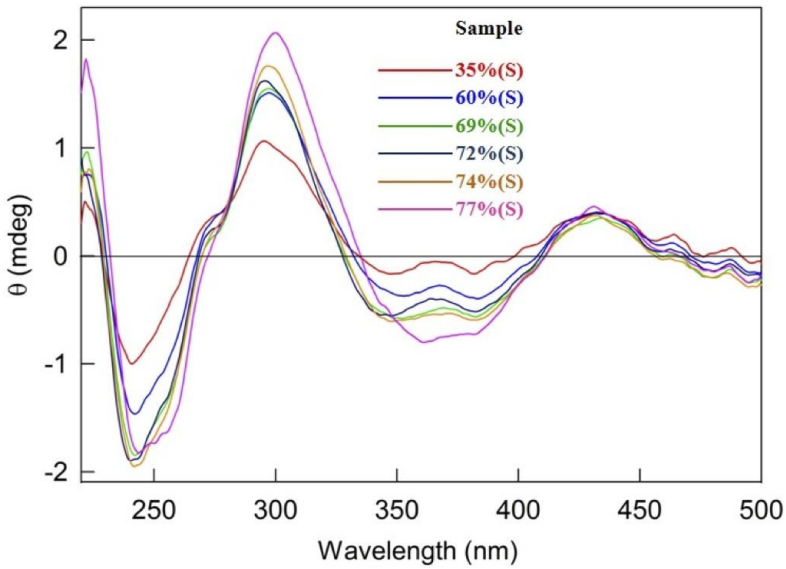

Figure 7. Comparison of the CD spectra of the clusters $Au_{25}(SMeBu)_{18}^{0}$ as a function of the e.e. of the thiol employed for the synthesis. As shown in the legend, the e.e. varies from 35 to 77 % in the (*S*)-isomer. The measurements were performed in a quartz cuvette with an optical path of 10 mm. All clusters were dissolved in hexane at an accurately checked concentration of 3.72 x 10^{-6} M, corresponding to an absorbance of 0.2 at 401 nm. 4 s response time.

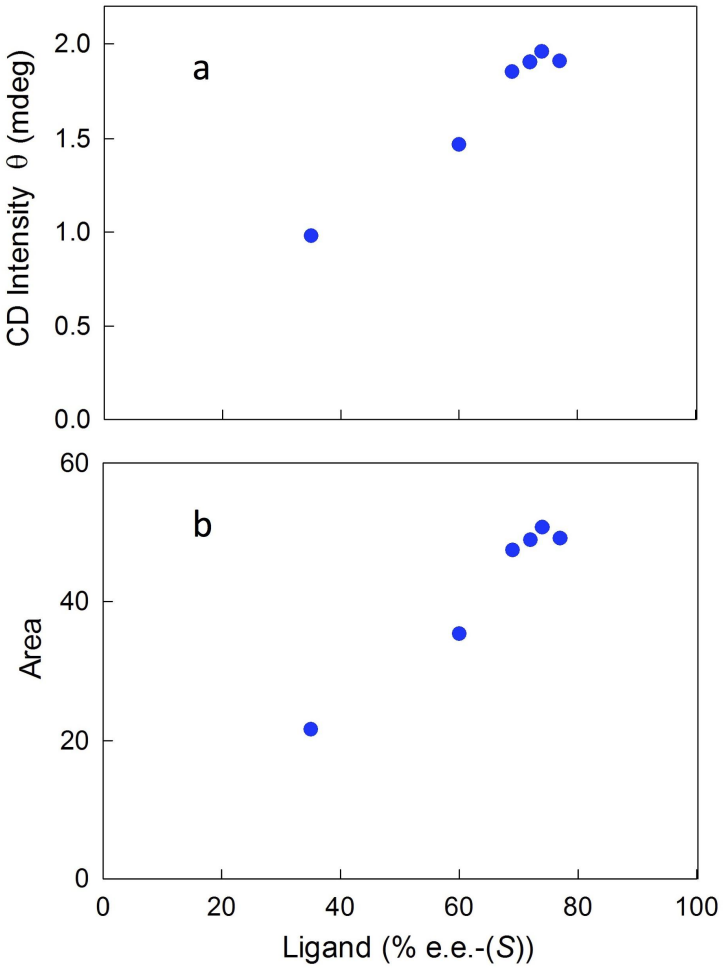

Figure 8. Dependencies of (a) intensity and (b) area on the original thiol e.e.-(*S*). The results pertain to the band that peaks at ca. 240 nm, which magnifies the e.e. effect.

6.3.7 NMR of $Au_{25}(SMeBu)_{18}$

As already described in detail, in $Au_{25}(SR)_{18}$ clusters the 18 thiolated ligands split into a group of 12 inner ligands and 6 outer ligands. The two groups of ligands display distinct NMR spectroscopy patterns, a difference that is magnified when the cluster becomes paramagnetic.[35-37] Figure 9 compares the ^{1}H NMR spectra of the native cluster $[n\text{-}Oct_4N^+][Au_{25}(SMeBu)_{18}^-]$ and its oxidized form, $Au_{25}(SMeBu)_{18}^0$. Both spectra were obtained in dichloromethane-d_2 at 25 °C, 3 mM, and pertain to the clusters prepared from the AA-HSMeBu thiol. The proton assignments were performed by standard chemical shift correlations as well as by 2D correlation spectroscopy (COSY), total correlation spectroscopy (TOCSY), and nuclear Overhauser enhancement spectroscopy (NOESY) experiments, as already described for the other Au_{25} clusters.

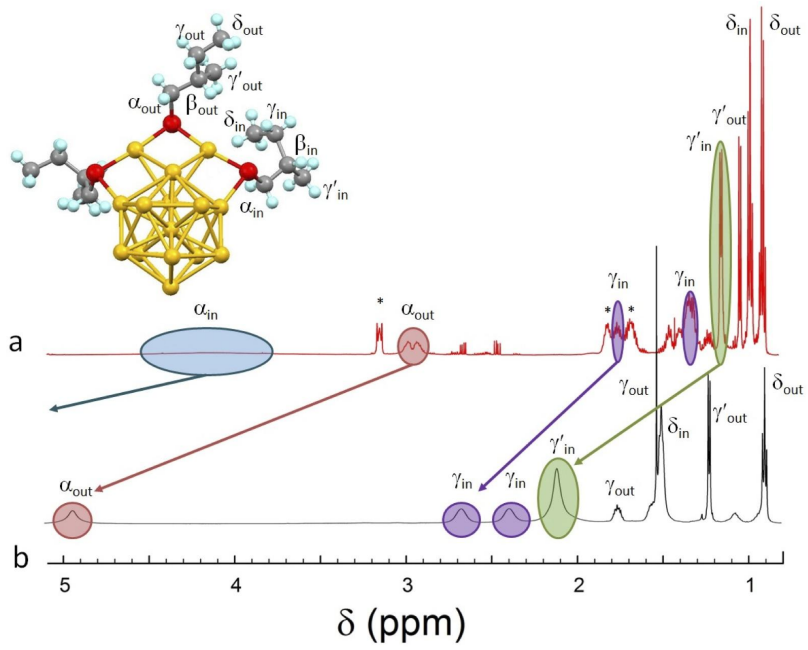

Figure 9. ^{1}H NMR spectrum of [n-Oct$_4$N$^+$][Au$_{25}$(SMeBu)$_{18}^-$] (a, red line). The peaks marked with an asterisk (*) pertain to n-Oct$_4$N$^+$. (b) ^{1}H NMR spectrum of Au$_{25}$(SMeBu)$_{18}^0$. Both samples were in dichloromethane-d_2 at 25 °C. Symbols α and γ refer to the positions of inner and outer methylene groups from sulfur, as indicated in the structure (for clarity, only one staple is displayed). Symbol β pertains to the secondary carbon of the ligand, γ' and δ correspond with the methyl groups. Arrows indicate the most significant shifts observed upon oxidation of Au$_{25}$(SMeBu)$_{18}^-$ to Au$_{25}$(SMeBu)$_{18}^0$. In the oxidized cluster the (α-CH$_2$)$_{in}$ resonance is at about 13 ppm.

We note that so far it was not possible to completely purify the anionic cluster [n-Oct$_4$N$^+$][Au$_{25}$(SMeBu)$_{18}^-$], as could be possible for all linear alkanethiolate-protected cluster. In fact, the signals pertaining to the free thiol are still visible in ^{1}H NMR spectrum of the anion, especially in the region around at 2.5 ppm. The strong broadening of the resonances, particularly that of the α-methylene of the inner ligands, is due to presence of traces of the paramagnetic oxidized cluster. Instead, the Au$_{25}$(SMeBu)$_{18}^0$ cluster, which is the subject of this Chapter, is void of contaminations.

Figure 9 illustrates that the effect of the unpaired electron mostly concerns all the groups in positions α, β, γ and δ of the inner ligands and the α methylene of the outer ligands (at room temperature, the β resonances are hidden under more intense signals: see below). This NMR behavior is caused by the contact

interaction of the nuclear magnetic moments with the unpaired electron and can be taken as a probe of whether the SOMO, and thus the spin density, spreads onto those specific nuclei. Differently from $Au_{25}(SC_nH_{2n+1})_{18}$, however, some resonances split owing to the presence of the stereogenic carbon in the β positions of the ligands, as expected for a chiral molecule.[38]

To study the effect of changing the e.e. of the thiols used to prepare the MPC, we used benzene-d_6 as the deuterated solvent. This choice was dictated by possible comparisons with the other Au_{25} MPCs, but also to perform measurements at higher temperatures. Figure 10 compares the ^{1}H NMR spectra of $Au_{25}(SMeBu)_{18}^0$, obtained from AA-HSMeBu (77% e.e. in the (*S*)-isomer) at 25 (black line) and 75 °C (red line). The usefulness of the high-temperature measurements is evident in that the resonances become more resolved, and some signals that at room temperature are concealed by accidental superposition to other stronger peaks become clearly separated.

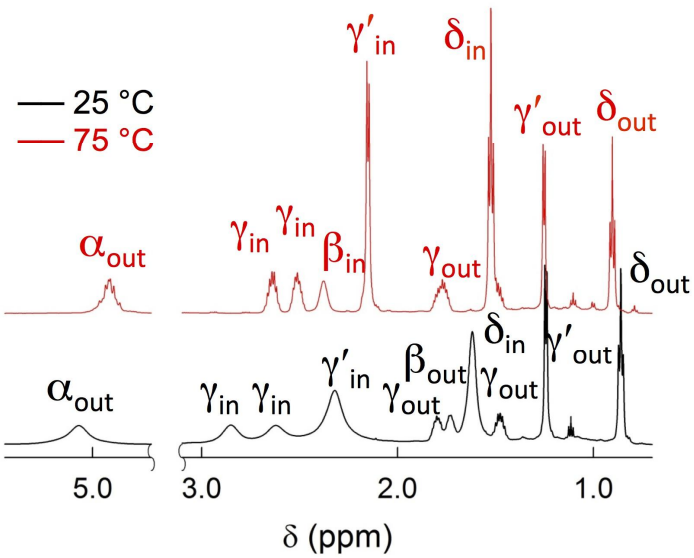

Figure 10. ^{1}H NMR spectrum of $Au_{25}(SMeBu)_{18}^0$ at 25 (black line) and 75 °C (red line) in benzene-d_6.

Figure 11 illustrates the behavior of the α-$(CH_2)_{in}$ resonance, as the temperature changes from 25 to 75 °C. As for the clusters $Au_{25}(SR)_{18}^0$ protected with linear alkanethiols, these methylene protons have a resonance strongly broadened and shifted to low field, in this case to ca. 13 ppm at room temperature. In fact, this δ value is decisively smaller than that observed for a number of $Au_{25}(SR)_{18}^0$ clusters protected by linear-chain thiolates: under the same conditions (temperature, solvent, concentration), it is routinely located at 25

ppm. In the case of $Au_{25}(SMeBu)_{18}^{0}$, increasing the temperature initially shifts the broad peak toward lower fields (in contrast with the behavior of linear-chain thiolate-protected $Au_{25}(SR)_{18}^{0}$, for which the shift is always in the opposite direction), while the peak width sensibly decreases. At about 50-60 °C, however, the shift trend is inverted, and the signal slightly move to high field. The fact that the peak doubles and the general behavior can be ascribed to the presence of the secondary, chiral carbon at the β position.

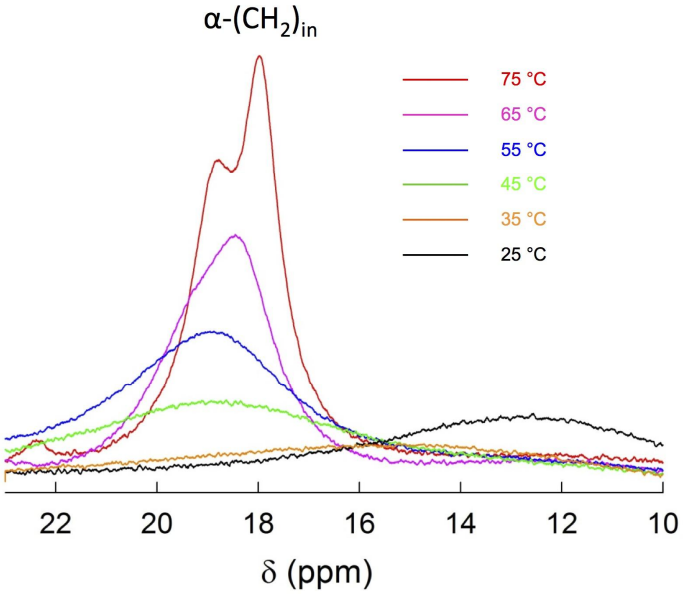

Figure 11. Variation of the position of the α-$(CH_2)_{in}$ resonance of 3 mM $Au_{25}(SMeBu)_{18}^{0}$ (sample F) as the temperature changes from 25 to 75 °C.

Figures 12-15 show how other main resonances of $Au_{25}(SMeBu)_{18}^{0}$ change with temperature (In all cases, the sample is F): they feature α-$(CH_2)_{out}$, the couple of γ-$(CH_2)_{in}$ signals, β-$(CH)_{in}$ and the couple of γ'-$(CH_3)_{in}$ signals, and the series of peaks pertaining to γ-$(CH_2)_{out}$, β-$(CH)_{out}$, δ-$(CH_3)_{in}$, and γ-$(CH_2)_{out}$. The outer-ligands' γ′ and δ methyl resonances do not change appreciably in chemical shift and shape. The spectra at the different temperatures were normalized by matching the intensities of the δ methyl of the outer ligand.

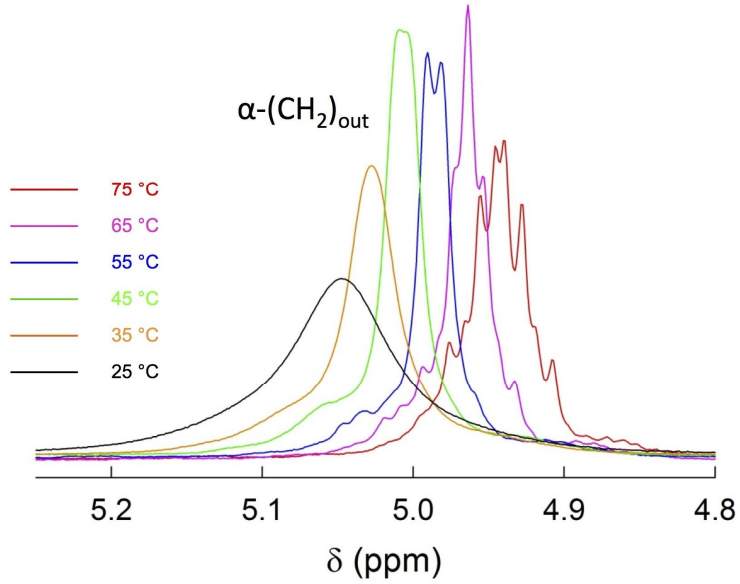

Figure 12. Variation of the position of the α-$(CH_2)_{out}$ resonance of 3 mM $Au_{25}(SMeBu)_{18}^0$ (sample F) as the temperature changes from 25 to 75 °C.

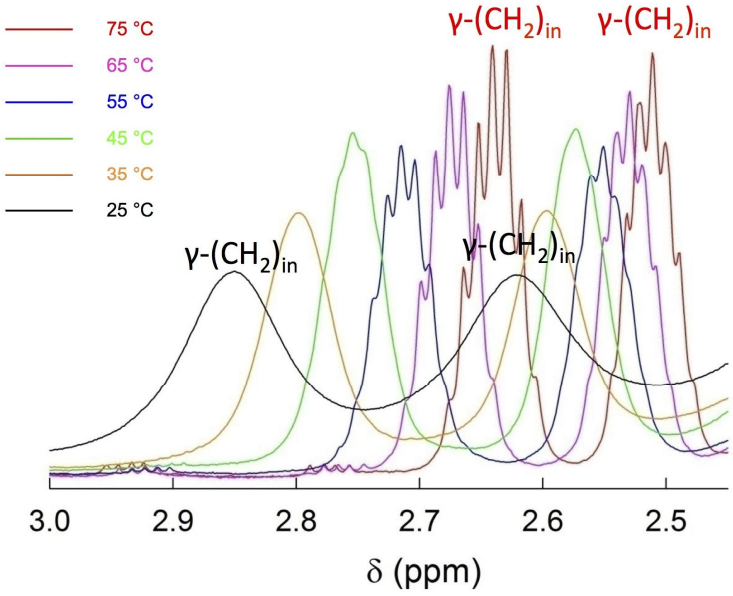

Figure 13. Variation of the position of the γ-$(CH_2)_{in}$ resonances of 3 mM $Au_{25}(SMeBu)_{18}^0$ (sample F) as the temperature changes from 25 to 75 °C.

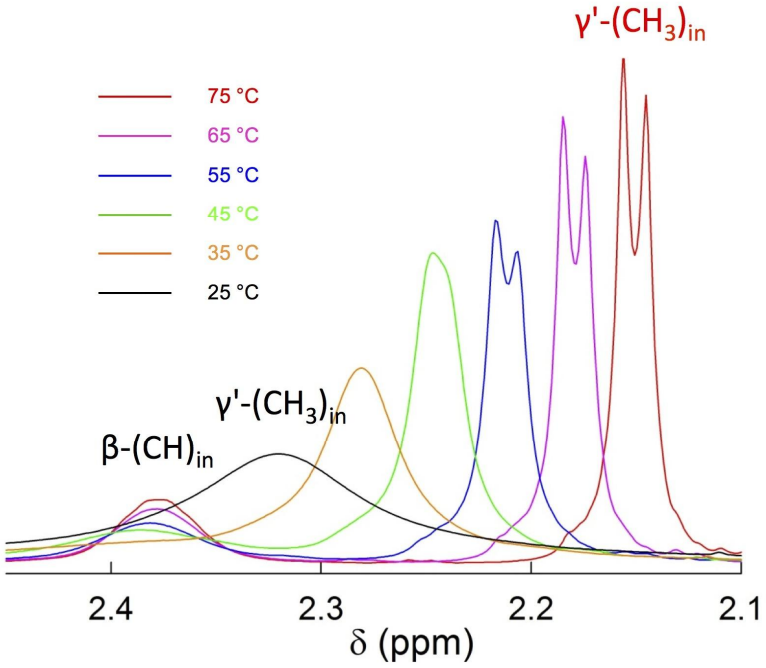

Figure 14. Variation of the position of the β-$(CH)_{in}$ and the couple of γ'-$(CH_3)_{in}$ resonances of 3 mM $Au_{25}(SMeBu)_{18}^{0}$ (sample F) as the temperature changes from 25 to 75 °C.

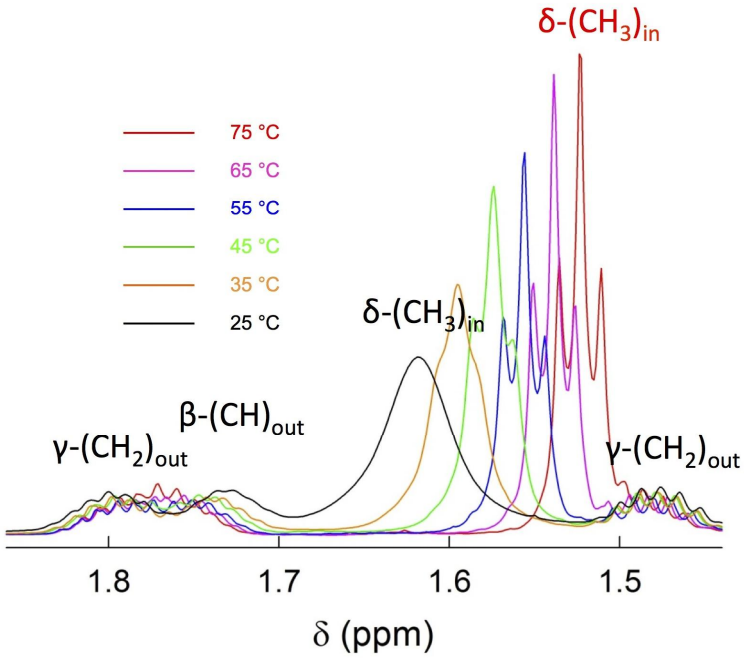

Figure 15. Variation of the position of the β-$(CH)_{out}$, the couple of δ-$(CH_3)_{in}$, and the couple of γ-$(CH_2)_{out}$ resonances of 3 mM $Au_{25}(SMeBu)_{18}^{0}$ (sample F) as the temperature changes from 25 to 75 °C.

On these grounds, we carried out an extensive analysis of the influence of the e.e. of the ligands on the NMR behavior. Figure 16 show the typical effect of changing this parameter on the NMR pattern at high field values.

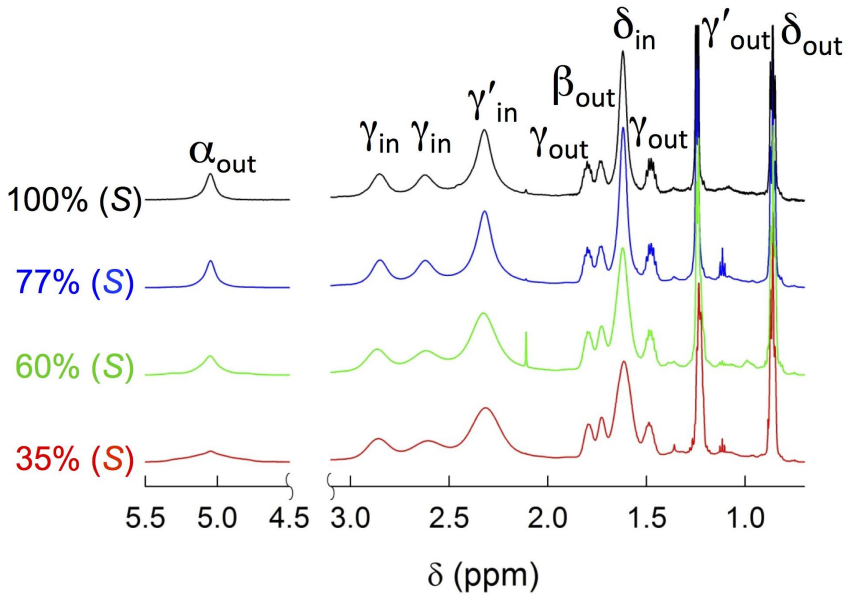

Figure 16. ^{1}H NMR spectra of 3 mM $Au_{25}(SMeBu)_{18}^{0}$ samples, corresponding to (top to bottom) 100, 77, 60, and 35% e.e. in the (*S*)-thiol used in the synthesis. Benzene-d_6, 25 °C.

Figure 16 illustrates a detectable effect of e.e. of the clusters on the width of most ^{1}H NMR peaks. Some resonances are particularly sensitive to this parameter and show that the trend is that when the e.e. increases, the width decreases (sharper peaks) accordingly. We speculated that this effect is caused by an increase of the different chemical environments experienced by different proportions of the (*R*)- and (*S*)-isomers inside the monolayer. Indeed, we should note that different individual clusters may be capped by thiolates of slightly different e.e., in analogy with what happens for monolayers containing two different thiolates as obtained by ligand place exchange.[39] Even by considering an exactly identical e.e. in the monolayer, one cannot exclude differences in terms of location of the various (*R*)- and (*S*)-isomers; the fact that the clusters are protected by 18 ligands show that the possible combinations are numerous. These chemical-environment differences are thus expected to produce a range of slightly different chemical shifts for each resonance. Simple stereochemical

considerations also suggest that some resonances should experience this effect more than others.

The X-ray crystallographic results obtained with sample F (made form AA-HSMeBu) show that only the (*S*)-enantiomer is present in the monolayer. On these grounds, we can take the temperature effect on the spectra of Figures 11-15 as truly showing the behavior of a cluster protected by a single chiral ligand. According to the CD results, the cluster containing the smallest e.e. is that of sample A (made form SA-HSMeBu). We thus expected this cluster as that affected by the largest "chemical-environment difference" effect. Figures 17-21 show for sample A the outcome of the equivalent NMR experiments carried out for sample F and shown in Figures 11-15. In keeping with our expectation, all spectral regions are indeed broader and less resolved than those of sample F.

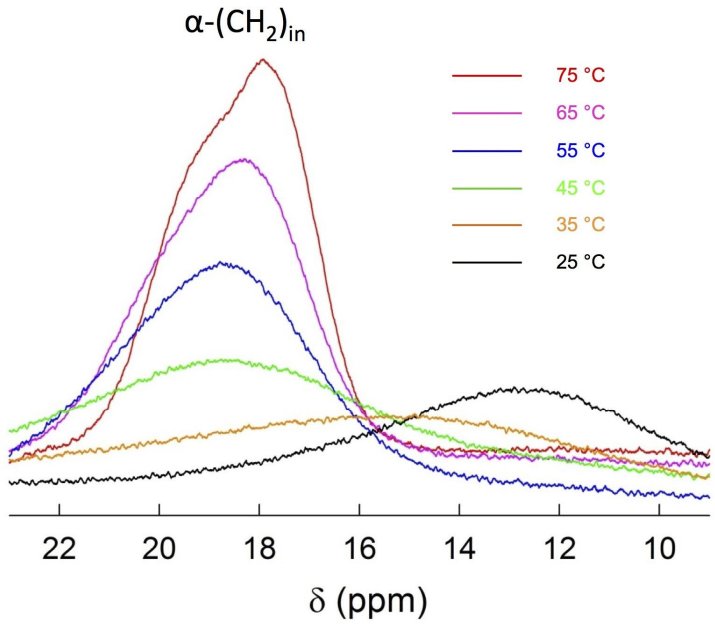

Figure 17. Variation of the position of the α-$(CH_2)_{in}$ resonance of 3 mM $Au_{25}(SMeBu)_{18}^{0}$ (sample A) as the temperature changes from 25 to 75 °C.

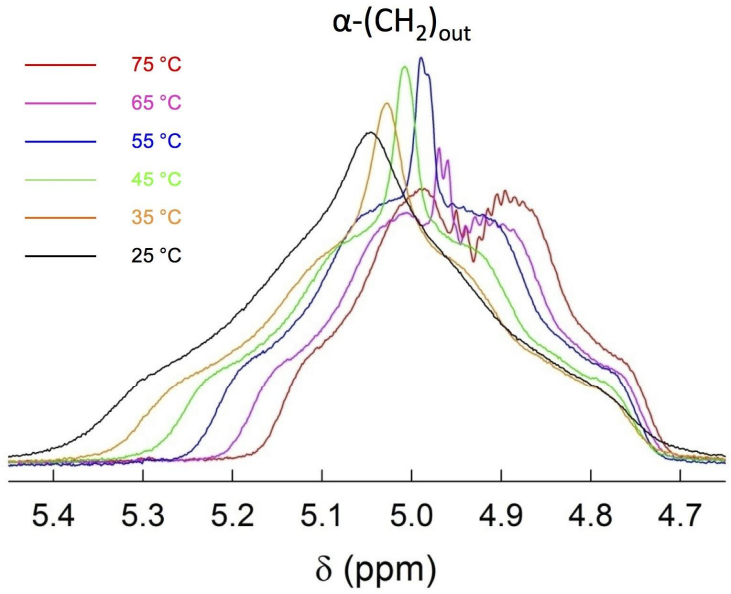

Figure 18. Variation of the position of the α-$(CH_2)_{out}$ resonance of 3 mM $Au_{25}(SMeBu)_{18}^0$ (sample A) as the temperature changes from 25 to 75 °C.

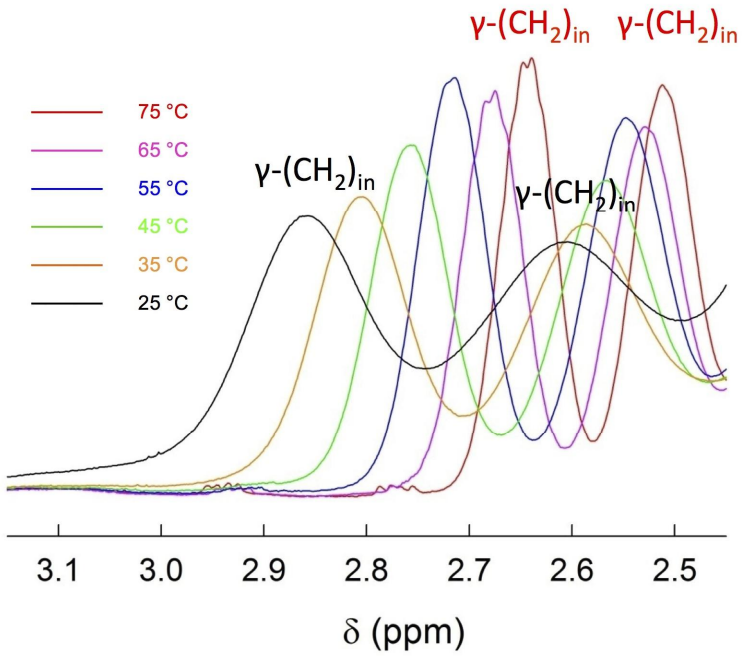

Figure 19. Variation of the position of the γ-$(CH_2)_{in}$ resonances of 3 mM $Au_{25}(SMeBu)_{18}^0$ (sample A) as the temperature changes from 25 to 75 °C.

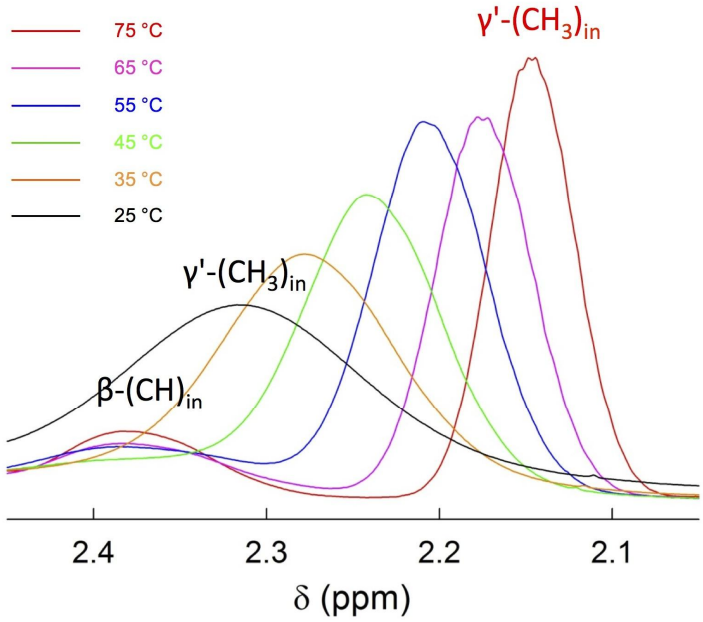

Figure 20. Variation of the position of the β-$(CH)_{in}$ and γ'-$(CH_3)_{in}$ resonances of 3 mM $Au_{25}(SMeBu)_{18}^0$ (sample A) as the temperature changes from 25 to 75 °C.

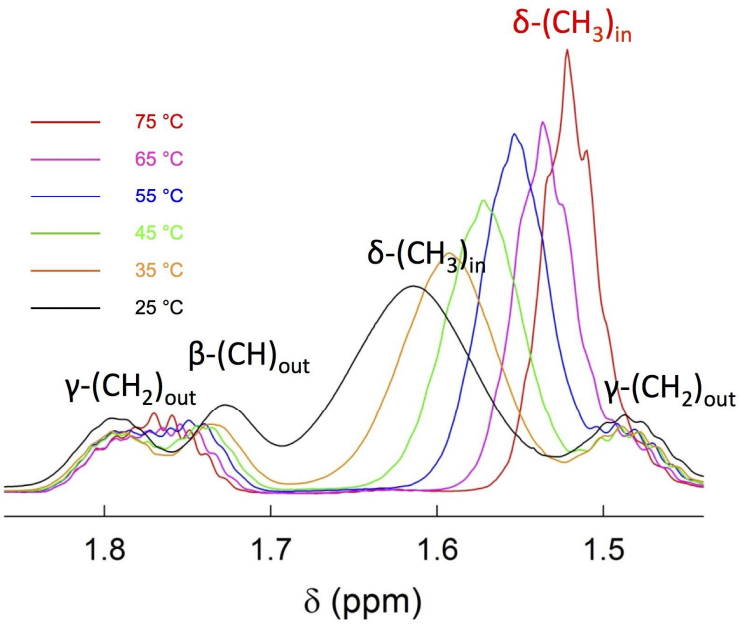

Figure 21. Variation of the position of the β-$(CH)_{out}$, the δ-$(CH_3)_{in}$, and the couple of γ-$(CH_2)_{out}$ resonances of 3 mM $Au_{25}(SMeBu)_{18}^0$ (sample A) as the temperature changes from 25 to 75 °C.

On these grounds, the question now is: can we use the peak width to estimate the average e.e. of the thiolates forming the monolayer of a given

cluster sample? It is quite obvious that some resonances are not particularly suitable for the purpose because of either the lack of significant effects or the complex multiplicity of the signal. On the other hand, the α-$(CH_2)_{out}$ resonance appears as particularly suitable. The peak widths were calculated as full-width-at-half-maximum (FWHM). Figure 22 shows the evolution of the α-$(CH_2)_{out}$ resonance as a function of the specific sample (from A to G) and thus of the corresponding e.e., at 25 °C.

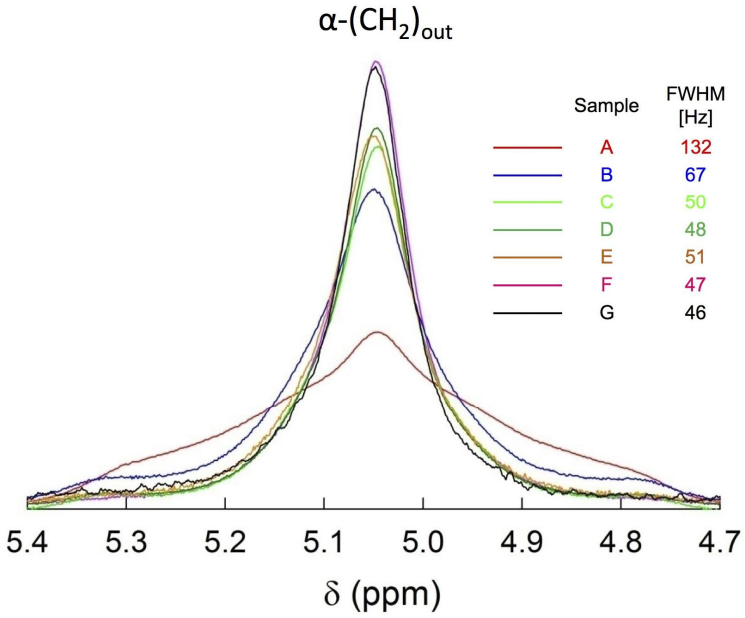

Figure 22. Variation of the width of the α-$(CH_2)_{out}$ resonance for 3 mM $Au_{25}(SMeBu)_{18}^{0}$ samples from A to G, at 25 °C.

Figure 23 shows these FWHM values as a function of the e.e. of the thiol employed in the synthesis of the cluster. A red dashed line connecting the values obtained for the samples with the poorest (A) and maximum e.e. (G) has been added just for the sake of evidencing the nonlinear trend better. Qualitatively, a similar NMR outcome is observed also through analysis of the δ-$(CH_3)_{in}$, the γ'-$(CH_3)_{in}$, and the couple of γ-$(CH_2)_{in}$ resonances. Concerning α-$(CH_2)_{out}$, a similar evolution of the (average) peak width as a function of the specific sample is observed also at 75 °C. Due to the aforementioned experimental issues, sample G could not be studied at this temperature. Figures 24 and 25 show the results obtained α-$(CH_2)_{out}$ at 75 °C, and are thus the equivalent of Figures 22 and 23 obtained at 25 °C.

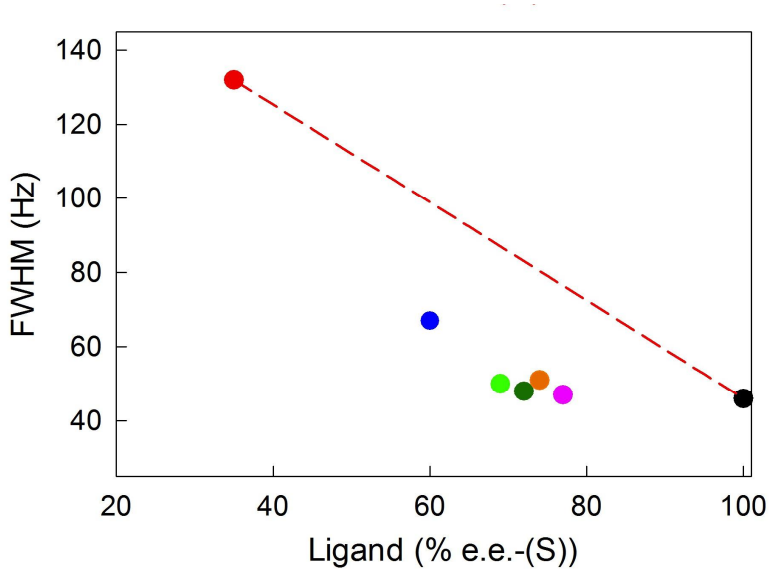

Figure 23. Plot of FWHM obtained at 25 °C as a function of the e.e. of the thiols employed in the syntheses of the corresponding clusters.

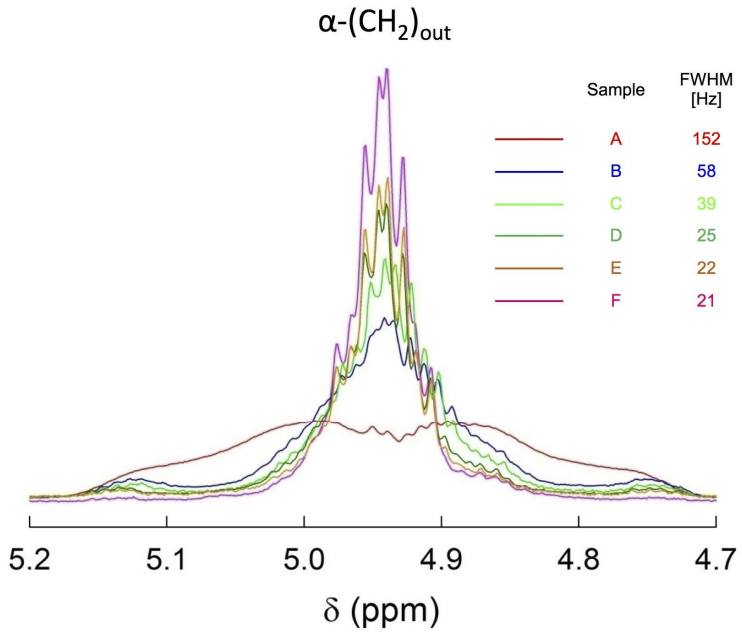

Figure 24. Variation of the width of the α-$(CH_2)_{out}$ resonance for 3 mM $Au_{25}(SMeBu)_{18}^{0}$ samples from A to F, at 75 °C.

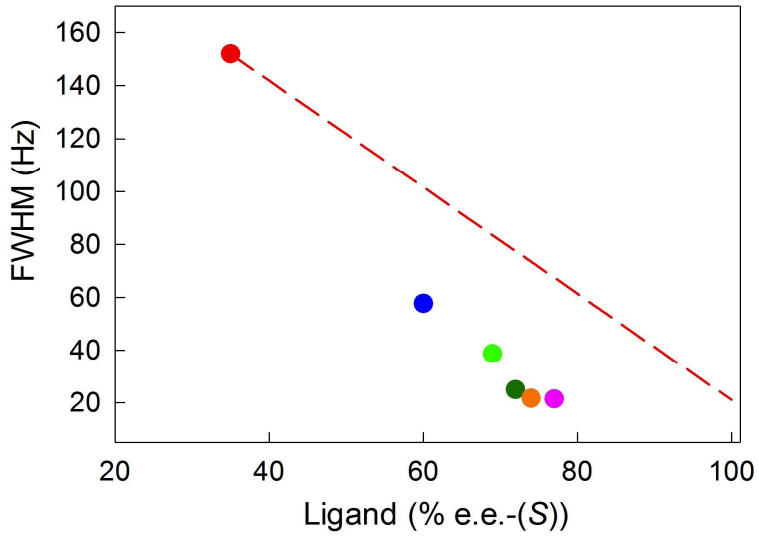

Figure 25. Plot of FWHM obtained at 75 °C as a function of the e.e. of the thiols employed in the syntheses of the corresponding clusters.

These results illustrate in a qualitative but yet convincing manner that at ca. 75% e.e. a saturation limit is reached, at least in terms of the peak width. On the other hand, this outcome is perfectly in line with the CD results and, notably, the X-ray structure of the cluster that should have contained a theoretical 77% e.e. of the (*S*)-enantiomer.

6.4 Conclusions

In this Chapter we aimed at understanding the properties of Au_{25} clusters capped by ligands of different e.e. values. We introduced one methyl group in place of one hydrogen at position β (with respect to the sulfur atom) along a butanethiolate chain, and this introduces a stereogenic center. We found that commercially available racemic 2-methyl-1-butanethiol samples, as obtained from two companies, are nonracemic but possess an e.e. of the (*S*)-enantiomer, as verified through synthesis of the (*S*)-enantiomer. We prepared several $Au_{25}(SMeBu)_{18}^{0}$ clusters and characterized them. ^{1}H NMR spectroscopy and CD spectroscopy indicated that as the e.e. of the thiol employed reaches a value of ca. 75%, the resulting Au_{25} clusters only contain the (*S*)-thiolate. These conclusions were perfectly confirmed by solving with X-ray crystallography the single crystal structure of a cluster that, in principle, should have contained thiols possessing 77% e.e. of the (*S*)-enantiomer: the structure shows that only the (*S*)-enantiomer is capping the Au_{25} core. We thus observed, for the first time, the

phenomenon of spontaneous resolution for an MPC. Overall, these results thus nicely merge to point to the occurrence of the phenomenon of spontaneous resolution. We are still working on this project, for example about the mechanism of spontaneous resolution. Nonetheless, we can already conclude that this is an unprecedented result for MPCs. It also is a very important result on a more general viewpoint, particularly if one considers that the opportunity of studying what happens in an atomically precise system composed by as many as 18 chiral, identical molecules assembled onto a "surface" is indeed only possible for molecular MPCs.

6.5 Experimental Section

The UV-vis spectra were obtained at 0.1 mM concentration in DCM, with 2 mm cuvettes. We used a Thermo Scientific Evolution 60S spectrophotometer or, during syntheses, an Ocean Optics QE65000 spectrophotometer equipped with a DH-2000-BAL light source. The spectra resolution was 1 or 0.8 nm, respectively.

The electrochemical experiments were carried out in DCM/0.1 M TBAH, under an Ar atmosphere in a glass cell thermostatted at 25 °C, using a 0.55 mm radius glassy-carbon disk electrode. The counter electrode was a Pt wire and an Ag wire served as the quasi-reference electrode. The latter was then calibrated against the KCl saturated calomel electrode, SCE. We used a CHI 660c electrochemical workstation and the positive feedback correction was applied.

The polarimetric measurements were performed with a polarimeter JASCO P1010, at 589 nm (the sodium D line), with standard (10 cm) optical path. As a reference, we employed the enantiomeric pure (*S*)-(−)-2-methyl-1-butanol.

The solvent employed in the CD measurements was acetonitrile (cutoff wavelength at 200 nm). The thiols were analyzed at 3 mM concentration, using cuvettes with an optical path of 10 mm. The instrument employed was a spectropolarimeter JASCO 810. The measurements were carried out at a scan rate of 50 nm min^{-1} and 2 or 4 s as the response time. The spectra correspond to 16 accumulations.

^{1}H NMR spectra were obtained at ~1 mM MPC concentration in C_6D_6 with a Bruker Avance DMX-600 MHz spectrometer equipped with a 5 mm TX-1 x,y,z-gradient powered, triple-resonance inverse probe operating at 599.90 MHz. The temperature was controlled (25 ± 0.1 °C, unless otherwise indicated) with a Bruker BVT-300 automatic temperature controller. Chemical shifts are in part per millions (δ) units with reference to tetramethylsilane used as an internal standard.

To ensure a complete relaxation for all the resonances, integral values for the proton spectra were obtained by a prescan delay of 10 s. The proton assignments were performed by standard chemical shift correlations as well as by 2D correlation spectroscopy (COSY), total correlation spectroscopy (TOCSY), and nuclear Overhauser enhancement spectroscopy (NOESY) experiments, as previously done for $Au_{25}(SC_2H_4Ph)_{18}$.[40] FWHM were calculated using the macro lhcal in TopSpin-Bruker 3.2.

6.6 References

(1) Helgert, C.; Pshenay-Severin, E.; Falkner, M.; Menzel, C.; Rockstuhl, C.; Kley, E. B.; Tunnermann, A.; Lederer, F.; Pertsch, T. Chiral metamaterial composed of three-dimensional plasmonic nanostructures. *Nano Lett*. **2011**, 11, 4400−4404.

(2) Tamura, M.; Fujihara, H. Chiral bisphosphine BINAP-stabilized gold and palladium nanoparticles with small size and their palladium nanoparticle-catalyzed asymmetric reaction. *J. Am. Chem. Soc.* **2003**, 125, 15742–15743.

(3) Zhu, Y.; Wu, Z.; Gayathri, C.; Qian, H.; Gil, R. R.; Jin, R. Exploring stereoselectivity of Au_{25} nanoparticle catalyst for hydrogenation of cyclic ketone. *J. Catal*. **2010**, 271, 155–160.

(4) Knoppe, S.; Bürgi, T. Chirality in Thiolate-Protected Gold Clusters. *Acc. Chem. Res.* **2014**, 47, 1318−1326.

(5) Schaaff, T. G.; Whetten, R. L. Giant gold-glutathione cluster compounds: Intense optical activity in metal-based transitions. *J. Phys. Chem*. *B* **2000**, 104, 2630–2641.

(6) Goldsmith, M. R.; George, C. B.; Zuber, G.; Naaman, R.; Waldeck, D. H.; Wipf, P.; Beratan, D. N. The chiroptical signature of achiral metal clusters induced by dissymmetric adsorbates. Phys. *Chem. Chem. Phys*. **2006**, 8, 63–67.

(7) Gautier, C.; Bürgi, T. Chiral gold nanoparticles. *ChemPhysChem* **2009**, 10, 483–492.

(8) Garzon, I. L.; Reyes-Nava, J. A.; Rodriguez-Hernandez, J. I.; Sigal, I.; Beltran, M. R.; Michaelian, K. Chirality in bare and passivated gold nanoclusters. *Phys. Rev. B* **2002**, 66, 073403.

(9) Roman-Velazquez, C. E.; Noguez, C.; Garzon, I. L. Circular dichroism simulated spectra of chiral gold nanoclusters: a dipole approximation. *J. Phys. Chem. B* **2003**, 107, 12035–12038.

(10) Noguez, C.; Garzon, I. L. Optically active metal nanoparticles. *Chem. Soc. Rev.* **2009**, 38, 757–771.

(11) Lopez-Acevedo, O.; Tsunoyama, H.; Tsukuda, T.; Hakkinen, H.; Aikens, C. M. Chirality and electronic structure of the thiolate-protected Au_{38} nanocluster. *J. Am. Chem. Soc.* **2010**, 132, 8210–8218.

(12) Provorse, M. R.; Aikens, C. M. Origin of intense chiroptical effects in undecagold subnanometer particles. *J. Am. Chem. Soc.* **2010**, 132, 1302–1310.

(13) Sanchez-Castillo, A.; Noguez, C.; Garzon, I. L. On the origin of the optical activity displayed by chiral-ligand-protected metallic nanoclusters. *J. Am. Chem. Soc.* **2010**, 132, 1504–1505.

(14) Jadzinsky, P. D.; Calero, G.; Ackerson, C. J.; Bushnell, D. A.; Kornberg, R. D. Structure of a thiol monolayer-protected gold nanoparticle at 1.1 Å resolution. *Science* **2007**, 318, 430–433.

(15) Qian, H.; Eckenhoff, W. T.; Zhu, Y.; Pintauer, T.; Jin, R. Total structure determination of thiolate-protected Au_{38} nanoparticles. *J. Am. Chem. Soc*. **2010**, 132, 8280–8281.

(16) Gautier, C.; Bürgi, T. Chiral inversion of gold nanoparticles. J*. Am. Chem. Soc.* **2008**, 130, 7077–7084.

(17) Gautier, C.; Bürgi, T. Chiral N-isobutyryl-cysteine protected gold nanoparticles: preparation, size selection, and optical activity in the UV-vis and infrared. *J. Am. Chem. Soc*. **2006**, 128, 11079–11087.

(18) Yao, H.; Miki, K.; Nishida, N.; Sasaki, A.; Kimura, K. Large optical activity of gold nanocluster enantiomers induced by a pair of optically active penicillamines. *J. Am. Chem. Soc*. **2005**, 127, 15536–15543.

(19) Yao, H.; Fukui, T.; Kimura, K. Chiroptical responses of D-/L-penicillamine-capped gold clusters under perturbations of temperature change and phase transfer. *J. Phys. Chem. C* **2007**, 111, 14968–14976.

(20) Knoppe, S.; Dharmaratne, A. C.; Schreiner, E.; Dass, A.; Bürgi, T. Ligand exchange reactions on Au_{38} and Au_{40} clusters: a combined circular dichroism and mass spectrometry study. *J. Am. Chem. Soc*. **2010**, 132, 16783–16789.

(21) Schaaff, T. G.; Knight, G.; Shafigullin, M. N.; Borkman, R. F.; Whetten, R. L. Isolation and Selected Properties of a 10.4 kDa Gold: Glutathione Cluster Compound. *J. Phys. Chem. B* **1998**, 102, 10643-10646.

(22) Gautier, C.; Taras, R.; Gladiali, S.; Bürgi, T. Chiral 1,1′-binaphthyl-2,2′-dithiol-stabilized gold clusters: Size separation and optical activity in the UV–vis. *Chirality* **2008**, 20, 486-493

(23) Zhu, M.; Qian, H.; Meng, X.; Jin, S.; Wu, Z.; Jin, R. Chiral Au_{25} nanospheres and nanorods: synthesis and insight into the origin of chirality. *Nano Lett*. **2011**, 11, 3963-3969.

(24) Yanagimoto, Y.; Negishi, Y.; Fujihara, H.; Tsukuda, T. Chiroptical activity of BINAP-stabilized undecagold clusters. *J. Phys. Chem. B* **2006**, 110, 11611-11614.

(25) Qi, H.; Hegmann, T. Postsynthesis racemization and place exchange reactions. Another step to unravel the origin of chirality for chiral ligand-capped gold nanoparticles. *J. Am. Chem. Soc.* **2008**, 130, 14201-14206.

(26) Dolamic, I.; Knoppe, S.; Dass, A.; Bürgi. T. First enantioseparation and circular dichroism spectra of Au_{38} clusters protected by achiral ligands. *Nature Communications* **2012**, 3, 798, 1-6.

(27) Jiang, D.; Chen, W.; Whetten, R. L.; Chen, Z. What protects the core when the thiolated Au cluster is extremely small? *J. Phys. Chem. C* **2009**, 113, 16983-16987.

(28) Tlahuice, A.; Garzon, I. L. On the structure of the $Au_{18}(SR)_{14}$ cluster. *Phys. Chem. Chem. Phys*. **2012**, 14, 3737-3740.

(29) Tlahuice, A.; Garzon, I. L. Structural, electronic, optical, and chiroptical properties of small thiolated gold clusters: the case of Au_6 and Au_8 cores protected with dimer $[Au_2(SR)_3]$ and trimer $[Au_3(SR)_4)]$ motifs. *Phys. Chem. Chem. Phys.* **2012**, 14, 7321-7329.

(30) Knoppe, S.; Kothalawala, N.; Jupally, V. R.; Dass, A.; Bürgi, T. Ligand dependence of the synthetic approach and chiroptical properties of a magic cluster protected with a bicyclic chiral thiolate. *Chem. Commun*. **2012**, 48, 4630-4632.

(31) Kumar, S.; Jin, R. Water-soluble $Au_{25}(Capt)_{18}$ nanoclusters: synthesis, thermal stability, and optical properties. *Nanoscale* **2012**, 4, 4222-4227.

(32) Cao, T.; Jin, S.; Wang, S.; Zhang, D.; Zhu, X. A comparison of the chiral counterion, solvent, and ligand used to induce a chiroptical response from Au_{25}^{-} nanoclusters. *Nanoscale* **2013**, 5, 7589-7595

(33) http://www.sigmaaldrich.com/catalog/product/aldrich/a83407.

(34) Kricheldorf, H. R.; Sun, S.; Gerken, A.; Chang, T. Polymers of Carbonic Acid. 22. Cholesteric Polycarbonates Derived from (*S*)-((2-Methylbutyl)thio)hydroquinone or Isosorbide. *Macromolecules* **1996**, 29, 8077-8082.

(35) Dainese, T.; Antonello, S.; Gascón, J. A.; Pan, F.; Perera, N. V.; Ruzzi, M.; Venzo, A.; Zoleo, A.; Rissanen, K.; Maran, F. $Au_{25}(SEt)_{18}$, a Nearly Naked Thiolate-Protected Au_{25} Cluster: Structural Analysis by Single Crystal X-ray Crystallography and Electron Nuclear Double Resonance. *ACS Nano* **2014**, 8, 3904–3912.

(36) Antonello, S.; Arrigoni, G.; Dainese, T.; De Nardi, M.; Parisio, G.; Perotti, L.; René, A.; Venzo, A.; Maran, F. Electron Transfer through 3D Monolayers on Au_{25} Clusters. *ACS Nano* **2014**, 8, 2788–2795.

(37) Venzo, A.; Antonello, S.; Gascón, J. A.; Guryanov, I.; Leapman, R. D.; Perera, N. V.; Sousa, A.; Zamuner, M.; Zanella, A.; Maran, F. Effect of the Charge State (z = -1,0,+1) on the Nuclear Magnetic Resonance of Monodisperse $Au_{25}[S(CH_2)_2Ph]_{18}^{z}$ Clusters. *Anal. Chem.* **2011**, 83, 6355–6362.

(38) Schurig, V. *Differentiation of enantiomers, Part II.*, *Series: Topic in Current Chemistry*, Vol. 341. Springer International Publishing: Switzerland, **2013**.

(39) Si, S.; Gautier, C.; Boudon, J.; Taras, R.; Gladiali, S.; Bürgi, T. Ligand Exchange on Au_{25} Cluster with Chiral Thiols. *J. Phys. Chem. C* **2009**, 113, 12966–12969.

(40) Antonello, S.; Perera, N. V.; Ruzzi, M.; Gascón, J. A.; Maran, F. Interplay of Charge State, Lability, and Magnetism in the Molecule-like $Au_{25}(SR)_{18}$ Cluster. *J. Am. Chem. Soc*. **2013**, 135, 15585–15594.

6.7 Acknowledgements

A special thank is due to Alfonso Venzo for his invaluable assistance in the NMR studies.